MINERALOGY AND PETROLOGY OF THE APOLLO 12 LUNAR SAMPLE

J. A. WOOD, U. B. MARVIN, J. B. REID, Jr.,
G. J. TAYLOR, J. F. BOWER, B. N. POWELL,
and J. S. DICKEY, Jr.

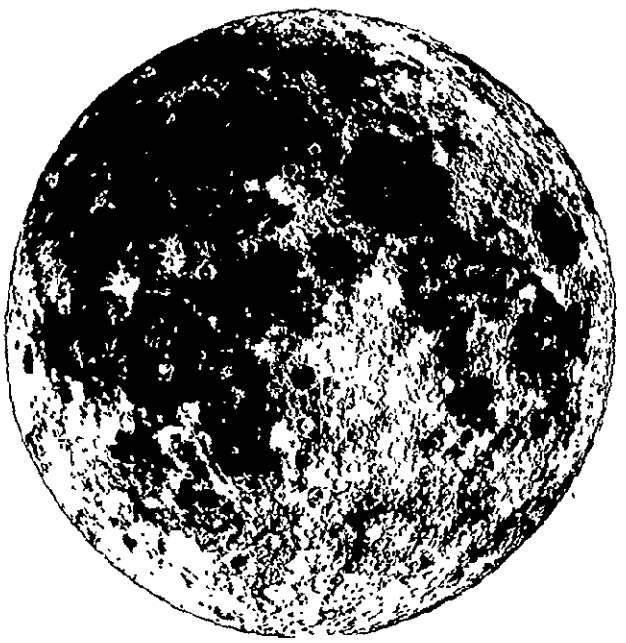

Smithsonian Astrophysical Observatory
SPECIAL REPORT 333

Research in Space Science
SAO Special Report No. 333

MINERALOGY AND PETROLOGY OF THE APOLLO 12 LUNAR SAMPLE

J. A. Wood, U. B. Marvin, J. B. Reid, Jr., G. J. Taylor,
J. F. Bower, B. N. Powell, and J. S. Dickey, Jr.

May 20, 1971

Smithsonian Institution
Astrophysical Observatory
Cambridge, Massachusetts 02138

TABLE OF CONTENTS

ABSTRACT

Page

We sectioned, examined, and classified 499 coarse (>0.6 mm) particles from five of the Apollo 12 soil samples: 12070, collected on the rim of Surveyor Crater; 12032 and 12037, from the rim of Bench Crater; 12033, from a light-colored layer in a trench dug in the rim of Head Crater; and 12001, collected between craters. 14

Samples 12070 and 12001 appear to be well-gardened soils, random mixtures of debris fragments, most of which derive from bedrock near at hand. The particles consist largely of mare basalts or degradation products thereof (microbreccia, cindery glasses of composition equivalent to the bulk soil), samples of the volcanic flows of Eratosthenian age that cover this portion of Oceanus Procellarum. Textures and mineral compositions of virtually all the basalt fragments we examined point to their formation in one or more relatively thin (~10 m) lava flows. 20, 139, 111, 25, 189

All the soils contain about 10% of particles that are noritic in composition (low-Ca pyroxenes and calcic plagioclase in nearly equal amounts), but most of these have the textures of thermally recrystallized microbreccias. Many of the Apollo 11 anorthosites (a type that was not found in the Apollo 12 soil) have similar textures; we suggest that primary igneous anorthosites and norites were brecciated and recrystallized in an early, hot regolith. 63, 89, 238

Soils 12032 and 12033 contain major amounts of a component alien to the local soil (as represented by 12070 and 12001) in the form of twisted, ropy particles of brownish glass. These are noritic in composition, but apparently derive from a different source than the crystalline norites in the soil. We believe the latter came from small terra exposures in the vicinity of the Apollo 12 site and from beneath the local mare basalt, while the ropy glasses are ejecta from the Crater Copernicus, samples of a Copernican ray that crosses the Apollo 12 site. 14, 111, 121, 211, 222, 224

Page

227, 228 Petrological characteristics of the lunar rocks and geophysical (gravity, topography) properties of the lunar surface are consistent with
234 a structural model in which Oceanus Procellarum and the non-mascon maria are underlain by ~25 km of norite (with a thin covering of basalt), the mascon maria by lunar mantle material (covered by >1 km of basalt), and the highlands by ~25 km of anorthosite. Most of this structure ap-
236 pears to have developed during crystallization and differentiation of an early lunar surface magma system; the mare basalts were erupted in a
239 later episode of igneous activity, probably owing to decay of long-lived radioactivity at depth in the Moon.

We found several unusual particles among the 499 studied: A
107, 203 rhyolite or micrographic granite rich in K and Fe; an agglomeration of
165, 214, glassy spherules of composition unmatched by any other known lunar
225 material (high in normative ilmenite and mafics, low in plagioclase);
177 and a meteorite, more similar to Type II carbonaceous chondrites than to any other known meteorite class.

RESUME

Page

Nous avons sectionné, examiné et classé 499 particules grossières (>0,6 mm) provenant de cinq échantillons de sol du site Apollo 12: 12070, récolté sur le bord du Surveyor Crater; 12032 et 12037, du bord du Bench Crater; 12033, d'une couche de couleur claire dans une tranchée creusée dans le bord du Head Crater; et 12001, récolté entre des cratères. 14

12070 et 12001 se révèlent être des sols bien jardinés, mélanges homogènes de débris provenant principalement du bedrock le plus proche. Les particules consistent surtout en basaltes de Mers ou de leurs produits de dégradation (microbrèches, cendres vitreuses de composition équivalant à celle du sol en vrac), qui sont des échantillons des coulées volcaniques d'âge Eratosthénien qui couvrent cette partie de l'Océan des Tempêtes. Les textures et compositions minéralogiques de presque tous les fragments de basaltes que nous avons examinés indiquent qu'ils se sont formés dans une ou plusieurs coulée(s) de lave relativement mince(s) (±10 m). 20, 139, 111, 25, 189

Tous les sols contiennent environ 10% de particules de composition noritique (pyroxènes à faible teneur en Ca et plagioclase calcique, en quantités à peu près égales), mais la plupart d'entre elles ont des textures de microbrèches recristallisées thermiquement. Beaucoup d'anorthosites du site Apollo 11 (un type qui n'a pas été trouvé dans le sol du site Apollo 12) ont des textures similaires; nous proposons que les anorthosites et les norites primaires, ignées, ont été bréchifiées et recristallisées dans un régolithe précoce et chaud. 63, 89, 238

Les sols 12032 et 12033 contiennent des quantités importantes d'un composant étranger au sol local (représenté par 12070 et 12001) formé de particules tordues, cordées, de verre brunâtre. Elles ont une composition noritique, mais elles dérivent apparemment d'une source différente de celle des norites cristallisées du sol. Nous supposons que ces dernières sont venues 14, 111, 121, 211

Page

222 de petits affleurements de Continent proches du site Apollo 12 et de dessous le basalte local de Mer, alors que les verres cordés sont des projections du
224 Cratère Copernic, des échantillons d'un rayon Copernicien qui traverse le site Apollo 12.

227, 228 Les caractères pétrologiques des roches lunaires et les propriétés géophysiques de la surface lunaire (gravité, topographie) répondent de façon
234 cohérente à un modèle structural suivant lequel l'Océan des Tempêtes et les Mers sans mascon recouvrent ±25 km de norite (couverte d'une mince couche de basalte), les Mers à mascon recouvrent du matériel de manteau lunaire (avec moins d'un km de basalte) et les continents sont recouverts de ±25 km d'anorthosite. Le gros de cette structure semble s'être formé lors de la
236 cristallisation et la différenciation d'un système magmatique ancien de la surface lunaire; les basaltes des Mers ont été emis lors d'un épisode
239 postérieur d'activité ignée, probablement due à une radioactivité à longue période de désintégration, située en profondeur.

Nous avons trouvé de nombreuses particules inhabituelles parmi les 499
107, 203 étudiées: une rhyolite ou un granite micrographique riche en K et Fe; un
165, 214, agrégat de sphérules vitreuses de composition différant de tout autre
225 matériaux lunaire connu (fortes teneurs en ilménite et ferromagnésiens normatifs, faible teneur en plagioclase), ainsi qu'une météorite, plus
177 semblable à une chondrite carbonée du Type II qu'à toute autre classe connue de météorite.

(J. Jedwab)

РЕЗЮМЕ

Из пяти образцов грунта, доставленных "Аполлоном-12", - 12070, взятого с вала кратера Сорвейор; 12032 и 12037 с вала кратера Уступ; 12033 из светлого слоя траншеи, вырытой на валу кратера Мыс; и 12001, взятого между кратерами - нами было выделено, исследовано и расклассифицировано 499 крупных частиц (>0,6 мм).

Образцы 12070 и 12001 представляют собой хорошо перемешанный грунт, однородную смесь осколочных фрагментов, большинство которых извлечено из подстилающего слоя с небольшой глубины. В основном это частицы морских базальтов или продуктов их разрушения (микробреккчии, шлаковых стекол такого же состава, что и грунт в целом), образцы вулканических потоков эратосфеновского возраста, которые покрывают эту часть Океана Бурь. Текстура и минеральный состав фактически всех исследованных нами базальтовых фрагментов свидетельствует о том, что они образовались в одном или нескольких сравнительно тонких (~10 м) лавовых потоках.

Все почвы содержат около 10% частиц норитового состава (бедные кальцием пироксены и кальциевый плагиоклаз почти в равных количествах), но большинство их обладает текстурой микробрекчий, подвергшихся термической рекристаллизации. Сходной структурой обладает большинство анортозитов "Аполлона-11" (в грунте "Аполлона-12" они не найдены); мы предполагаем, что первичные изверженные анортозиты и нориты подверглись брекчированию и рекристаллизации в молодом, горячем реголите.

Образцы 12032 и 12033 в большом количестве содержат компонент, чуждый местному грунту (который представлен образцами 12070 и 12001), в виде вытянутых, изогнутых частиц коричневых стекол.

Страница

Они имеют норитовый состав, но источник их происхождения несом-
121,211 ненно иной, чем у обнаруженных в грунте кристаллических норитов.
Мы полагаем, что последние образовались в небольших материковых
222 выходах в окрестностях "Аполлона-12" и под местными морскими
базальтами, тогда как стекла неправильной формы представляют
224 собой частицы, выброшенные из Коперника и входят в состав луча
этого кратера, пересекающего место посадки "Аполлона-12".

227,228 Петрологические характеристики лунных горных пород и геофизические свойства (сила тяжести, топография) лунной поверхности
234 согласуются со структурной моделью, в которой Океан Бурь и моря, не содержащие масконов, располагаются под ~25-километровым слоем норита (покрытого тонким слоем базальта), моря, содержащие масконы залиты веществом мантии (покрытого слоем базальта толщиной > 1 км), а материки несут ~25-километровый слой анортозита.
236 Большинство этих структур развились, по-видимому, во время кристаллизации и дифференциации в молодой системе поверхностной лунной магмы; морские базальты были извержены в более поздние
239 периоды магматической активности, связанной, вероятно, с распадом долгоживущих радиоактивных изотопов в недрах Луны.

Среди 499 изученных частиц обнаружено несколько необычных:
107,203 богатые K и Fe частицы риолита или микрографического гранита;
165,214, агломераты стеклянных шариков, состав которых не похож на состав
225 известных лунных веществ (богаты ильменитом и основными породами
177 и бедны плагиоклазом); и метеорит, более похожий на углистые хондриты 11 типа, чем на остальные известные нам типы метеоритов.

(А. Н. Симоненко)

Figure I-1. Apollo 12 astronaut with tongs for collecting rock specimens on lunar surface.

Figure I-2. Astronaut driving core tube into lunar soil. The tool carrier (rack at left) and core tube were used on a geological traverse during the second period spent outside the LM.

MINERALOGY AND PETROLOGY OF THE APOLLO 12 LUNAR SAMPLE

J. A. Wood, Ursula B. Marvin, J. B. Reid, Jr., G. J. Taylor, J. F. Bower, B. N. Powell, and J. S. Dickey, Jr.

I. INTRODUCTION

The rock and soil samples returned by the Apollo 12 astronauts were collected from several sites in the vicinity of the Lunar Module, Intrepid, which landed on the northwest rim of Surveyor Crater in Oceanus Procellarum at Latitude 3.2°S, Longitude 23.4°W.

The stated purpose of the flight, to demonstrate pin-point landing capabilities on the lunar surface, was accomplished with a high degree of success when astronauts Charles Conrad, Jr., and Alan L. Bean guided the Module to the crater rim within 600 m of the Surveyor 3 spacecraft. The landing took place on November 19, 1969, at 2:12 AM EST. During the next 16 hr, the astronauts spent two 4-hr periods on the lunar surface, performing experiments and collecting samples (Figures I-1 and I-2).

It is our purpose to unravel the geological history of the Moon, insofar as possible, from mineralogical and petrological studies of the rock fragments occurring in the lunar soils.

This work was supported in part by contract NAS 9-8106 from the National Aeronautics and Space Administration.

Geological Setting

Oceanus Procellarum is a vast, dark, lowland area occupying more than 3×10^6 km^2 near the western margin of the Earth-facing lunar disk. It is the largest topographic feature of the Moon and the only lowland area designated as an "ocean" rather than a "sea." It extends from about Latitude 40°N to 5°S, curving southeastward in such a way that its northerly portions extend from 45° to 75°W and its southerly portions extend from 20° to 60°W. Unlike most of the smaller maria, the Oceanus has borders that are irregular and, in many places, poorly defined. To the west, the dark basalt flows of Oceanus Procellarum border ancient highlands, flooding the "oceanward" rims and floors of innumerable older craters along a deeply embayed "shoreline." To the north, east, and south some of the Procellarum flows overlap or surround rugged exposures of terra material or of ejecta from the Imbrium basin, while elsewhere they merge imperceptibly with the dark basalts filling adjacent depressions such as Sinus Roris, Mare Imbrium, and Mare Nubium. "Islands" of older materials protruding through the flows indicate that, in the region of the landing site, the mare basalts are relatively thin.

A general view of Oceanus Procellarum and its relationship to other lunar features is shown in the Lunar Orbiter photograph of Figure I-3. A regional topographic chart is reproduced in Figure I-4. Here the landing site is seen to lie about 450 km south of the border of Mare Imbrium and 370 km south of the Crater Copernicus, which is approximately 90 km in diameter and 3 km deep. The Fra Mauro region, site of the Apollo 14 landing, lies about 225 km to the east-southeast. The most prominent feature near the Apollo 12 site is the Crater Lansberg, 40 km in diameter, about 120 km to the west. Figures I-5 and I-6 show a Lunar Orbiter photograph and the corresponding geological map of the area surrounding the landing site.

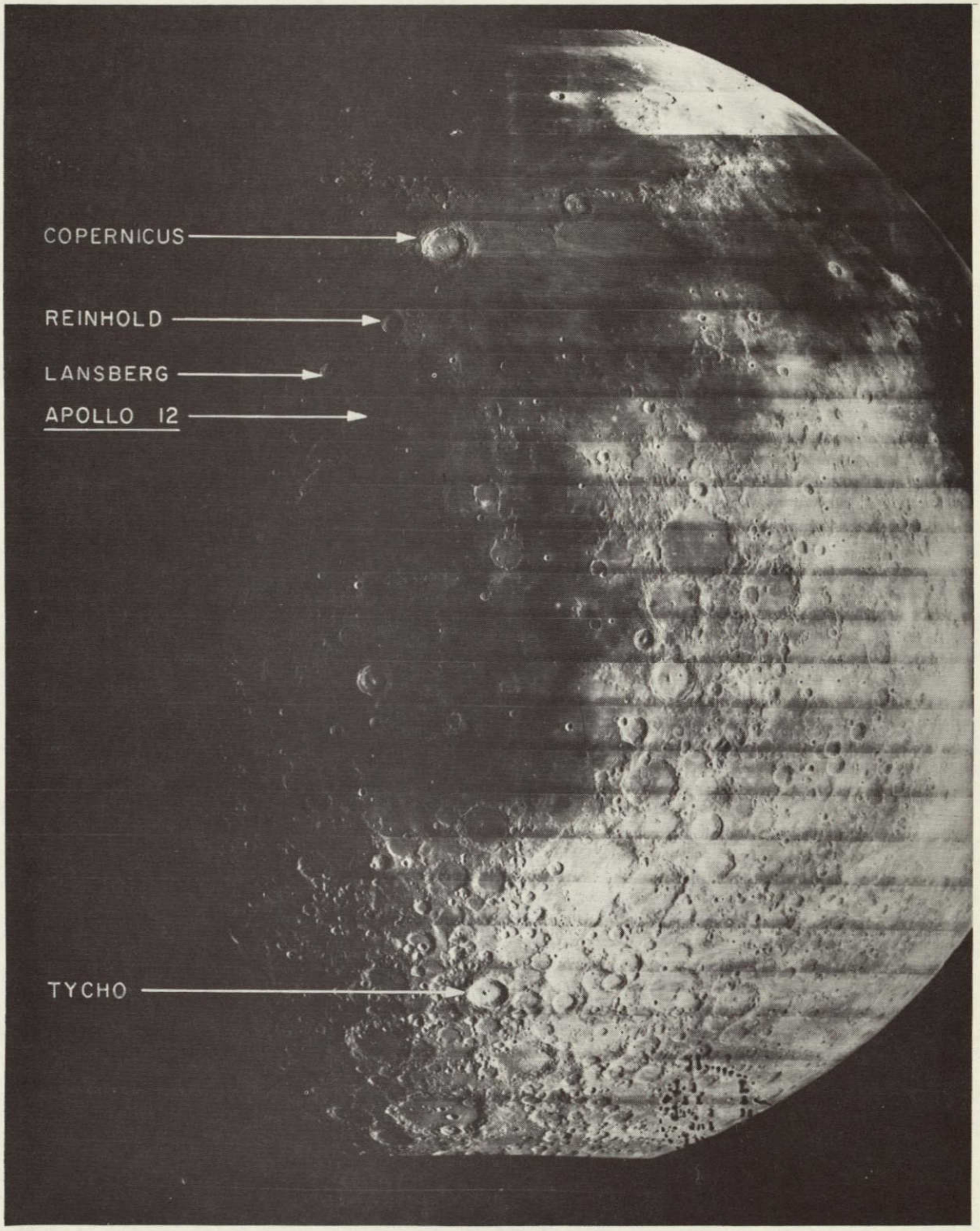

Figure I-3. Lunar Orbiter photograph IV-120M, showing the southeastern portion of Oceanus Procellarum and the Apollo 12 landing site in relation to the craters Copernicus, Reinhold, Lansberg, and Tycho.

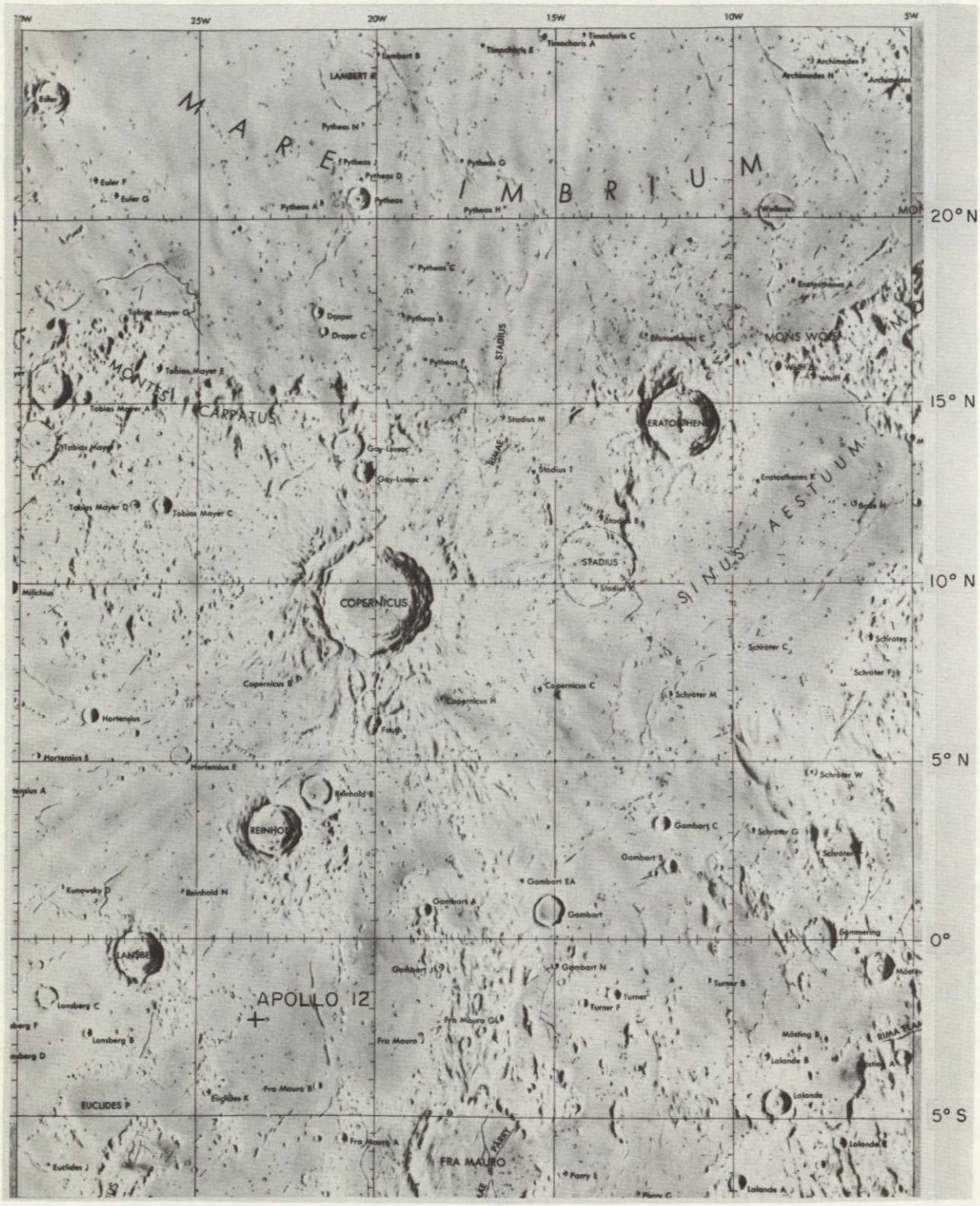

Figure I-4. Topographic chart of the region extending from the Apollo 12 landing site to the southern portion of Mare Imbrium. Scale: each 5° of longitude or latitude at the equator = 150 km. (From Lunar Planning Chart LOC - 2, prepared by the Air Force for NASA, 1969.)

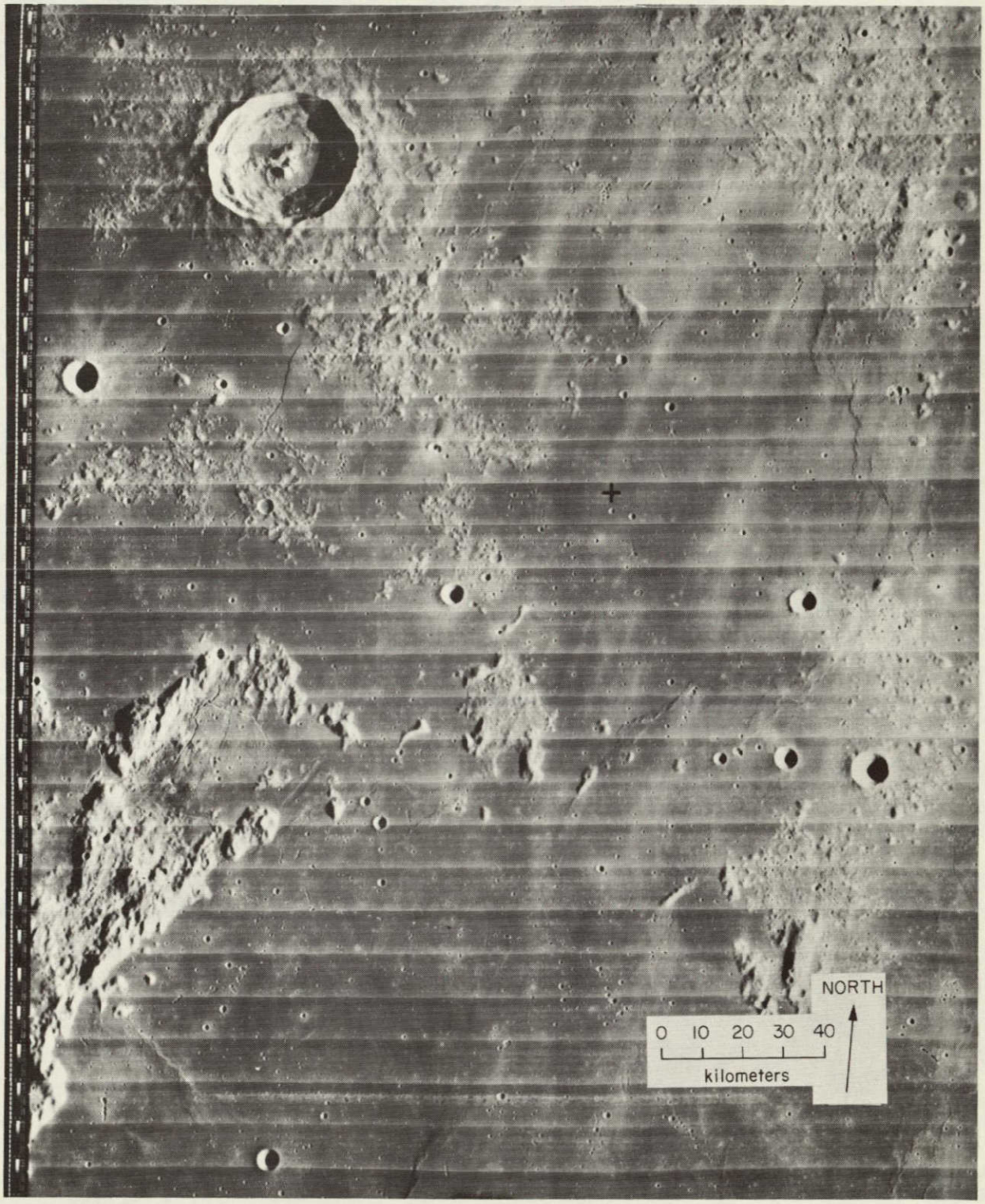

Figure I-5. Lunar Orbiter photograph IV-84H$_3$, showing topography and geological formations in the area of the Apollo 12 landing site (+). Note light streaks, which are part of the ray system centered on Copernicus. The crater at upper left is Lansberg.

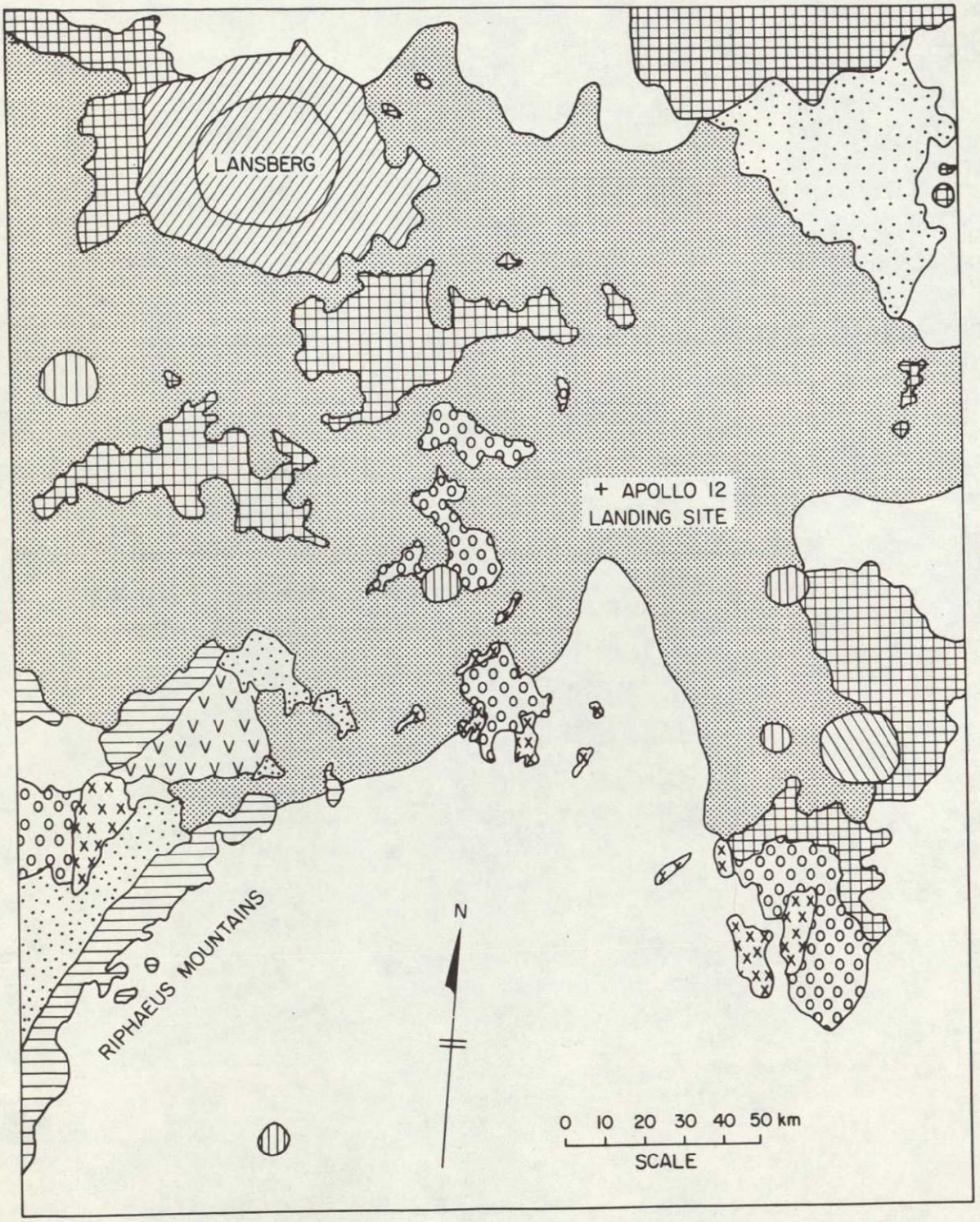
LANSBERG
+ APOLLO 12
LANDING SITE
RIPHAEUS MOUNTAINS
N
0 10 20 30 40 50 km
SCALE

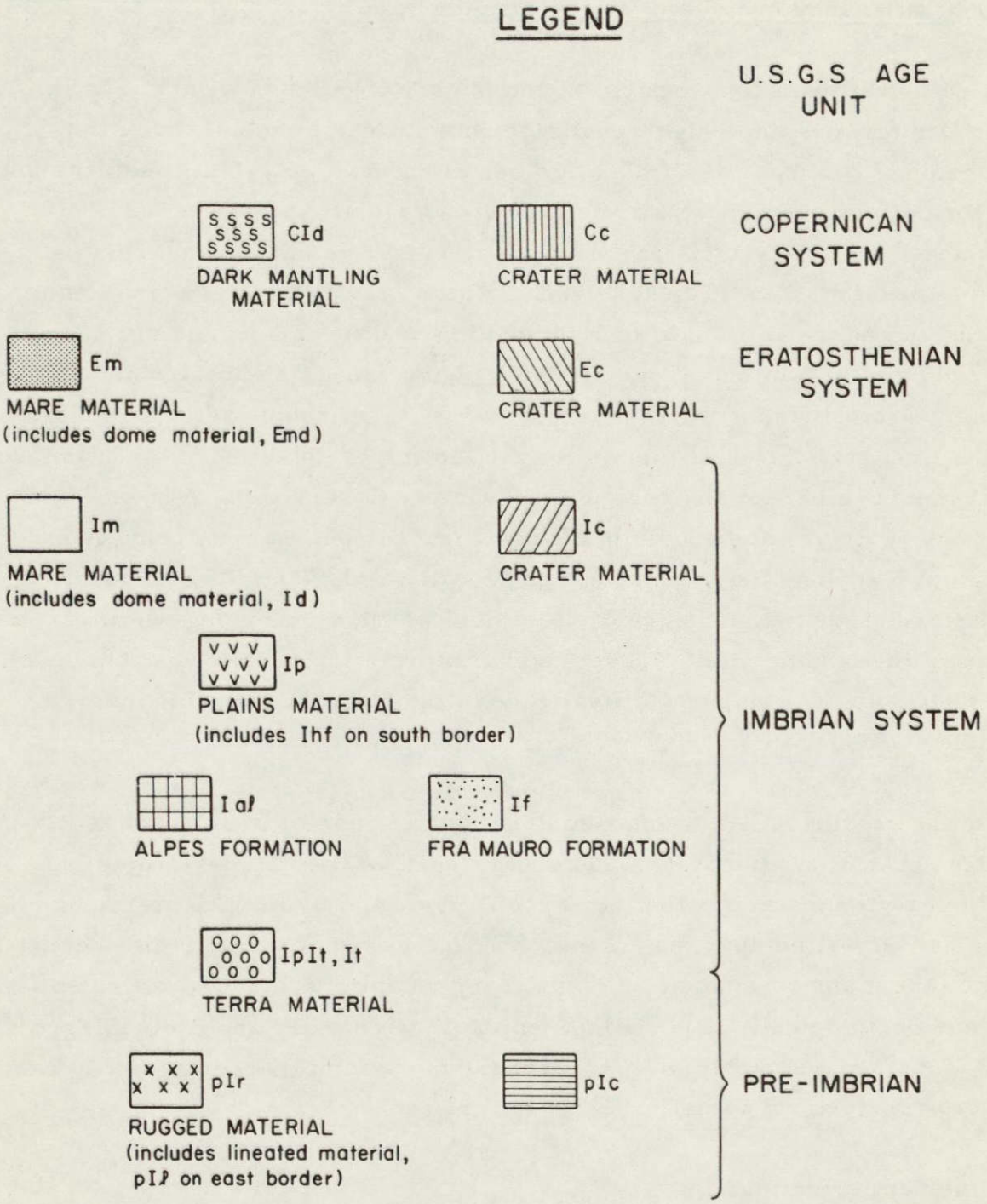

Figure I-6. Facing page, geological formations in the vicinity of the Apollo 12 site; same area as covered by Figure I-5. Above, legend to map. (Geology is taken from the U. S. Geological Survey Map of the Near Side of the Moon by Wilhelms and McCauley (1971).)

Lunar Stratigraphy in Relation to the Landing Site

Geological maps and sections of the Moon have been worked out from Lunar Orbiter and other high-resolution photographs by members of the Astrogeology Branch of the U. S. Geological Survey. The lunar features and rock formations are separated into four broad age groups on the basis of superposition, cross-cutting relationships, crater densities, and relative states of preservation. The key event in lunar history is the excavation of the Imbrium basin: all older rock formations and topographic features are referred to as pre-Imbrian; successively younger ones are designated as Imbrian, Eratosthenian, or Copernican. This terminology reflects the fact that the first stratigraphic column for the Moon was established by Shoemaker and Hackman (1962) for the region of the Crater Copernicus. Although numerous revisions and subdivisions have proved necessary in subsequent geological mapping, the main sequence is still valid. The map, Figure I-6, shows the distribution and ages of 11 geological units occurring within some 150 km of the landing site. All geological information in this report is taken from the Geological Map of the Near Side of the Moon by Wilhelms and McCauley (1971).

In the interpretation of lunar geology it is of special importance to distinguish between newly crystallized rocks, such as basaltic lava flows, and newly excavated materials that have been pulverized by impact-cratering events and deposited upon the surface. Such superimposed detritus, designated on the maps by a small "c," is "young" stratigraphically, but chemically and petrologically it is still a sample of some older and deeper layer in the Moon. Shock metamorphism transforms a small percentage of impact ejecta to new textural varieties of the parent rock.

Pre-Imbrian formations

The pre-Imbrian formations of the Moon include most of the light-colored, heavily cratered terra materials. Terra (land) is used as the complement to mare (sea) in preference to "highlands," which implies a marked topographic

contrast. The terrae make up two-thirds of the near side and nearly all of the far side of the Moon. They are the oldest portions of the lunar crust.

The pre-Imbrian, and all younger, formations are subdivided on the basis of their textural and structural characteristics. Those appearing in Figure I-6 are pre-Imbrian rugged (pIr) and pre-Imbrian crater (pIc) material. Within the map area, however, most terra materials are classed as Imbrian (It), or gradational between Imbrian and pre-Imbrian (IpIt). Exposures of these materials lie within 25 km northwest of the landing site. They are the closest formations other than the mare basalts.

Imbrian formations

The Imbrium basin is the largest and one of the youngest of the circular depressions that were sculptured by impacting bodies early in lunar history. The Imbrium event probably excavated a crater that was about 700 km in diameter, 100 km deep, and ringed by mountains alternating with valleys in a concentric pattern of the type we can still see associated with Mare Orientale. Eventually the entire structure was flooded with mare basalts, not only within the central basin but all the way to the outermost ring so that Mare Imbrium is now over 1300 km in diameter. The southernmost portion of the outer rim forms the Carpathian and Apennine mountain ranges.

The vast tonnages of material excavated from the basin were deposited over large areas beyond the perimeter. These ejecta, termed the Fra Mauro Formation, cover extensive areas south of the mountains and almost bury their namesake, the Crater Fra Mauro (with which they have no genetic association). The Imbrian Fra Mauro Formation (If) grades laterally into the Alpes Formation (Ial), which, in turn, grades into older pre-Imbrian materials. The Alpes Formation is distinguished by its blocky texture and may consist in part of Imbrium ejecta and in part of pre-Imbrian bedrock. The closest deposits of Alpes Formation lie within 40 km northwest of the landing site; those of the Fra Mauro lie about 95 km to the northeast.

Smooth plains-forming materials have been subdivided into three groups, two of which are classified as Imbrian, the third is Eratosthenian in age. The oldest plains materials are relatively light-colored and are tentatively classified as volcanic flows or tuff beds. These Imbrian plains materials (Ip), which include the Cayley Formation, are conspicuous in the region of the Crater Fra Mauro and also occur in the Riphaeus Mountains region some 105 km southwest of the landing site. The Cayley Formation is younger than the Fra Mauro Formation but older than the darker-colored mare basalts.

Imbrian mare materials (Im) cover nearly one-third of the Earth-facing side of the Moon including the Apollo 11 landing site in Mare Tranquillitatis. The Apollo 12 site, however, is underlain by younger Eratosthenian basalts. The nearest Imbrian basalts lie about 20 km to the south.

Imbrian crater material (Ic) characterizes the Crater Lansberg, a feature that is somewhat older than the surface flows of mare basalt, which flood the edges of its ejecta blanket. Lansberg may be sculptured in deeper mare material and also in Alpes Formation.

Eratosthenian formations

Eratosthenian mare materials (Em) were added to the lunar geological maps after Lunar Orbiter photographs became available. These mare materials are darker in color and less densely populated with small impact craters than are those designated as Imbrian. At the Apollo 12 landing site, all mare basalts within a radius of some 20 km, and most within 100 km, are mapped as Eratosthenian in age.

The radiometric ages determined on mare basalts from the two Apollo landing sites confirm a somewhat younger age for the specimens from Oceanus Procellarum. Strontium-rubidium ages for basalts from Tranquillity Base are $3.65 \pm 0.05 \times 10^9$ yr (Albee et al., 1970); those for basalts from the Apollo 12 landing site are 3.26 and $3.36 \pm 0.10 \times 10^9$ yr (Papanastassiou and Wasserburg, 1970).

Crater materials of this age group (Ec) are typified by the Crater Eratosthenes, shown in Figure I-4. These craters have lost their original sharpness of profile and are surrounded by ejecta blankets of low albedo, presumably as a result of long-continued micrometeoroid impact.

Copernican formations

Copernicus is the type example of lunar craters with sharp morphological outlines that are the foci of light-colored ejecta blankets and the brilliant rays that become visible at full Moon. The rays streak across other formations and are therefore among the youngest features on the lunar surface. Ray material is not mapped in Figure I-6 but can be seen crossing the Apollo 12 landing site in the photograph, Figure I-5.

If the lunar soils are composed of small fragments, spalled from bedrock, altered and admixed by means of meteoroid impact, which of the rock formations shown in Figure I-6 may we expect to find represented in our samples of the Apollo 12 regolith? This problem will be considered in detail in Section IIIE, where we will attempt to trace the source of each rock type identified in our samples.

Topography of the Landing Site

In the immediate vicinity of the landing craft there is a group of small craters ranging in diameter from 10 to 400 m (see Figure I-7). On the basis of the sharpness of their profiles and the angularity of their ejecta blocks, these craters have been assigned the following relative ages (LSPET, 1970a).

Youngest	Sharp Crater, 14-m diam.; Block Crater, 13-m diam.; Halo Crater, 3-m diam.
	Bench Crater, 70-m diam.
	Surveyor Crater, 200-m diam.; Head Crater, 100-m diam.
Oldest	Middle Crescent Crater, 330-m diam.

Figure I-7. Topography of the Apollo 12 landing site and locations of the soil samples studied in our laboratory. (Enlargement from Lunar Orbiter photograph III-154H_2.)

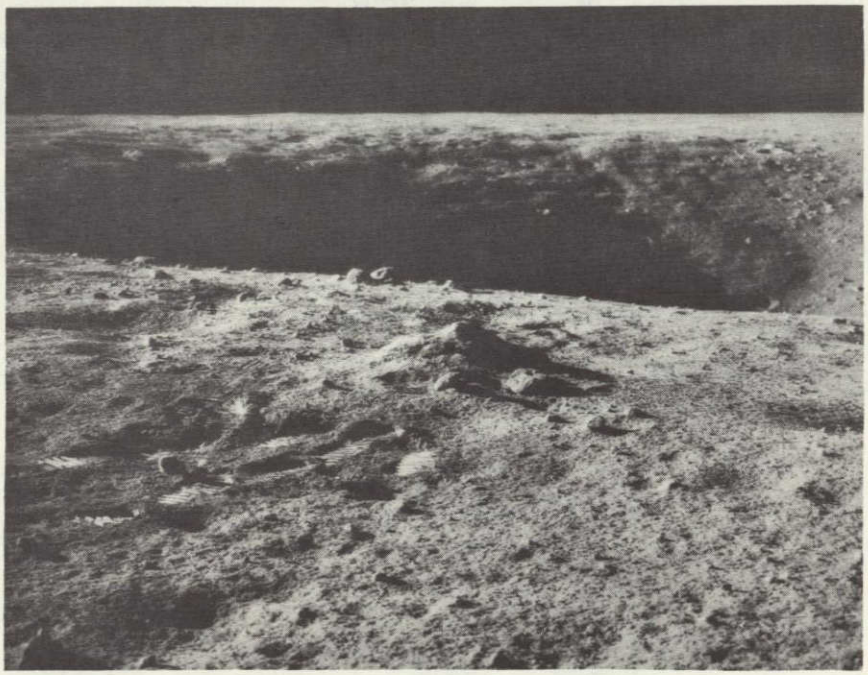

Figure I-8. The approach to Head Crater. Blocky ejecta and astronaut footprints in foreground.

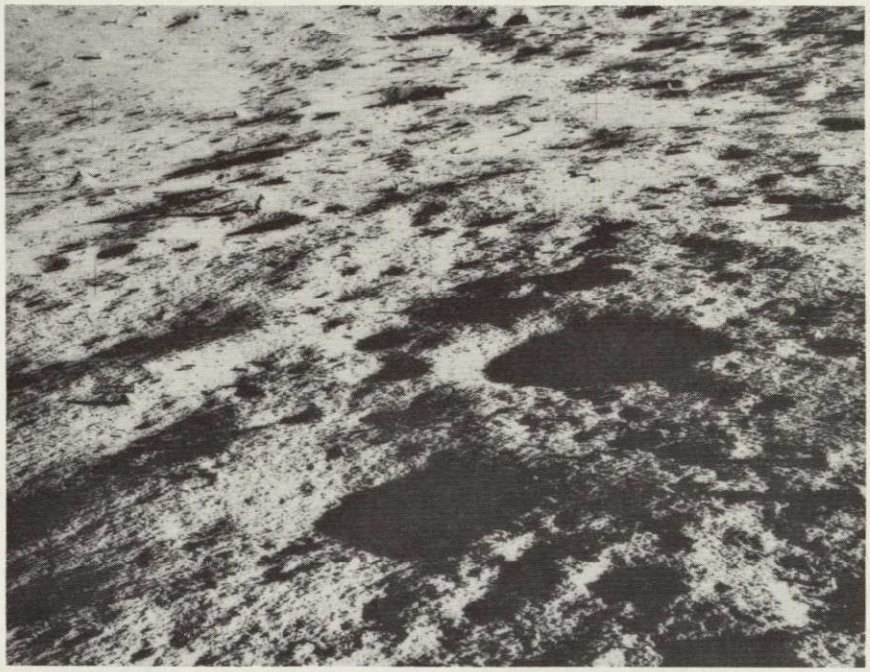

Figure I-9. The rim of Surveyor Crater. The crater bowl is at upper left of picture.

Figure I-10. Gnomon and core tube in use at rim of Bench Crater, which slopes toward upper part of photograph.

Photographs of crater rims on which some of our soil samples were collected are shown in Figures I-8, I-9, and I-10.

The relationships between these craters have been subject to two different interpretations. The LSPET investigators concluded, largely from the fresh, blocky appearance of the rocks in and around them, that all these craters penetrate the thin lunar regolith and are partially excavated in bedrock. On the other hand, Warner (1970) has described all the younger craters as formed within the throwout from Middle Crescent Crater.

The thickness of the regolith at the landing site is estimated at about 1 to 3 m by Swann, Schaber, and Sutton (1970). So thin a soil blanket could easily be penetrated by small cratering events. At Tranquillity Base, where only one or two craters contained blocky material or had profiles suggestive of excavation in bedrock, the thickness of the regolith was estimated by Shoemaker et al. (1970) as 3 to 6 m.

From the lunar module, perched on the rim of Surveyor Crater, the astronauts collected the samples we have studied at sites shown in Figure I-7. While on the lunar surface, they noted streaks of light-colored materials contrasting with the darker soils, both on the surface and in the walls of a trench they dug. They speculated that the light particles might be ray material from Copernicus.

Samples Examined

The samples we have examined consist principally of splits of the "fines" (bulk soil samples of particle size less than 1 cm) collected on the Apollo 11 and 12 missions, as listed in Table I-I.

Major mineralogical and textural differences between the five soil samples we received from the Apollo 12 collections were clearly apparent upon preliminary visual inspection. Samples 12032 and 12033 (Figures I-11 and I-12), for example, abound in particles of ropy glass covered with very fine-grained, gray dust some of which is firmly welded to the glassy surfaces.

Table I-I. Soil samples examined from the Apollo 11 and 12 missions.

Sample number	Size	Weight	Source
		Apollo 11	
10084,108	< 1 mm	5 g	Bulk sample collected at base of the LM ladder.
10085,24	> 1 mm	11	Bulk sample collected at base of the LM ladder.
		Apollo 12	
12070,35	< 1 mm	0.48 g	Contingency sample, 10 m W of the LM; NW rim of Surveyor Crater.
12032,27	< 1 mm	0.50	NW rim of Bench Crater.
12037,20	< 1 mm	0.50	NW rim of Bench Crater.
12037,42	> 1 mm	0.48	NW rim of Bench Crater.
12033,23	< 1 mm	0.50	Collected at a depth of 15 cm from a trench in the N rim of Head Crater.
12033,66	> 1 mm	0.45	Collected at a depth of 15 cm from a trench in the N rim of Head Crater.
12001,71	< 1 mm	0.50	Composite sample collected on a traverse between Surveyor and Middle Crescent Craters.
12001,88	> 1 mm	0.50	Composite sample collected on a traverse between Surveyor and Middle Crescent Craters.

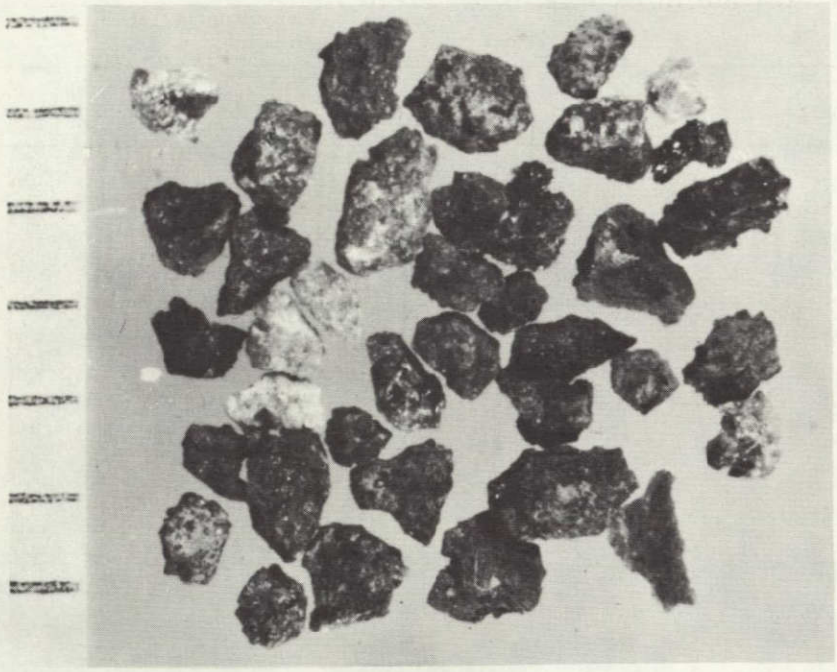

Figure I-11. Sample 12032, 27. 0.6- to 1-mm fraction. Light fragments are basalts and norites, dark ones are mainly the red-brown, ropy glasses described in Section IID. No soil breccias occur in this fraction (millimeter scale).

Figure I-12. Sample 12033, 66. The large, twisted fragment at far left, and numerous others in the photograph, are red-brown, ropy glass with feldspar-rich rock inclusions. The black grain with embedded spherules (arrow) is the unique Ti-rich microbreccia described in Section IIE (millimeter scale).

Figure I-13. Sample 12001, 88. Most of the dark fragments are microbreccias or cindery glasses; very few are the ropy glasses that are abundant in Figure I-12. The light fragments are mainly basalts (millimeter scale).

Figure I-14. Sample 12070, 35. 0.6- to 1-mm fraction. The irregular lustrous fragments are the dark, cindery glasses described in Section IID. The large, gray teardrop (lower center) is glassy, full of fragments, and hollow. White particle at top is potash rhyolite described in Section IIC (millimeter scale).

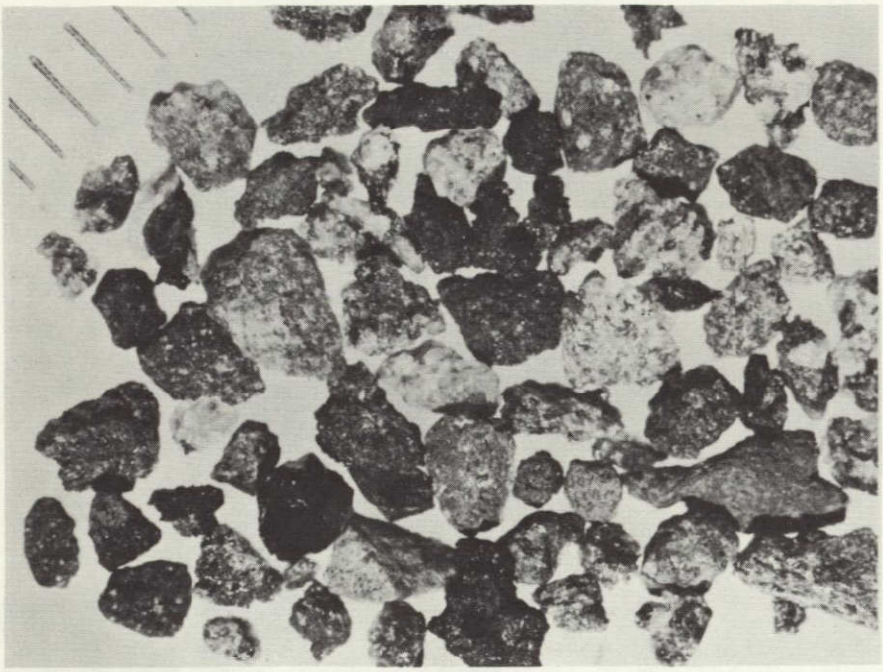

Figure I-15. Sample 12037, 42. Light-colored basalts are the most abundant rock present. The large, twisted grain at lower right is a feldspathic glass with norite inclusions. The long, narrow black grain, top center, is the carbonaceous chondrite described in Section IF (millimeter scale).

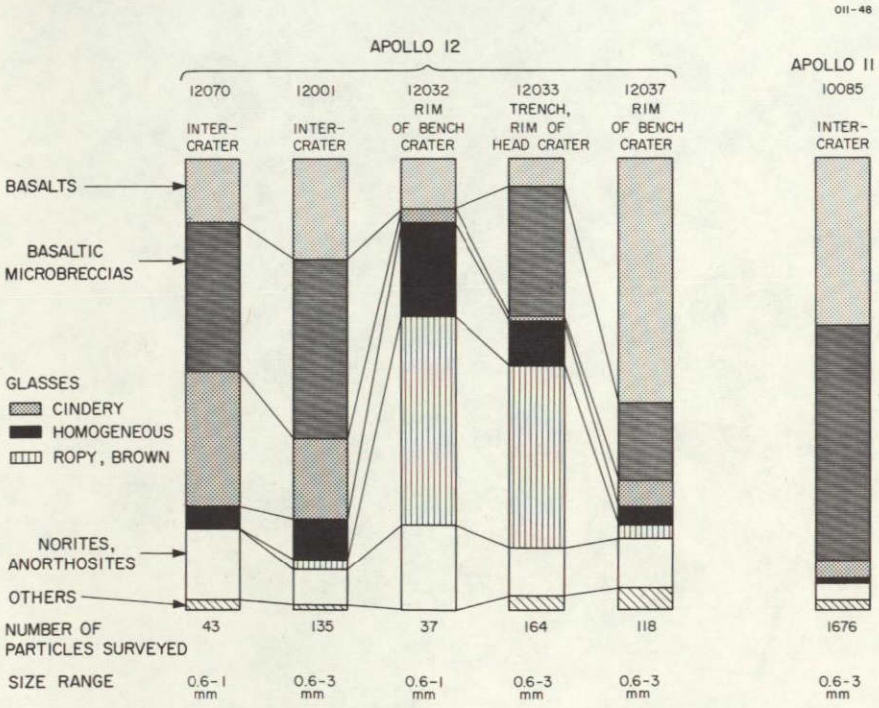

Figure I-16. Relative proportions of rock types and glasses in coarse fractions of five Apollo 12 and one Apollo 11 soil samples.

Two other samples, Nos. 12001 and 12070 (Figures I-13 and I-14), consist mainly of dark, cindery particles. No. 12037 (Figure I-15) is by far the most distinctive of the five samples. It contains an abundance of fresh, coarse-grained rock and mineral fragments. The predominance of these grains, however, may be an artifact of the manner of collection. Rock 12036, which is a vuggy, friable gabbro, was, according to LSPET (1970a), carried for a time in the same sack with Soil Sample 12037 and undoubtedly contributed much fresh material to the fines. Therefore, constituents of Sample 12037 are omitted from our statistical analysis of the rock types in the soils.

Grain-size distributions of Apollo 12 soil samples (< 1 mm)

The five samples of "fine-fines" (size range < 1 mm) we received, each weighing about 0.5 g, were rinsed with acetone through a series of Nytex screens.

The grain-size distributions are shown in Table I-II. The soils are all poorly sorted but have a preponderance of particles finer than 74 μ. Sample 12037,20 is by far the coarsest and the most poorly sorted, a clear reflection of its contamination with fragments of Rock 12036.

Proportions of rock types in soil samples

All the particles in the two coarsest fractions of our samples were mounted in epoxy and cut into thin sections. The grain size, number of particles, and weight of each fraction sectioned are shown in Table I-III. In this report, we identify each soil particle discussed by a double number of the form (115-30), which consists of the number of the thin section it is mounted in followed by an identifying number within that section (recorded on our photographic maps of the sections). The relationship between our section numbers and the LRL sample numbers is shown in the last column of Table I-III.

Petrographic surveys of the thin sections were made to determine the proportions of rock types in each sample. For this purpose, the rocks were classified into six broad categories and numerous subcategories. It was discovered very early that no sharp distinction can be made between microbreccias, many of which have glass-rich matrices, and glasses, which often contain an abundance of rock and mineral fragments. On further examination, however, we were able to recognize the following four main types of fragmental-glassy materials and two types of crystalline rock:

1. Microbreccias. Detrital aggregates with or without glass in the matrix.

2. Cinders. Highly vesicular glassy particles that are generally rich in rock and mineral fragments.

3. Ropy glasses. Red-brown or greenish-yellow glasses with pronounced flow banding (and, rarely, stretched vesicles) that resemble pieces of pulled taffy. Detrital inclusions are mainly fragments of feldspar or of noritic rock.

4. Glasses. Spherules or glass particles, of any color, that are largely free of detrital inclusions.

5. Basalts.

6. Norites and anorthosites.

7. Others. This category includes broken mineral grains and exotic materials such as meteorites and rhyolite.

The proportions of these seven types of material, as they occur in our thin sections, are illustrated in Figure I-16 and Table I-IV. These proportions confirm our earlier visual impression that our samples include two strikingly different varieties of lunar soil. Samples 12070,35 and 12001,71, for example, contain nearly 40% of microbreccias and over 30% of cindery glasses, along with 14 to 18% of basaltic fragments. Of these two, the first was the contingency sample collected near the lunar module and the second was a composite sample taken from the traverse to Middle Crescent Crater. Sample 12001 was reportedly carried in a sack with some larger rock fragments, but our surveys do not suggest that the soil was seriously contaminated.

Samples 12070 and 12001 appear to be fairly representative of the regolith over the mare basalt.

Samples 12032,27 and 12033,23, in contrast, contain over 40% of the red-brown ropy glasses and 20% of other glasses, with relatively few of the cindery-type particles or microbreccias. Sample 12033,23 was collected from a light-gray streak at a depth of 15 cm in a trench dug by the astronauts in the rim of Head Crater, and Sample 12032,27 came from the rim of Bench Crater. These samples are similar in character and clearly derive from a highly specialized source material.

Table I-II. Grain-size distributions in the < 1-mm fractions of five Apollo 12 soil samples. Percentages by weight of particles in each size category.

Sieve size	Range of particle sizes (μ)	12032,27	12033,23	12070,35	12001,71	12037,20
	>600	7	9	4	6	11
30 mesh						
	250 - 600	13	14	11	13	25
60 mesh						
	149 - 250	9	10	12	9	14
100 mesh						
	74 - 149	15	17	20	18	20
200 mesh						
	44 - 74	31	27	28	30	24
325 mesh						
	< 44	25	23	25	24	6

Table I-III. Coarse fractions mounted in thin sections.

Sample number	Grain size (mm)	Number of particles	Weight (g)	% of total sample	Serial numbers of thin sections
12033,66	> 1	115	0.45	100	130-135
12033,23	0.6-1	50	0.04	11	110
12001,88	> 1	105	0.50	100	122-129
12001,71	0.6-1	31	0.03	7	111
12032,27	0.6-1	37	0.04	6	109
12070,35	0.6-1	43	0.02	4	101,102,104-107
12037,42	> 1	75	0.48	100	112-119
12037,20	0.6-1	43	0.05	12	108

Table I-IV. Relative proportions of rocks and glasses in coarse fractions of six lunar soil samples.

	Apollo 12					Apollo 11
	12070	12001	12032	12033	12037	10085,24
Basalts	14%	22%	11%	6%	54%	37%
Basaltic Microbreccias	33	40	0	29	17	52
Glasses:						
Cindery	30	18	3	1	6	4
Homogeneous	5	9	21	10	4	1
Ropy	0	2	46	40	3	0
Norites, Anorthosites	16	8	19	11	11	4
Others (Meteorites, unclassified particles)	2	1	0	3	5	2
	100%	100%	100%	100%	100%	100%
Number of Particles Surveyed	43	135	37	164	118	1676
Size Range (mm)	0.6-1	0.6-3	0.6-1	0.6-3	0.6-3	0.6-3

II. DESCRIPTION OF ROCK TYPES

IIA. Basalts

In texture and in the relative proportions of their constituent minerals, the Apollo 12 basalts are considerably more varied than those from Apollo 11. The latter are generally fine grained and display a relatively restricted range of grain size within a given rock (Wood, Marvin, Powell, and Dickey, 1970). By contrast, Apollo 12 basalts range from vitrophyres (porphyritic rocks with ultra-fine to glassy matrices) to coarse equigranular gabbros. Although both groups of rocks are composed of the same major phases (clinopyroxene, olivine, plagioclase, ilmenite, and spinel), the range in modal compositions in the 12 suite is considerably larger than for the Apollo 11 rocks (Figure IIA-1).

Nearly all the 202 basaltic fragments we have examined from Soil Samples 12001, 12032, 12033, 12037, and 12070 match quite closely one or another of the 10 textural types shown (all to the same scale) in Figures IIA-2 to IIA-11. The rock types vary from vitrophyres to coarse gabbros, and when viewed in the order presented, the 10 types form a smooth continuum in which the grain size and textural appearance of the plagioclase-ilmenite-pyroxene groundmass are the dominant variables. In the descriptions and discussion that follow, the textural varieties have been grouped somewhat arbitrarily into three categories: vitrophyres, variolitic and subophitic basalts, and coarse gabbros. The first two textural types (Figures IIA-2 and IIA-3) are vitrophyres. Those in Figures IIA-4 through IIA-9 range from variolitic basalts to subophitic basalts, while the coarse gabbros are represented by the rocks in Figures IIA-10 and IIA-11. Macroscopic photographs of three of the large crystalline rocks allotted to us by NASA appear in Figures IIA-12, IIA-13, and IIA-14. Four basaltic particles of the 202 examined do not fit into this sequence; an example of these dense, very fine-grained, relatively nonporphyritic basalts is shown in Figure IIA-15a, b, c, and d.

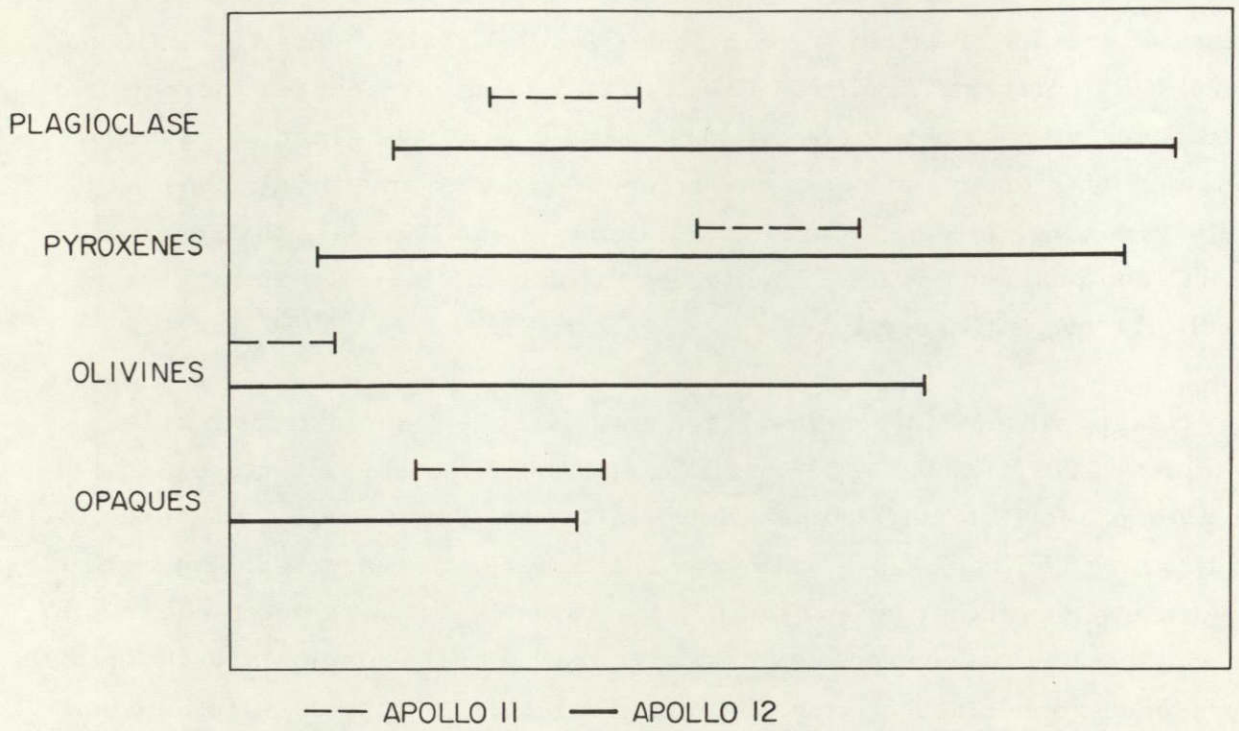

Figure IIA-1. A comparison of the ranges in modal composition of the large crystalline rocks from Apollo 11 and Apollo 12 (after LSPET, 1970b).

Figures IIA-2 through IIA-11 show the range of textural appearances displayed by the basaltic rocks and soil particles we have examined. The photomicrographs, all to the same scale, are arranged in order of increasing matrix grain size. All photos are taken in unpolarized, transmitted light.

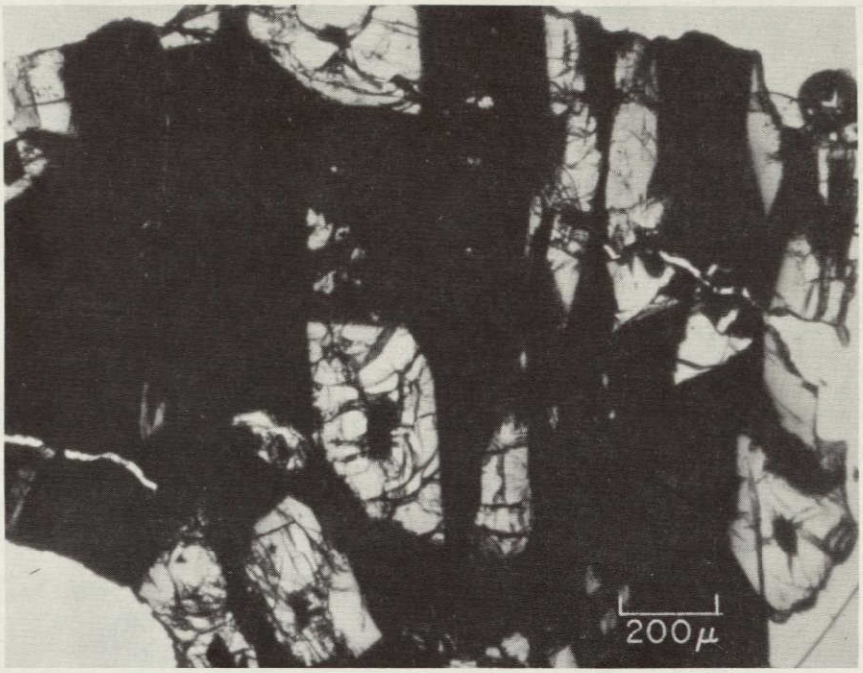

Figure IIA-2. Vitrophyre (127-11). Skeletal phenocrysts of olivine and pyroxene are imbedded in an ultra-fine-grained groundmass of feathery ilmenite, plagioclase, and clinopyroxene. A view in reflected light of this rock appears in Figure IIA-16.

Figure IIA-3. Vitrophyre (127-25). Similar to (127-11), except that the phenocrysts are less sharply defined, and the groundmass grain size is somewhat larger.

Figure IIA-4. Rock 12065. Skeletal pyroxene phenocrysts with resorbed margins in a variolitic matrix slightly coarser than that of (127-25) (Figure IIA-3). A variolitic basalt in the terminology used here.

Figure IIA-5. Variolitic basalt (114-2). Phenocrysts are less skeletal and are imbedded in a groundmass of larger grain size than those in (127-11), (127-25), and 12065.

Figure IIA-6. Variolitic basalt (114-6). Phenocrysts are rounded and nearly free of skeletal texture. Groundmass larger in grain size than those above.

Figure IIA-7. Variolitic-subophitic basalt (114-1). Strongly zoned phenocrysts are enclosed in a matrix bordering between variolitic and subophitic. The large grain in the upper right is pyroxene; the light-colored laths in the groundmass are plagioclase.

Figure IIA-8. Rock 12014. The variolitic nature of the groundmass is subordinate to a subophitic texture. Rounded phenocrysts are larger than the matrix phases, but the contrast in grain size is smaller than in any of the above rocks. White grains are plagioclase, light gray grains are pyroxene and olivine, and black grains are dominantly ilmenite, with occasional chromite-ulvöspinel.

Figure IIA-9. Rock 12063. Similar in texture to 12014, but slightly coarser in grain size, and with more strongly developed ophitic texture. Ilmenite is more abundant than in 12014, and there are fewer regions where the groundmass displays sheaves with variolitic texture.

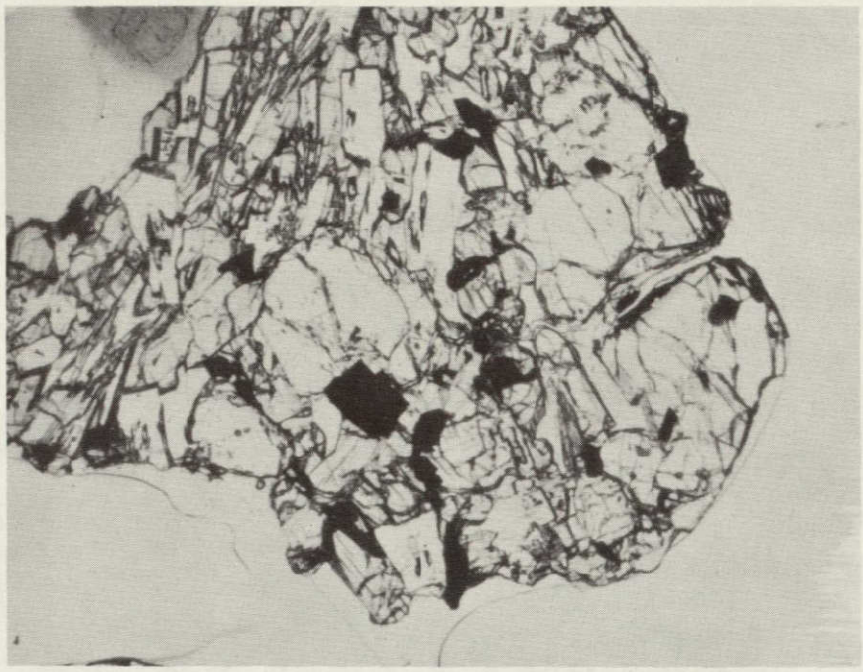

Figure IIA-10. Gabbro fragment (113-13). Euhedral chromite-ulvöspinel grains imbedded in anhedral rounded pyroxenes, and smaller olivines. Ophitic texture is moderately well developed in upper left.

Figure IIA-11. Rock 12035. A coarse equigranular olivine-rich gabbro containing euhedral olivine and pyroxene grains enclosed in large poikilitic plagioclase crystals. Large opaque anhedra are ilmenite; smaller opaque euhedra are spinel.

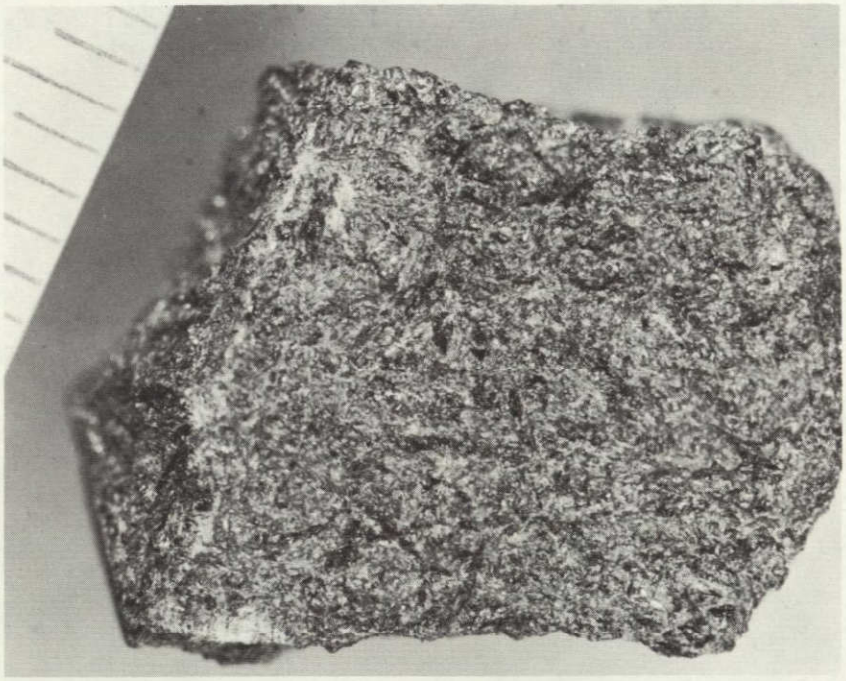

Figure IIA-12. Macroscopic view of Rock 12065. A transmitted light view in thin section of this variolitic basalt appears in Figure IIA-4. Scale is in millimeters.

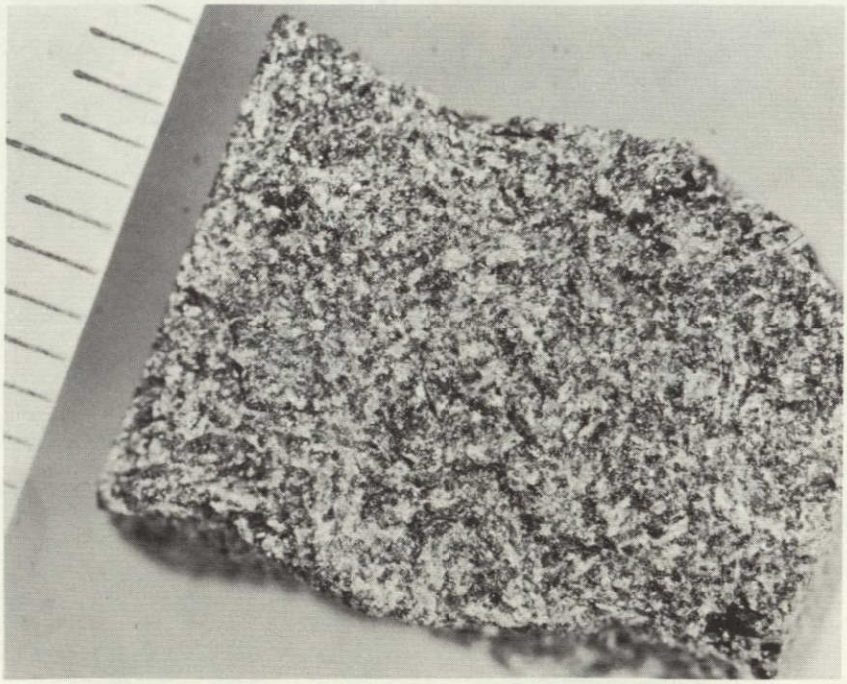

Figure IIA-13. Macroscopic view of Rock 12063. A thin-section view appears in Figure IIA-9. Scale is in millimeters.

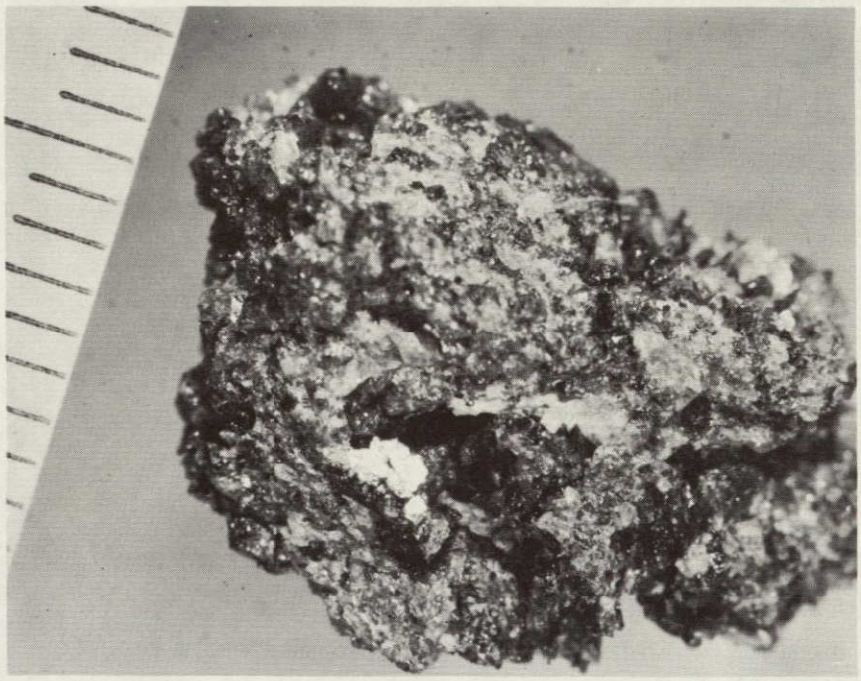

Figure IIA-14. Macroscopic view of portion of Rock 12035. A thin section view of 12035 appears in Figure IIA-11. Scale is in millimeters.

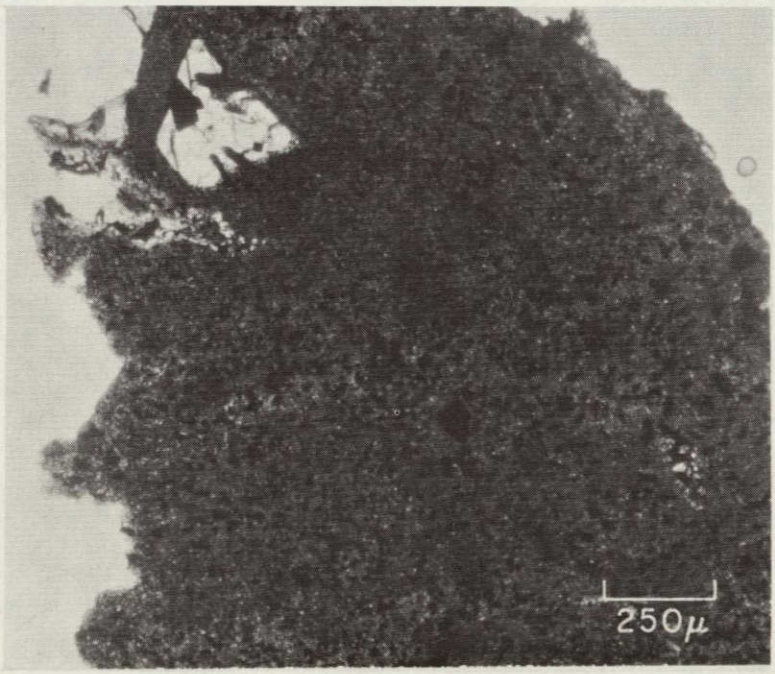

Figure IIA-15a. View in transmitted light of basalt fragment (124-3). A phenocryst (or xenocryst) of olivine and chromite appears at the upper left. The fragment appears to have been shocked, and partly recrystallized.

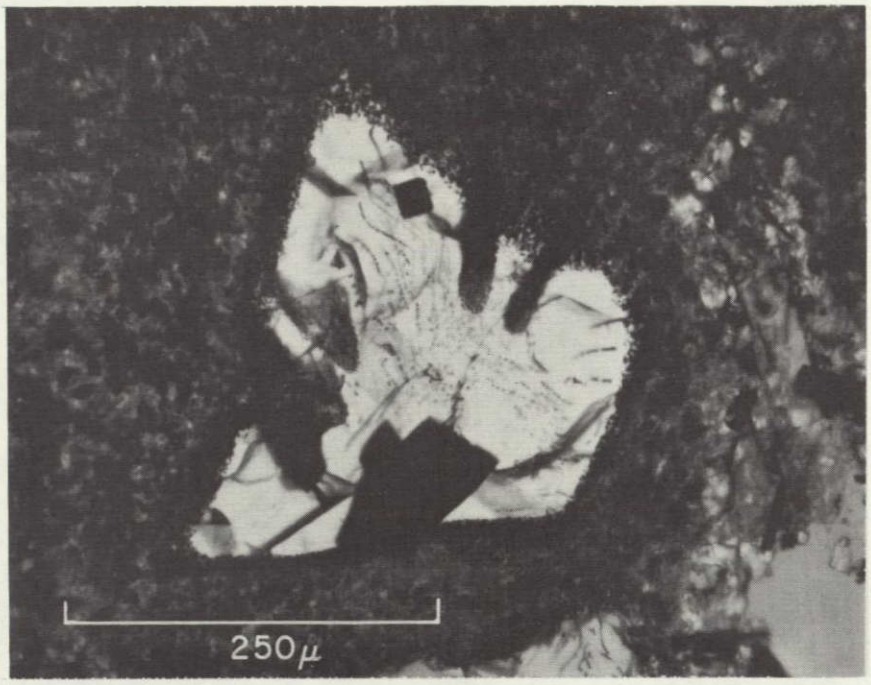

Figure IIA-15b. An enlarged view of the phenocryst (or xenocryst) appearing in Figure IIA-15a; transmitted unpolarized light. Note the reaction rim separating olivine (white) from the groundmass. A region of silica appears at the far right (light gray).

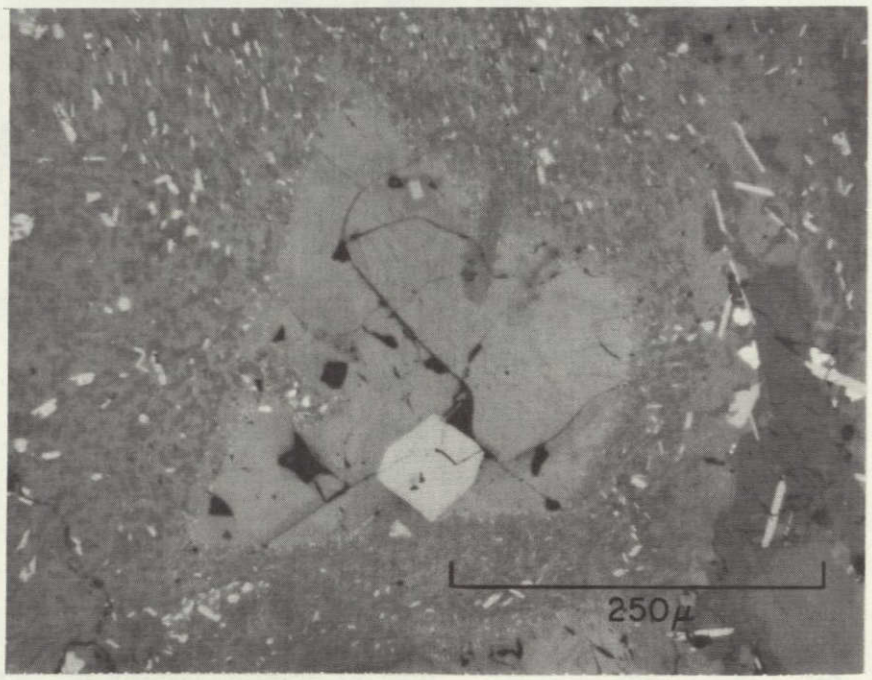

Figure IIA-15c. Same view as in Figure IIA-15b, taken in reflected light. Note the sprinkling of ultra-fine opaque minerals in the olivine reaction rim.

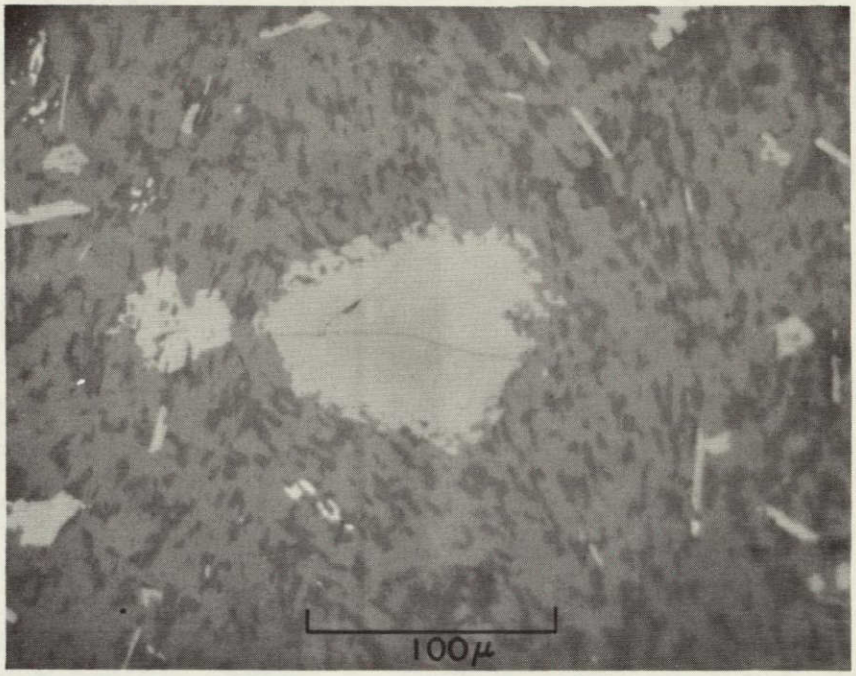

Figure IIA-15d. View in reflected light of a spinel grain in the matrix of basalt fragment (124-3). The core of the grain is a zoned chromite–chromian ulvöspinel and contains a spongy overgrowth of Ti-rich spinel. Spinels in the groundmass are also "porous," similar to ones found in recrystallized norites.

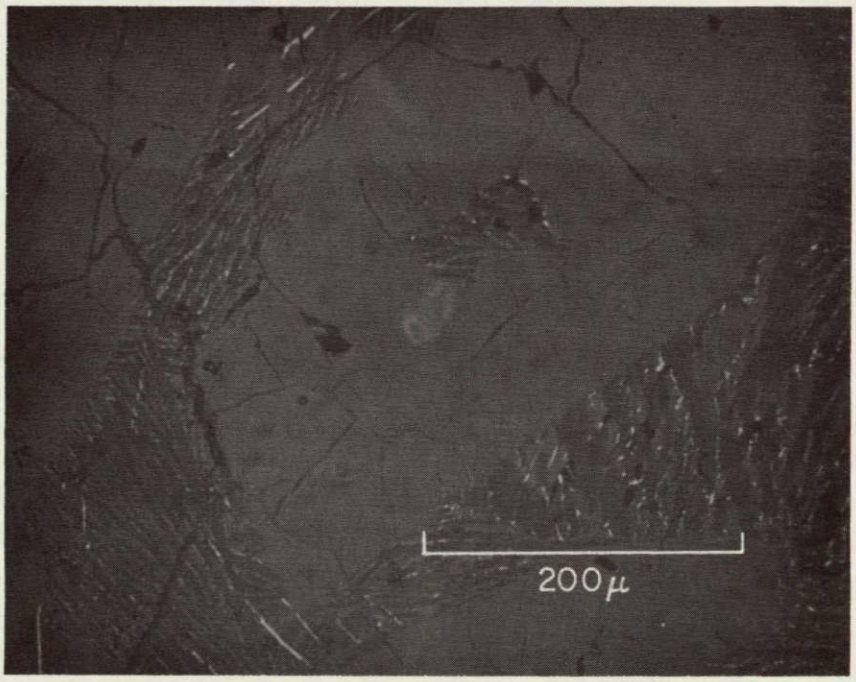

Figure IIA-16. View in reflected light of a skeletal pyroxene phenocryst in vitrophyre fragment (127-11). The material filling the core of the phenocryst has a similar appearance to the groundmass.

The numbers of each basalt type in each of three particle sizes range from Soil Samples 12001, 12032, 12033, 12037, and 12070 are shown in Table IIA-I. Table IIA-II shows the percentages of the total soil samples in those grain sizes represented by the same basaltic particles. Except for 12037, the relative proportions of the three basaltic types in each sample are fairly similar, given the statistics of so few particles. (Sample 12037 was returned from the Moon in the sample bag containing 12036, a coarse, rather friable gabbroic rock. Debris from this rock undoubtedly contaminated the soil sample and rendered meaningless the relative proportions of types in the soil sample.) In the other four soil samples, variolitic and subophitic basalts are the most numerous, being generally two to three times as abundant as the vitrophyres. The coarse gabbros are usually the least abundant type in a given sample. In Samples 12001, 12032, 12033, and 12070 taken together, the relative proportions – vitrophyres: variolitic and subophitic basalts: coarse gabbros – are 36:68:26. (Coincidentally, perhaps, the 10 textural types shown in Figures IIA-2 through IIA-11 are divided among these 3 basalt types in nearly the same proportions – 2:6:2.)

From a textural standpoint, the 10 types display several characteristics that vary smoothly from 1 rock type to the next. The variable most readily recognized is that of the groundmass grain size and texture. Clinopyroxene, ilmenite, and plagioclase form feathery sheaves of elongate crystals that vary in thicknesses from 5 μ or less in the vitrophyres (Figures IIA-2, IIA-3, and IIA-16) to about 50 μ in the variolitic basalts of intermediate grain size (Figures IIA-6 and IIA-7). The variolitic nature of the groundmass is most striking in the first 4 or 5 of the 10 textural types, giving way in the coarser rocks to subophitic basalts, ophitic basalts, and finally coarse, rather equigranular gabbros.

Pyroxene and olivine phenocrysts are noticeably skeletal in the vitrophyric rocks (Figure IIA-2 and IIA-16), with material similar to the ultrafine variolitic matrix material filling the cores of these phenocrysts. As the grain size of the groundmass increases (Figures IIA-3 through IIA-7), the skeletal nature of the phenocrysts decreases, and the grain size of the

core-filling ilmenite-plagioclase-clinopyroxene assemblage increases slightly, though remaining considerably finer than the average groundmass in the rocks. The coarser subophitic, ophitic, and granular basalts and gabbros contain phenocrysts without skeletal cores. In general, the pyroxenes and olivines become less euhedral in the progression from Figures IIA-2 to IIA-10. An exception is Rock 12035, a coarse gabbro (shown in Figure IIA-11) containing well-developed euhedral pyroxene and olivine, whose mutual contacts along euhedral faces have been interpreted as indicative of a cumulative origin (Warner, 1970).

Compositional zoning is highly developed, especially in the intermediate variolitic and subophitic basalts (Figure IIA-17). Pyroxenes show light-buff cores grading to darker pinkish-brown rims. Pyroxenes in the coarser rocks are uniformly yellow brown. Olivines in the finer grained rocks are also chemically zoned, but no color differences are exhibited.

Spinels range widely in composition from nearly pure chromite cores in many cases to rims approaching pure ulvöspinel. In the rocks of intermediate grain size, ulvöspinel exteriors are separated from chrome-rich cores by a sharp color and compositional boundary. Chromite cores are a light pearl-gray; ulvöspinel rims a light pinkish-grayish-tan. The width of the ulvöspinel rim increases in relation to the size of the chromite core as the grain size of the rock increases. Vitrophyre spinels are dominantly chromite with very thin ulvöspinel rims (Figure IIA-18). Spinels in variolitic to subophitic basalts have wider rims of ulvöspinel (Figures IIA-19 and IIA-20), while those in the coarse gabbros generally show little optical evidence of compositional zoning (Figure IIA-21).

The habit exhibited by ilmenite also varies smoothly through the sequence shown in Figures IIA-2 through IIA-11. In the vitrophyric basalts, ilmenite occurs exclusively in the groundmass, as very thin (less than 5 μ), long plates in sheaves with clinopyroxene and plagioclase (Figure IIA-16). As the groundmass grain size increases, ilmenite plates become thicker and stubbier. In the coarsest gabbroic rocks, ilmenites often occur as large

amoeboid (anhedral) grains. The transition from vitrophyres with very fine-grained variolitic matrices to subophitic basalts involves a similar variation of plagioclase habit. Plagioclase ranges from thin fibers or plates in vitrophyres to stubby subhedral crystals in the subophitic basalts. Plagioclase in the coarse gabbros like 12035 occurs as very large anhedral grains enclosing pyroxene and olivine euhedra.

Chemistry of the Basaltic Fragments

Detailed chemical analyses of olivines, pyroxenes, and spinels have been made in three crystalline rocks and a large number of basaltic soil particles chosen to represent all the textural types shown in Figures IIA-2 through IIA-11. Emphasis was placed on these three minerals because of the large and generally systematic variations they showed within a given rock. The compositional trends displayed by the olivines, pyroxenes, and spinels of each basalt textural type are in general distinctive and are different from trends in the other types. In the descriptions that follow, the chemistry of each mineral is considered in terms of the three textural categories described in the petrographic section above.

The following generalizations appear valid:

Olivines

1. When their compositions are plotted on a diagram showing Cr_2O_3 (wt. %) as a function of mole % fayalite (Figure IIA-22a, b), the olivines from Apollo 11 and Apollo 12 basalts fall in two distinct groups. In each case, the Cr content decreases with increasing fayalite content, but for a given Cr_2O_3 content, the Apollo 12 basalt olivines are more Fe-rich than those from Apollo 11. These olivines are generally zoned, with relatively magnesian cores and Fe-rich exteriors. The Cr is concentrated in the earlier-crystallizing cores.

2. Olivines from noritic fragments from Apollo 12 contain relatively little Cr_2O_3 and are considerably more Mg-rich than the basaltic olivines. Olivines from Apollo 11 anorthosites plot with those from Apollo 12 norites (Figure IIA-22b).

3. Olivines from the three textural categories of Apollo 12 basalts fall into distinct but overlapping clusters of points on a plot of Cr_2O_3 vs. fayalite content (Figure IIA-23a, b, c). Vitrophyre olivines are concentrated at the Cr- and Mg-rich portion of the compositional range spanned by all basaltic olivines (Figure IIA-23a). Variolitic and subophitic basalt olivines cover the entire composition range (Figure IIA-23b). (Rock 12014, for example, contains the most magnesian and the most fayalitic olivine analyzed.) Olivines in the coarse gabbros are less strongly zoned and are concentrated in the intermediate compositions (Figure IIA-23c).

A selection of olivine compositions, chosen to represent all portions of the range in Figure IIA-22a, appears in Table IIA-III.

Pyroxenes

1. Compositional zoning in pyroxenes is often extreme, especially in the medium-grained size variolitic to subophitic basalts. The results of a step scan of a single pyroxene grain in 12014 are shown in Figure IIA-24. This grain ranges from pigeonite compositions with Fe/(Fe + Mg) near 0.28 in the core to pyroxferroite rims with Fe/(Fe + Mg) $\cong$ 0.98. Pyroxene phenocrysts in vitrophyres are also strongly zoned, while those in the coarser gabbroic rocks are more nearly homogeneous.

2. When Apollo 12 basalt pyroxenes are plotted on diagrams showing Cr_2O_3 as a function of Fe/(Fe + Mn + Mg), patterns similar to the corresponding plots for the olivines appear (Figure IIA-25). Pyroxenes richest in Mg relative to Fe contain the highest Cr contents. The rate of decrease in Cr_2O_3 with increasing Fe/(Fe + Mn + Mg) is initially very large but decreases, giving a cluster of points resembling a sock in shape.

Table IIA-I. Numbers of particles of various basalt types in three size fractions of Soil Samples 12001, 12032, 12033, 12037, and 12070.

Particle size fraction	Type	12001	12032	12033	12037	12070
> 1 mm	A	7	--	2	3	--
	B	14	--	3	10	--
	C	2	--	3	30	--
	D	0	--	0	1	--
	Total grains in sample	105	--	115	75	--
0.6-1 mm	A	1	0	0	1	2
	B	3	1	1	3	4
	C	2	3	1	19	0
	D	0	0	0	0	0
	Total grains in sample	31	37	50	43	43
<0.6 mm	A	--	--	--	--	26
	B	--	--	--	--	42
	C	--	--	--	--	15
	D	--	--	--	--	3
	Total grains in sample	--	--	--	--	815

Key

A. Vitrophyres.

B. Variolitic-subophitic basalts.

C. Coarse gabbros.

D. Very fine, dense, equigranular, relatively nonporphyritic basalts.

Table IIA-II. Percentages of various basalt types in three size fractions of Soil Samples 12001, 12032, 12033, 12037, and 12070.

Particle size fraction	Type	12001	12032	12033	12037	12070
> 1 mm	A	6.7	--	1.7	4.0	--
	B	13.4	--	2.6	13.3	--
	C	1.9	--	2.6	40.0	--
	D	1.9	--	0.0	1.3	--
		23.9	--	6.9	58.6	--
0.6-1 mm	A	3.2	0.0	0.0	2.4	4.7
	B	9.6	2.8	2.0	7.2	9.4
	C	6.4	8.1	2.0	44.2	0.0
	D	0.0	0.0	0.0	0.0	0.0
		19.2	10.9	4.0	53.8	14.1
< 0.6 mm	A	--	--	--	--	3.2
	B	--	--	--	--	5.1
	C	--	--	--	--	1.8
	D	--	--	--	--	0.4
		--	--	--	--	10.5

Key to Basalt Types

A. Vitrophyes.

B. Variolitic-subophitic basalts.

C. Coarse gabbros.

D. Very fine, equigranular, relatively nonporphyritic basalts (possibly shocked).

Table IIA-III. Major element compositions of selected olivines.

	Weight percentages of oxides								
	1	2	3	4	5	6	7	8	9
SiO_2	38.55	37.56	37.58	37.83	35.62	36.50	35.37	34.13	32.95
TiO_2	0.02	0.08	0.08	0.05	0.03	0.04	0.06	0.06	nd
Al_2O_3	0.08	nd	nd	0.02	0.06	0.02	0.00	0.04	nd
Cr_2O_3	0.45	0.44	0.43	0.38	0.21	0.26	0.15	0.10	0.10
FeO	22.08	24.51	27.86	27.20	30.46	31.85	39.07	44.42	46.30
MnO	0.26	0.28	0.30	0.27	0.32	0.43	0.36	0.36	nd
MgO	37.67	37.04	35.19	33.89	30.55	28.95	25.12	18.69	18.52
CaO	0.28	0.31	0.35	0.29	0.28	0.30	0.32	0.29	0.33
Sum	99.58	100.34	101.79	99.94	98.38	98.35	100.45	98.09	98.20

Key

1. Core, olivine in variolitic-subophitic basalt (12014).
2. Core, olivine in vitrophyre (127-25) basalt.
3. Core, olivine in vitrophyre (127-11).
4. Rim, olivine in variolitic-subophitic basalt (12014).
5. Coarse olivine gabbro (108-2).
6. Rim, olivine in variolitic-subophitic basalt (12014).
7. Coarse olivine gabbro (108-40).
8. Rim, olivine in variolitic-subophitic basalt (12014).
9. Coarse olivine-rich gabbro (12035).

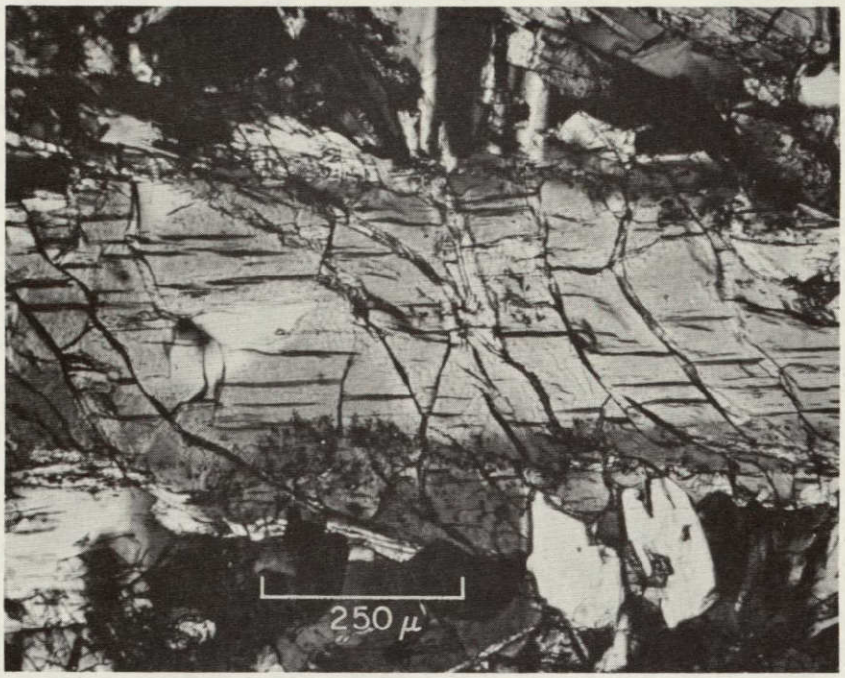

Figure IIA-17. View by transmitted polarized light of a strongly zoned pyroxene phenocryst in 12014. Compositional data for this grain are plotted on a pyroxene quadrilateral diagram in Figure IIA-24.

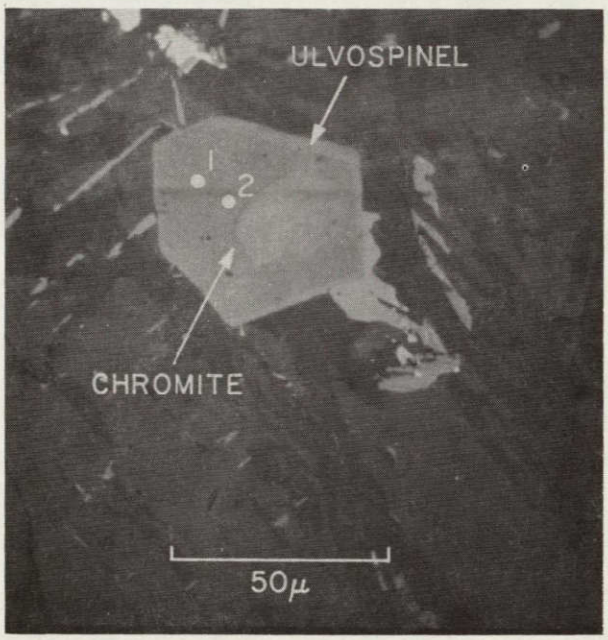

Figure IIA-18. View by reflected light of a spinel grain in vitrophyre (127-11). The core is fairly homogeneous chromite; the thin darker rim is chromian ulvöspinel. Numbers on the photomicrograph refer to compositional data in Table IIA-V.

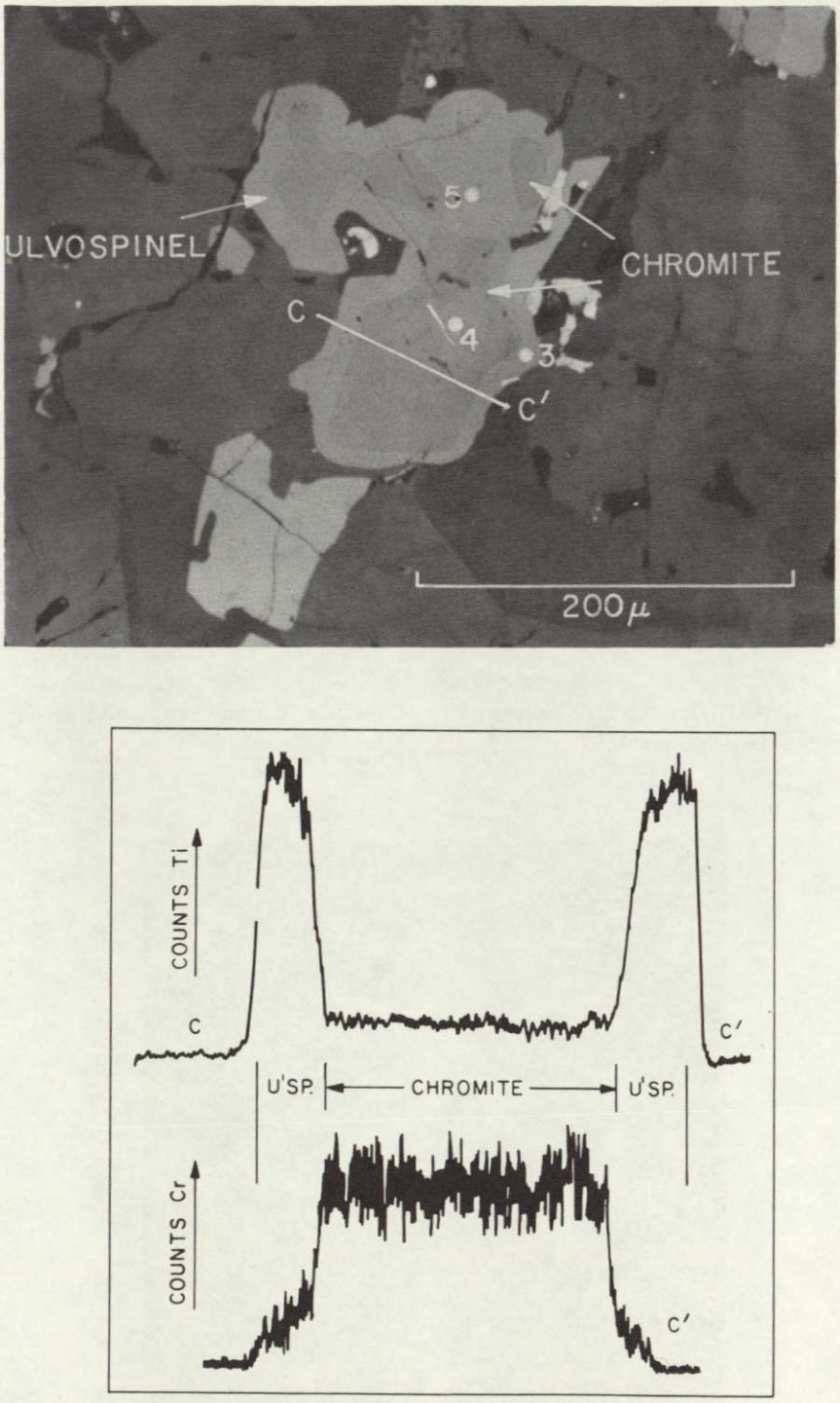

Figure IIA-19. Zoned spinels in rock 12014. Grain cores are titanian chromite; rims are chromian ulvöspinel. Shown beneath the reflected-light photomicrograph are qualitative microprobe traverses for Ti and Cr, showing the complementary behavior of the two elements. Numbers on photomicrograph refer to compositional data in Table IIA-V.

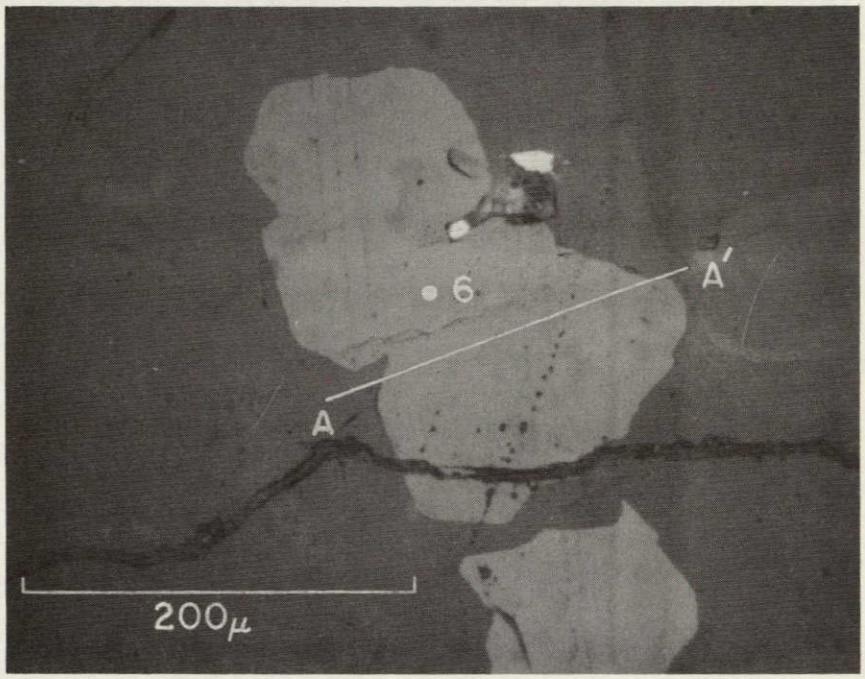

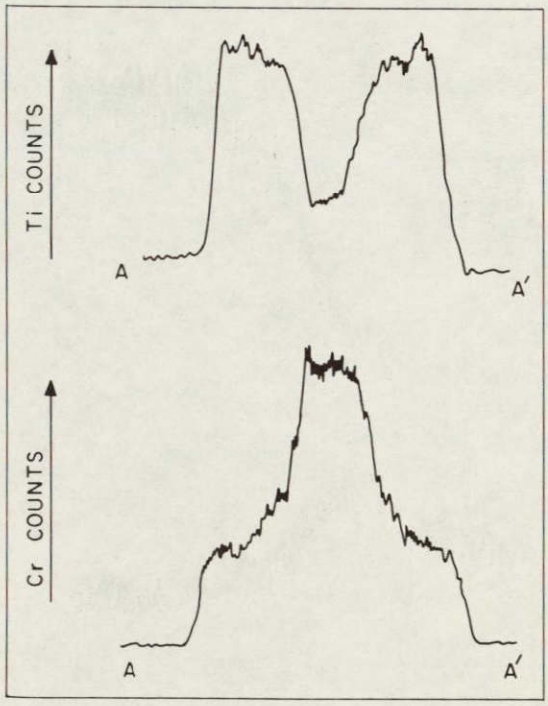

Figure IIA-20. A zoned spinel in Rock 12063. Note that the optical evidence for compositional zoning, and the compositional hiatus itself, are less pronounced in 12063 than in Rock 12014 (Figure IIA-19). Number on photomicrograph refers to compositional data in Table IIA-V.

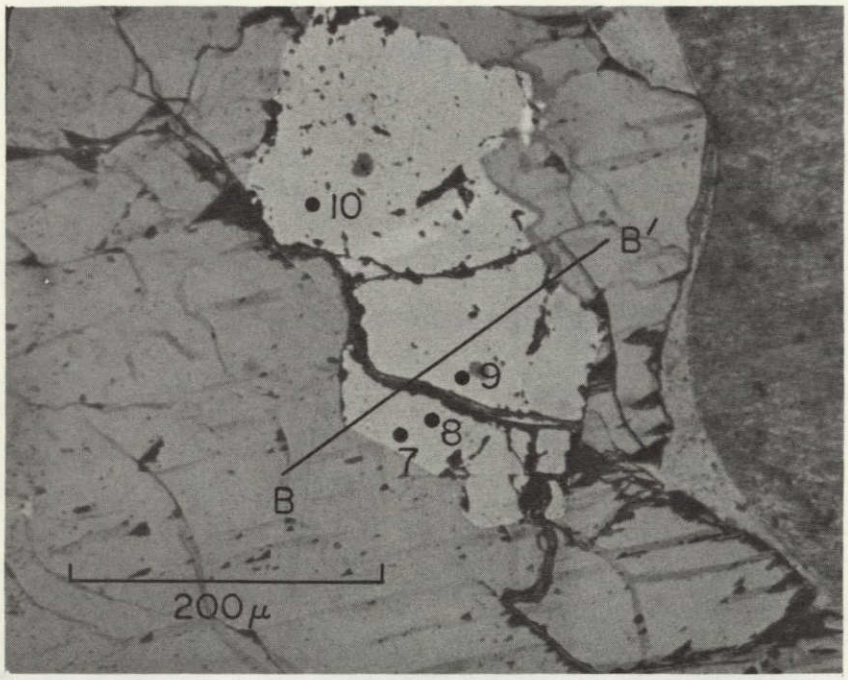

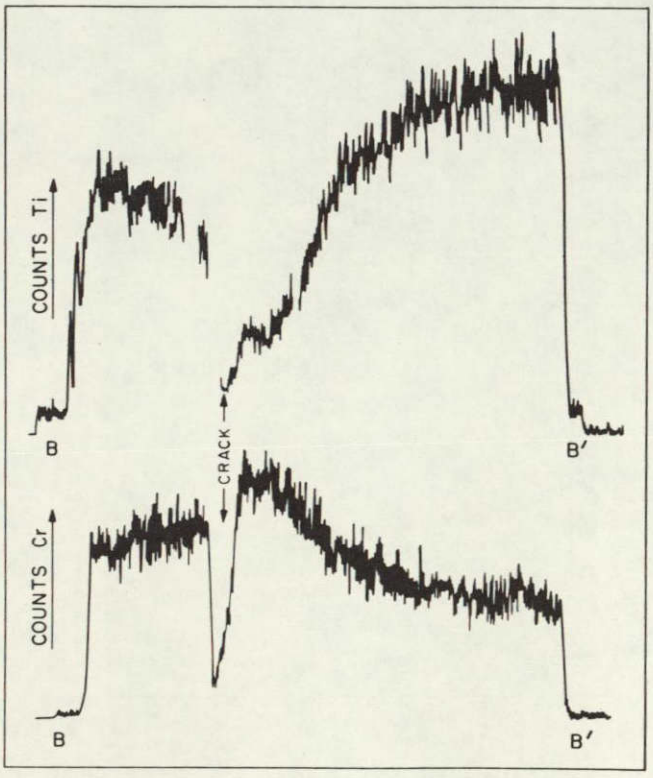

Figure IIA-21. A zoned spinel in coarse basalt fragment (113-14). Very little optical evidence of compositional zoning is present, yet a large, smoothly continuous compositional gradient exists. Numbers on photomicrograph refer to compositional data in Table IIA-V.

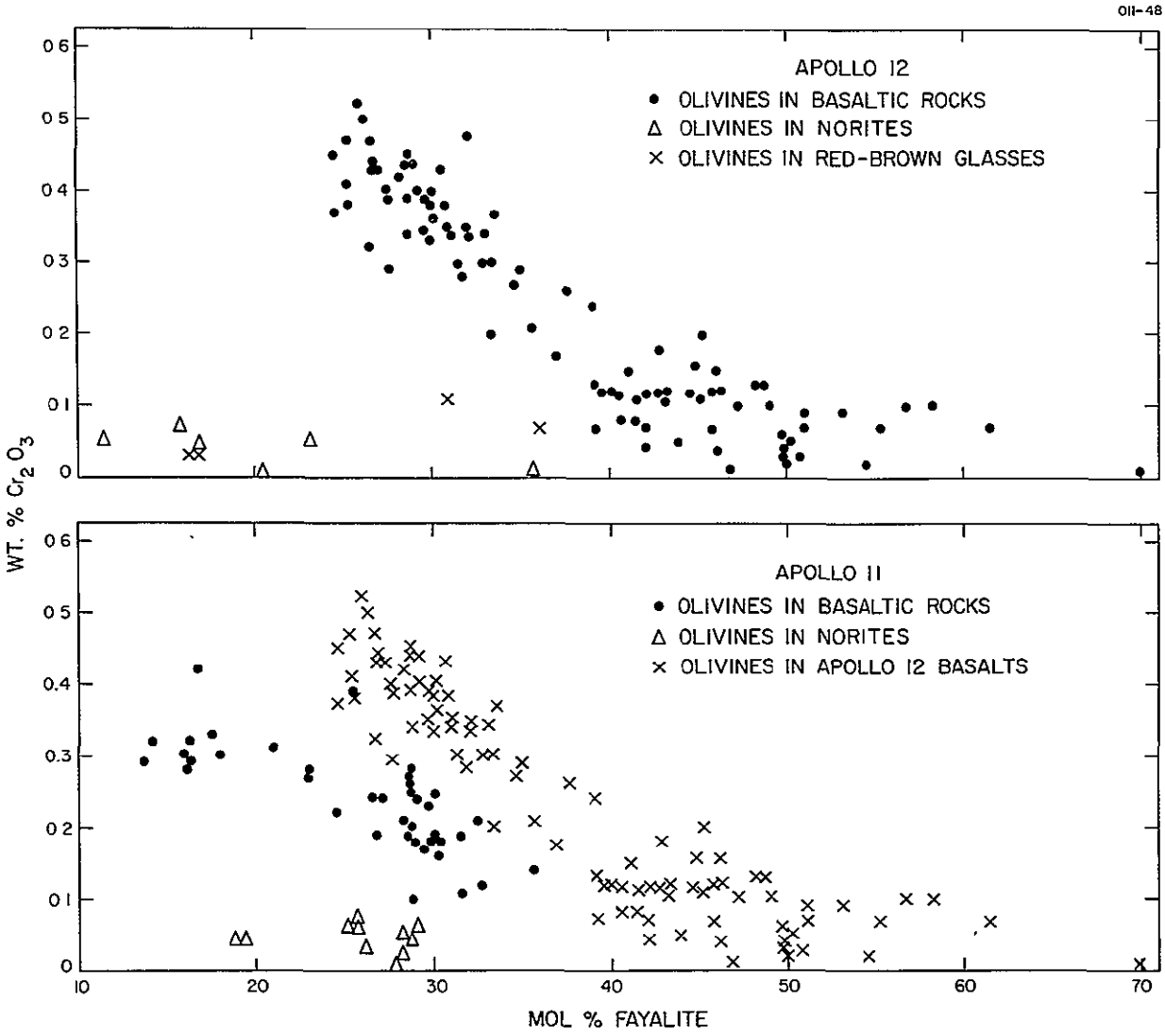

Figure IIA-22a, b. Wt. % Cr_2O_3 plotted against mole % fayalite, for olivines from a variety of Apollo 11 and Apollo 12 rocks and glasses.

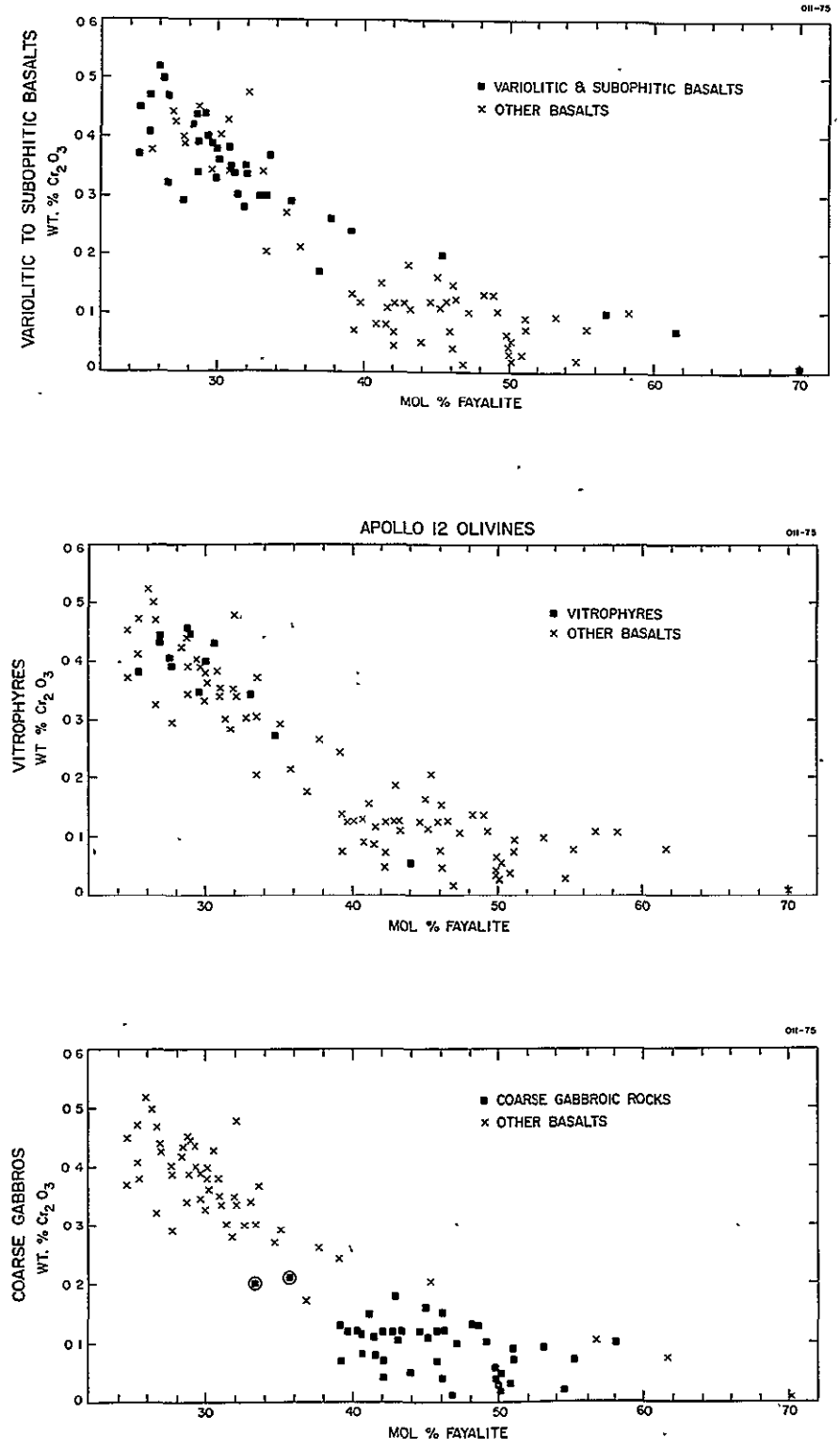

Figure IIA-23a, b, c. Wt. % Cr_2O_3 vs. mole % fayalite, for olivines from the three texturally based basalt categories. Vitrophyre olivines are concentrated in the Mg- and Cr-rich part of the range; medium-grained basalts cover the entire range; olivines from the coarse gabbros are less strongly zoned.

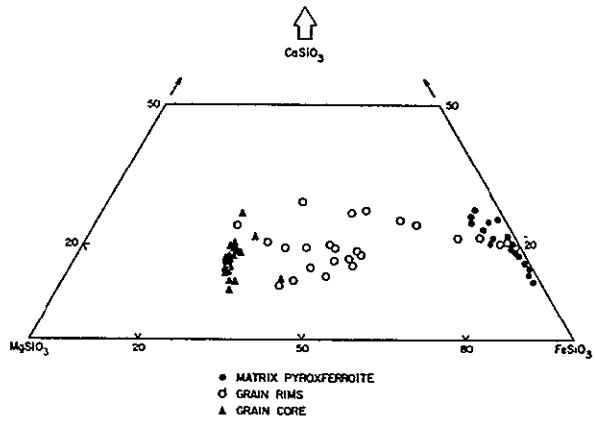

Figure IIA-24. Compositional relationships in a strongly zoned pyroxene grain from Rock 12014. A thin section view of this grain appears in Figure IIA-17.

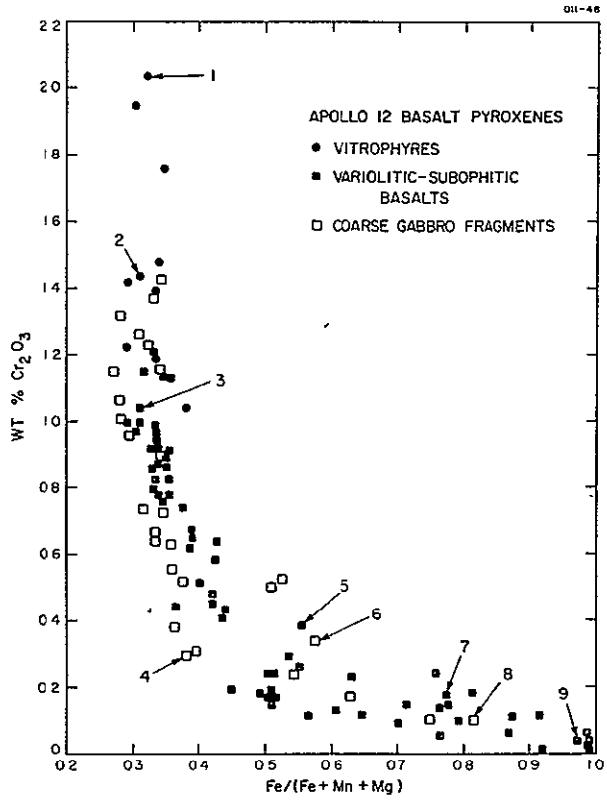

Figure IIA-25. Wt. % Cr_2O_3 vs. Fe/(Fe + Mn + Mg) for pyroxenes from a variety of Apollo 12 basalts. As with olivines, vitrophyre pyroxenes are richest in Cr and Mg. Numbers refer to compositions given in Table IIA-IV.

3. As with the olivines, pyroxenes from vitrophyres, variolitic to subophitic basalts, and coarse gabbros plot in nonidentical groups in Figure IIA-26a, b, c. Vitrophyre pyroxenes (Figure IIA-26a), like their corresponding olivines, fall only in the Mg-rich portion of the compositional range and in fact contain considerably higher concentrations of Cr_2O_3 than do pyroxenes from either other group. Pyroxenes from variolitic and subophitic basalts cover a large portion of the range (Figure IIA-26b). The most Cr-rich pyroxenes from this second group overlap the least Cr-rich pyroxenes in the vitrophyres. As with their olivines, coarse gabbro pyroxenes are not as heterogeneous as those from the finer grained rocks, and they plot in intermediate compositions (Figure IIA-26c).

4. Unlike the olivines, the pyroxenes from Apollo 12 basalts are not distinctly separated from those from Apollo 11 on plots of Cr_2O_3 vs. Fe/(Fe + Mn + Mg), though the Apollo 11 pyroxenes are slightly less Fe-rich for given Cr_2O_3 contents (Figure IIA-27).

5. Noritic pyroxenes from Apollo 11 and Apollo 12 fall in the same field on a plot of Cr_2O_3 (wt. %) vs. Fe/(Fe+Mn+Mg) (Figure IIA-28).

6. A plot of the TiO_2 contents in Apollo 12 basalt pyroxenes as a function of their Fe/(Fe + Mn + Mg) ratios appears in Figure IIA-29. Several things are worth noticing. Nearly all the analyses for the Apollo 12 material fall in the lower half of the diagram; Apollo 11 basalt pyroxenes contain up to twice their TiO_2 levels. An exception is fragment (114-6), whose pyroxenes are comparable to the high-TiO_2 Apollo 11 basalt pyroxenes. The rim portions of vitrophyre (127-11) also contain higher TiO_2 than do the other Apollo 12 basalt pyroxenes. Aside from these, the range of TiO_2 contents exhibited by the pyroxenes of any given rock or rock fragment is often nearly as large as the range for the whole group of analyses. Rock 12014 is a good example. On the other hand, pyroxenes in some gabbroic fragments are clustered at low TiO_2 levels, while those in others group in the upper portion of the range of analyses. Systematic variation of TiO_2 with Fe/(Fe + Mn + Mg) is much less obvious than the variation of Cr_2O_3 with the same ratio (Figure IIA-25)

for the same analysis points. Data from Rock 12014 suggest that the level of TiO_2 reaches a maximum for intermediate Fe/(Fe + Mn + Mg) ratios. Intermediate Fe/(Fe + Mn + Mg) ratios occur roughly midway between phenocryst cores and rims, and it is probable that the decrease in TiO_2 with further increase in Fe/(Fe + Mn + Mg) results from the onset of ilmenite crystallization.

A selection of pyroxene analyses, chosen to represent all portions of the curve in Figure IIA-25, appears in Table IIA-IV.

Spinels

1. Chromites tend to be euhedral and occur closely associated with early-crystallizing olivines and pyroxene phenocrysts; Ti-rich spinels are generally anhedral and occur interstitially and as overgrowths on chromite.

2. All spinels from all rocks analyzed fall on the same straight line on a plot of Ti vs. Cr ± Al (atom %, Figure IIA-30). The line, positioned by eye, has a slope of -0.499, with intercepts 34 and 67. Pure ulvöspinel would plot at (0.0, 33.3) and Ti-free aluminous chromite at (66.7, 0.0). The slope of the line indicates that in the substitution scheme relating the Apollo 12 spinels, a unit increase in the Ti atomic proportion is accompanied by a twofold decrease in the atomic proportion of Cr + Al. A schematic diagram showing this relationship appears in Figure IIA-31. As suggested by Agrell et al. (1970), the substitution involves the replacement of 2(Cr + Al) by Ti + (Mg, Fe). A second substitution scheme, Mg for Fe, is possible in the divalent site common to both chromite and ulvöspinel. Evidence supporting this view has recently been given by Gibb et al. (1970).

3. Some chromites are homogeneous, but generally spinels are strongly zoned with Cr-rich interiors and Ti-enriched exteriors. In the finer grained rocks, chromite cores and ulvöspinel rims are separated by sharp compositional discontinuities. Figure IIA-19 shows a photomicrograph and related microprobe traverses for Ti and Cr, for a spinel grain in 12014. The core portions of the grain are quite homogeneous, while the rims are both

heterogeneous themselves and are separated from the core by a sharp compositional change. Within the rims, Ti continues to increase and Cr to decrease outward.

A corresponding pair of probe traverses for a spinel grain in coarse gabbro fragment (113-14) appears in Figure IIA-21. Here, although the range in Ti and Cr variation is still very large, there is no compositional hiatus separating the inner and outer portions of the grain. Vitrophyres contain spinels that are quite homogeneous and Cr-rich, except for very thin ulvöspinel rims (Figure IIA-18). The numbers appearing on Figures IIA-18, IIA-19, IIA-20, and IIA-21 correspond to chemical analyses appearing in Table IIA-V.

4. On plots of Ti/(Cr + Al + 2Ti)* vs. Fe/(Fe + Mn + Mg) (Figures IIA-31a, b, c, d) spinels from the fine-grained variolitic and subophitic basalts fall on nearly identical curves that are composed essentially of two straight line segments of significantly different slope. Compositional variation in early chromites is largely in Fe/Mg. Later crystallizing spinels show variations dominated by the substitution of Ti + (Fe, Mg) for 2(Cr + Al). Vitrophyre spinels are homogeneous and Mg- and Cr-rich except for thin rims of a more Ti-rich spinel. Spinels in the coarse gabbros fall on straight lines parallel to and generally more Mg-rich than portions of the trends for the finer grained basalts where the dominant variation is in Ti/Cr. Considering the variolitic and subophitic basalts alone, spinels with intermediate Fe/(Fe + Mn + Mg) ratios, say 0.85, seem to divide their host rocks into two groups on the basis of Ti contents. Spinels from Rock 12014 and fragments (127-19) and (127-23) have Ti/(Cr+Al+2Ti) about 0.6, while those in Rocks 12052, 12063, and 12065 have Ti/(Cr + Al + 2Ti) about 0.9. Ti/(Cr + Al + 2Ti) values of 0.6 and 0.9 correspond to TiO_2 contents of 4.5 wt. % and 6.5 wt. %, respectively.

*"2Ti" in the bracketed denominator is simply a shorthand way of saying "Ti plus an equal atomic portion of (Mg, Fe)."

Plagioclases

Plagioclases in general show a rather restricted range of composition, with most of the analyses we have made falling in the range An85 to An96. Several grains have An contents as low as 77.5%, with a surprisingly large amount of the remainder consisting of orthoclase molecule. A plot of the molecular proportions of orthoclase vs. albite for all the basalt feldspars analyzed is shown in Figure IIA-33. The region in which feldspars from Apollo 11 basalts fall is denoted by a dashed line. The basalts from Apollo 12 contain plagioclases with generally higher K_2O and lower Na_2O contents than Apollo 11 basalts. The plagioclases with the highest K_2O contents occur in two coarse gabbroic fragments ((108-40) and (108-23)) as small, anhedral interstitial grains. A sampling of plagioclase analyses is presented in Table IIA-VI.

Other Minerals

A number of other mineral phases occur in the Apollo 12 basalts but have received less detailed attention in our investigation. Metallic iron and troilite are nearly ubiquitous. The textures reported by Reid et al. (1970), involving the occurrence of troilite and metallic iron in close association with zoned chromite-ulvöspinel grains and ilmenite, occur commonly in the fragments we have examined, particularly the medium-grained variolitic and subophitic basalts. Some Fe metal analyses are given in Table IIA-VII.

Table IIA-IV. Major element compositions of selected pyroxenes.

	Weight percentages of oxides								
	1	2	3	4	5	6	7	8	9
SiO_2	50.79	50.88	51.47	51.16	46.86	48.28	48.47	45.79	44.75
TiO_2	1.52	0.98	0.98	1.51	2.03	2.40	1.20	1.45	0.59
Al_2O_3	4.19	2.95	1.92	1.49	1.93	2.54	1.25	1.50	0.60
Cr_2O_3	2.03	1.43	1.03	0.30	0.39	0.34	0.16	0.10	0.01
FeO	17.27	17.57	16.82	17.26	23.77	25.51	33.09	37.06	46.77
MnO	0.32	0.36	0.39	0.43	0.41	0.44	0.50	0.48	0.50
MgO	19.84	21.13	20.14	15.56	10.44	10.45	5.13	4.32	0.21
CaO	5.81	4.71	5.74	12.69	12.42	11.35	9.53	8.65	4.87
Na_2O	0.09	0.00	0.00	0.13	0.00	0.08	0.00	0.00	0.19
K_2O	0.00	0.00	0.02	0.00	0.00	0.01	0.02	0.00	0.00
Sum	101.86	100.10	98.51	100.52	98.25	101.40	99.35	99.35	98.49

Key

1. Core of phenocryst in pyroxene vitrophyre (108-22).
2. Central part, phenocryst in pyroxene vitrophyre (127-11).
3. Core, small pyroxene phenocryst in variolitic-subophitic basalt (12014).
4. Augite in gabbro (108-6).
5. Augite in variolitic-subophitic basalt (12014).
6. Subcalcic ferroaugite in gabbro (110-3).
7. Rim, subcalcic ferroaugite, in variolitic-subophitic basalt (12014).
8. Subcalcic ferroaugite in (110-3).
9. Matrix pyroxferroite, in variolitic-subophitic basalt (12014).

Table IIA-V. Major element compositions of some Apollo 12 spinels. (Key numbers correspond to points on Figures IIA-18, IIA-19, IIA-20, and IIA-21.)

	Weight percentages of oxides									
	1	2	3	4	5	6	7	8	9	10
SiO_2	--	--	0.07	0 03	0.04	--	0.14	0.17	0.11	0.27
TiO_2	5.44	5.81	30.27	4.55	27.44	9.67	15.63	6.70	4.99	24.68
Al_2O_3	11.97	11.19	2.45	11.85	2.97	9.33	8.78	12.89	13.53	5 53
Cr_2O_3	47.75	46 34	7.27	50.21	11 54	40.90	29.72	44.27	45.22	17.77
FeO	27.30	27.81	59.95	29.42	56.23	41.71	42 43	33.14	32.62	48 93
MnO	--	--	0.35	0.22	0.35	--	--	--	--	--
MgO	7 08	6 08	0.00	5.24	0.05	0.81	3.68	3.73	3 66	3 33
CaO	--	--	0.09	0.00	0.01	--	0.09	0.05	0.05	0.00
Sum	99.54	97.23	100 47	101.51	98.62	102 43	100.48	100.94	100 19	100 52

Table IIA-VI. Major element analyses of some Apollo 12 basalt feldspars.

	Weight percentages of oxides							
	1	2	3	4	5	6	7	8
SiO_2	46.80	48.87	45.76	45.07	46.70	48.10	51.21	49.78
TiO_2	0.05	0.05	0.07	0.07	0.05	0.06	0.09	0.08
Al_2O_3	33.83	31.70	33.61	34.57	34.21	32.50	31.29	33.21
Cr_2O_3	0.00	0.02	0.05	0.00	--	--	--	--
FeO	0.67	1.20	0.72	0.61	0.39	0.87	0.87	0.63
MnO	0.00	0.02	0.00	0.00	--	--	--	--
MgO	0.24	0.18	0.18	0.27	--	--	--	--
CaO	17.97	16.78	17.80	18.38	18.21	17.23	14.74	16.08
K_2O	0.05	0.17	0.07	0.06	0.00	0.05	1.14	0.81
Na_2O	0.58	0.86	0.75	0.50	0.51	0.76	1.66	1.40
NiO	0.02	0.00	0.03	0.00	--	--	--	--
SO_3	0.00	0.00	0.00	0.04	--	--	--	--
Sum	100.22	99.85	99.04	99.57	100.08	99.57	101.01	101.98

Key

1. Grain core in 12014 (variolitic to subophitic basalt).
2. Near grain rim in 12014 (variolitic to subophitic basalt).
3. Grain core in 12014 (variolitic to subophitic basalt).
4. Grain core in 12014 (variolitic to subophitic basalt).
5. (108-1) (coarse gabbro).
6. (108-4) (coarse gabbro).
7. (108-40) (coarse gabbro).
8. (108-40) (coarse gabbro).

Table IIA-VII. Major element analyses of some Fe-Ni grains in 12014.

	Weight percentages of metals			
	Fe	Ni	Co	Sum
1	95.01	3.94	1.05	100.00
2	92.96	4.27	0.98	98.21
3	91.60	5.39	1.22	98.21
4	93.82	4.09	0.98	98.89
5	94.92	3.96	0.98	99.86
6	94.61	4.87	0.93	100.41
7	94.62	4.76	1.02	100.40
8	94.72	3.81	0.85	99.39
9	93.66	4.18	0.91	98.75

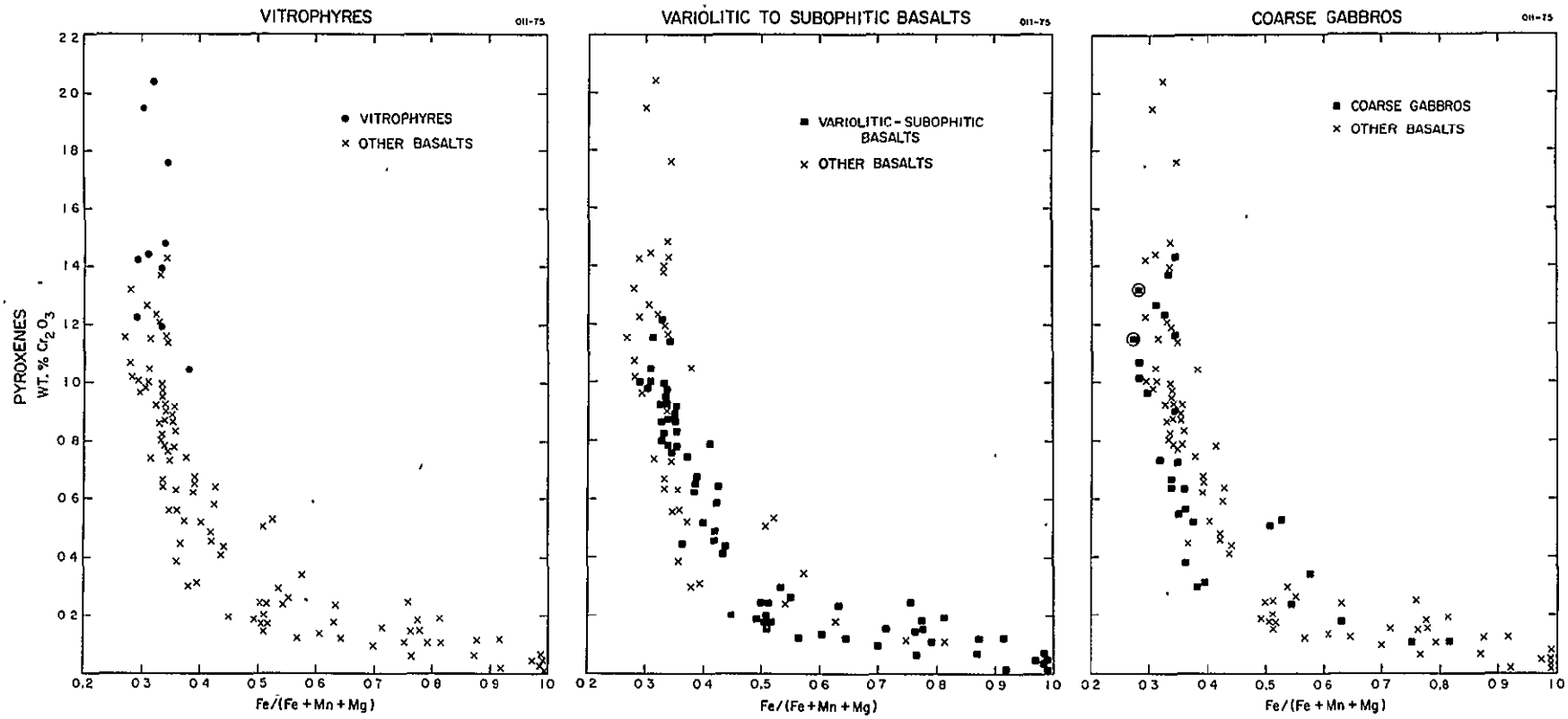

Figure IIA-26a, b, c. Wt. % Cr_2O_3 vs. Fe/(Fe + Mn + Mg) for pyroxenes from the three texturally based basalt categories. Vitrophyre pyroxenes concentrate in the Mg- and Cr-rich portion of the range.

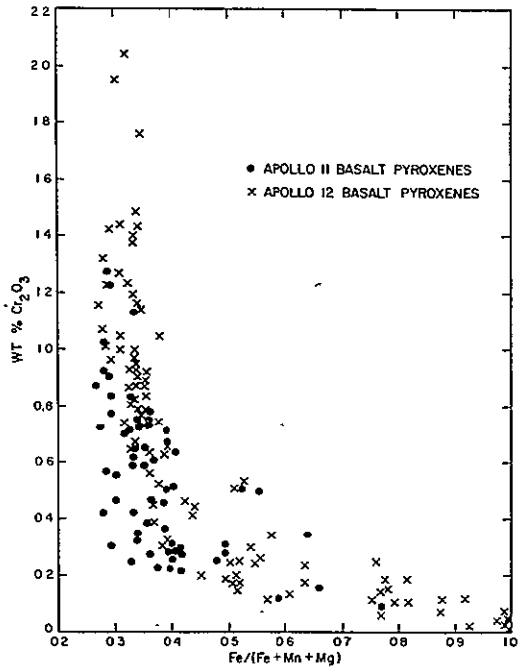

Figure IIA-27. Wt. % Cr_2O_3 vs. Fe/(Fe + Mn + Mg) for pyroxenes from Apollo 11 and Apollo 12 basalts. Note that, unlike the olivines (Figure IIA-22b), there is no sharp separation of the two groups of pyroxenes.

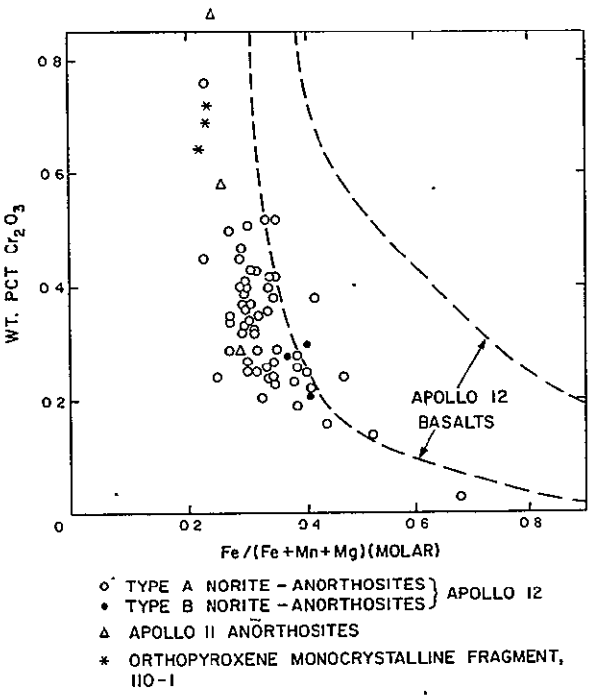

Figure IIA-28. Wt. % Cr_2O_3 vs. Fe/(Fe + Mn + Mg) for pyroxenes from Apollo 11 and Apollo 12 norites.

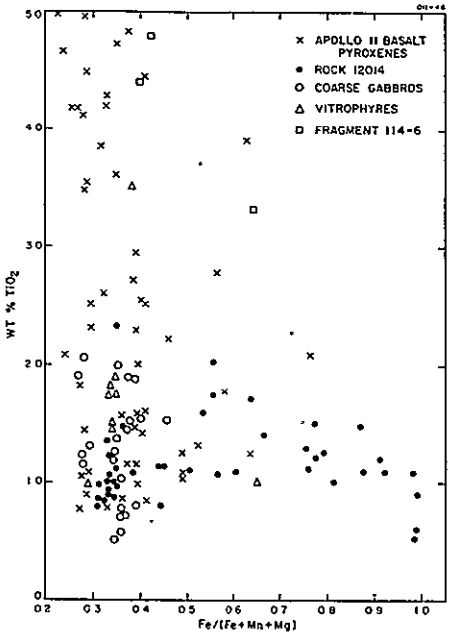

Figure IIA-29. A comparison of pyroxenes from Apollo 11 and Apollo 12 basalts on the basis of wt. % TiO_2 vs. Fe/(Fe + Mn + Mg). Aside from fragment (114-6), pyroxenes in all Apollo 12 basalt fragments analyzed have maximum TiO_2 contents that are roughly half as great as maximum TiO_2 contents of Apollo 11 basalt pyroxenes.

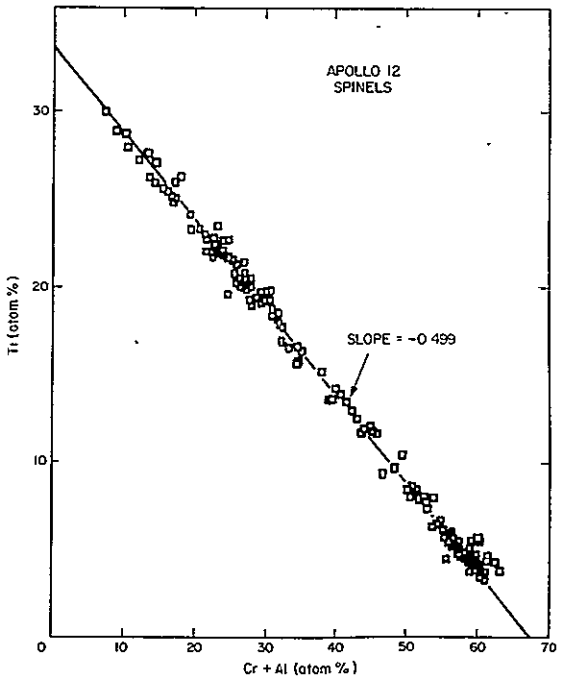

Figure IIA-30. Ti vs. (Cr + Al) (atom %) for all Apollo 12 spinels analyzed.

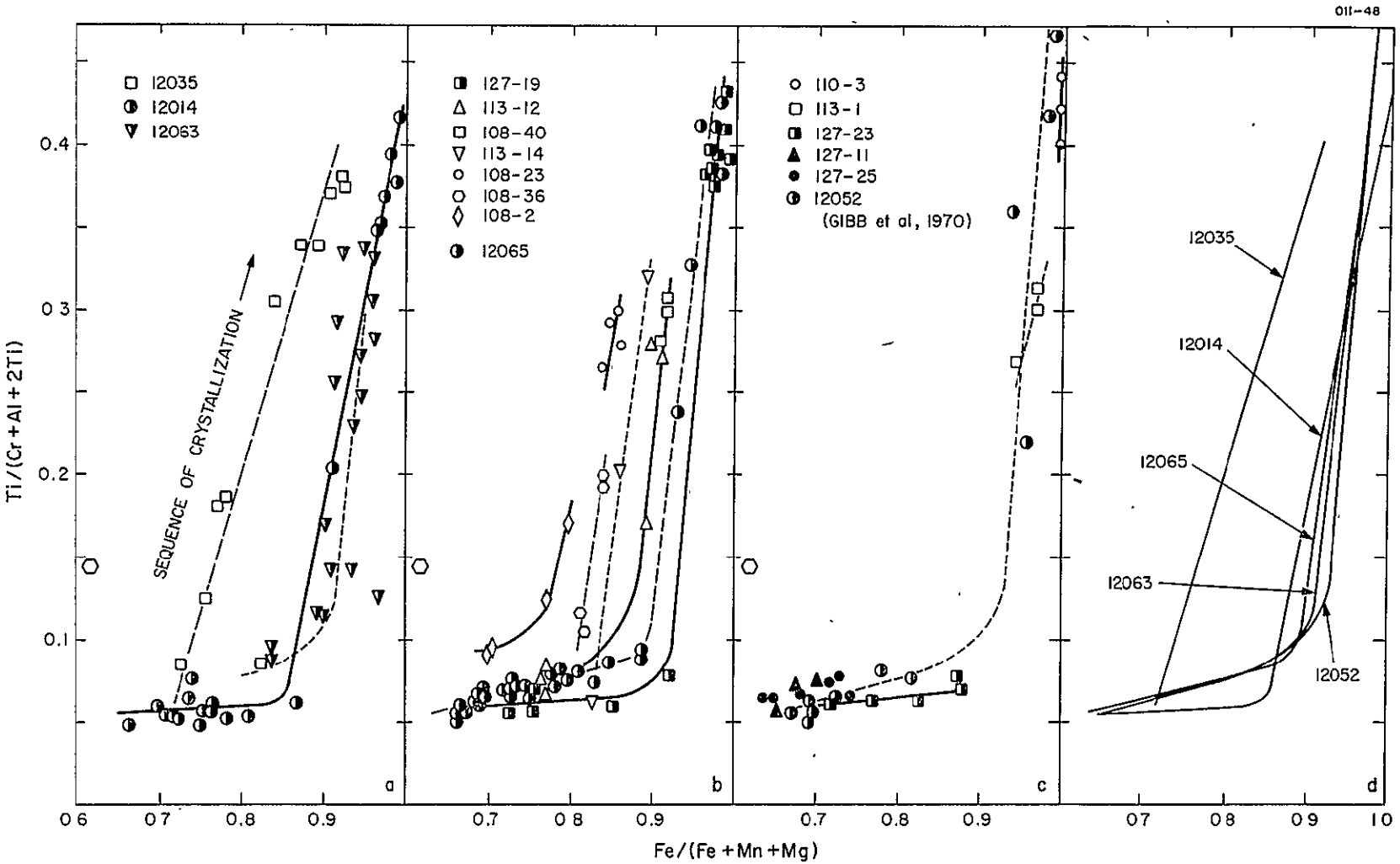

Figure IIA-31a, b, c, d. Spinel compositional relationships for a variety of Apollo 12 basaltic rocks and rock fragments. Solid symbols correspond to vitrophyres; half-open symbols to variolitic and subophitic basalts; open symbols to coarse gabbros ("2Ti" is shorthand for Ti plus an equal atomic proportion of (Fe, Mg)).

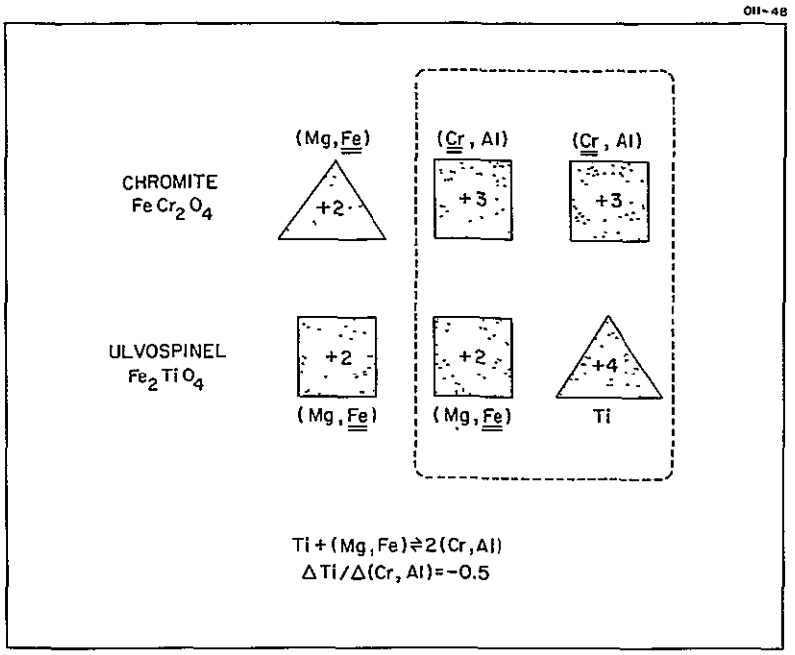

Figure IIA-32. A schematic diagram showing the solid-solution relationship between chromite and ulvöspinel. Squares represent octahedrally coordinated cations; triangles represent tetrahedrally coordinated cations. The substitution relating the two spinels is 2(Cr + Al) = Ti + (Fe, Mg). A second substitution (Fe = Mg) can take place as well.

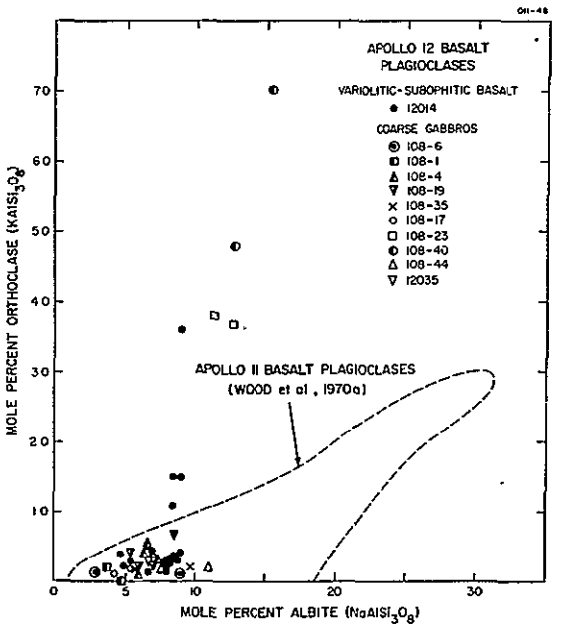

Figure IIA-33. A comparison of plagioclases from Apollo 11 and Apollo 12 basalts. Apollo 12 basalt plagioclases are richer in K_2O relative to Na_2O than are Apollo 11 basalt plagioclases.

IIB. Anorthositic and Related Rocks

The most unexpected and interesting component of the Apollo 11 soil sample consisted of light-colored fragments of anorthositic rock: naturally, we were much interested to learn whether such fragments also occur in the Apollo 12 soils. Light-colored particles are indeed present in the Apollo 12 soil samples we examined (Figure IIB-1), at levels comparable to their abundance in the Apollo 11 soil (Figure I-16), but most of them are not anorthositic. They range in composition from gabbroic (or, more properly, noritic, in view of the low-Ca character of their pyroxenes) to anorthositic, but the noritic end of the spectrum is the more densely populated. Two properties serve to set these rocks apart from the familiar lunar mare basalts: their textures, which are usually those of breccias rather than of primary igneous rocks; and the low-Ca content of their pyroxenes. In addition, they contain less ilmenite than most mare basalts and are, as already noted, lighter in color.

Among the Apollo 12 soil particles with anorthositic affinities, two classes may be distinguished. These are sufficiently dissimilar, we feel, to suggest different sources on the Moon and different modes of origin. One (termed Type A) consists largely of recrystallized breccias with fairly uniformly sized clasts; the other (Type B), of unrecrystallized breccias in which relatively large clasts are embedded in a matrix of glass and/or microcrystalline matter. These two classes will be discussed separately.

Type A Norite–Anorthosites

The first and more numerous class of light-colored particles ranges texturally from recrystallized breccias with fairly uniformly sized clasts (Figure IIB-2) to clearly igneous rocks of comparable grain size (Figure IIB-3); a composite case is shown in Figure IIB-4. Particles from the breccia end of the spectrum are more abundant. Petrographically, the Type A fragments

range from norites almost to gabbroic anorthosites, but most are noritic in character. They are very similar to the Caltech "Luny Rock" (Albee and Chodos, 1970) in texture and mineral compositions, but differ in that none of the Apollo 12 Type A particles we examined contain so little plagioclase as the "Luny Rock" (~15%); few if any are as severely shocked.

Mineral modes of all the coarse (>0.5 mm) Type A norite–anorthosite particles in our soil samples are shown in Figure IIB-5. These are based on a relatively small number of point counts (~100 per particle), so much statistical uncertainty attaches to the reports of minor mineral content. The estimates of plagioclase and mafic content are reliable, however, and the proportions of minor minerals for the grand average of all Type A particles are also statistically valid.

Bulk chemical compositions (defocused-beam microprobe analyses) of eight Apollo 12 Type A particles are shown in Table IIB-I, together with representative analyses of Apollo 11 anorthosites for comparison. The Apollo 12 norms are generally in good agreement with the modes reported in Figure IIB-5, with the exception of levels of phosphate minerals. Evidently, these were often not recognized during modal surveys. Properties of the minerals that comprise the Type A particles are discussed in the paragraphs to follow.

Plagioclase feldspar

Plagioclase crystals in Type A particles range in form from euhedral laths in the igneous fragments (Figure IIB-6) to anhedral or subhedral grains in the recrystallized breccias (Figure IIB-7). The larger clasts and laths display polysynthetic twinning. No obvious signs of a cumulate texture were seen in the igneous particles.

Representative microprobe analyses of plagioclase from Type A particles are reported in Table IIB-II; mineral compositions in mole % anorthite and orthoclase for all Type A plagioclase grains microprobed are plotted in

Figure IIB-8. It is likely that the few high K analyses are spurious, having been performed in small plagioclase grains close to regions of K-rich residual glass (described below). Plagioclase in these Apollo 12 Type A particles does not differ significantly in composition from the plagioclase of Apollo 11 anorthosite fragments, either in the distribution of anorthite contents or in the levels of minor elements (K, Fe, Ti).

Zoning is relatively feeble. Typically, in going from the center of a feldspar crystal to the outermost position that is safely probable (a distance of 30 μ, say), the anorthite content decreases by 0.2 to 2.0 mole % while the orthoclase content rises by 0.1 to 0.2 mole %. On the other hand, much greater compositional variations were observed between individual plagioclase grains and clasts within a given soil particle (Figure IIB-9), showing that complete chemical equilibration did not accompany the textural recrystallization these rocks have experienced.

Pyroxenes

The great majority of pyroxene grains in Type A norite–anorthosites are Ca poor (Figure IIB-10). Most seem to be orthopyroxenes, judging from their chemistry, and a smaller number are pigeonites; however, because of their small dimensions and irregular forms, we cannot confirm this distinction optically for most of the individual pyroxene grains analyzed. Where extinction angles can be observed, the pyroxene is usually monoclinic. Both forms of pyroxene are present, however (Figure IIB-11). The presence of orthopyroxenic rock fragments in the Apollo 12 soil was first reported by Fuchs (1970). Relatively few (~15%) of the pyroxene grains in this class of particles are augitic.

The pyroxene grains are usually anhedral in form (Figure IIB-7), but occasionally near-euhedral forms appear. They are clear and colorless in thin section. An example of the complex relations existing between primary (clast) pyroxene and pyroxenes newly formed during the recrystallization is shown in Figure IIB-12.

Table IIB-I. Bulk chemical analyses (defocused-beam microprobe analyses) and norms of light-colored particles from Apollo 12 and Apollo 11 soil samples.

	Weight percentages of oxides													
	Apollo 12 (12037)								Apollo 11 (10085)					
	A	B	C	D	E	F	G	H	I	J	K	L	M	N
SiO_2	46.7	54.6	42.7	45 0	50 4	51 1	49 4	47 4	47 8	46.6	43 9	44 2	46 0	45 4
TiO_2	2.4	2.0	4.2	0.4	0 6	0.4	2.8	0.5	0 4	0 1	0 3	0.0	0 3	0.0
Al_2O_3	22.4	19.5	16.4	30.2	18.3	17.3	18.4	18.5	25 5	32.5	32 9	34.6	27.3	33.8
Cr_2O_3	0.1	0.1	0.1	0.1	0.2	0.2	0.1	0.1	0.1	0.0	0.1	0.0	0.2	0.0
FeO	6 9	8.5	11 5	2 4	9 0	8 3	9.8	8 7	6.2	1.6	4 0	1 1	6.2	2 8
MnO	0 1	0 1	0 1	0.0	0.1	0.1	0.1	0.1	0.1	0.0	0.0	0.0	0.1	0.1
MgO	7 1	4.1	4 6	6 4	9.7	8.9	8 0	10 5	7 2	2 3	3.8	1 3	7 9	1 7
CaO	12.1	9.3	12.2	15.3	10.0	10 0	9 4	9.9	14.6	17.7	17.0	18.3	14.1	17.5
Na_2O	0.6	1 2	0.9	0 6	0 8	0.9	1.1	1.0	0 4	0 6	0 5	0.7	0 3	0.4
K_2O	0.5	1.1	1.6	0.1	0.6	2.0	0.8	0.3	0.1	0.0	0.1	0.1	0.0	0.0
NiO	0 0	0 0	0 0	0.0	0.0	0.0	0.1	0.0	0.0	0.0	0.1	0 0	0 0	0 0
P_2O_5	0 4	1 3	4 0	0.1	1.2	0.9	0.5	1.2	--	--	--	--	--	--
SO_3	0 2	0.1	0 4	0 0	0.1	0.1	0.2	0 1	0 2	0.1	0.1	0.0	0 0	0 0
Sum	97 5	101.9	98 7	100.6	101.0	100.2	100 8	98.3	102.6	101 5	102.8	100 3	102 4	101.7
	Norms[P]													
Fo	0.0	0 0	0.0	5.7	0.0	0.0	0.0	0.6	1.1	0.0	6.5	2 2	4.5	0 0
Fa	0.0	0 0	0.0	1 5	0.0	0.0	0.0	0 4	0.7	0.0	5.2	1 5	2 7	0 0
En	18 1	10 0	11.6	7 7	23.9	22.3	19.9	25.8	16 1	5 7	0.0	0 0	12.9	4.2
Fs	12 7	12.2	14 8	1.9	15.6	14.7	13.5	15 0	9 6	2 7	0.0	0 0	7 1	5.2
Wo	0.1	0.0	0 0	0.0	0.0	2.9	0.0	0 0	2 0	2 7	0 0	1.9	0 0	0.0
Or	3.3	6.2	9.7	0.5	3 7	12 1	4 6	1.9	0 5	0 2	0.5	0.4	0 0	0.0
Ab	5.4	9.8	8.0	5.5	6.4	7 9	8.9	8.9	3.0	4 8	3 9	6.1	2 5	3.3
An	58.3	36.9	35.0	74.8	41.7	36.9	43.0	42.0	66.1	84.7	82.2	86.1	68.4	85.4
Ilm	0 7	3.8	8.0	0.7	1 1	0 8	5 3	1.0	0.8	0.3	0.5	0.1	0.6	0 0
Chr	0.2	0.1	0.1	0.1	0 2	0.2	0.2	0.2	0.2	0.0	0.1	0.0	0.3	0.0
Qtz	0 1	15.5	2.7	0 0	3 7	0 2	3.3	0.0	0.0	0.8	0.0	0 0	0.0	0 5
Cor	0.0	2 6	0.5	1 5	1.0	0.0	0.0	1 4	0.0	0.0	1.1	1 7	1.2	1 3
Apa	1 1	2 9	9.4	0.3	2.7	2.0	1.2	2 7	--	--	--	--	--	--
S	0.1	0.0	0.2	0 0	0.1	0.0	0.1	0.0	0 1	0.0	0.0	0.0	0.0	0.0

Key

A. Type A anorthositic gabbro (115-1).
B Type A norite (115-2).
C. Type A norite (115-3).
D. Type A anorthositic gabbro (115-4)
E. Type A norite (115-5).
F Type A norite (115-6).
G. Type A norite (115-7).
H Type A norite (115-8).
I Heavily shocked anorthositic gabbro (19-57).
J. Unrecrystallized breccia of igneous gabbroic anorthosite (19-1)
K. Gabbroic anorthosite, probably recrystallized breccia (37-9)
L. Anorthosite, igneous or recrystallized breccia (37-1).
M. Anorthositic gabbro, diabasic texture (9-8).
N. Gabbroic anorthosite, recrystallized breccia (37-7).
P. Computed weight percentages of forsterite, fayalite, enstatite, ferrosilite, wollastonite, orthoclase, albite, anorthite, ilmenite, chromite, quartz, corundum, apatite, and elemental sulfur

Table IIB-II. Analyses of representative plagioclase feldspar grains in light-colored particles.

	Weight percentages of elements						
	A	B	C	D	E	F	G
Si	21.4	22.4	22.9	22.3	20.4	28.7	29.1
Ti	0.0	0.1	0.1	0.1	0.0	0.1	0.1
Al	19.3	18.2	18.5	17.4	18.0	10.7	9.8
Fe	0.1	0.2	0.1	0.2	0.0	0.0	0.0
Ca	13.3	12.0	12.2	11.5	13.5	0.5	0.3
Na	0.3	0.9	1.0	1.5	0.3	1.3	1.3
K	0.0[3]	0.1	0.1	0.1	0.1	11.4	12.0
O[H]	47.0	47.0	48.0	46.1	44.8	45.2	45.0
Sum	101.4	100.9	102.9	99.2	97.1	97.9	97.6
Ab[I]	4.4	11.5	12.1	18.3	3.2	15.4	15.0
An	95.4	88.0	86.9	81.2	96.3	3.2	2.2
Or	0.2	0.5	1.0	0.5	0.5	81.4	82.8

Key

A. Typical highly calcic plagioclase from Type A norite (101-12).

B. Less calcic plagioclase from same type of rock (106-15).

C. Typical plagioclase from Type B anorthosite breccia (133-6).

D. More sodic plagioclase from Type B norite breccia (102-17).

E. Calcic plagioclase from olivine-plagioclase particle (130-9).

F, G. K feldspar from rhyolite fragment (102-5).

H. Oxygen by stoichiometry.

I. Mole percentages albite, anorthite, and orthoclase.

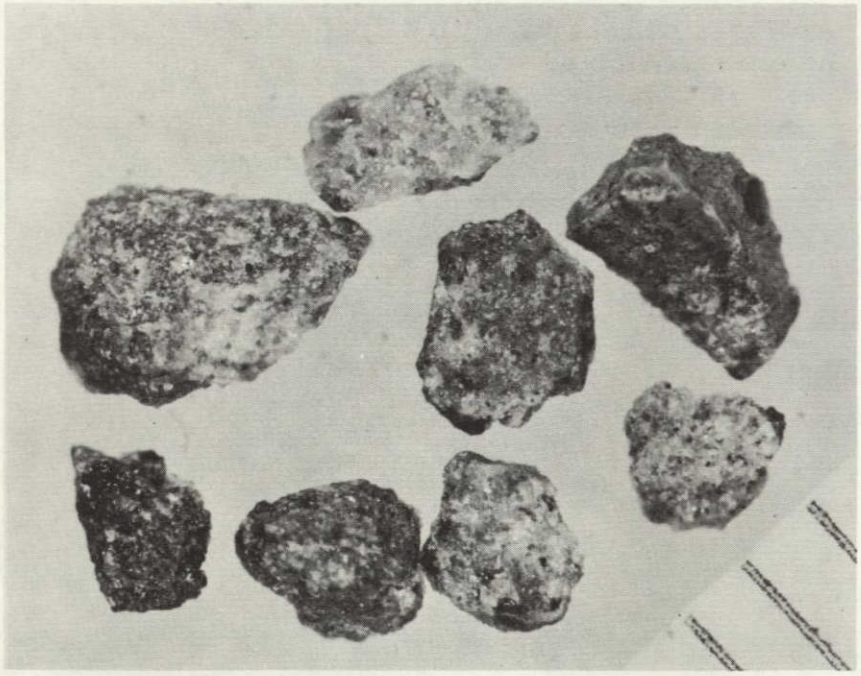

Figure IIB-1. Relatively light-colored particles hand-picked from Soil Sample 12037. These were made into section (115); all are Type A norite–anorthosites.

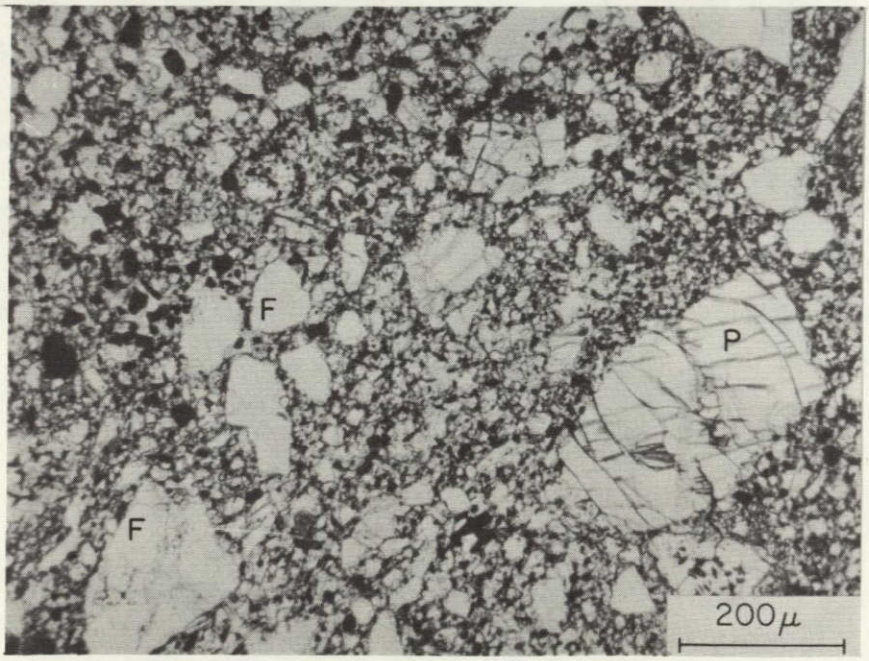

Figure IIB-2. A Type A norite particle (115-3) of the most common sort, by plain transmitted light. Texture is clearly that of a recrystallized breccia; angular forms of pyroxene (P) and plagioclase (F) clasts are preserved. Opaque grains are chiefly ilmenite.

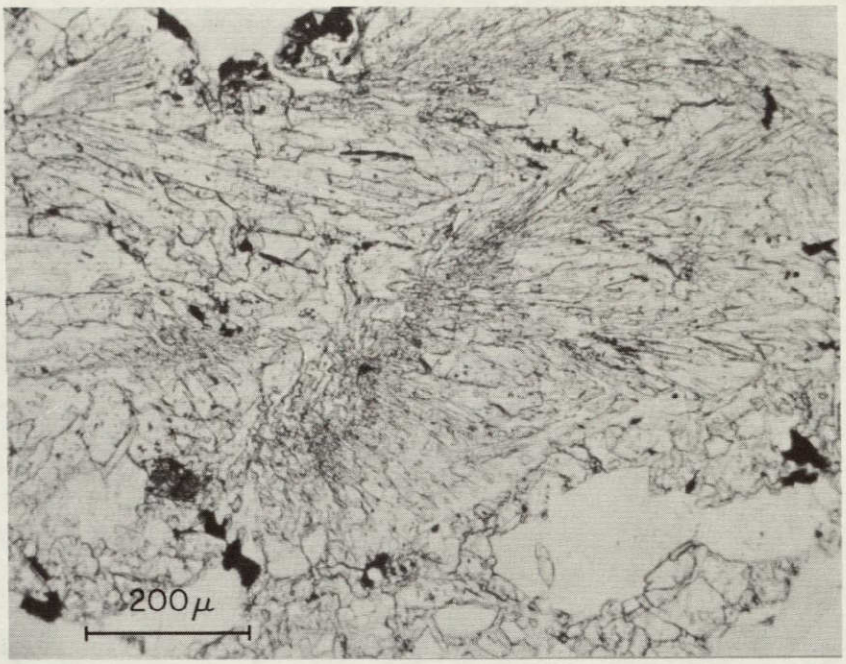

Figure IIB-3. Type A norite (130-12) with igneous texture, by plain transmitted light. Visible are diverging sheaves of feldspar and pyroxene crystals.

Figure IIB-4. Type A anorthositic gabbro particle (130-10) displaying both igneous (diabasic, left) and recrystallized breccia (right) textures. Arrow points to perfect tetrahedron of pale brown spinel embedded in plagioclase crystal (P). Plain transmitted light.

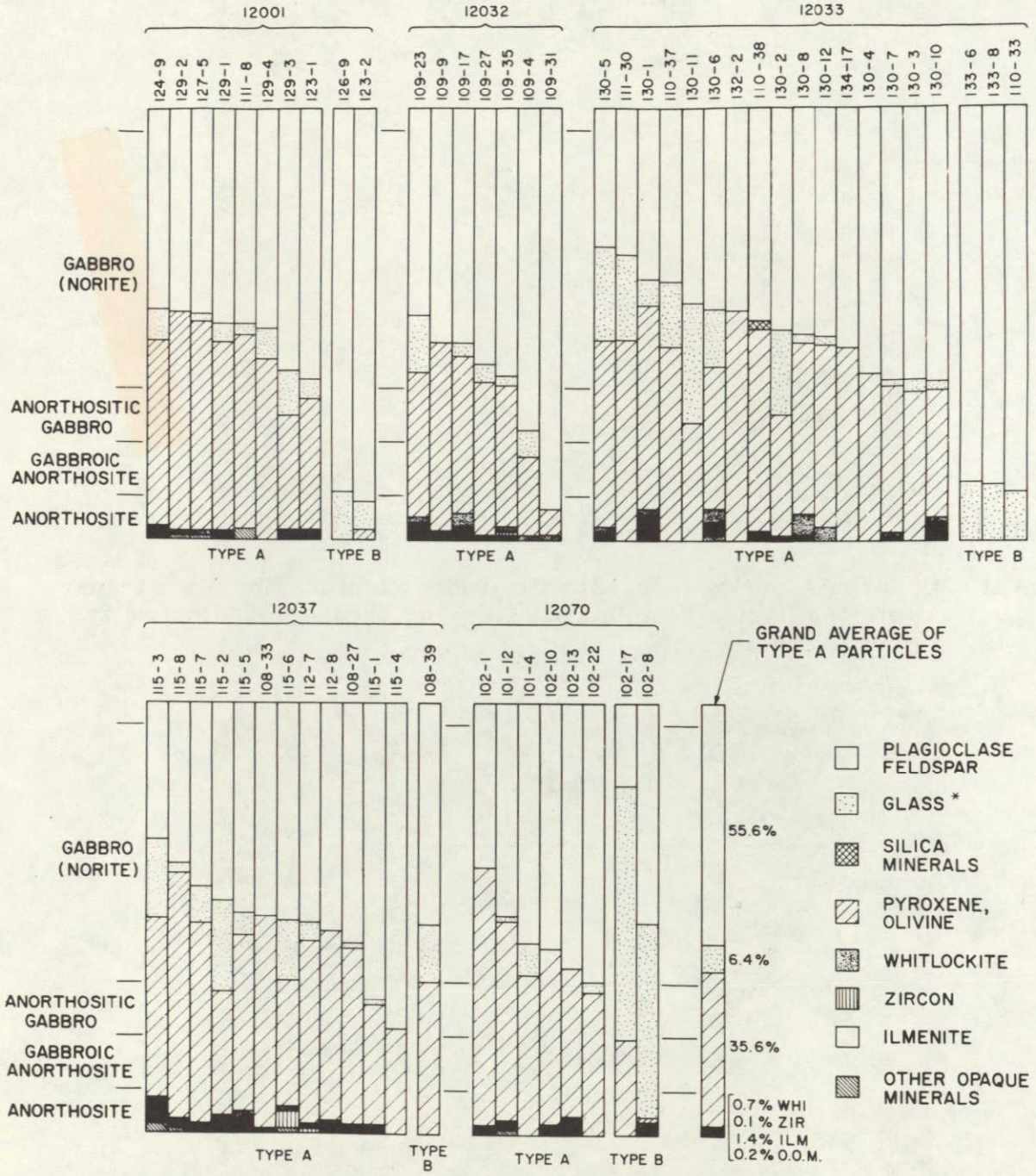

Figure IIB-5. Bar graph showing mineral proportions (modes) in 57 Type A and B light-colored particles, from surveys of ~100 points on each particle. Distance that plagioclase segment of each bar extends downward, read against the left edge of the diagram, gives rock classifications.

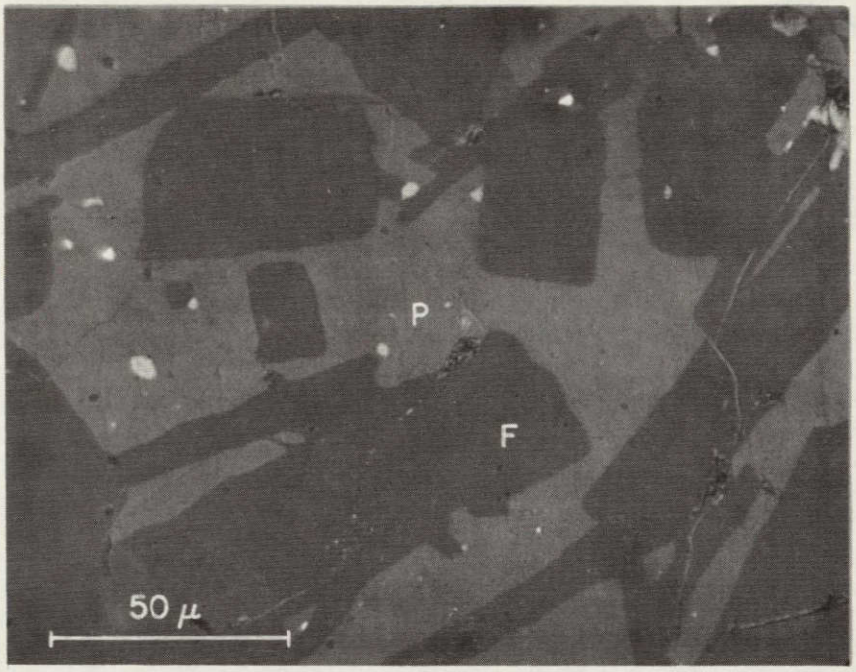

Figure IIB-6. Igneous (diabasic) texture in Type A anorthositic gabbro (130-10), by reflected light: laths of plagioclase (F) embedded in pyroxene (P).

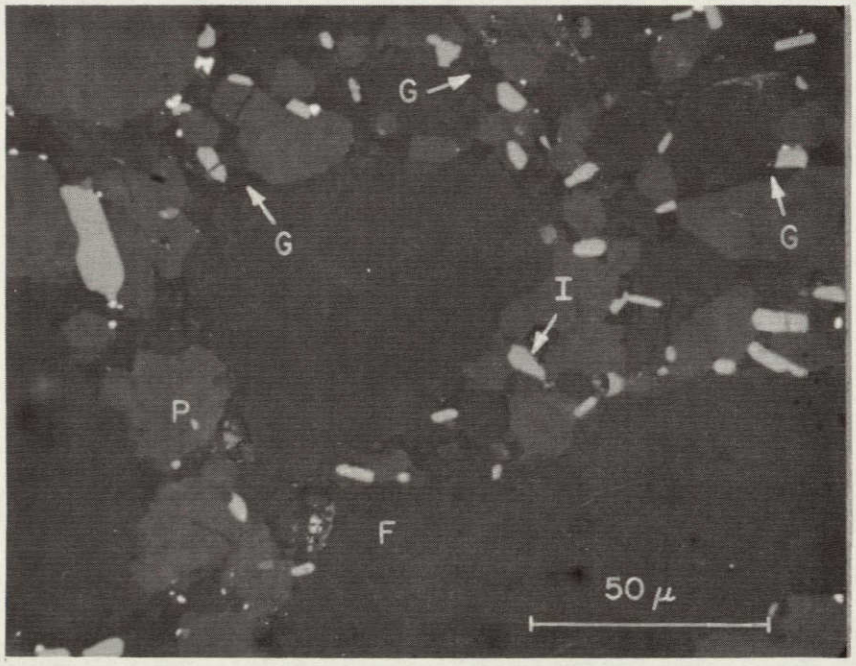

Figure IIB-7. The most common textural pattern in Type A norite–anorthosites, that of a recrystallized breccia, viewed by reflected light. Plagioclase (F), pyroxene (P), glass (G), and ilmenite (I) in (115-3). The rock is perfectly solid; recrystallization has eliminated all pore space between clasts.

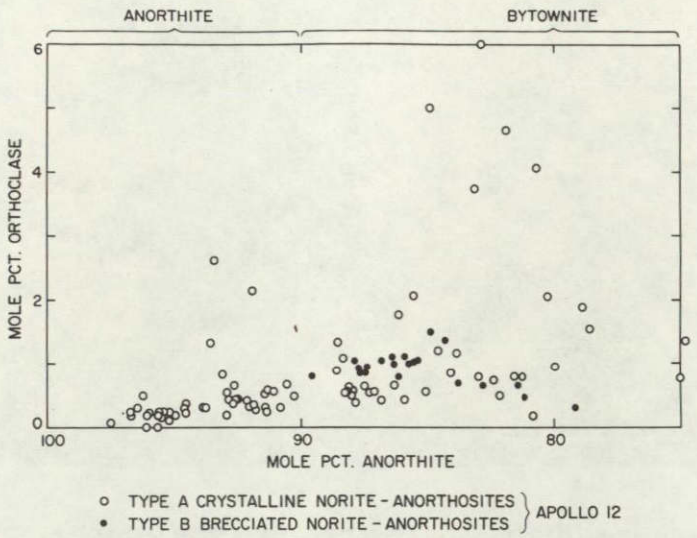

Figure IIB-8. Orthoclase ($KAlSi_3O_8$) vs. anorthite ($CaAl_2Si_2O_8$) content of plagioclase grains microprobed in light-colored particles. Analyses showing very high orthoclase content are probably erroneous.

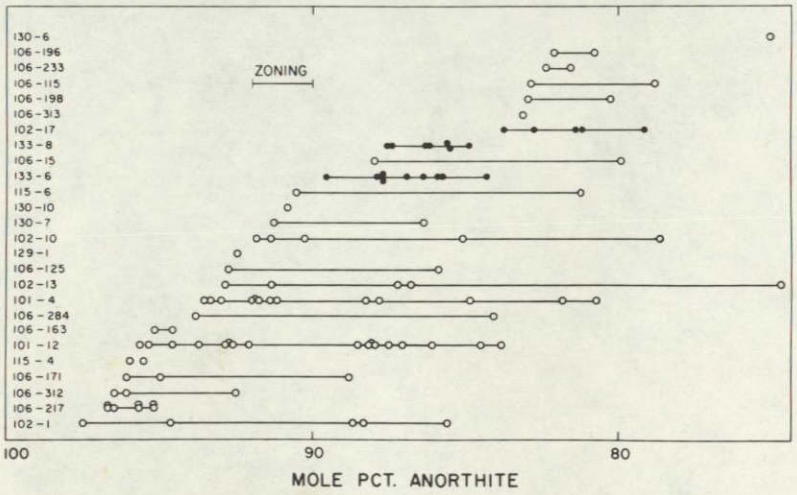

Figure IIB-9. Record of plagioclase compositions encountered in each of 26 light-colored particles studied (white vs. black entries as in Figure IIB-8). "Zoning" bar shows maximum compositional variability present in any single plagioclase grain or clast.

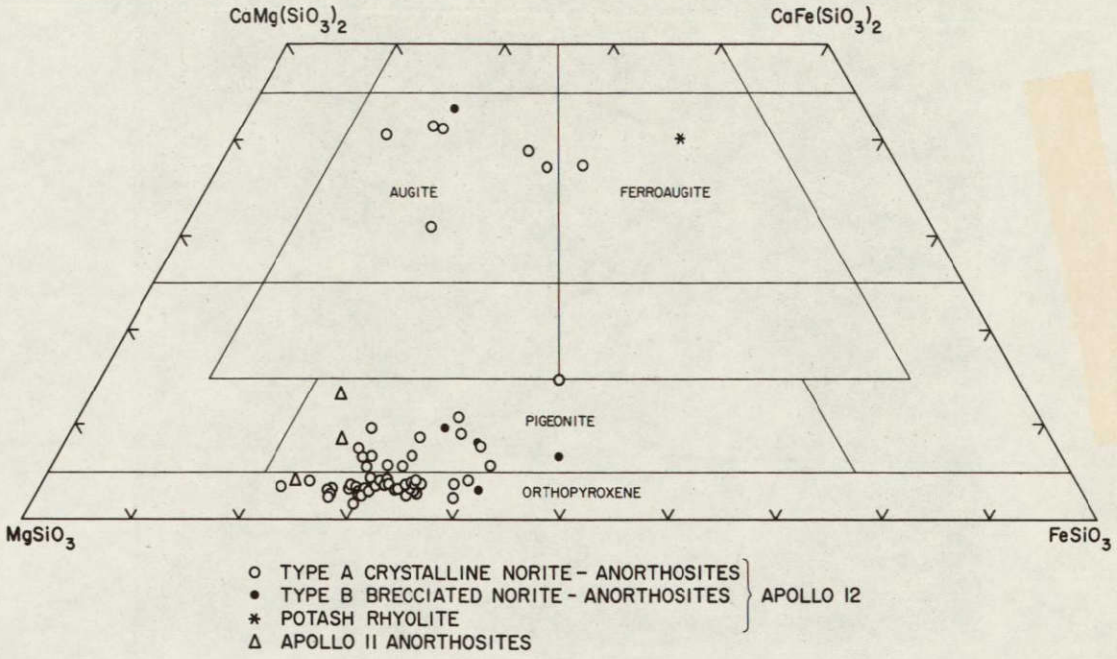

Figure IIB-10. Compositions of pyroxenes microprobed in Apollo 12 and Apollo 11 light-colored particles, in terms of their relative content (mole %) of ideal pyroxene end members.

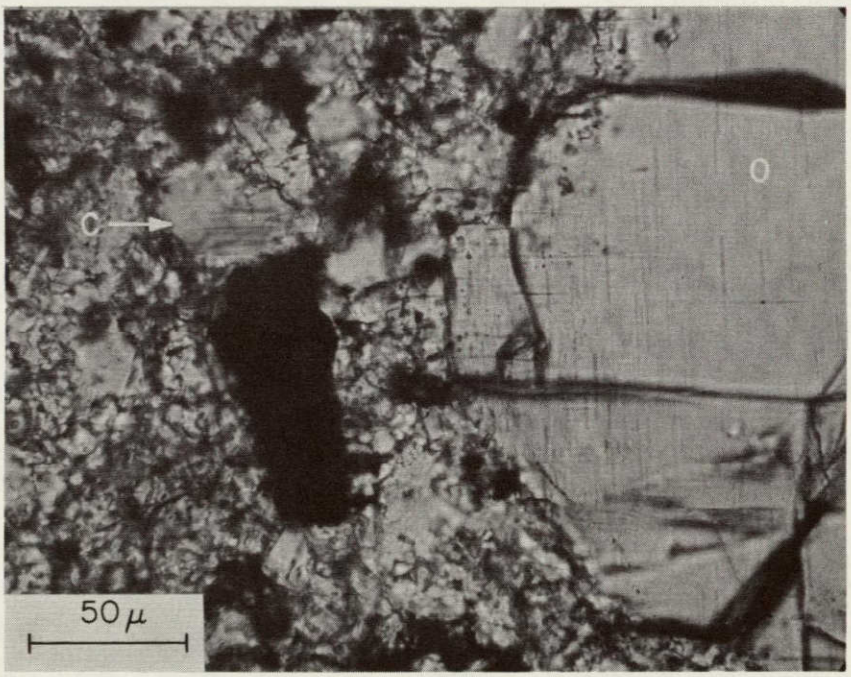

Figure IIB-11. Coexisting orthopyroxene (O) and clinopyroxene (C) in a Type A norite (129-4), by plain transmitted light. Clast O displays parallel extinction.

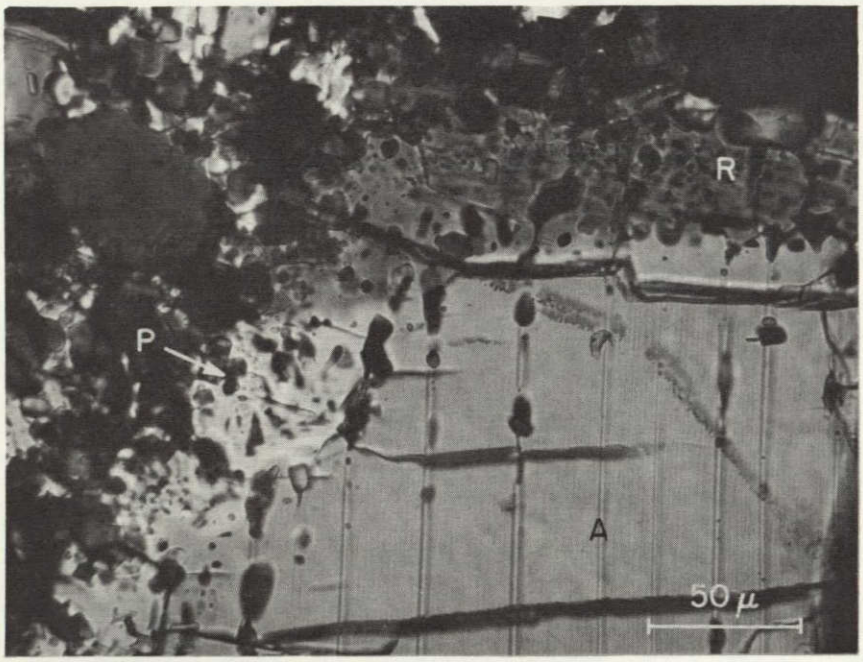

Figure IIB-12. Effect of recrystallization on a Type A norite (130-6): overgrowths of Ca-poor (P, $En_{56}Fs_{40}Wo_4$) and Ca-rich (R, $En_{33}Fs_{28}Wo_{39}$) clinopyroxene on an original clast of clinopyroxene (A, $En_{29}Fs_{34}Wo_{37}$). Transmitted polarized light.

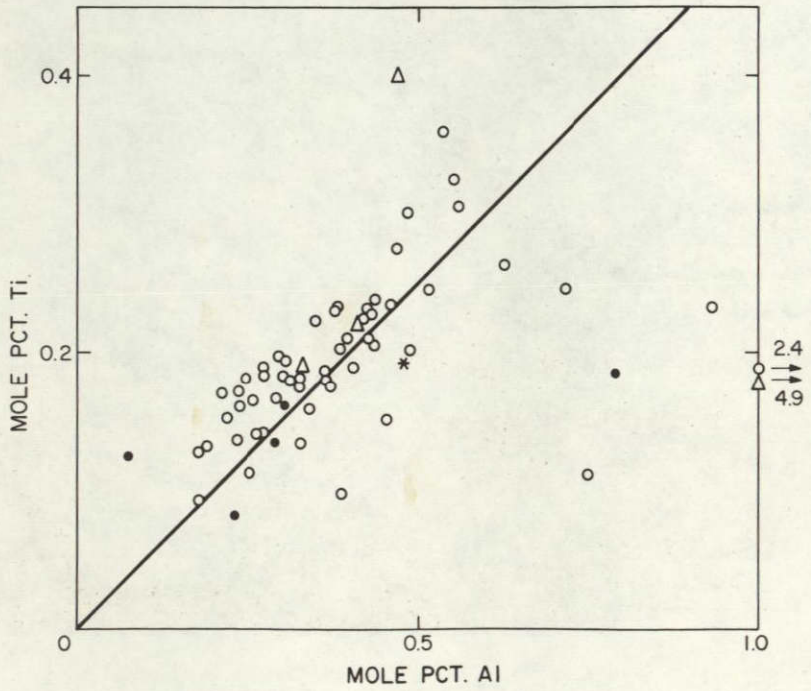

Figure IIB-13. Ti vs. Al content of pyroxenes in light-colored particles, showing 1:2 relationship (solid line) needed to maintain charge balance. Data symbols as in Figure IIB-10.

Chemical analyses of representative pyroxene grains are presented in Table IIB-III. These are somewhat richer in Fe than the pyroxenes we analyzed in Apollo 11 anorthosites, as Figure IIB-10 demonstrates. Pyroxenes in Apollo 12 light-colored fragments display the same relationship between Ti and Al content as was found in Apollo 11 basaltic pyroxenes (Wood et al., 1970; and others); i.e., two Al atoms substitute for Si for every Ti atom that substitutes for Mg, Fe, in order to maintain charge balance (Figure IIB-13). The levels of Al and Ti in the pyroxenes now being described are lower than those we encountered in the Apollo 11 (augitic) basalt pyroxenes, by almost an order of magnitude.

The Cr_2O_3 contents of the pyroxenes of lunar light-colored particles are shown in Figure IIB-14. The Cr level in mafic minerals is of particular interest, because it provides a key to the evolutionary history of a magma system (Section IIIA). There is no obvious relationship between Cr content and the ortho- or clino-character of the pyroxene (Ca content).

Zoning in the Ca-poor pyroxenes of Type A norite–anorthosite particles is not pronounced: typically, the rim of a pyroxene grain of 100-μ diameter contains ~5 mole % more ferrosilite than the center. In contrast to the situation with feldspars described above, the variability of pyroxene compositions from one grain to another in Type A fragments is not much greater than this (Figure IIB-15). The high-Fe clusters of data points for particles (101-4) and (101-12) (which were most thoroughly studied) in Figure IIB-15 were taken in the smallest pyroxene grains, those presumably most affected by recrystallization; the divergent low Fe measurements came from the centers of relatively large clasts. Except for these centers, it appears that the pyroxenes in these rocks are fairly well equilibrated; the individual pyroxene grains must have "communicated" more successfully with one another than did the feldspar grains during the thermal event that recrystallized textures.

Glass

Type A norite–anorthosites contain abundant glassy material along grain boundaries between the major minerals This is usually visible only by

reflected light (Figure IIB-7). Sometimes close examination shows that what seemed to be a single plagioclase grain is actually a complex of euhedral plagioclase crystals embedded in glass (Figure IIB-16). The glass may be featureless and clear, or it may have the mottled appearance characteristic of (at least) partly microcrystalline material.

The glass is rich in K and Al. Microprobe analyses of typical occurrences are shown in Table IIB-IV, columns A and B. Orthoclase is the dominant normative mineral. Both of these grains show normative corundum, but while one is quartz normative, the other shows normative feldspathoids. These glasses are generally similar to the areas of K-rich residual material found in some Apollo 11 basalts (Roedder and Weiblen, 1970; Wood et al., 1970; and others); principal differences are that the norite—anorthosite glasses contain substantially more Al and less Fe than the basaltic residua.

Olivine

Approximately 5% of the mafic mineral grains in Type A norite—anorthosite particles consist of olivine. These occur as clasts or grains mingled with the pyroxene and plagioclase; there is rarely if ever an obvious reaction relationship with pyroxene. Microprobe analyses of representative grains are shown in columns A and B of Table IIB-V. Compositions of olivines from Apollo 12 light-colored particles and basalts are compared in Figure IIA-22, and implications of the differences are discussed in Section IIIA.

Whitlockite

The Type A norite—anorthosites contain approximately 3% by volume of phosphate minerals; all the grains microprobed are of whitlockite. Occasionally, this appears in large clasts (Figure IIB-17), but usually as small, anhedral grains that would be inconspicuous if it were not for their hollowed-out appearance by offset reflected illumination (Figure IIB-18). Being a softer mineral than the surrounding silicates, whitlockite on a section surface tends to polish away faster and leave low-lying areas.

The lunar whitlockite contains astonishing amounts of yttrium and rare-earth elements (Figure IIB-19). Six microprobe analyses of this mineral are presented in Table IIB-VI; they are remarkably similar to one another. We have not confirmed the identification of this mineral by x-ray diffraction, but the low halogen content of two of the analyses seems to rule out the possibility that they might be apatite. Rare-earth-rich whitlockite was first reported in this type of lunar material by Albee and Chodos (1970), who observed it in the Caltech group's "Luny Rock," 10085-LR-1.

The average of these analyses reduces to the approximate formula 2.22 CaO · 0.23 MgO · 0.01 Na_2O · 0.06 FeO · 0.09 Y_2O_3 · 0.08 rare-earth oxides · P_2O_5. This is somewhat short of the ideal whitlockite formula, 3 CaO · P_2O_5; the fault may lie with the incomplete reduction of microprobe data or with failure to analyze for yet another unexpected element.

Zircon

This mineral is remarkably abundant in the Type A norite—anorthosites. It occurs in irregular anhedral grains, usually enclosing several euhedral pyroxene and feldspar crystals, which give the surrounding zircon a Swiss-cheese-like appearance (Figure IIB-20). These zircon complexes (apparently monocrystals, in spite of their tortuous shape) can be quite large, more than 100 μ in diameter. They are more easily recognized by reflected than by transmitted light (Figure IIB-21).

The chemistry of zircons from the lunar soil (presumably derived from norite—anorthosites, since they have not been observed <u>in situ</u> in basalt sections) is discussed in Section IIE.

Silica mineral

Small amounts of an unidentified silica mineral are present in a few of the particles studied (Figure IIB-22). In appearance and occurrence, it usually resembles the more abundant areas of K-rich residual glass.

Table IIB-III. Analyses of representative pyroxene grains in light-colored particles.

	Weight percentages of elements						
	A	B	C	D	E	F	G
Si	26.0	25.5	25.0	24.0	24.2	24.4	23.5
Ti	0.5	0.3	0.5	0.2	0.3	0.4	0.4
Al	0.6	0.3	0.4	0.3	0.4	0.9	0.5
Cr	0.3	0.3	0.3	0.2	0.2	--	0.0
Fe	14.2	15.2	8.4	19.2	17.9	8.8	18.0
Mn	0.2	0.2	0.1	0.4	0.4	--	0.3
Mg	14.0	12.0	8.4	11.7	11.0	7.7	3.6
Ca	1.1	3.0	14.2	1.0	2.7	14.6	12.9
Na	0.0	0.0	0.1	0.0	0.0	--	0.0
O^H	44.4	43.2	43.0	41.5	41.9	42.3	40.2
Sum	101.3	100.0	100.4	98.5	99.0	99.1	99.4
En^I	3.3	8.8	41.4	3.0	7.9	43.4	40.3
Fs	30.0	32.6	17.9	40.9	38.7	18.7	41.1
Wo	66.7	58.6	40.7	56.1	53.4	37.9	18.6

Key

A. Typical orthopyroxene grain in Type A norite (101-4).
B. Typical pigeonite grain in Type A norite (101-12).
C. Typical augite grain in Type A norite (101-12).
D. Typical orthopyroxene grain in Type B breccia (102-17).
E. Typical pigeonite grain in Type B breccia (102-17).
F. Augite grain in Type B breccia (102-8).
G. Ferroaugite grain in potash rhyolite fragment (102-5).
H. Oxygen by stoichiometry.
I. Mole percentages enstatite, ferrosilite, and wollastonite.

Table IIB-IV. Chemical compositions and norms of representative glasses in light-colored particles.

	Weight percentages of elements					
	A	B	C	D	E	F
O[G]	46.4	45.0	43.4	42.6	45.5	44 3
Na	1 1	0.9	0.4	0.9	0.1	0 2
Mg	0.1	0.1	4.8	5.2	12.5	10.1
Al	12.4	11.2	8.6	7 6	12 1	11 4
Si	27.8	28.0	22.3	21 9	19.5	19.8
P	0 0	0 0	0 0	0 0	0 1	0 0
S	0.0	0.0	0 1	0.0	0.0	0 0
K	6.8	11 9	1.7	0 5	0.0	0.1
Ca	4.2	0 4	7.5	8.7	8.3	9.0
Ti	0.1	0.2	1.5	1 8	0.0	0 0
Cr	0.0	0.0	0 1	0.1	0 0	0 0
Mn	0 0	0.0	0.1	0.1	0.0	0.0
Fe	0 1	0.3	8.6	7.6	2.7	3.9
Ni	0.0	0.0	0.0	0 0	0 0	0.0
Sum	99.0	98.0	99.1	97 0	100.8	98 8
			Norms[H]			
				[illegible]	35.9	29 5
				[illegible]	5.0	7.4
				[illegible]	0 0	0 0
				[illegible]	0 0	0 0
				[illegible]	1 5	2.9
Or	49.2	81.8	12.5	3.8	0.3	0.4
Ab	12 5	0 0	4 6	10 5	1.6	2.7
An	29.3	0.0	36.0	33.1	52 1	56.5
Ne	0.0	8.4	0.0	0 0	0 0	0 0
Leu	0.0	3.9	0 0	0.0	0.0	0.0
Ilm	0.4	0 6	4 8	6.0	0.1	0.0
Chr	0.0	0.0	0.3	0.2	0 0	0 0
Qtz	6.7	0 0	0.0	0.0	0 0	0 0
Cor	1 5	3 5	0 0	0.0	3 1	0.5
Apa	0.0	0.0	0.0	0 0	0.4	0.0
S	0.1	0.1	0.1	0.0	0.0	0.0

Key

A Colorless residual glass in Type A norite (130-2)

B. Colorless residual glass in Type A norite (130-6)

C Brown interstitial glass in Type B breccia (133-6).

D. Brown interstitial glass in Type B breccia (133-8).

E, F Colorless glass in unique olivine-plagioclase particle (130-9)

G. Oxygen by stoichiometry.

H Computed weight percentages of forsterite, fayalite, enstatite, ferrosilite, wollastonite, orthoclase, albite, anorthite, nepheline, leucite, ilmenite, chromite, quartz, corundum, apatite, and elemental sulfur.

Table IIB-V. Compositions of representative olivine grains in light-colored particles.

	Weight percentages of elements				
	A	B	C	D	E
O[F]	39.6	42.4	41.0	43.1	33.3
Mg	18.6	27.2	23.3	28.0	3.1
Al	0.0	0.1	0.0	0.3	0.0
Si	17.9	18.4	18.4	19.1	14.9
Ca	0.1	0.1	0.1	0.3	0.1
Ti	0.0	0.0	0.0	0.0	0.1
Cr	0.0	0.1	0.0	0.0	0.0
Mn	0.2	0.2	0.2	0.1	0.7
Fe	23.9	11.9	16.1	8.6	48.4
Ni	0.0	0.0	0.0	0.0	0.0
Sum	100.3	100.4	99.1	99.5	100.6
Mole % fayalite	35.8	16.0	23.2	11.8	87.0

Key

A. Olivine in Type A norite (102-1).

B. Magnesian olivine in Type A spinel-bearing gabbroic anorthosite (115-4).

C. Olivine in Type B breccia (102-17).

D. Magnesian olivine in unique olivine-plagioclase particle (130-9).

E. Iron-rich olivine in potash rhyolite particle (102-5).

F. Oxygen by stoichiometry.

Table IIB-VI. Microprobe analyses of whitlockite grains in Type A norite–anorthosites.

	Weight percentages of elements					
	A	B	C	D	E	F
O[G]	42.7	40.3	40.9	41.8	40.4	42.0
Na	0.2	0.2	0.2	0.0	0.2	0.1
Mg	1.9	1.6	1.7	1.9	1.7	2.0
Al	0.1	0.1	0.0	0.0	0.0	0.0
Si	0.2	0.1	0.2	0.2	0.2	0.2
P	21.3	20.1	19.4	19.7	18.8	19.8
S	0.0	0.0	0.0	0.0	0.0	0.0
K	0.0	0.0	0.0	0.0	0.0	0.0
Ca	30.0	28.2	27.7	29.1	28.3	28.3
Ti	0.0	0.0	0.0	0.0	0.0	0.0
Cr	0.0	0.0	0.0	0.0	0.0	0.0
Mn	0.0	0.0	0.0	0.0	0.0	0.0
Fe	0.7	0.8	1.2	1.4	1.3	1.2
Ni	0.0	0.0	0.0	0.0	0.0	0.0
Y[H]	2.0	2.7	3.1	2.2	2.5	2.5
La	0.5	0.7	0.6	0.7	0.6	0.6
Ce	1.3	1.6	1.0	1.6	1.4	1.8
Pr	0.3	0.4	0.3	0.3	0.2	0.4
Nd	0.8	0.9	0.9	0.8	0.6	0.9
Sm	0.4	0.4	0.4	0.3	0.4	0.4
Gd	0.5	0.5	0.3	0.3	0.3	0.4
Cl[H]	0.01 ±0.01	0.04 ±0.01	--	--	--	--
F	0.0 ±0.1	0.3 ±0.1	--	--	--	--
Sum	102.9	98.6	97.9	100.3	96.9	100.6

Key

A. Whitlockite in (129-1).

B. Grain shown in Figure IIB-17 (129-3).

C, D. Two analyses in same grain (130-8).

E, F. Analyses in another grain (130-8).

G. Oxygen by stoichiometry.

H. Yttrium, rare earths, and halogens corrected only for background. Errors shown for halogens are one-sigma counting statistics.

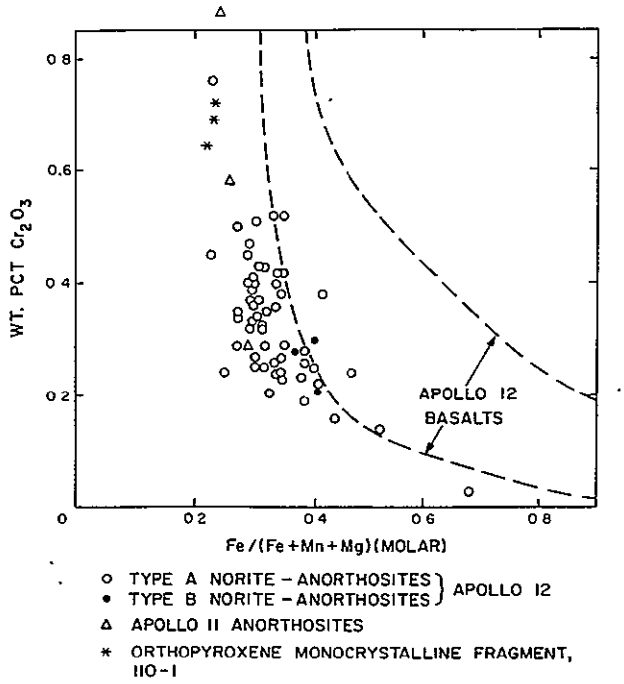

Figure IIB-14. Chromium content (as Cr_2O_3) of pyroxenes in light-colored particles, as a function of major element composition (Fe/(Fe + Mn + Mg)).

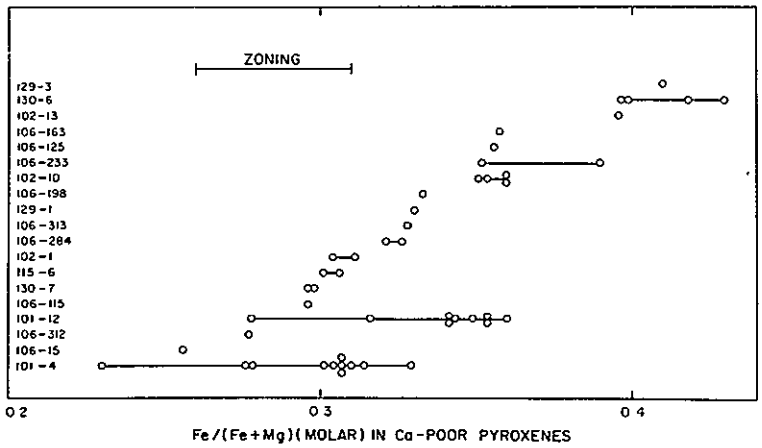

Figure IIB-15. Record of low-Ca pyroxene compositions encountered in each of 19 Type A norite–anorthosites studied. "Zoning" bar shows maximum compositional variability present in any single pyroxene grain or clast.

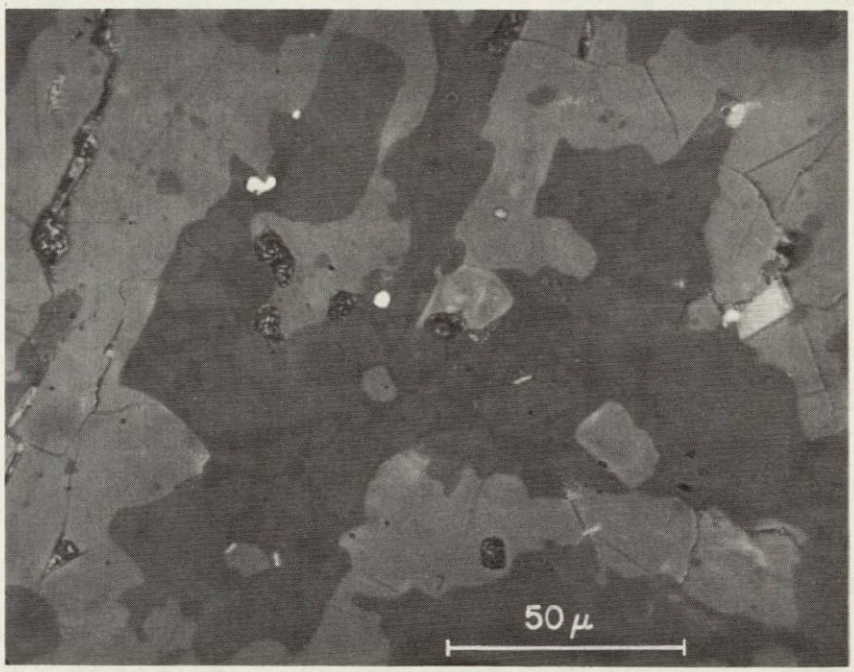

Figure IIB-16. "Feldspathic" regions (darker colored) in a Type A norite (115-6) by reflected light, showing these to consist actually of blocky plagioclase crystals embedded in glass (appears darkest of all).

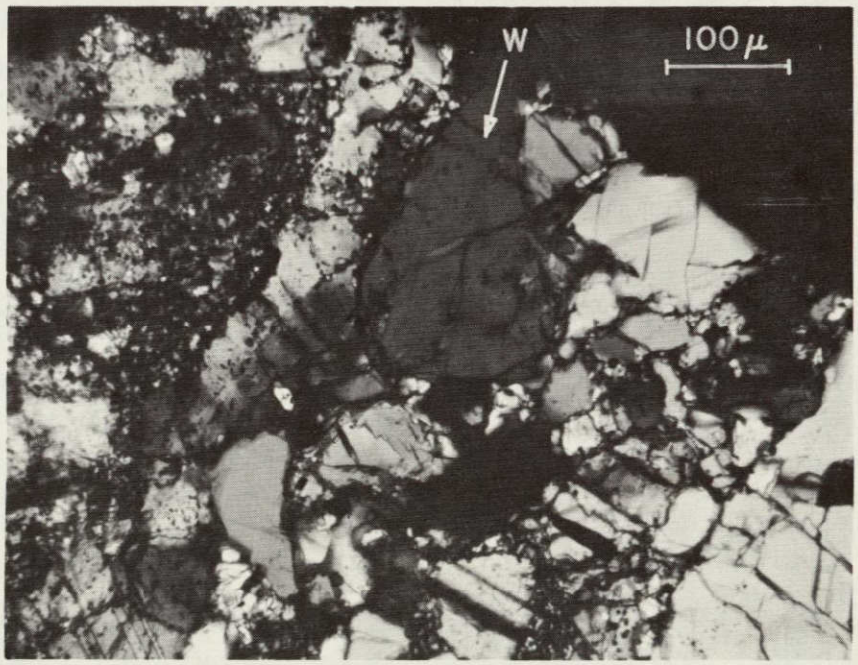

Figure IIB-17. Large clast of the phosphate mineral whitlockite (W), in Type A anorthositic gabbro (129-3). A unique occurrence. Transmitted polarized light. Analysis of this grain appears in Table IIB-VI.

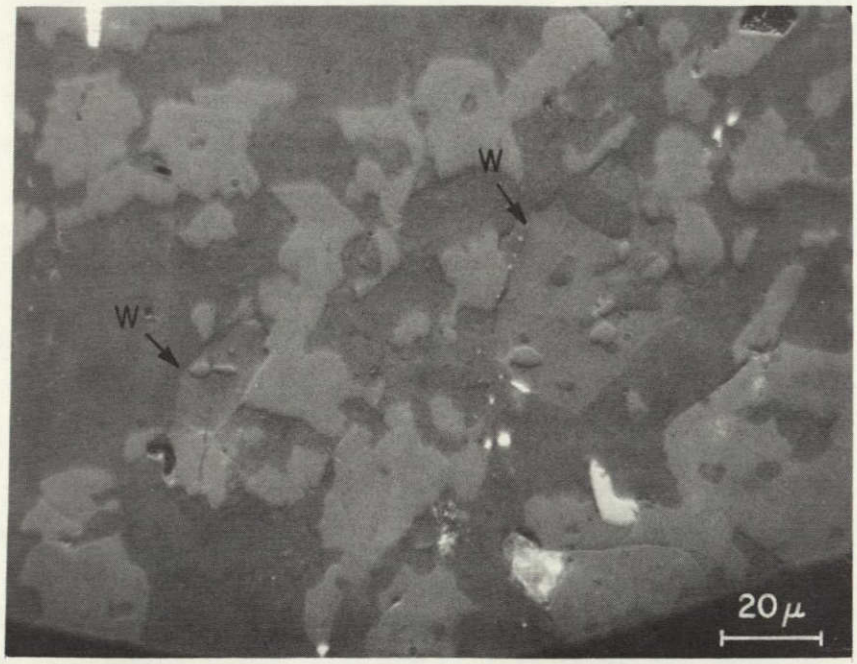

Figure IIB-18. Lunar whitlockite (W) in its most typical form, in Type A norite (115-5). Whitlockite is softer than surrounding silicates and tends to polish out in relief; these depressions become apparent when the specimen is illuminated by an offset incident light source.

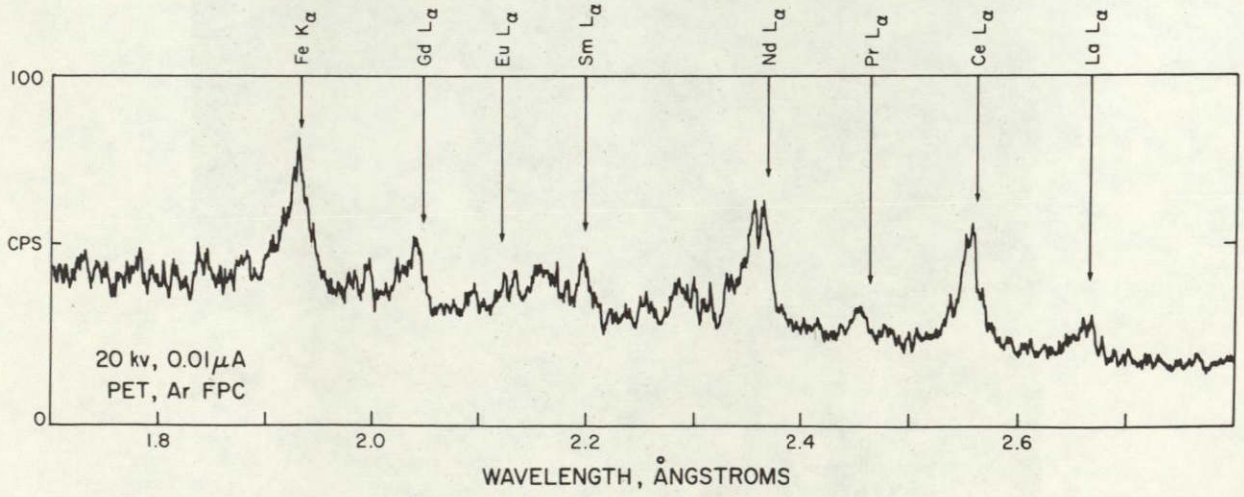

Figure IIB-19. Microprobe data on whitlockite grain in a lunar norite: spectral scan through the wavelength range of rare-earth element L_a x-radiation.

Figure IIB-20. A complex grain of zircon (Z), of almost 200-μ extent, by reflected light. The crystal is riddled with plagioclase and pyroxene inclusions, giving it the appearance of Swiss cheese. Type A norite (115-6). Scale as shown below.

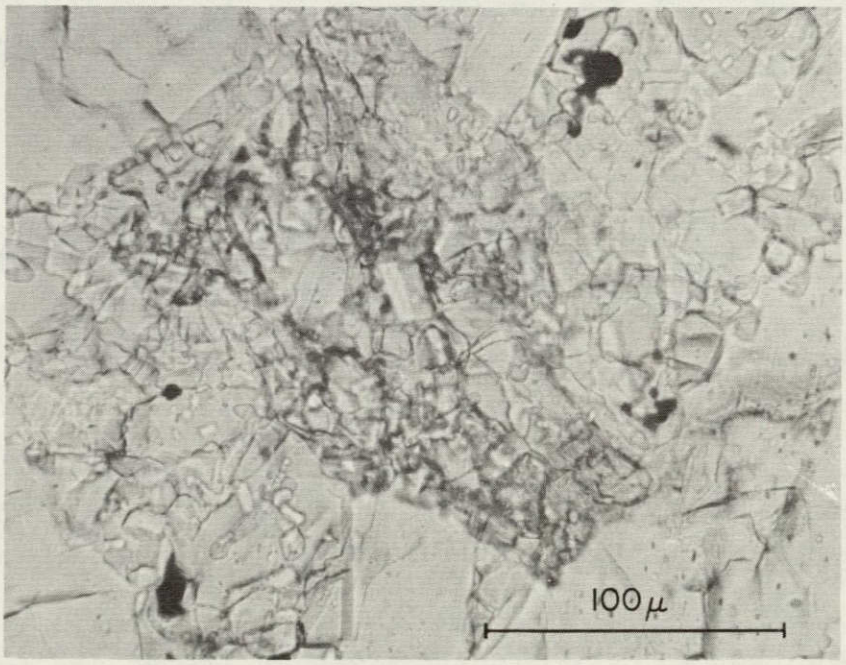

Figure IIB-21. Zircon crystal of Figure IIB-20, by plain transmitted light.

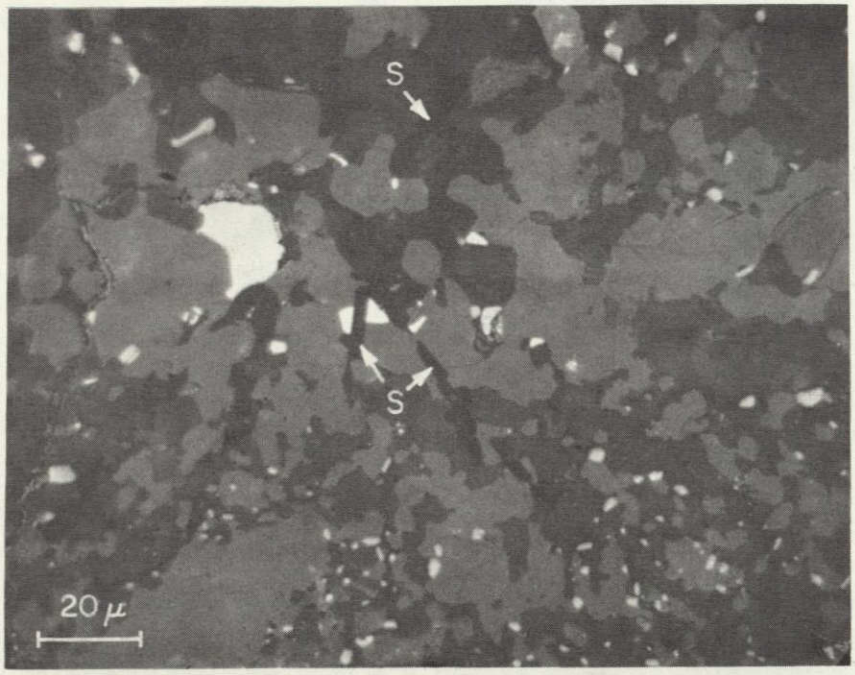

Figure IIB-22. Elongated crystals and irregular grains of a silica mineral (S) in Type A norite (115-2) by reflected light.

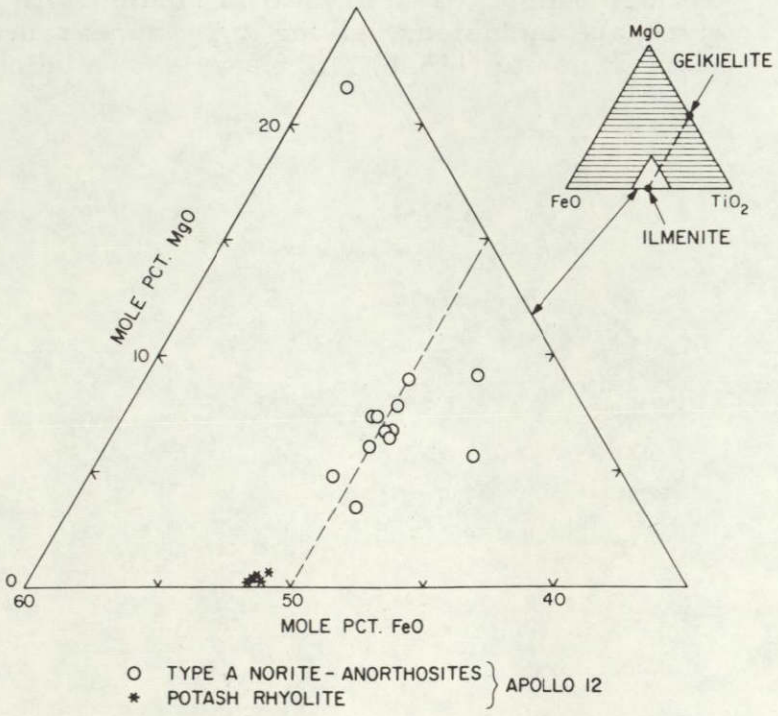

Figure IIB-23. Compositions of ilmenite grains in Type A norite–anorthosites and potash rhyolite (102-5), in terms of their three principal oxides.

Ilmenite

Ilmenite is the most abundant opaque phase in the Type A norite–anorthosites, comprising about 1.5% of them by volume. It occurs as anhedral to subhedral grains, usually of small size (typically 10 to 20 μ; see Figure IIB-7). A representative microprobe analysis is shown in Table IIB-VII, column A. There is some substitution of the geikielite molecule ($MgTiO_3$) for $FeTiO_3$ in the ilmenite of these rocks (Figure IIB-23).

Metal

Nickel-iron metal is present in very small amounts as minute grains (usually 1 to 2 μ). The Ni and Co contents of grains analyzed are shown in Figure IIB-24. They are quite similar to meteoritic kamacite in composition; it seems likely they were contributed to the lunar rock by meteoritic infall, though their compositions may have been modified by reaction with one another and with the lunar material during recrystallization (meteoritic kamacite does not contain more than about 7% Ni).

Other minor minerals

The Type A norite–anorthosites contain trace amounts of troilite, chromite, spinels of unusual composition, and armalcolite (see Table IIB-VII, Figures IIB-25, IIB-26, and IIB-27).

Type B Breccias

A second, less numerous class of plagioclase-rich particles was found, which are distinguishable texturally and mineralogically from the Type A norite–anorthosite series. It is misleading to lump these with the Type A fragments as "light-colored particles," because they are not conspicuously light in macroscopic color (Figure IIB-28). They eluded our attempts to hand-pick norite–anorthosite particles, often ending up in the batches we took to be basaltic in character.

Textures

The Type B particles are unrecrystallized breccias, assemblages of relatively large mineral fragments embedded in glass or a finely crystalline mesostasis (Figure IIB-29, IIB-30, and IIB-31). The close-fitting relationships of many adjacent mineral fragments and the small proportion of interstitial glass in most Type B particles indicate that the rock was brecciated in situ, not mixed and gardened as in a regolith. Some Type B particles are heavily shocked (Figure IIB-30 and IIB-32).

Mineralogy

Compositions of minerals in Type B breccia particles are listed in Tables IIB-II, IIB-III, IIB-IV, and IIB-V and plotted in Figures IIB-8, IIB-9, IIB-10, IIB-13, and IIB-14. It appears that there are systematic differences between Types A and B mineralogy, but we have not accumulated enough data for the latter class of particles to say this conclusively.

1. Type A pyroxenes are richer in Fe than are those of Type B or Apollo 11 anorthosite particles. It appears that their Mn content may be substantially higher (Table IIB-III), but more analyses would be needed to confirm this.

2. Type A plagioclase is somewhat more sodic than Type B plagioclase.

3. Opaque minerals are almost totally lacking. Rare occurrences of ilmenite, armalcolite, whitlockite, and silica were observed, but no zircon.

The interstitial glass in Type B particles is unrelated to the K-rich residual glass in Type A particles. It is brown basaltic glass (Table IIB-IV), of composition similar to the Type A norite–anorthosites (Table IIB-I) and to the brown glasses, abundant in the Apollo 12 soil, that appear to be derived from them (Table IID-VI). This glass was undoubtedly shock-melted and injected into the pore space of shattered anorthositic minerals, where it cooled rapidly. It does not seem to have been generated locally; its high Ti content ($\sim 5\%$ normative ilmenite, higher than that of most Type A norite–anorthosites) contrasts sharply with the near-zero Ti content of the mineral fragments it intrudes.

Chemistry

Most of the Type B fragments are conspicuously more anorthositic, i.e., contain a higher proportion of plagioclase feldspar, than the Type A norite–anorthosites (Figure IIB-5).

Unique Olivine-Plagioclase Particles (130-9)

This particle (Figure IIB-33) has an unusually simple mineralogy and texture: rounded crystals of magnesian olivine (Fa_{12}, Table IIB-V), each surrounded by a shell of glass, are studded in a coarsely crystalline matrix of calcic plagioclase (An_{96}, Table IIB-II). No other minerals are present. Modal proportions are: plagioclase, 61%; olivine, 27%; glass, 12%. This appears to be an igneous rock, and the high contents of anorthite in the plagioclase and of forsterite in the olivine indicate that it crystallized during an early stage of evolution of its parent magma.

The composition of the glass is similar to that of the rock as a whole (Table IIB-IV); differences are not great enough to suggest that it might be residual after primary crystallization. Evidently it is secondary: the rock was reheated at some time, and eutectic melting occurred along olivine-plagioclase grain boundaries. The rock then cooled relatively rapidly, and the melted regions were quenched to glass.

Apollo 11 Revisited

According to our Special Report describing the Apollo 11 sample (Wood et al., 1970), the light-colored particles in the soil from Tranquillity Base are of a very different character from the Apollo 12 particles discussed above: we interpreted them as igneous cumulates and reported higher plagioclase contents than the present Report speaks of. It seemed desirable to reexamine the Apollo 11 anorthosites in the light of our current observations to see whether or not the two groups of particles grade into one another in properties, and if not, how fundamental is the gap between them.

Table IIB-VII. Compositions of oxide minerals in light-colored particles.

	Weight percentages of elements				
	A	B	C	D	E
O^F	32.4	31.3	38.1	32.5	34.1
Mg	2.1	0.0	4.1	4.5	4.1
Al	0.0	0.1	0.1	6.6	15.4
Si	0.1	0.1	1.0	0.1	0.0
Ca	0.2	1.5	0.1	0.1	0.1
Ti	32.2	29.4	44.4	7.8	1.6
Cr	0.3	0.2	1.2	28.7	22.6
Mn	0.3	0.3	0.2	0.1	0.1
Fe	31.7	36.5	13.6	17.4	21.4
Ni	0.0	0.0	0.0	0.0	0.0
Sum	99.3	99.4	102.8	97.8	99.4

Key

A. Typical ilmenite composition, Type A norite (101-12).

B. Ilmenite, potash rhyolite (102-5).

C. Armalcolite, Type A gabbroic anorthosite (115-4).

D. Titanian chromite coexisting with armalcolite (C) and ilmenite in (115-4), Figure IIB-25.

E. Chromian pleonaste in Type A norite (107-8), Figure IIB-26.

F. Oxygen by stoichiometry.

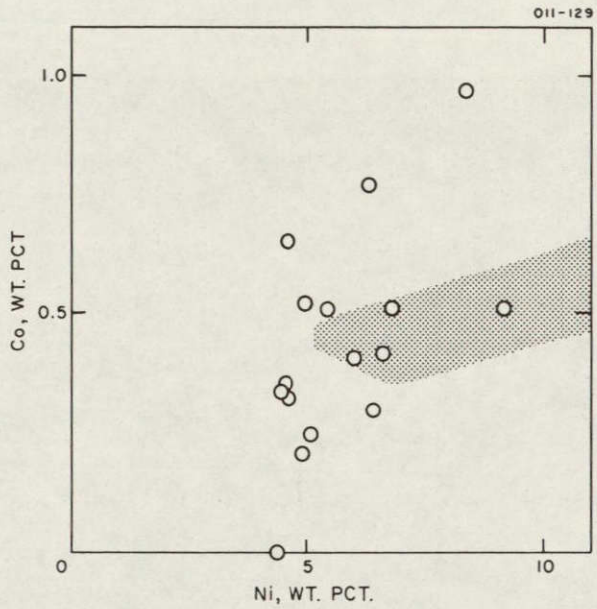

Figure IIB-24. Ni vs. Co contents of metal grains microprobed in Type A norite–anorthosites. Shaded area shows compositional range of iron meteorites (Moore, Lewis, and Nava, 1969).

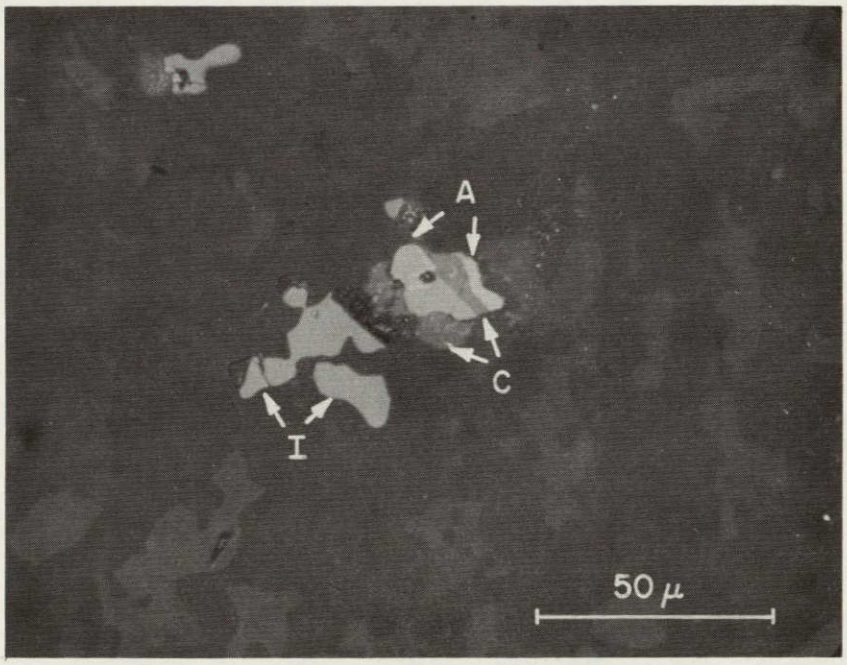

Figure IIB-25. Coexisting armalcolite (A), chromite (C), and ilmenite (I) in (115-4), which is one of the most anorthositic (plagioclase-rich) of the Apollo 12 Type A particles examined. Reflected light. Compositions shown in Table IIB-VII.

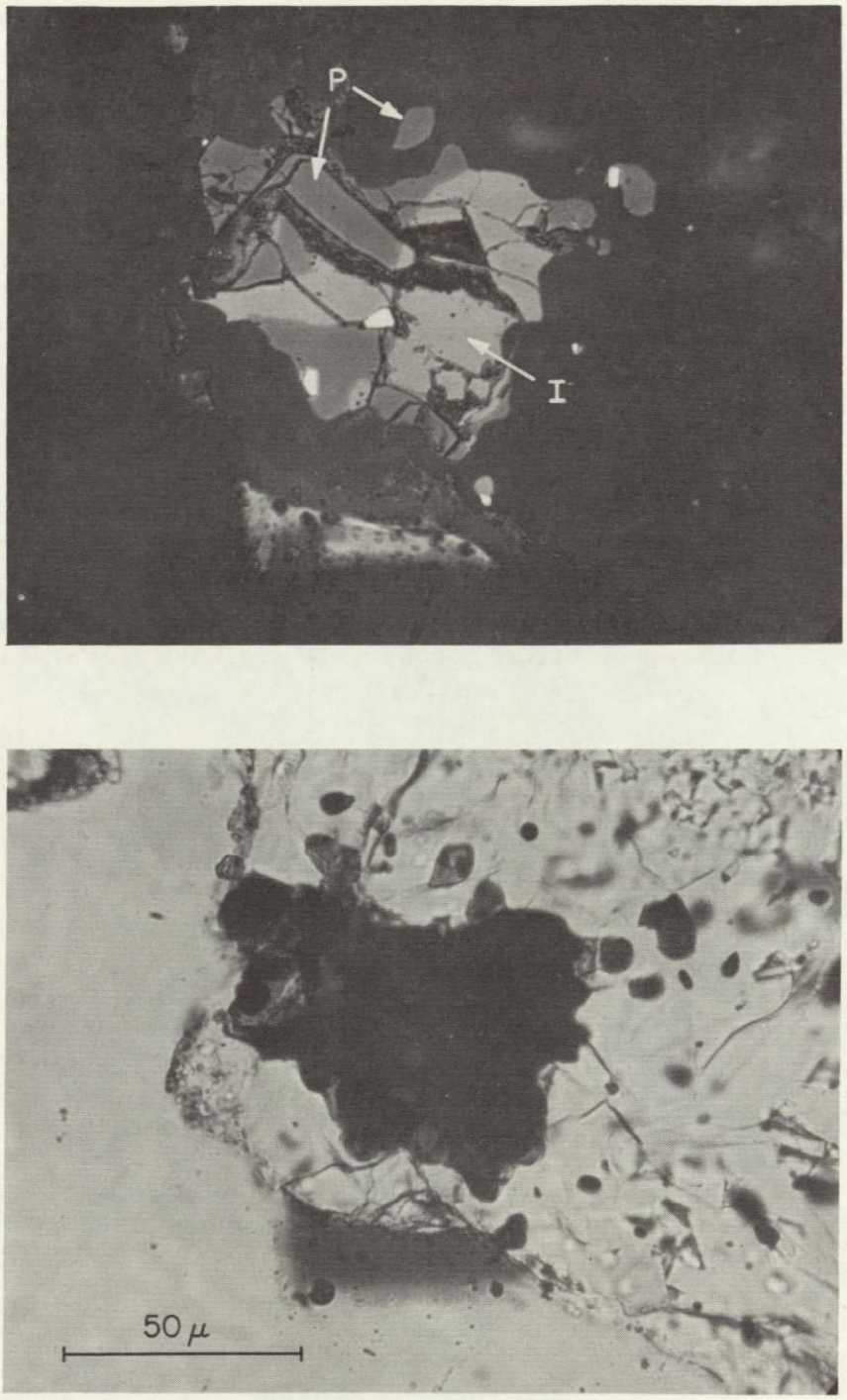

Figure IIB-26. Coexisting spinel (chromian pleonaste (P)), ilmenite (I), and metal (white grains) in the Type A norite (107-8), by reflected light (above) and plain transmitted light (below). The spinel is transparent and has a pale greenish hue. Spinel composition shown in Table IIB-VII.

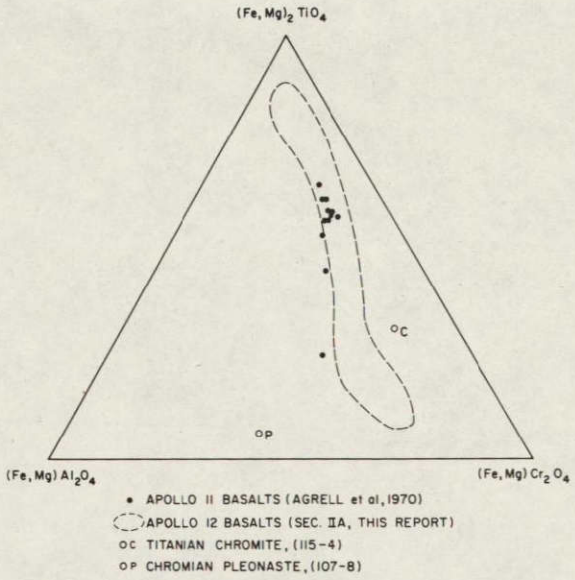

Figure IIB-27. Compositions of two spinel grains analyzed in Type A norite–anorthosites, vs. Apollo 11 and Apollo 12 basaltic spinels.

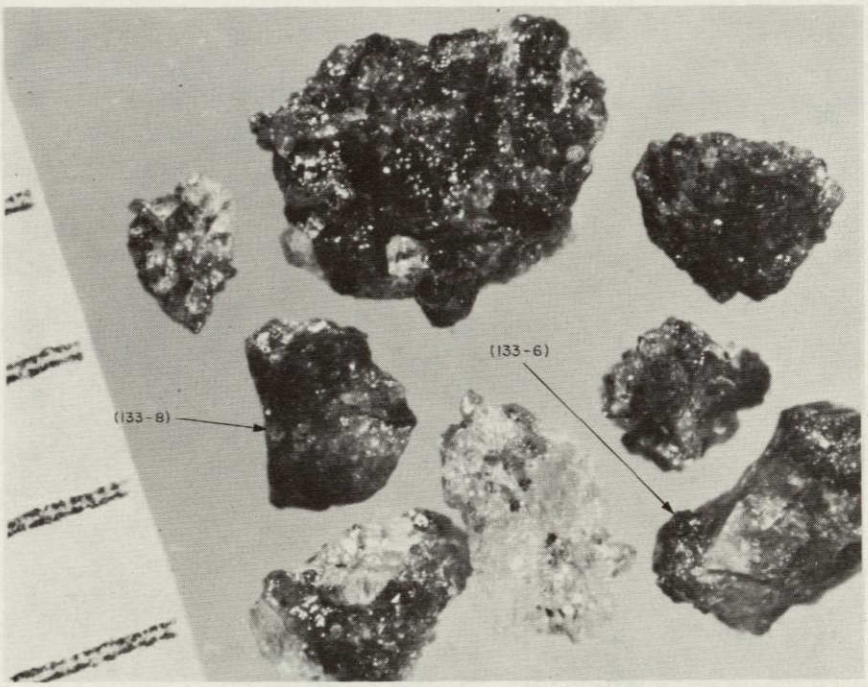

Figure IIB-28. Particles hand-picked from 12033 and thought to be coarse basalts; two (numbered) turned out to be Type B anorthositic breccias. Dark color is probably imparted by brown glass interstitial to feldspar clasts (see Figure IIB-31).

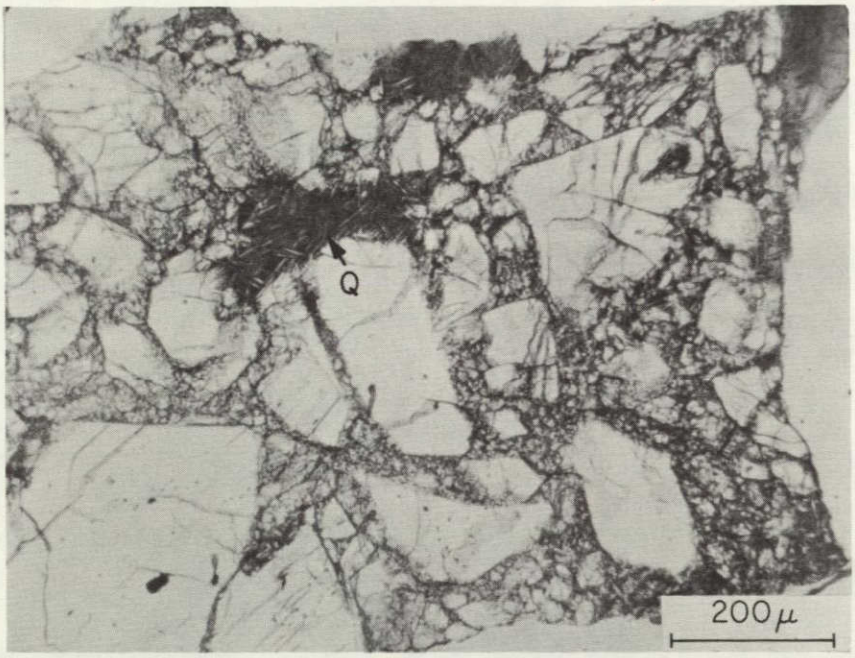

Figure IIB-29. Plagioclase-rich Type B breccia (110-33), by plain transmitted light. All visible clasts are plagioclase. These are separated by red-brown glass; where the glass occurs in sizable volumes, it has precipitated plagioclase microlites (Q).

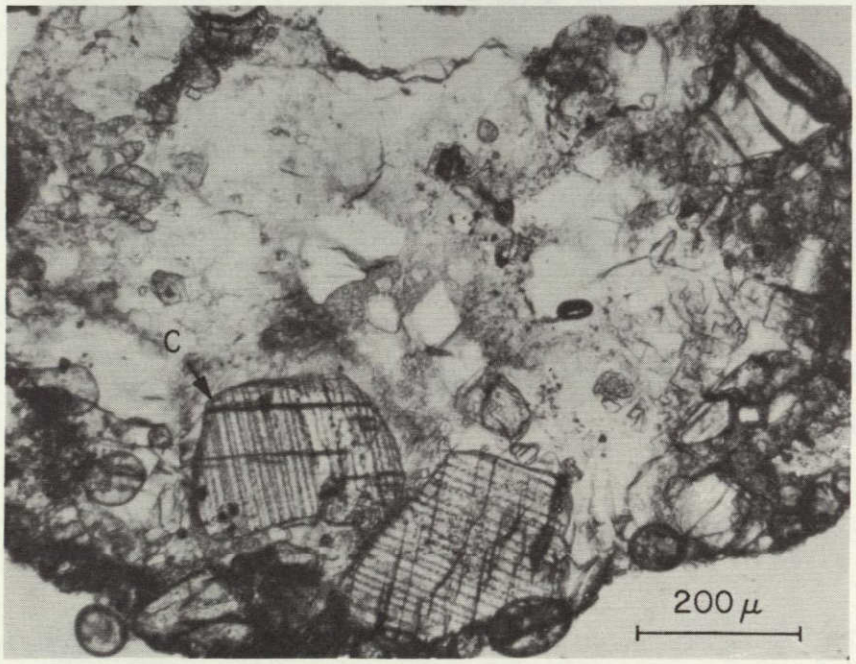

Figure IIB-30. Heavily shocked Type B breccia (102-17) containing abundant clasts of pyroxene as well as plagioclase, by plain transmitted light. Most of particle is shock-melted glass. Clinopyroxene clasts (C) contain submicron inclusions in parallel planar array, producing striped appearance.

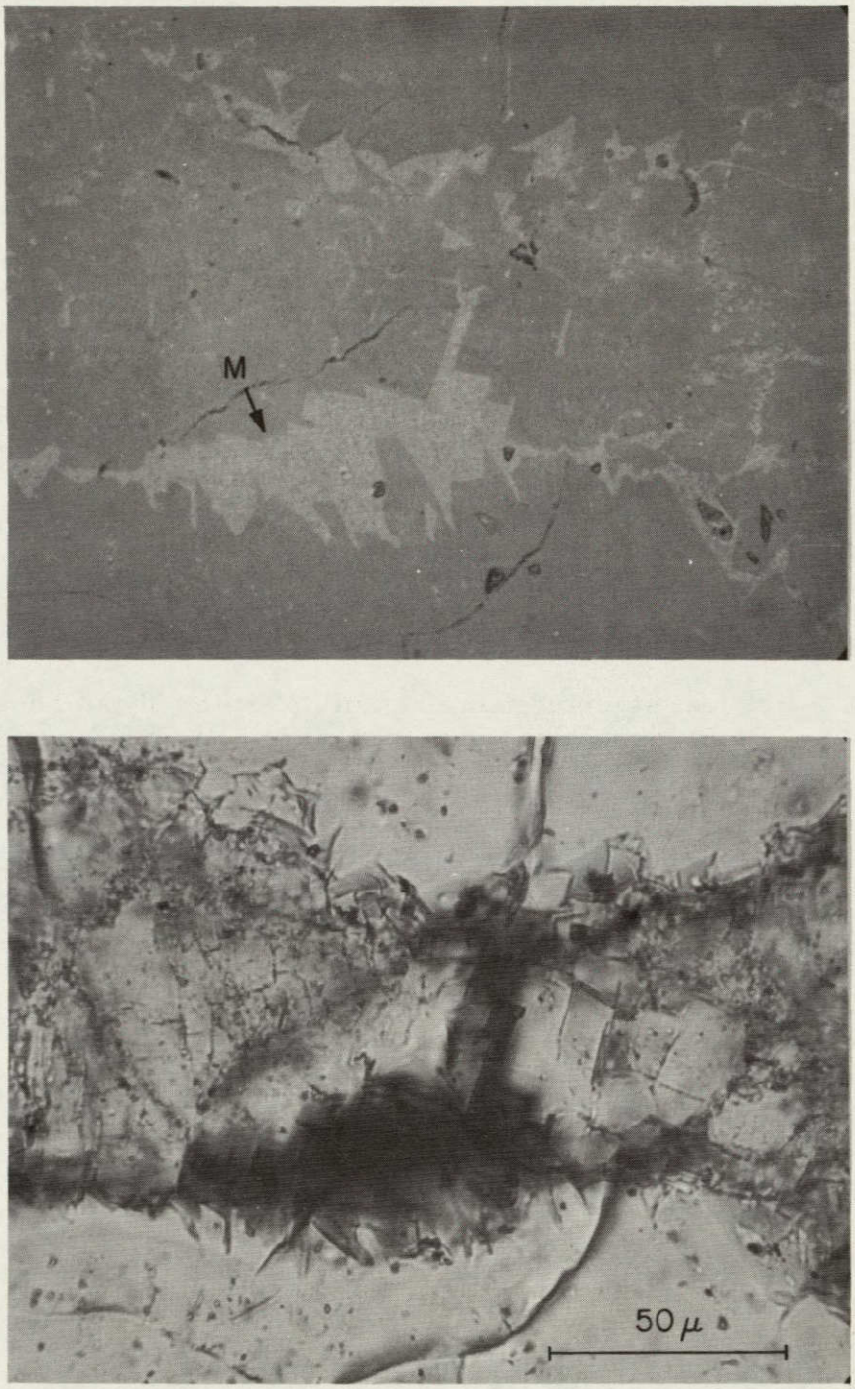

Figure IIB-31. Red-brown glassy (to microcrystalline) mesostasis (M) separating plagioclase clasts in Type B breccia (133-8). Above, reflected light; below, plain transmitted light. Blocky form of plagioclase surfaces is at least in part constructional; red-brown glass is residual after precipitation of some plagioclase on surfaces of original clasts. Glass analysis appears in Table IIB-IV.

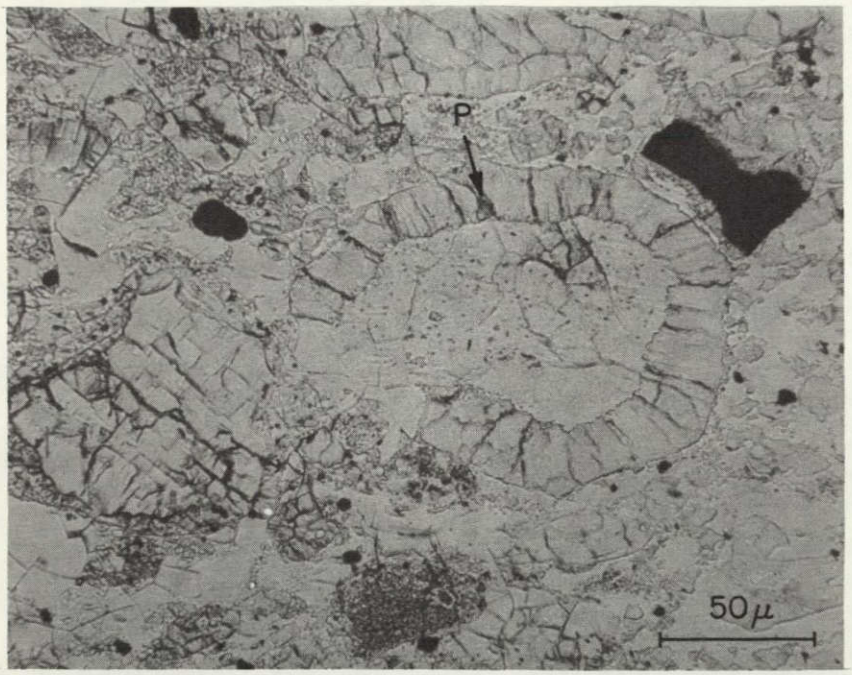

Figure IIB-32. Unusual structure in a heavily shocked Type B breccia (108-39): radiating pigeonite crystallites (P) surround a core of silica glass. Plain transmitted light.

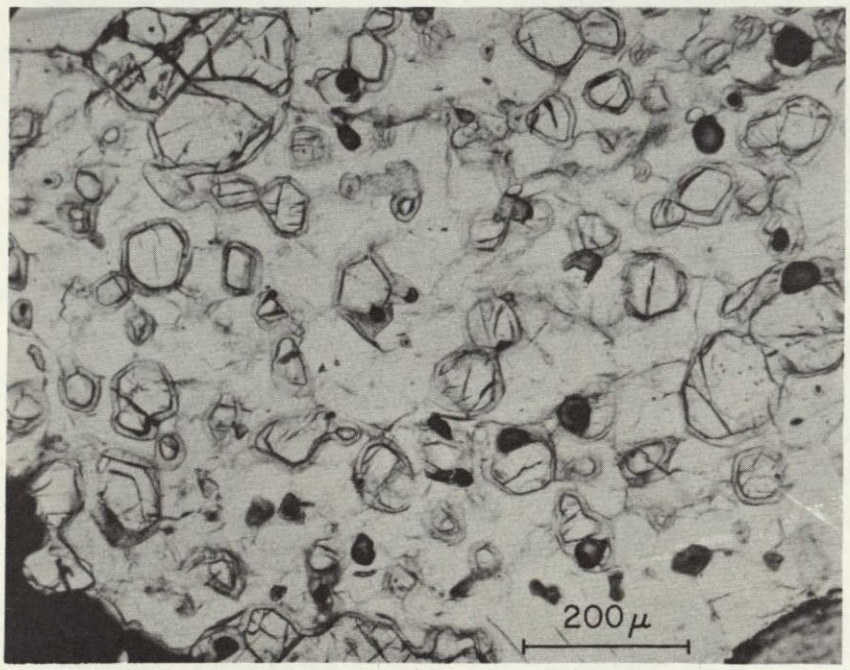

Figure IIB-33. Unique particle (130-9): rounded, equant crystals of magnesian olivine are studded in a matrix of calcic plagioclase. A rim of mafic glass surrounds each olivine crystal. Dark, rounded structures are voids, which apparently existed in the rock before sectioning. Plain transmitted light.

Thirty-four anorthositic particles in our Apollo 11 sections were studied. The largest single category that emerged (12 particles) consists of rocks that are clearly recrystallized breccias (from the angular clasts still visible in their textures) and equivocal rocks that can be interpreted either as breccias in an advanced stage of recrystallization or as very fine-grained igneous rocks. All degrees of obliteration of the primary breccia texture can be observed. An example is shown in Figure IIB-34.

The mineralogical differences we remembered were confirmed. The plagioclase content of these recrystallized breccias is much higher than that of the Apollo 12 norite–anorthosites; the former are true anorthosites. They contain little or no ilmenite and no phosphates, zircon, or residual glass. This is true with a single exception: one of the 34 particles is a true Apollo 12 Type A norite–anorthosite, complete with whitlockite, Swiss-cheese-like zircon, residual glass, and abundant ilmenite in uncommonly large grains. It contains ~60% plagioclase.

The next largest category of particles (9 examples) consists of heavily shocked, unrecrystallized, coarse plagioclase breccias (Figure IIB-35). These are similar to the Apollo 12 Type B breccias, except that glass interstitial to the clasts is colorless (probably feldspathic) rather than red-brown.

Of the remaining particles surveyed, six have been very heavily shocked and either isotropized or completely melted (with subsequent precipitation of plagioclase microlites); four have been melted (presumably by shock), but afterward have crystallized or divitrified to a large extent, to a dense assemblage of plagioclase fibers and microlites; one is an unequivocally igneous rock; and two are unclassifiable.

Clearly, the Apollo 11 sample contains light-colored rocks that are texturally the equivalents of the Apollo 12 Type A and Type B materials. We minimized the importance of these classes in our earlier report and overplayed the significance of igneous processes.

However, there are significant differences in the chemistry and mineralogy of light-colored particles from the two sites. From the bulk chemical compositions of Apollo 11 and 12 particles in Table IIB-I, the comparisons shown in Figure IIB-36 were drawn to see if the differences are clear cut or if there is not a smooth progression of rock types and compositions from one site to the other. The question is not very satisfactorily answered. When the analyses are arrayed according to their plagioclase content (i.e., how "anorthositic" they are), their contents of Ti and K and the proportion of olivine in their normative mafic minerals vary, but not smoothly. There is an abrupt break at about 50% plagioclase, suggesting that two discrete populations of rock types are involved. Yet the break is not a step function, only an abrupt steepening of the relationship; and there is a smooth if limited chemical overlap of the two populations (entries between 65 and 85 mole % plagioclase). Petrographic examination of the three particles in this range of overlap shows them to have an appropriately intermediate or equivocal character. On balance, it seems most likely that the ranges of properties of Apollo 11 and Apollo 12 light-colored particles overlap and grade into one another and that the two groups of particles are genetically related. In summary, the two groups have in common the following:

1. Each clan has anorthositic affinities (at least some members contain substantially more than 50% plagioclase).

2. The pyroxene, where present, is dominantly Ca-poor (pigeonite and/or orthopyroxene).

3. The same two textural types are present among light-colored rocks from both sites: recrystallized breccia (Type A), and coarser unrecrystallized breccia (Type B).

4. Metallic minerals of meteoritic composition are present in Type A rocks from both sites.

Differences are the following:

1. The average plagioclase content of Type A particles is higher in the Apollo 11 soil (they are more anorthositic).

2. The Apollo 11 Type A particles contain no whitlockite, zircon, or residual K-rich glass, and little or no ilmenite; all these are present at significant levels in most Apollo 12 Type A particles.

3. The ratio of Type B to Type A particles is higher in the Apollo 11 material; considering that the very heavily shocked (isotropized, melted) Apollo 11 particles probably have Type B rather than Type A affinities, Type B particles may actually form the bulk of the Apollo 11 light-colored soil fragments.

4. Type B particles appear to be more heavily shocked in the Apollo 11 sample than in the Apollo 12.

Fluorine and Phosphorus in Lunar Light-Colored Rocks

The compositions of Apollo 11 anorthosite particles, as determined by defocused-beam microprobe analysis, are strikingly similar to the composition of ejecta from the great crater Tycho in the lunar highlands, as determined by the Surveyor 7 alpha back-scattering experiment (Patterson, Turkevich, Franzgrote, Economou, and Sowinski, 1970; Wood, 1970). Results of this comparison are crucial to the interpretation that anorthosite particles in the soil at Tranquillity Base derive from the lunar highlands.

However, the comparison has not been drawn for two elements, fluorine and phosphorus. The alpha back-scattering experiment detected a surprisingly high level of fluorine in Tycho ejecta, several tenths of an atomic percent; fluorine (which is normally a trace element in rocks) had not been measured in our defocused-beam analyses. We felt confident that it was not present at tenth-percent levels, as we had not observed fluorine minerals in the anorthosites.

To complete the comparison, we recently measured bulk F levels in a number of Apollo 11 and 12 light-colored particles by electron microprobe analysis. The usual defocused-beam technique was employed (10 randomly placed 50-μ beam spots, aggregate counting time 300 sec) at 10 kv, 0.05 μA,

KAP crystal, thin-window light element flow proportional detector. Results for particles from both sites are presented in Table IIB-VIII and plotted in Figure IIB-37, which is a grand comparison of analytical results for all elements from Surveyor 7, Apollo 11 anorthosites, and Apollo 12 Type A norite–anorthosites. As expected, F is an order of magnitude less abundant in Apollo 11 anorthosites than the levels detected by Surveyor 7. The F content in Apollo 12 particles is somewhat higher but still falls short of the Tycho values.

Phosphorus was also omitted from our defocused-beam analyses of Apollo 11 particles (Table IIB-I); to fill this gap, we made defocused-beam surveys of P in 14 anorthosites. Results appear in Table IIB-IX and Figure IIB-37, where levels of P and S in light-colored particles from both sites are seen to be in agreement with the Surveyor 7 values. Both F and P are more abundant in Apollo 12 particles than in Apollo 11, which is consistent with the greater abundance of visible phosphate minerals in the Apollo 12 particles and with the supposition that at least part of the F in the particles occurs in the phosphates.

In spite of the apparent fluorine discrepancy, we feel that the compositional similarity between Tycho ejecta and the Apollo light-colored particles is very striking and convincing. Both classes of particles are a good match to the Tycho highlands material, but it might be argued (on the basis of the three heaviest element groups) that the Apollo 11 anorthosites provide the closest fit. To split hairs even finer, a material intermediate in composition between the Apollo 11 and 12 particles would furnish the closest match of all.

Table IIB-VIII. Microprobe measurements of F content of Apollo 11 anorthosites and Apollo 12 norite–anorthosites (Type A).

Fragment number	Counting times (sec)	Counts at $\lambda(FK_\alpha)$	Counts at background offset 1	Counts at background offset 2	Counts above background and uncertainty[a]	F content (wt. %), and uncertainty[a]
			Apollo 11			
Standard[b]	30	1521	30	45	1484	48.6
(37-6)	300	85	98	90	- 9 ± 9	-0.030 ± 0.030
(37-2)	300	94	80	79	5 ± 10	0.016 ± 0.033
(37-11)	300	98	106	84	3 ± 10	0.010 ± 0.033
(37-17)	300	72	109	68	-16 ± 8	-0.052 ± 0.026
(37-16)	300	88	95	84	- 2 ± 9	-0.007 ± 0.030
(37-12)	300	103	95	71	20 ± 10	0.066 ± 0.033
Standard[b]	30	2350	115	92	2247	48.6
(37-7)	300	79	92	61	3 ± 9	0.006 ± 0.019
(37-1)	300	71	107	100	-32 ± 8	-0.069 ± 0.017
(37-5)	300	95	92	78	10 ± 10	0.022 ± 0.022
(37-4)	300	91	111	65	3 ± 10	0.006 ± 0.022
(37-3)	300	86	101	91	-10 ± 9	-0.022 ± 0.019
(37-13)	300	82	82	86	- 2 ± 9	-0.004 ± 0.019
(37-14)	300	69	93	72	-13 ± 8	-0.028 ± 0.017
(37-9)	300	93	129	81	-12 ± 10	-0.026 ± 0.022
			Apollo 12			
Standard[b]	30	1628	28	39	1579	48.6
(115-1)	300	81	79	74	5 ± 9	0.015 ± 0.028
(115-2)	300	76	87	88	-11 ± 9	-0.034 ± 0.028
Standard[b]	30	1782	45	14	1752	48.6
(115-3)	300	145	118	77	47 ± 12	0.130 ± 0.033
(115-4)	300	130	86	80	47 ± 11	0.130 ± 0.030
(115-5)	300	122	127	74	22 ± 11	0.061 ± 0.030
(115-8)	300	118	107	84	23 ± 11	0.064 ± 0.030
Standard[b]	30	1831	41	19	1801	48.6
(115-6)	300	84	111	88	-16 ± 9	-0.043 ± 0.024
(115-7)	300	80	106	77	-11 ± 9	-0.030 ± 0.024

[a] One-sigma counting statistics. Data corrected only for background.

[b] CaF_2.

Table IIB-IX. Phosphorus contents of 14 Apollo 11 light-colored particles.

Particle number	Type	P content (wt. %) with one-sigma counting error
(37-6)	B	0.019 ± 0.004
(37-2)	D	0.037 ± 0.009
(37-11)	C	0.001 ± 0.001
(37-17)	A	0.027 ± 0.007
(37-16)	C	0.007 ± 0.004
(37-12)	A	0.039 ± 0.009
(37-7)	A	0.013 ± 0.005
(37-1)	A	0.012 ± 0.005
(37-5)	C	0.028 ± 0.008
(37-4)	C	0.011 ± 0.005
(37-3)	E	0.023 ± 0.007
(37-13)	C	0.025 ± 0.007
(37-14)	A	0.012 ± 0.005
(37-9)	A	0.022 ± 0.007

Key to rock types

A. Recrystallized breccia (Type A).

B. Unrecrystallized breccia (Type B).

C. Isotropized or shock-melted anorthosite.

D. Norite (Type A, as in Apollo 12).

E. Other (plagioclase mosaic).

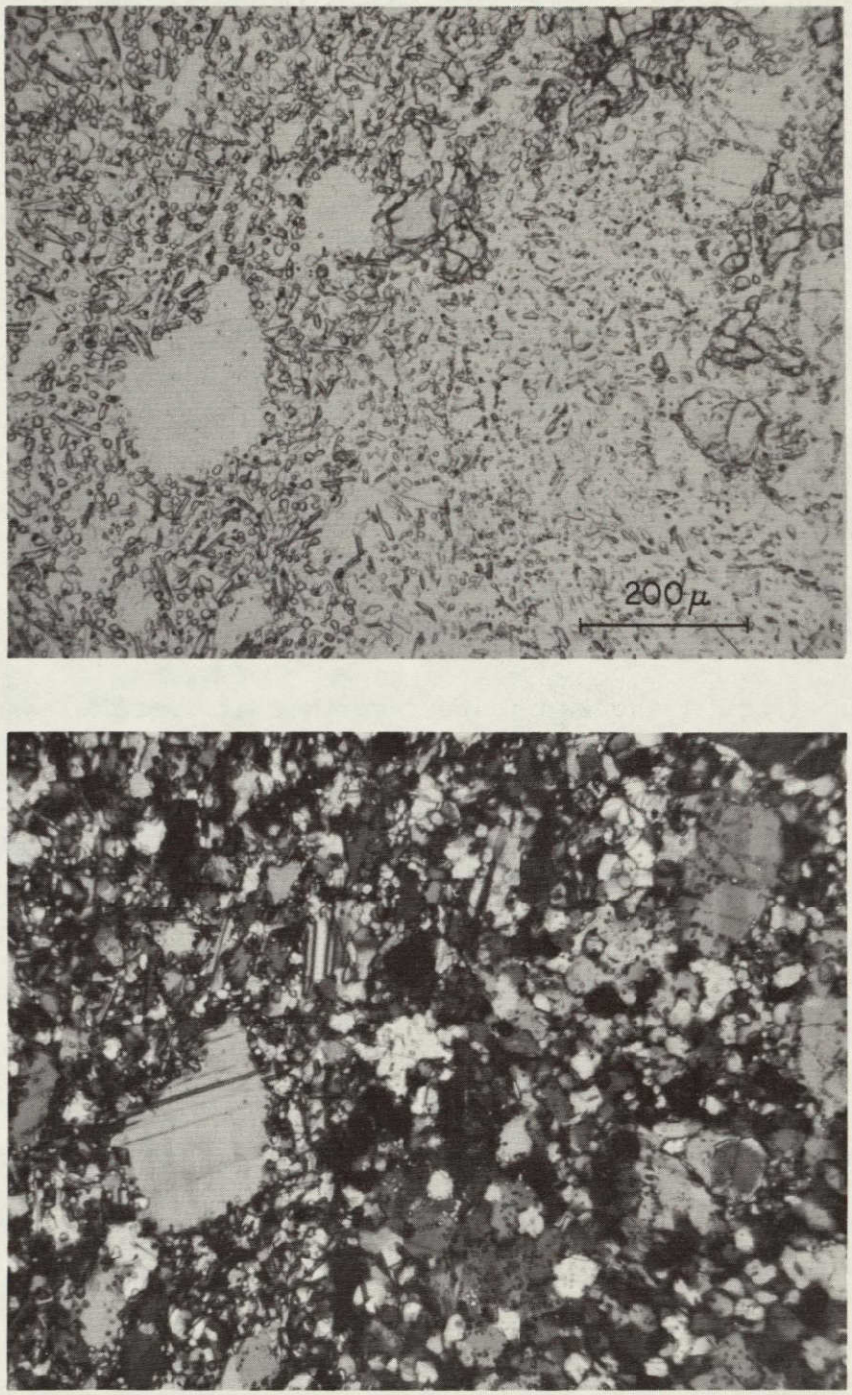

Figure IIB-34. Apollo 11 anorthosite (37-17), with recrystallized breccia texture similar to that of Type A Apollo 12 particles. Above, plain transmitted light; numerous minute crystals of pigeonite (elongated) and olivine (equant) are visible. Note absence of ilmenite. Below, polarized transmitted light.

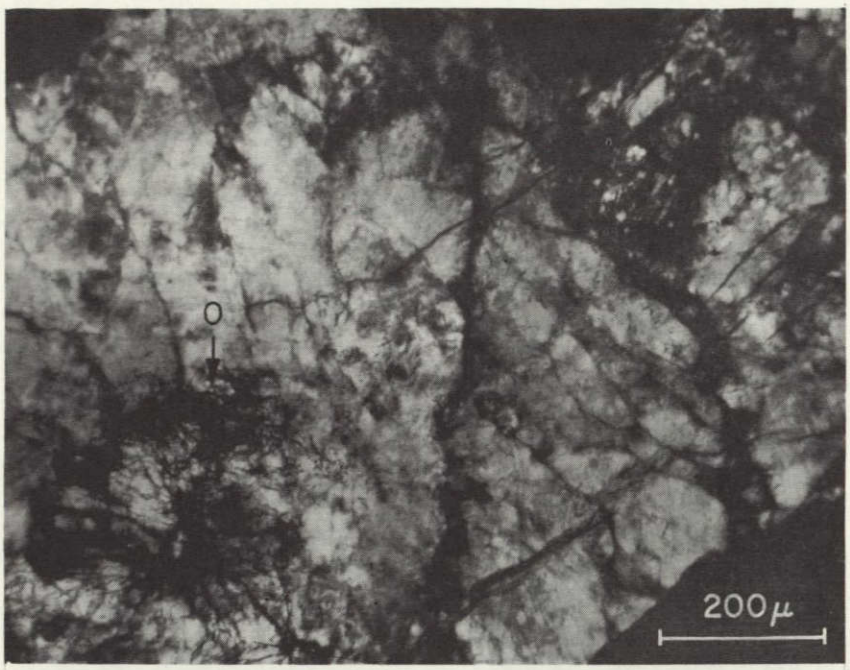

Figure IIB-35. Heavily shocked coarse anorthositic breccia fragment (40-7), Apollo 11, by polarized transmitted light. Similar to Apollo 12 Type B particles. O, olivine; remainder of particle is distorted plagioclase.

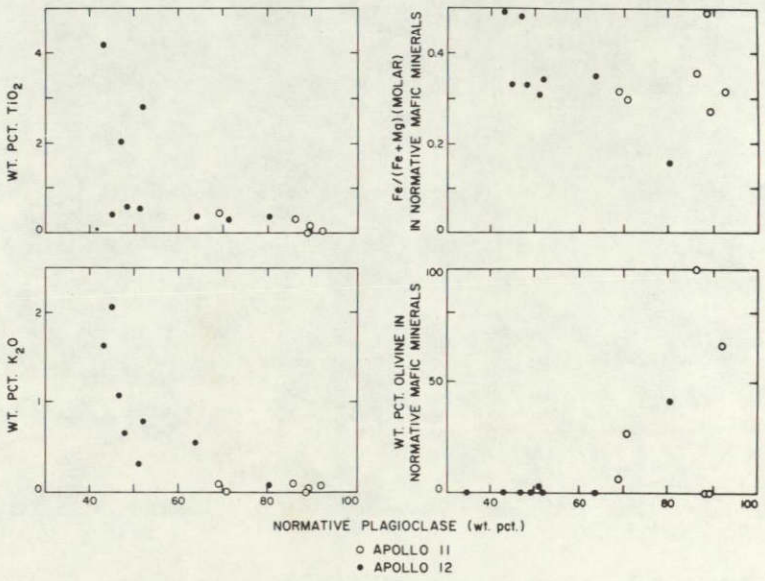

Figure IIB-36. Plots of several chemical and (normative) mineralogical parameters vs. (normative) plagioclase content for Apollo 11 and Apollo 12 light-colored particles listed in Table IIB-I. Fairly smooth trends are revealed, consistent with proposition that light particles from both sites are genetically related.

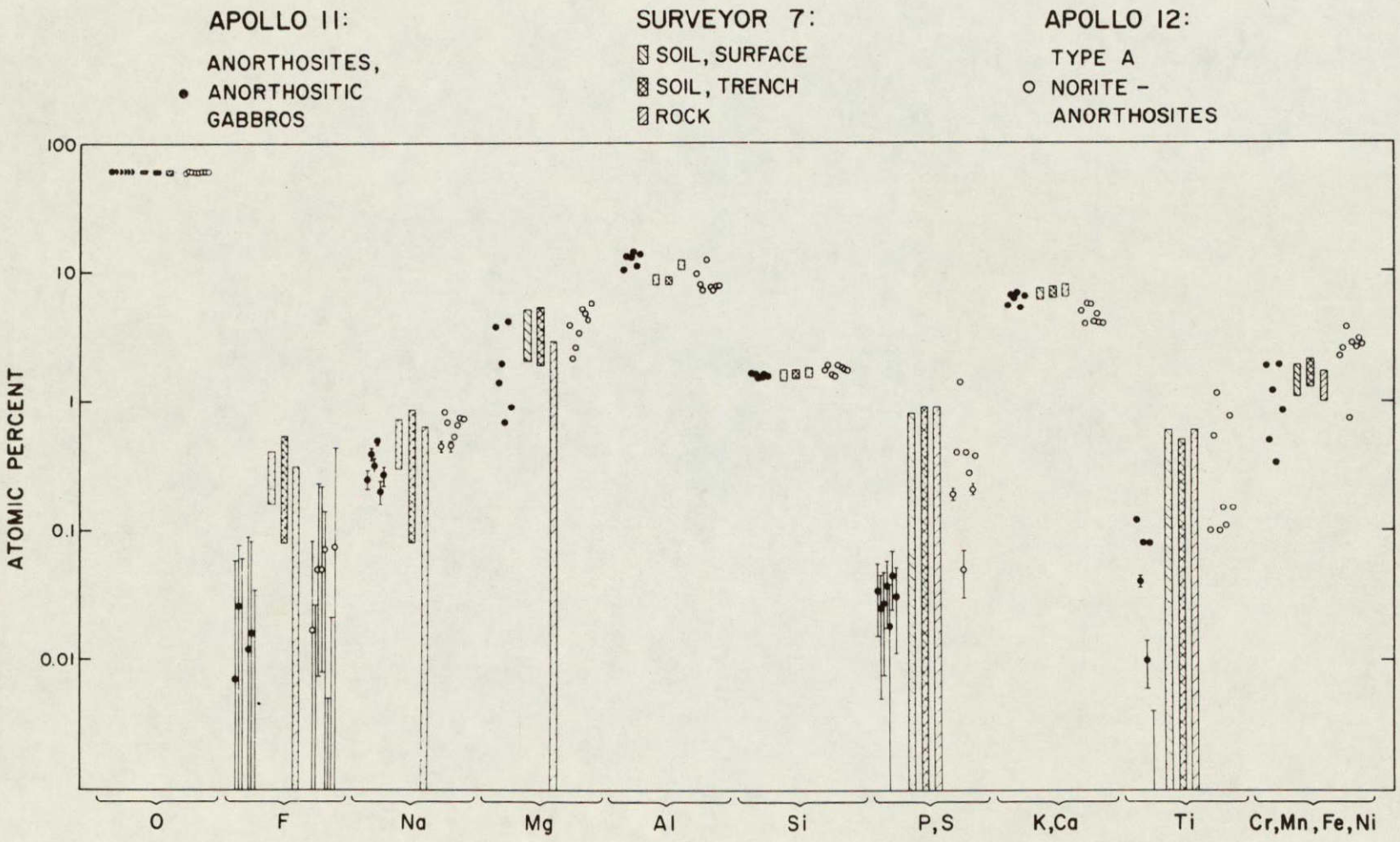

Figure IIB-37. Comparison of compositions of Apollo 11 and Apollo 12 light-colored particles (defocused-beam microprobe surveys) with the composition of crater ejecta in the lunar highlands (Surveyor 7 alpha back-scattering analyses; Patterson et al., 1970). Error bars shown (except where they are smaller than circles representing probe surveys) represent two-sigma counting statistics. Apollo 11 F and P measurements were made on different particles than those surveyed for other elements.

IIC. Potash Rhyolite Fragment

One of the 1302 particles we examined is unique: (102-5) consists chiefly of a silica mineral and potassium feldspar, finely intergrown in a fabric reminiscent of perthite or myrmekite (Figure IIC-1). We have not identified the polymorphs of silica and feldspar: the fine grain size of the particle prevented optical determinations, and we did not want to destroy this unique thin section by making it into an x-ray diffraction mount. Microprobe analyses of the feldspar are shown in Table IIB-II.

Olivine, clinopyroxene, ilmenite, whitlockite, and apatite are present in minor amounts (Figures IIC-1 and IIC-2). The mafic minerals are much enriched in Fe: the olivine contains 87 mole % fayalite (Table IIB-V), and the pyroxene is ferroaugite (Table IIB-III, Figures IIB-10 and IIB-13). Of course, the observed coexistence of olivine and free silica would not be possible unless the olivine were Fe-rich; all but the Fe-rich olivines tend to react with silica to form pyroxene. Ilmenite in particle (102-5) is more nearly pure $FeTiO_3$ (contains less Mg) than the ilmenites of norite–anorthosites (Table IIB-VII, Figure IIB-23).

A defocused-beam analysis of (102-5) is shown in Table IIC-I, where it is compared with other possibly related lunar K-rich substances. The comparisons are discussed in Section IIIC. The norm for (102-5) also appears in Table IIC-I; here all the Mg and Fe have been made to appear in pyroxenes, because the program for computing norms forbids the coexistence of olivine and quartz. This rock has no terrestrial counterpart; it seems closer in its properties to a potash rhyolite than to anything else, and we use this term to describe it, without meaning to imply that its mode of origin was necessarily very similar to that of terrestrial rhyolites.

Table IIC-I. Composition of potash rhyolite (102-5) and comparisons with other lunar K-rich substances (wt. %; microprobe analyses).

	A	B	C	D	E	Norm of analysis A (wt. %)	
SiO_2	70.8	73.5	75.4	70.2	60.7	En	1.1
TiO_2	0.6	0.5	0.5	1.0	0.3	Fs	10.6
Al_2O_3	12.7	12.2	11.5	11.2	20.5	Wo	0.0
Cr_2O_3	0.0	--	--	--	--	Or	43.0
FeO	6.3	0.9	2.5	3.7	0.2	Ab	9.0
MnO	0.1	--	--	--	0.0	An	0.1
MgO	0.4	0.4	0.3	--	0.2	Ilm	1.1
CaO	1.0	1.2	1.8	2.9	3.5	Qtz	30.5
BaO	--	0.9	--	--	--	Cor	2.9
NiO	0.0	--	--	--	--	Apa	1.6
Na_2O	1.1	1.4	0.4	0.6	1.1		
K_2O	7.4	6.9	6.5	6.6	13.1		
P_2O_5	0.7	--	--	--	--		
S	0.0	--	--	--	0.0		
Sum	101.1	97.9	98.9	96.2	99.6		

Key

A. Defocused-beam analysis of potash rhyolite (102-5).

B. Rock 12013: salic components in ovoid fillings of dark lithology (average of eight fillings) (Drake, McCallum, McKay, and Weill, 1970).

C. Apollo 11 basalt: K-rich residual glass (average of 33 occurrences) (Roedder and Weiblen, 1970).

D. Apollo 11 basalts: K-rich residual glass (average of four analyses; Table IIB-VII, Wood et al., 1970).

E. Apollo 12 norite–anorthosites: K-rich residual glass (average of four analyses); see Table IIB-IV, this Report.

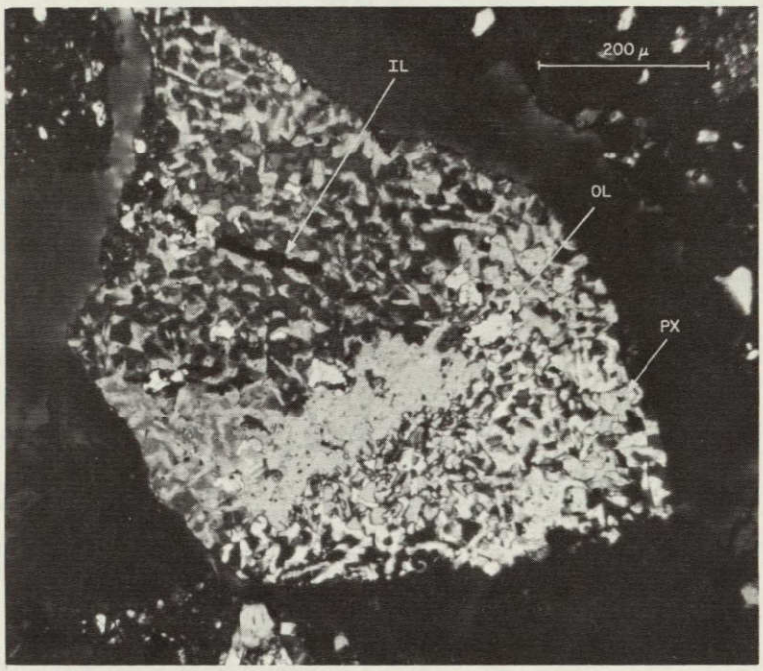

Figure IIC-1. Potash rhyolite particle (102-5), by transmitted polarized light. Most of the particle consists of a fine, uniform intergrowth of K feldspar and a silica mineral, but minor amounts of Fe-rich olivine (OL, Fa_{87}), ferroaugite (PX), and ilmenite (IL) are also present.

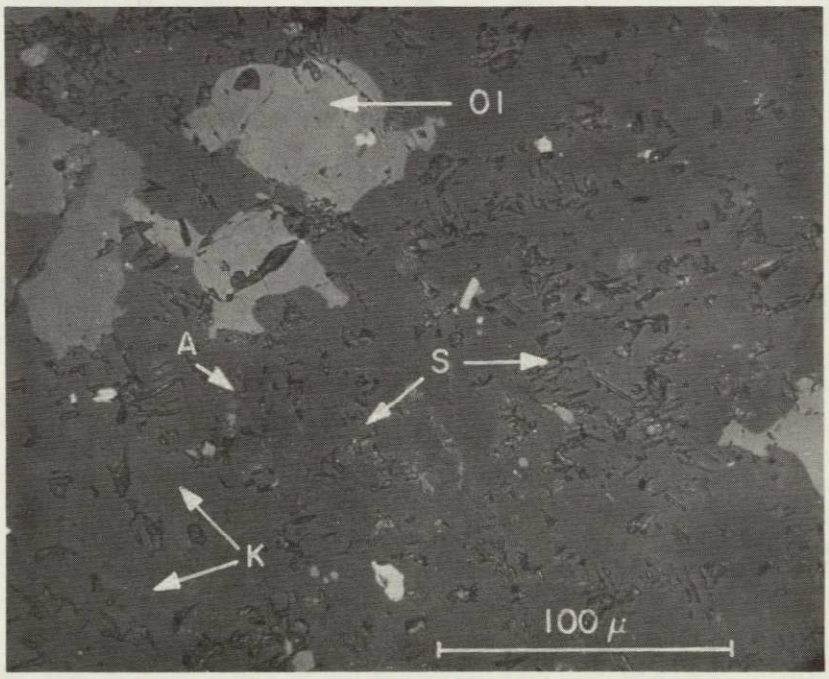

Figure IIC-2. Potash rhyolite (102-5), by reflected light. (S) silica mineral, showing curious crystallographically oriented patterns of elongate voids or soft inclusions; (K) K-feldspar (featureless); (Ol) olivine; (A) apatite (intersection of elongated needle with section surface).

IID. Glass

The Apollo 12 soil samples, like the Apollo 11, contain a large proportion of glass and glassy agglomerates (see Section I). This section describes the petrography and chemistry of the glassy particles present in our five soil samples from Oceanus Procellarum.

Cindery and Ropy Glasses

There are two main types of glassy particles, "cindery" and "ropy," in the Apollo 12 fines. The former appear irregular in shape and are obviously vesicular, dark in color, and coated with shiny glass on some or all surfaces (Figure IID-1). In thin sections, they appear highly vesicular (Figure IID-2), and their glass color is pale yellowish to greenish (see Plate 1, A and B), occasionally brownish; most have Munsell colors from 10YR to 7.5Y. Cindery glasses usually contain fragments of compact breccia, basaltic rocks, or minerals. It is not uncommon to find breccia particles coated with cindery, i.e., highly vesicular, glass.

Ropy glasses appear macroscopically to have been pulled and twisted (Figure IID-3) and are coated with fine-grained light-gray material. In thin sections, they have a distinctive red-brown color (10R-5YR; see Plate 1, C and F) and often contain streaks of opaque material. Frequently, newly precipitated crystallites of feldspar can be seen in the red-brown glass, usually aligned parallel to the opaque streaks. The texture is highly suggestive of flow. The appearance of flow banding is emphasized by the stretched shape of the vesicles (Figure IID-4) when they are present; usually, in ropy glasses, they are not. The ropy glasses also contain lithic and mineral fragments, but in contrast to the cindery glasses, these are noritic–anorthositic fragments, rarely fragments of basaltic rocks.

LSPET (1970a) reported that the ropy glasses are concentrated in a light layer observed by the astronauts in a trench they dug near the rim of Head Crater; our sample 12033 came from this layer. Sample 12032 also contains a high concentration of ropy particles (see Section I). Two other samples examined, 12001 and 12070, contain few ropy glasses but have a high proportion of cindery glasses. LSPET also reported that the light layer at the bottom of the double-core tube (12025, 12028) contains glasses similar to those in 12033, so it seems that the ropy glasses are concentrated in one or more discrete layers.

A third type of glassy particle is also found in the soils, but in far less abundance than either of the first two categories. These particles resemble the ropy glasses in that they contain opaque streaks and crystallites but are yellowish or greenish in color rather than red-brown (Figures IID-5 and IID-6). These will be referred to as "greenish-yellow streaky" glasses to distinguish them from the more abundant red-brown ropy glasses. Significantly, the greenish-yellow streaky glasses are not found in those samples that contain a high concentration of ropy glasses (12033 and 12032).

Chemistry

These discrete textural classes of glassy particles can also be distinguished by their chemistry. Representative microprobe analyses are shown in Tables IID-I and IID-II. That the glasses fall into distinct groups is shown very clearly in Figure IID-7, where the wt. % of Al is plotted against the wt. % of Fe+Mg. The cindery glasses cluster near the overall composition of Apollo 12 fines (data for these are from the unpublished proceedings of the Apollo 12 Lunar Science Conference). The ropy glasses, however, plot to the higher Al, lower Fe+Mg side of the diagram, i.e., toward the more felsic end and nearer the norite–anorthosites (data from Section IIB). Significantly, the interstitial red-brown glasses in Type B anorthositic breccias (see Section IIB) also plot with the ropy glasses (Figure IID-7), suggesting that these rock types are related. The greenish-yellow streaky glasses plot with the red-brown group.

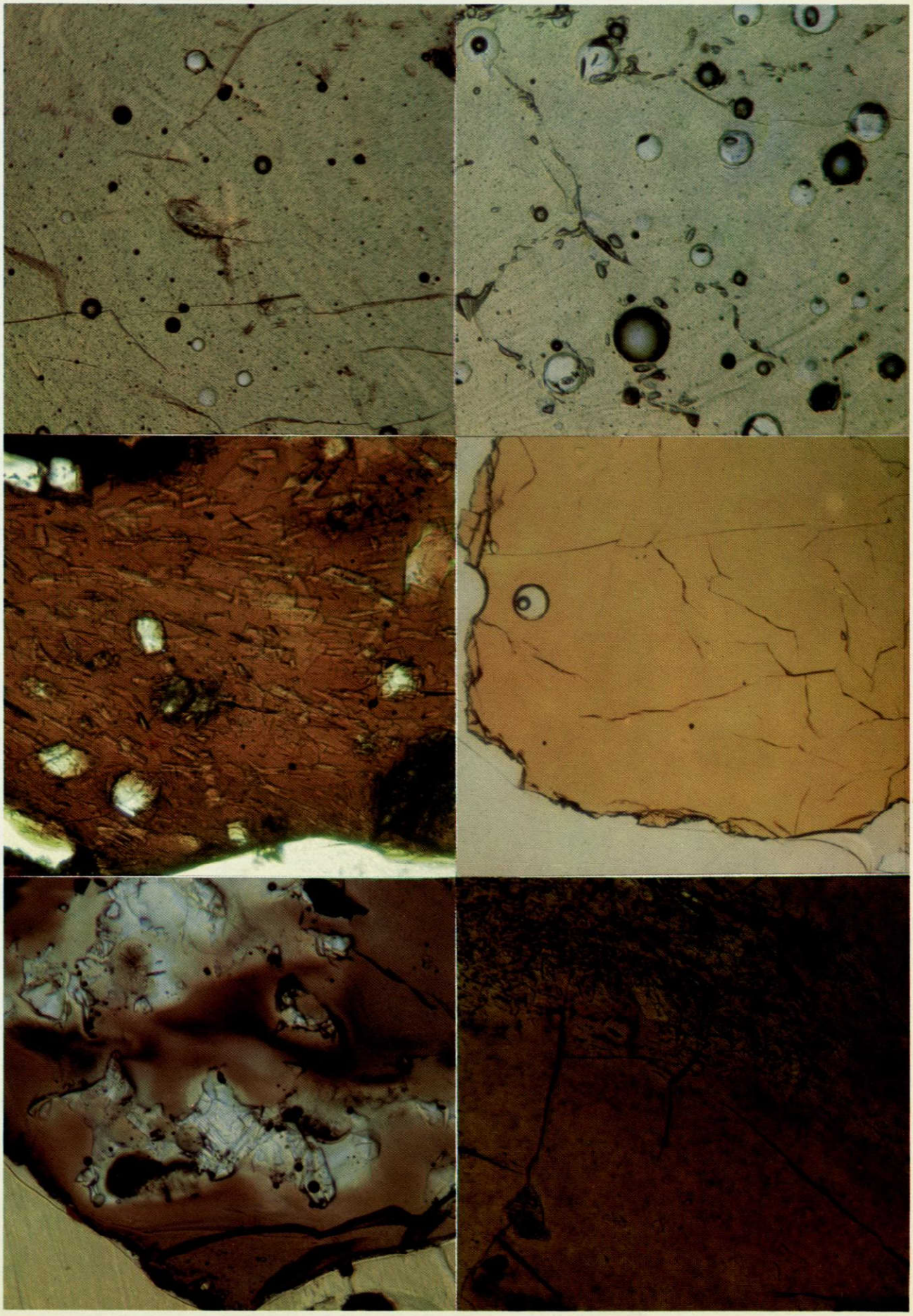

Plate 1. Lunar glasses in thin section.

A	B
C	D
E	F

Plate 1. Photomicrographs in plain light of lunar glasses. The map above identifies the photographs. A: This yellowish color is typical of cindery glasses from Apollo 12 (125-24). The dark circular inclusions are NiFe metal. Width of field is 500 μ. B: Greenish-yellow glasses like this one (101-13) are also common among Apollo 12 cindery glasses. Width of field is 550 μ. C: Typical red-brown ropy glass (134-15) containing crystallites of feldspar. Width of field is 500 μ. D: Typical Apollo 11 glass (50-2). Width of field is 1.3 mm. E: Inhomogeneous glass from Apollo 12 (110-10). Width of field is 500 μ. F: Red-brown ropy glass (132-6) with crystallites concentrated in one area. Width of field is 675 μ. The compositions of these glasses are given in Table IID-I.

Table IID-I. Compositions of the glasses shown in Plate 1. Analysis A refers to Plate 1, A, etc. Analysis E_l refers to the colorless glass and E_d refers to the darkest brown glass in Plate 1, E.

	A	B	C	D	E_l	E_d	F
Na	0.2	0.4	0.0	0.0	0.9	0.5	0.2
Mg	5.8	5.7	5.1	5.3	0.5	2.4	4.5
Al	6.1	7.3	8.2	7.5	14.1	7.7	9.2
Si	22.0	21.0	22.7	19.2	23.8	25.1	23.0
P	0.1	0.1	0.4	--	0.4	0.8	0.4
S	0.1	0.1	0.1	0.1	0.1	0.1	0.0
K	0.2	0.3	1.1	0.0	2.4	2.1	1.1
Ca	7.0	7.3	7.2	8.5	6.4	6.6	7.5
Ti	1.6	1.6	1.5	4.3	0.1	1.2	1.2
Cr	0.3	0.3	0.2	0.2	0.0	0.1	0.2
Mn	0.2	0.2	0.1	0.2	0.1	0.1	0.1
Fe	13.6	11.6	9.0	11.8	3.5	9.6	8.1
Ni	0.0	0.0	0.0	0.0	0.0	0.0	0.0
O	42.6	42.1	43.9	41.8	45.1	45.1	44.5
Sum	99.7	97.9	99.5	98.8	97.4	101.5	100.1
Fo	0.0	2.7	0.0	1.0	0.0	0.0	0.0
Fay	0.0	2.9	0.0	0.8	0.0	0.0	0.0
En	24.2	20.2	21.4	20.8	2.3	9.9	18.6
Fs	27.6	20.0	17.3	15.4	8.4	19.3	15.7
Wo	7.3	6.2	2.6	8.6	0.0	2.3	1.5
Or	1.1	2.2	7.7	0.4	17.2	14.9	7.8
Ab	1.7	4.1	0.1	0.0	10.1	5.5	2.4
An	30.0	35.4	38.7	38.8	39.5	28.7	42.3
Ilm	5.3	5.0	4.7	13.7	0.4	3.8	3.9
Chr	0.7	0.6	0.3	0.4	0.0	0.1	0.3
Qtz	1.6	0.0	5.1	0.0	11.9	11.4	5.2
Cor	0.0	0.0	0.0	0.0	7.8	0.0	0.0
S	0.1	0.1	0.1	0.1	0.1	0.1	0.0
Apa	0.4	0.5	1.9	0.0	2.2	4.0	2.2

Table IID-II. Compositions and norms of representative colorless glasses (A and B), greenish-yellow streaky glasses (C and D), glass with quench textures (E; defocused-beam analysis), and the brown sphere shown in Figure IID-14 (F).

	A (106-3)	B (122-2)	C (106-47)	D (124-8)	E (110-42)	F (110-4)
Na	0.0	0.1	1.1	0.6	0.7	0.2
Mg	5.3	5.4	4.6	5.0	4.6	6.2
Al	13.5	13.1	9.4	8.6	9.8	5.5
Si	21.4	21.8	22.7	22.3	22.3	20.8
P	0.0	0.0	0.2	0.4	0.2	0.0
S	0.0	0.0	0.1	0.1	0.1	0.1
K	0.0	0.0	0.7	0.7	0.5	0.1
Ca	10.2	10.0	7.4	7.4	7.8	7.5
Ti	0.2	0.2	1.1	1.2	1.3	1.6
Cr	0.1	0.1	0.1	0.1	0.1	0.3
Mn	0.0	0.1	0.1	0.1	0.2	0.2
Fe	4.3	4.9	7.7	7.9	7.5	14.2
Ni	0.0	0.0	0.0	0.0	0.0	0.0
O	45.3	45.5	44.3	43.5	44.1	41.3
Sum	100.3	101.0	99.7	98.1	99.2	98.0
Fo	3.7	3.3	0.6	0.0	0.0	4.6
Fay	1.8	1.8	0.5	0.0	0.0	5.7
En	16.7	17.2	18.4	21.1	19.3	19.8
Fs	7.3	8.7	14.7	15.9	14.6	22.4
Wo	0.4	1.1	3.3	3.1	2.6	11.0
Or	0.1	0.1	5.3	4.8	3.5	0.9
Ab	0.0	1.1	12.2	6.9	8.0	2.7
An	69.4	65.9	39.8	39.4	45.0	27.0
Ilm	0.6	0.5	3.5	3.9	4.2	5.3
Chr	0.1	0.2	0.3	0.3	0.3	0.6
Qtz	0.0	0.0	0.0	2.4	1.4	0.0
Cor	0.0	0.0	0.0	0.0	0.0	0.0
S	0.0	0.0	0.1	0.1	0.1	0.1
Apa	0.0	0.0	1.3	2.1	1.1	2.3

Figure IID-1. Macroscopic photograph of cindery glass particles (coarse fines, Sample 12070). The vesicular glass coats some or all surfaces of microbreccia fragments (millimeter scale).

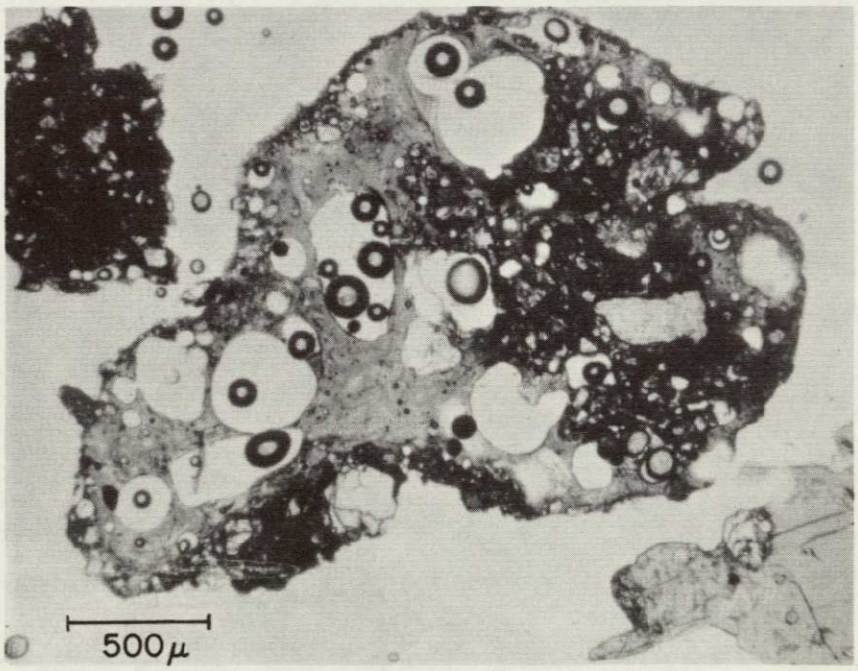

Figure IID-2. Photomicrograph in unpolarized transmitted light of a cindery glass particle (125-25).

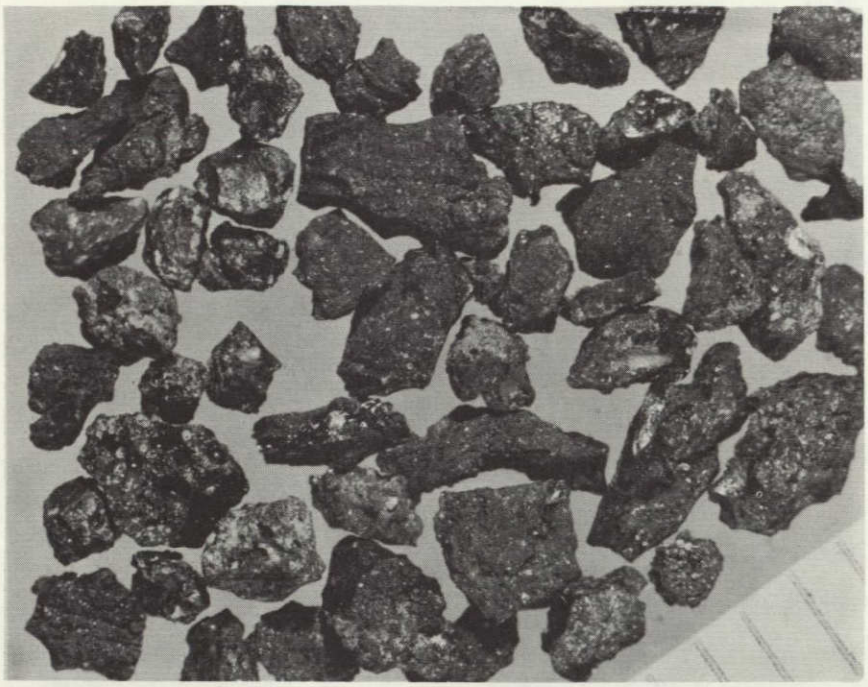

Figure IID-3. Macroscopic photograph of ropy glass particles (coarse fines, Sample 12033). The particles appear pulled and twisted and are covered with fine-grained dust. Only one particle is vesicular (millimeter scale).

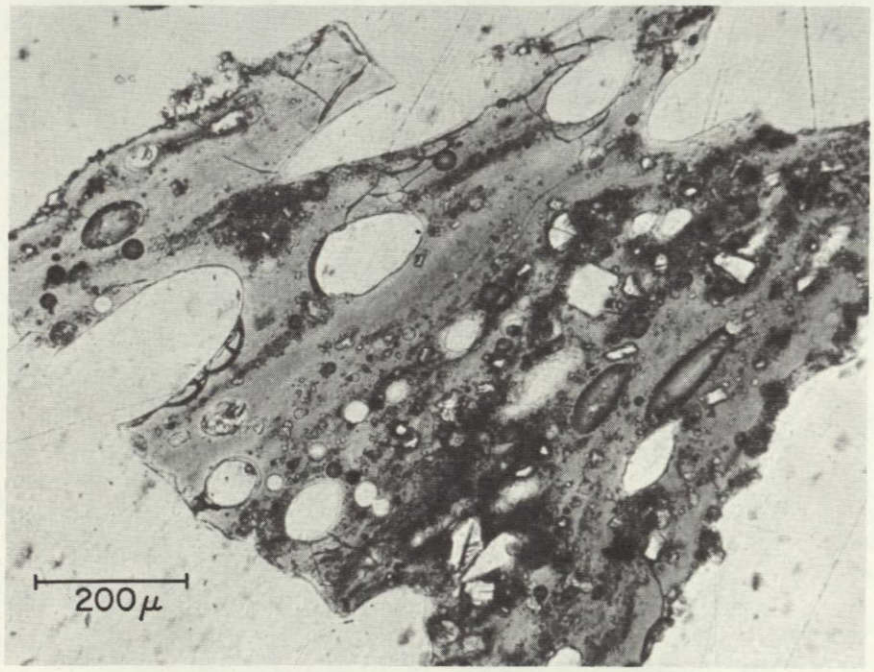

Figure IID-4. Photomicrograph in unpolarized transmitted light of a ropy glass particle (109-12). The stretched vesicles and parallel streaks of opaque material show that this particle flowed before it solidified.

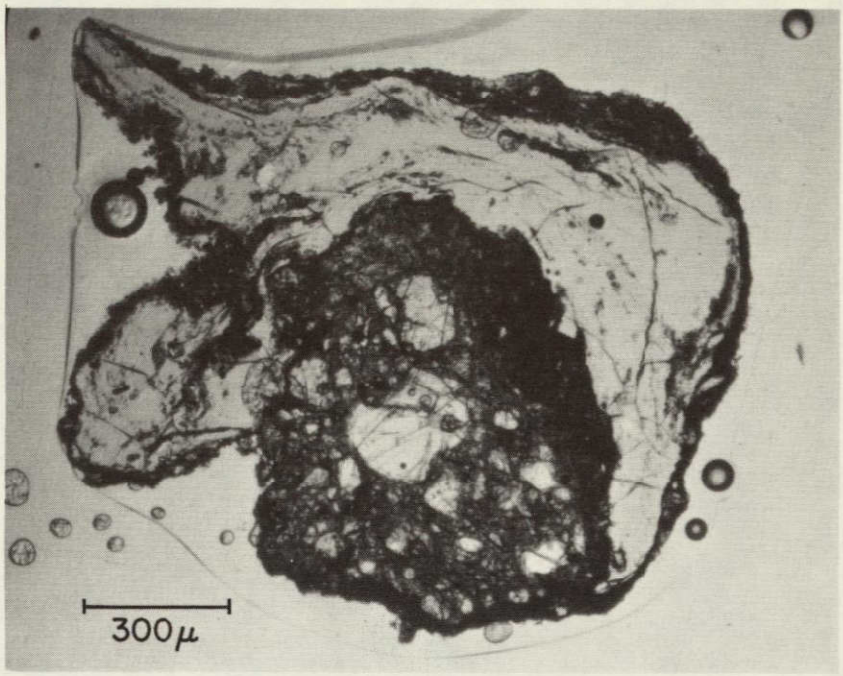

Figure IID-5. Photomicrograph in unpolarized transmitted light of a greenish-yellow streaky glass particle coating a feldspar-rich breccia (124-8). The chemical composition of the glass is given in Table IID-II, analysis D.

Figure IID-6. Photomicrograph in unpolarized transmitted light of a greenish-yellow streaky glass particle (106-47). The chemical composition of the glass is given in Table IID-II, analysis C.

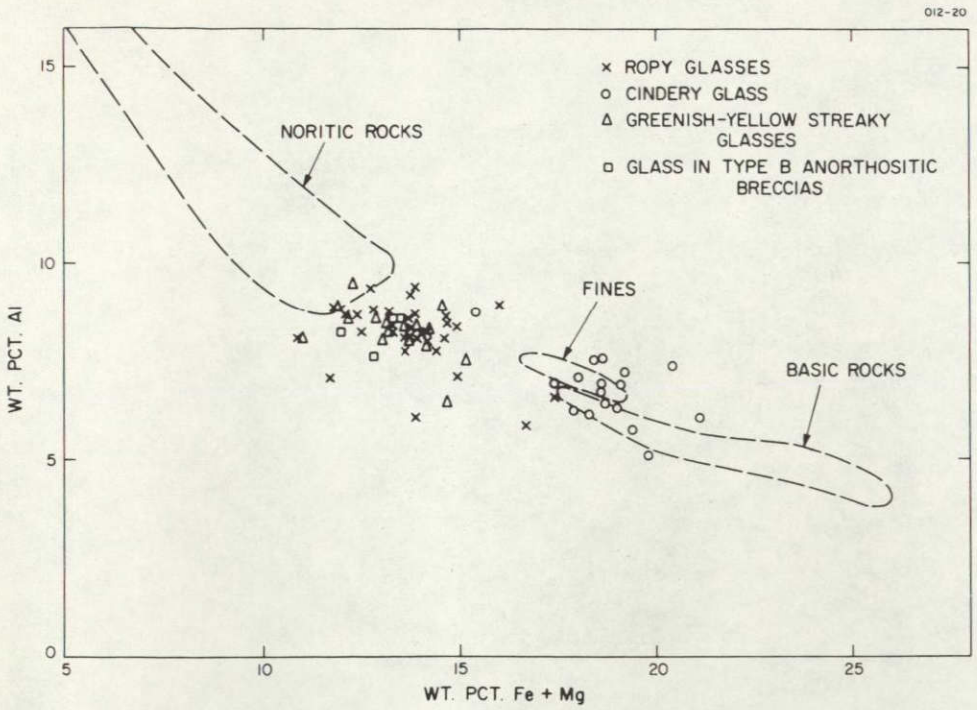

Figure IID-7. Ropy and cindery glasses plot in two distinct groups on this graph of Al vs. Fe+Mg. The compositions of the major rock types are indicated (the data for the noritic rocks are from Section IIB, that for the others are from various sources in the unpublished proceedings of the Apollo 12 Lunar Science Conference). The compositions of the cindery glasses closely correspond to those of the Apollo 12 fines and breccias.

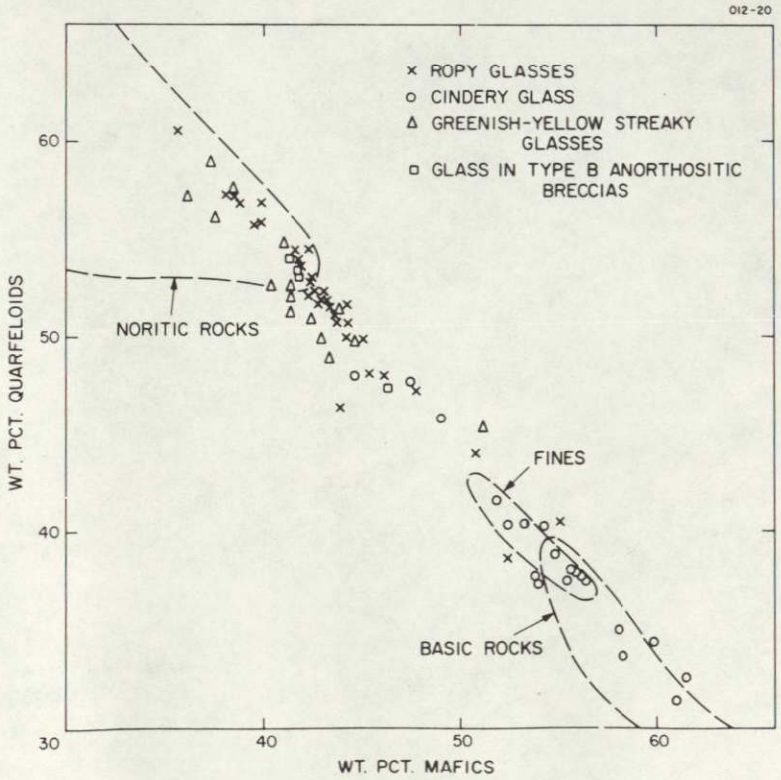

Figure IID-8. This plot of normative quarfeloids against normative mafics shows that the ropy glass particles are distinctly less mafic than the cindery ones. The latter again resemble the compositions of the fines and breccias.

The more felsic character of the ropy glasses is apparent in Figure IID-8, where the wt. % of normative feldspar and quartz (quarfeloids) is plotted against the wt. % of normative pyroxene and olivine (mafics). The cindery glasses fall between the compositions of bulk Apollo 12 soil and the basic rocks collected from the landing site; i. e., they reflect the composition of the Apollo 12 regolith (<~48% quarfeloids). Almost all the ropy glasses, however, contain more than ~50% quarfeloids. As in Figure IID-7, the ropy glasses are seen to be distinctly different than the cindery glasses, and they plot in the same region as the glass from Type B anorthositic breccias. The greenish-yellow streaky glasses again plot with the ropy glasses.

The most striking feature of the ropy glasses is their high concentrations of K and P. The P content ranges from 0.2 wt. % to 0.7 wt. %. Cindery glasses, in contrast, contain less than 0.1 wt. % P. According to Hubbard, Meyer, Gast, and Weismann (1971), the ropy glasses are also enriched in the rare-earth elements, as compared to mare basalts. To emphasize this special chemistry, Hubbard et al. (1971) have bestowed the acronym KREEP on all lunar materials rich in K, the rare earths, and P.

Figure IID-9 shows the relation between the wt. %K and the wt. %Fe+Mg. Most of the ropy glasses contain more than 0.5 wt. %K, whereas the cindery glasses have less than 0.25 wt. %K. Once again, we see that the glasses in Type B anorthositic breccias and the greenish-yellow streaky glasses are grouped with the ropy glasses. Moreover, the range of K contents of this group is similar to that of the noritic—anorthositic rocks, but the ropy glasses contain more Fe and Mg. The cindery glasses have less K than the fines but roughly the same Fe+Mg. This suggests that they lost some K when they were formed: the more volatile elements were boiled out of the melt. This would account for their highly vesicular nature. Since Na is also volatile, one would expect it to be lost, too; Figures IID-10 and IID-11 show that this is the case. In Figure IID-10, Ti, a highly refractory element, is plotted against K+Na. The cindery glasses are clearly depleted in alkalis relative to the fines. In Figure IID-11, Na is plotted against K, and we observe that both elements are less abundant in cindery glasses than in the fines.

The ropy glasses are again seen to be distinct from the cindery ones in Figure IID-10. The range of alkali contents of the ropy glasses is similar to that of the norites, but as noted above for Fe + Mg, Ti is enriched in the glasses. In Figure IID-11, we note a vague anticorrelation between Na and K in the ropy glasses and a distribution that is quite different than that in the norite–anorthosites.

Figure IID-12 is a plot of wt. % Cr_2O_3 against the atomic ratio Fe/(Mg + Mn + Fe). This plot produces the tightest clustering of the ropy glasses and sets them apart from both the cindery glasses (which plot with the fines and basic rocks) and the norites.

Table IID-III summarizes the compositional differences between the ropy and cindery glasses. It is interesting that the cindery glasses, which contain more Fe, Ti, and Cr, are less deeply colored than the red-brown glasses. These transition metals are the major coloring agents in the lunar sample. A plausible explanation is that these elements appear in different oxidation states in the two types of glass. This implies that the source areas for the two types were at significantly different states of oxidation. By similar reasoning, the greenish-yellow streaky glasses must come from a different source than do the red-brown ropy glasses, even though the compositions are very similar. In this respect, it is significant that the greenish-yellow streaky glasses are not observed in the samples that contain abundant red-brown glass.

To test the effect of oxidation state on glasses of lunar composition, we mixed oxides in the proportions present in typical ropy and cindery glasses and melted them in resistance-heated tungsten boats in a bell-jar vacuum. For both glass compositions, we varied the oxidation state by furnishing Fe to the mixture as Fe_2O_3, Fe_3O_4, 1 Fe_3O_4 + 1 Fe metal (to approximate the effect of FeO), or 1 Fe_3O_4 + 2 Fe metal (FeO plus free metal). The expected range of glass colors was produced, from medium brown (in a thin section of normal thickness) for the mixtures in which Fe was introduced as Fe_2O_3 to pale yellow or almost colorless for the most reduced mixtures; apparently

the lunar ropy glasses are more oxidized than the cindery glasses or the greenish-yellow streaky glasses.

None of our mixtures succeeded in reproducing the reddish cast of the lunar ropy glasses.

Crystalline inclusions in the ropy glass particles

The ropy glasses contain pyroxenes, feldspar, olivine, metal, and (rare) opaque crystal fragments. Most interesting are the pyroxenes. Those from the Apollo 12 basaltic rocks plot in a sock-shaped region on a wt. % Cr_2O_3 vs. Fe/(Mg + Mn + Fe) diagram (see Figure IIA-25). The pyroxenes from noritic—anorthositic rocks are confined to a different region of this diagram (see Figure IIB-14). In Figure IID-13, data for pyroxene inclusions in ropy particles are plotted on the same type of diagram, with the areas for basaltic and norite—anorthositic pyroxene outlined. It is clear that the pyroxenes in ropy glass particles are derived from both noritic and basaltic rocks. This explains why the ropy glass compositions always plotted between the norites and basalts in Figures IID-7 to IID-12: they represent a mixture of noritic and basaltic rock.

We also found one grain of pyroxferroite in a ropy glass particle. Its composition (wt. %) is as follows: SiO_2, 46.4; TiO_2, 0.9; Al_2O_3, 0.9; Cr_2O_3, 0.1; FeO, 42.9; MnO, 0.5; MgO, 1.1; CaO, 7.6; Sum, 100.3. No pyroxferroite was observed in our sections of norites, but it is a common accessory mineral in basaltic rocks (Section IIA). Again, this points to a derivation of the ropy glass particles from a mixture of norite and mare basalt.

The metal grains included in ropy glasses are relatively rich in Co. The compositions of iron grains in three ropy particles ranged from 0.8 to 1.5 wt. % Co and from 0.6 to 5 wt. % Ni. According to Goldstein and Yakowitz (1971), such Co contents are found in lunar, but not in meteoritic, metal. The presence of metal grains in ropy glasses, therefore, cannot be used as evidence of a meteorite impact origin for the glass.

Homogeneous Glass Fragments

We found some truly homogeneous glass fragments, uniform in color and devoid of inclusions or microlites. They occur as discrete soil particles and as fragments in various kinds of breccias. Some glasses classified as "homogeneous" actually contain some metallic droplets. One such case is shown in Figure IID-14. This is a brown sphere, somewhat vesicular, and full of tiny metal or metal-troilite grains. Compositions of the metal grains (5 wt.%Ni, 0.5 wt.%Co, remainder Fe) suggest a meteorite impact origin for the glass. The composition of the glass is given in Table IID-II. The same color range observed in red-brown ropy and yellowish to greenish cindery glasses (see Plate 1, A and C) holds for these fragments. Compositions of representative homogeneous glasses are given in Tables IID-I and IID-II. The microprobe data for these glasses are plotted in Figures IID-15, IID-16, and IID-17. The regions typical of ropy and cindery glasses have been outlined so that they can be compared with the homogeneous glasses. It is clear from these figures that the groupings according to composition and color are preserved, and it appears that the homogeneous colored glasses are members of the same three groups discussed above. The colorless glasses, on the other hand, do not plot in either of the groups. These glasses contain 65 to 70% normative plagioclase. Their compositions correspond most closely to those of anorthositic gabbros (e.g., Table IIB-I, analysis M).

It is interesting to note that red-brown glass fragments occasionally appear in cindery glass aggregates. This may imply that there has been some mixing of the regolith at the Apollo 12 site, such that the light-colored layer containing the ropy glasses has been disrupted locally. Or it could mean that small amounts of red-brown glass have been ejected from their source area and deposited at the Apollo 12 site not only by the event that created the light-colored layer sampled by the astronauts but also on many other occasions.

Crystallites in Glass

We noted previously that the ropy glasses contain newly precipitated crystals of feldspar. These are small and euhedral (see Plate 1, C). Because

Table IID-III. Summary of chemical differences between most ropy (including greenish-yellow, streaky) glasses and most cindery glasses.

	Ropy (wt. %)	Cindery (wt. %)
K	>0.5	<0.25
Na + K	>0.8	<0.7
P	>0.2	<0.1
Fe + Mg	~12.5–16.5	~17–21.5
Al	~6.5–10	~4.5–8
Ti	~1.0–1.9	~1.3–2.4
Cr_2O_3	~0.15–0.3	~0.3–0.5
Quarfeloids[a]	>49%	<47%

[a]Quarfeloids means the sum of normative quartz, feldspars, and feldspathoids.

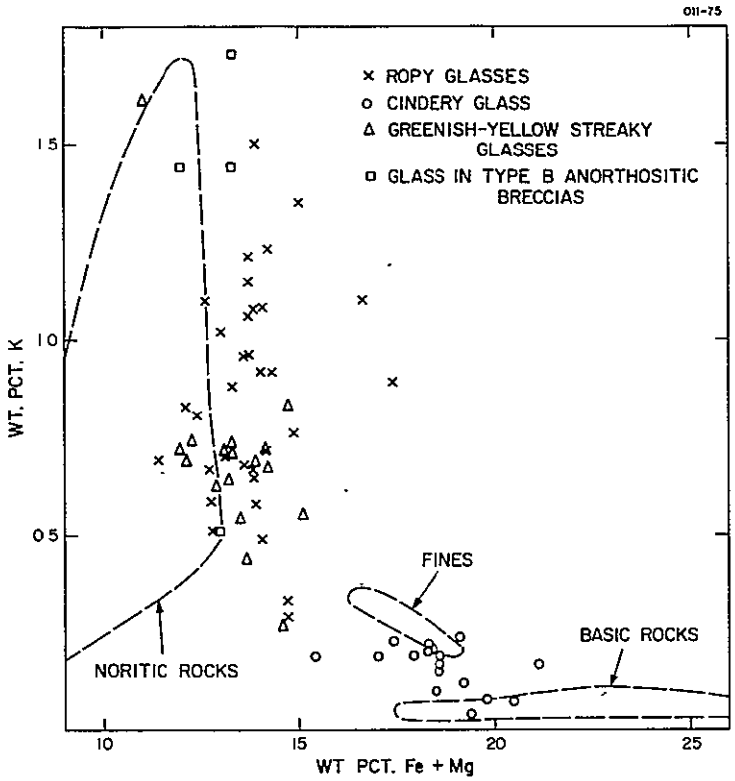

Figure IID-9. K vs. Fe+Mg for ropy and cindery glasses. The ropy glasses are very high in K compared to most lunar material, showing the same range of K contents as the noritic rocks.

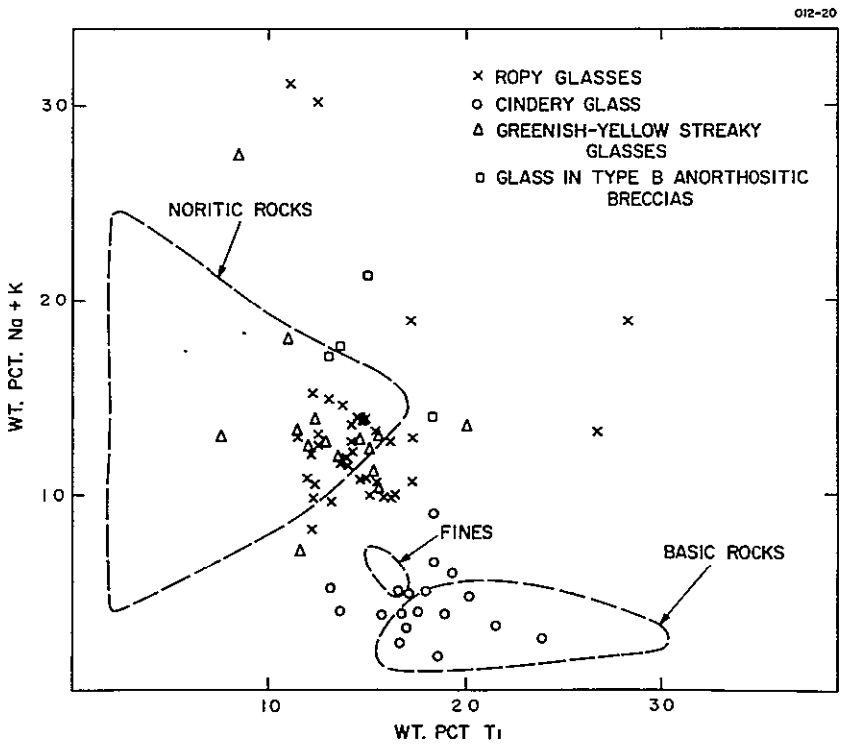

Figure IID-10. The ropy glasses are higher in Na+K than the cindery glasses. The cindery particles appear to have lost some of their Na and K when they were formed from the lunar soil, the composition of which is given by the fines and breccias.

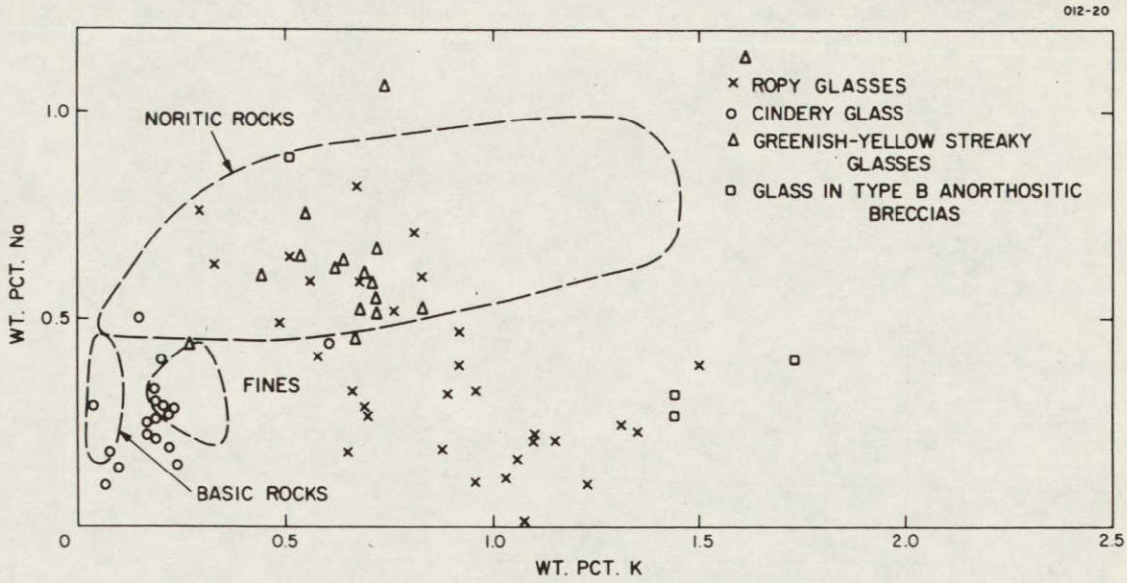

Figure IID-11. Na vs. K for glassy particles. There is a feeble anticorrelation between Na and K in ropy glasses.

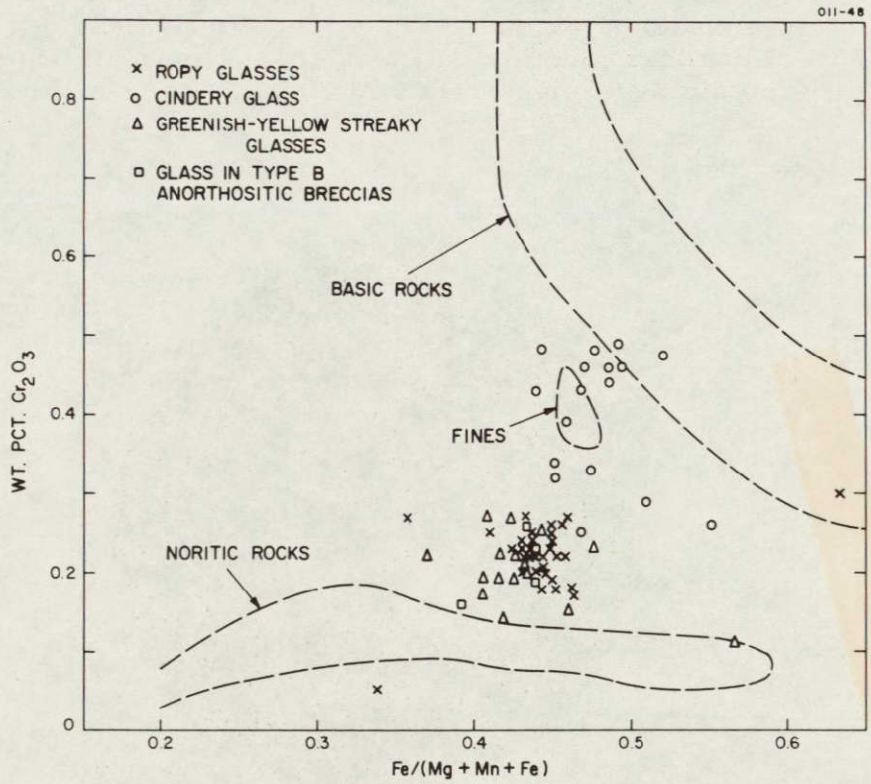

Figure IID-12. The ropy glasses plot in a very narrow range on this graph of Cr_2O_3 vs. the atomic ratio Fe/(Mg+Mn+Fe). This suggests that their source material is similarly restricted in composition.

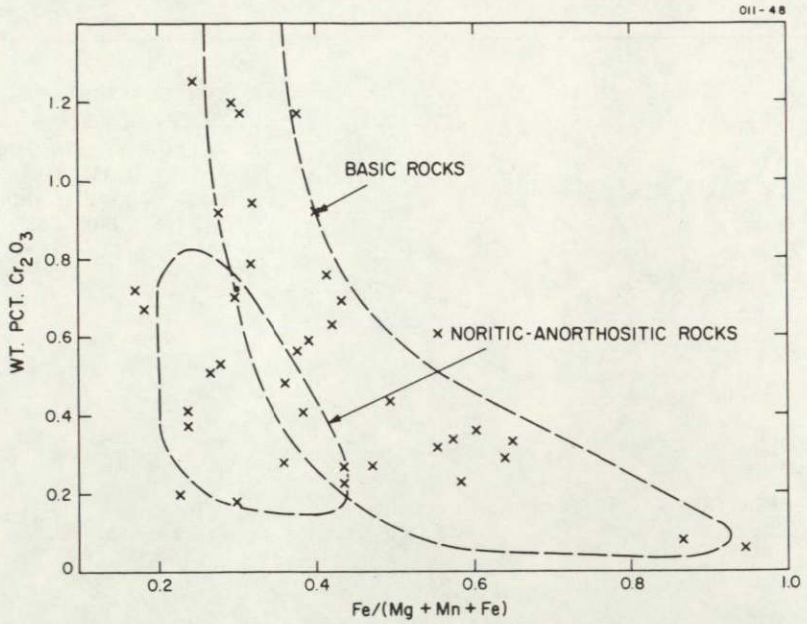

Figure IID-13. Cr_2O_3 vs. the atomic ratio of Fe/(Mg+Mn+Fe) for pyroxene grains included in ropy glass particles. The regions where pyroxenes from basic rocks (Section IIA) and noritic–anorthositic rocks (Section IIB) plot are outlined. The ropy glasses contain pyroxenes from both mare basalts and norites.

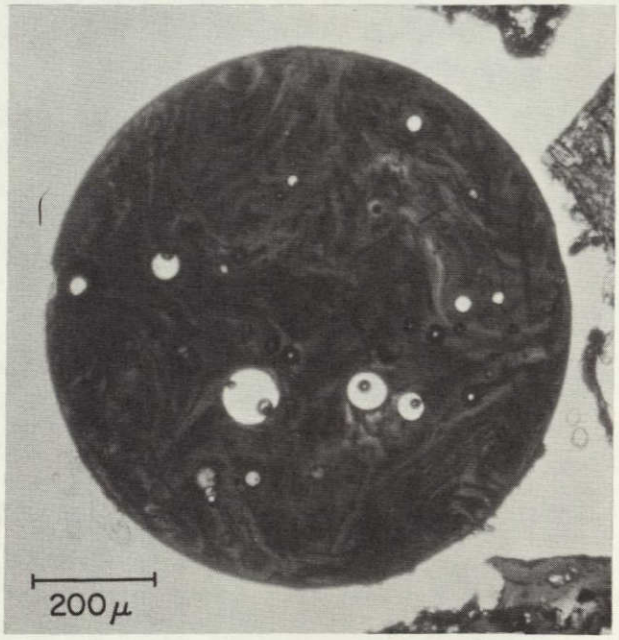

Figure IID-14. Photomicrograph in unpolarized transmitted light of a brown glass sphere (110-4). The glass is full of metallic NiFe or NiFe-FeS droplets. These give rise to the swirly appearance of the glass. The low Co content of the metal suggests a meteoritic origin. The composition of the glass is given in Table IID-II, analysis F.

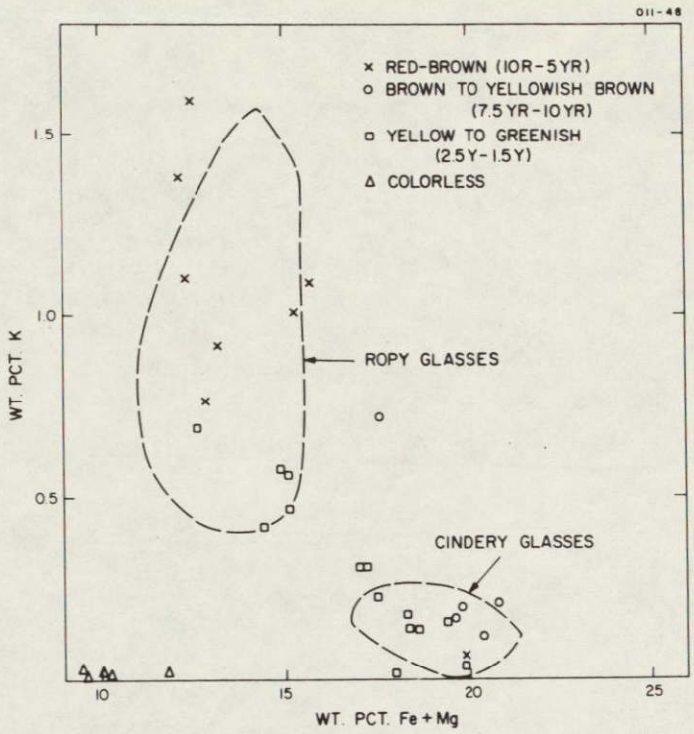

Figure IID-15. K vs. Fe+Mg for homogeneous glasses. The regions where most ropy and most cindery glasses plot are shown. The compositions of the homogeneous glass fragments, except for the colorless ones, clearly correspond to the compositions of the two textural groups discussed previously.

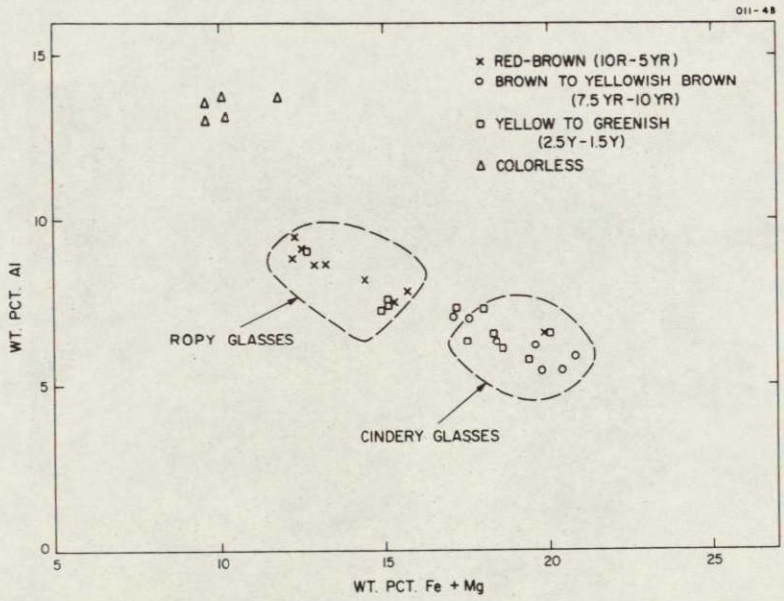

Figure IID-16. Al vs. Fe+Mg for homogeneous glass fragments. The compositions of the colored homogeneous glass particles correspond to either the ropy or cindery glasses. The colorless particles form a unique group of their own typified by lower Fe+Mg and higher Al than the other groups.

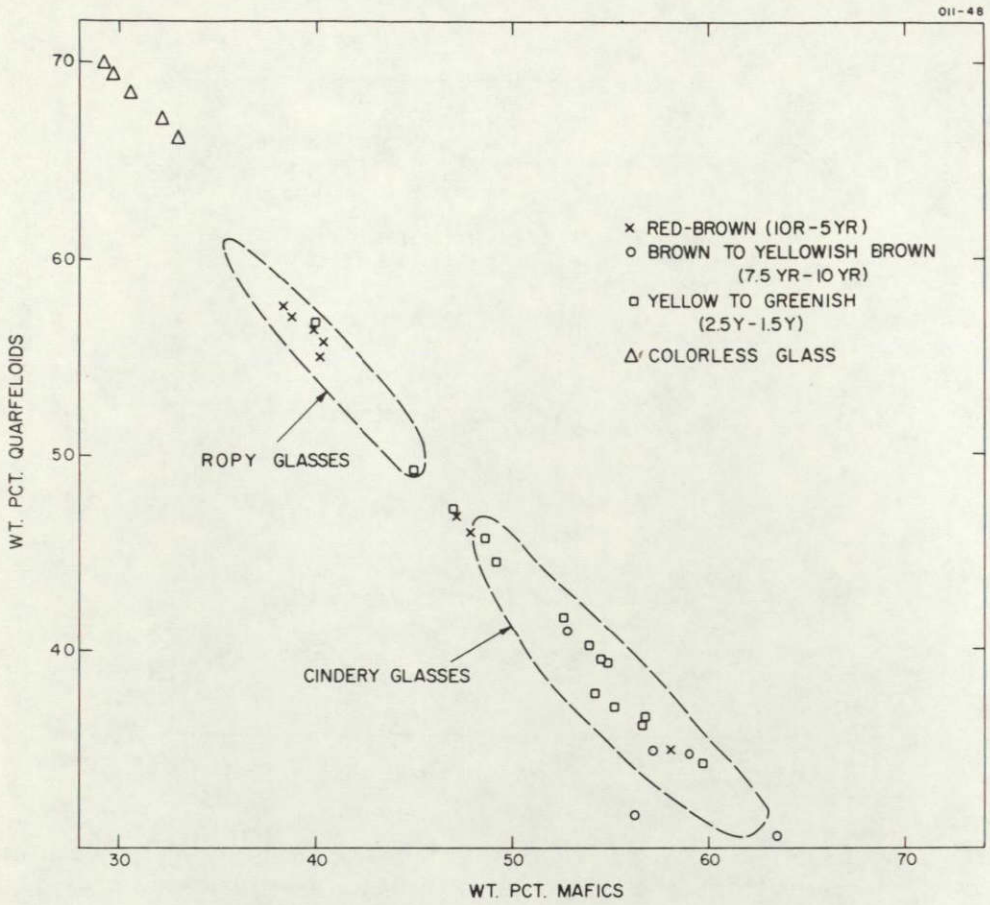

Figure IID-17. Quarfeloids vs. mafics for homogeneous glass. This plot again shows that the colored homogeneous glass particles correspond to one or the other of our textural-chemical groups. The colorless glasses form an additional distinct group of their own.

Figure IID-18. Photomicrograph in unpolarized transmitted light of a glass particle containing radiating crystals of feldspars and pyroxene (110-42). The composition of the particle is given in Table IID-II, analysis E.

of their small size, we were unable to measure their compositions with the microprobe: although up to about 10 μ wide, they appear to be at most only a few microns thick. The occurrence of feldspar that has crystallized from a melt of ropy glass composition means that these glasses precipitate feldspar on their liquidus, in contrast to lunar basaltic rocks, which do not (Ringwood and Essene, 1970; Roedder and Weiblen, 1970; Smith, Anderson, Newton, Olson, and Wyllie, 1970; Weill, McCallum, Bottinga, Drake, and McKay, 1970).

A number of glass particles display quench or devitrification textures. A typical example is shown in Figure IID-18; its composition (measured with a defocused electron beam) is given in Table IID-II. The radiating crystals are both feldspar and pyroxene. Attempts at measuring the composition of the crystallites by focused beam were not successful: only compositions consistent with composite materials could be gotten. The crystals may be very thin, so that the electron beam penetrates to underlying material.

Figures IID-19 and IID-20 show that the bulk compositions of these particles correspond to those of the ropy glasses; thus, ropy glasses may contain either no crystals, or euhedral feldspar crystallites, or radiating crystals of feldspar and pyroxene. The different textures undoubtedly reflect diverse thermal histories experienced by the particles.

Inhomogeneous Glass

A number of glass particles are extremely inhomogeneous, ranging from dark brown to colorless (Plate 1, E). Two were studied in some detail. The first is shown in Plate 1, E and Figure IID-21. The colorless glass is slightly birefringent in some regions, probably an effect of mechanical strain. Its composition is given in Table IID-IV, analysis A. It is quite rich in K (2.4%), containing more of this element than do any of the colorless glasses discussed previously (see Figure IID-15) and more even than all but a few of the red-brown glasses (Figure IID-9). It is high in normative feldspar and quartz and contains normative corundum. The presence of corundum in the norm

suggests loss of Na, and perhaps of K as well, when the glass was formed. Most significantly, the atomic ratio Fe/(Mg + Mn + Fe) is 0.72, higher than that of any other glass analyzed and substantially higher than that of the "normal" colorless glasses. Nor is this high ratio, coupled with the low Cr content, duplicated in the noritic or basaltic lunar rocks. Overall, analysis A shows a bulk composition more similar to that of the rhyolite particle discussed in Section IIC (i.e., high K, Si, Fe/Mg) than to anything else.

Analysis B, Table IID-IV, is for the darkest brown glass in the particle. For most elements, the composition is similar to that of the red-brown glasses, albeit higher in K (2.1%) than most. However, its low Cr content and high Fe/(Mg + Mn + Fe) ratio (0.63) suggest that it is not related to the "normal" red-brown glasses. It is different from the colorless glass, analysis A, in that it is enriched in Fe, Ti, and Mg and depleted in Al and Na. This explains the color difference; it is Fe and Ti that cause coloration in glasses. The lighter brown glass, analysis C in Table IID-IV, contains the most K of any point analyzed in the sample, more Si than A or B, and less Al and Ca. The Fe/Mg ratio is again high. Analysis D was made on a crystal included in the glass. It is clearly a silica polymorph (SiO_2 = 80%), but it is not certain whether the measured impurities (e.g., K, Al, etc.) are in the crystal or come from underlying colorless glass.

Figure IID-22 shows another of these interesting glass particles. In this case, the particle is enclosed by a dark-brown glassy aggregation very similar to a Type 3 breccia matrix (see Section IIE). The composition of the matrix-like region is given by analysis A, Table IID-V. In most respects, it is similar to ropy glass, except for the higher Fe and Mg. The Fe/(Mg + Mn + Fe) ratio is 0.47, which is not unusual for red-brown glass. Analyses B, C, and D (Table IID-V) are of colorless glass. The glass is strikingly rich in K and moderately rich in Si and Na. This is reflected in its mineral norm: high feldspar and quartz contents, and little pyroxene or olivine. The orthoclase content is almost 50%, and normative corundum is present, again suggesting loss of volatiles. Most important, the Fe/(Mg + Mn + Fe) ratios are 0.71, 0.67, and 0.74 for B, C, and D, respectively. As was the case for the particle shown in Figure IID-21, this suggests a relationship with lunar rhyolite (Section IIC).

Analyses E and F in Table IID-V are of brown glass. It is interesting that the lighter colored area contains more Fe and Ti than does the darker one. Both have relatively high Fe/(Mg + Mn + Fe) ratios and low Cr contents. The K content is also high, although lower than that in the colorless regions.

Figure IID-23 shows the results of traverses across this particle (the line traversed is indicated in Figure IID-22). K_α x-rays from K, Fe, and Si were monitored. Aside from the general correlation between K and Si and the anticorrelation of these with Fe, there are two interesting facts to notice. First, the colorless glass in which analysis B was made is zoned. Second, the K concentration varies widely across a region that appears to consist of two phases. Microscopic examination revealed this region to be a continuation of the zoned colorless glass and to contain lath-like grains of what appears to be maskelynite. The individual grains were too small to be analyzed accurately with the microprobe.

Summary

There are three major types of glass particles in the Apollo 12 soil, which we have designated red-brown ropy, greenish-yellow streaky, and cindery. These groups can be distinguished by their colors, textures, and compositions. Most homogeneous (i.e., uniform color, devoid of inclusions) glass fragments correspond in color and composition to one of the above groups. We can, therefore, combine all our data and compute the average compositions of the different types of lunar glass. These averages are reported in Table IID-VI. The red-brown ropy and greenish-yellow streaky glasses have nearly identical compositions, although Na is lower and K and P are higher in the red-brown type. These slight compositional differences, combined with the significant difference in their colors and their dissimilar abundances in our five soil samples, strongly suggest that these two types of glass do not have a common source area on the lunar surface.

In Table IID-VI we have listed the average composition of three samples of Apollo 12 soils. The agreement between this and the cindery glass is excellent. Obviously, the cindery glasses are samples of melted regolith.

The average of five analyses of colorless glasses is also given in Table IID-VI. Anorthositic gabbros that are low in K and P closely resemble the composition of these glasses.

Table IID-IV. Composition and norm at several different points of the inhomogeneous glass shown in Figure IID-21.

	A	B	C	D
Na	0.9	0.5	0.4	0.3
Mg	0.5	2.4	1.5	0.1
Al	14.1	7.7	6.8	7.8
Si	23.8	25.1	29.5	37.7
P	0.4	0.8	0.1	0.0
S	0.1	0.1	0.0	0.0
K	2.4	2.1	3.6	2.0
Ca	6.4	6.6	5.0	1.0
Ti	0.1	1.2	0.3	0.1
Cr	0.0	0.1	0.0	0.0
Mn	0.1	0.1	0.1	0.0
Fe	3.5	9.6	6.9	0.6
Ni	0.0	0.0	0.0	0.0
O	45.1	45.1	45.9	51.2
Sum	97.4	101.5	100.2	100.8
Fo	0.0	0.0	0.0	0.0
Fay	0.0	0.0	0.0	0.0
En	2.3	9.9	6.1	0.6
Fs	8.4	19.3	15.7	1.0
Wo	0.0	2.3	5.8	0.0
Or	17.2	14.9	25.4	14.1
Ab	10.1	5.5	5.2	3.0
An	39.5	28.7	19.6	6.6
Ilm	0.4	3.8	1.0	0.4
Chr	0.0	0.1	0.1	0.0
Qtz	11.9	11.4	20.6	65.3
Cor	7.8	0.0	0.0	9.0
S	0.1	0.1	0.0	0.0
Apa	2.2	4.0	0.4	0.0

Table IID-V. Composition and norm at different points of the inhomogeneous glass shown in Figure IID-22.

	A	B	C	D	E	F
Na	1.0	1.1	1.3	0.8	0.4	0.7
Mg	6.3	0.2	0.2	0.2	2.5	1.6
Al	7.9	12.8	9.8	7.5	5.6	6.6
Si	21.7	26.6	29.8	34.1	28.5	30.0
P	0.4	0.0	0.0	0.0	0.0	0.0
S	0.0	0.0	0.0	0.0	0.0	0.0
K	0.5	4.7	6.3	6.8	3.3	4.5
Ca	6.1	5.2	2.8	1.3	4.6	2.8
Ti	1.1	0.8	0.3	0.1	0.8	0.5
Cr	0.1	0.0	0.0	0.0	0.0	0.0
Mn	0.1	0.0	0.0	0.0	0.2	0.1
Fe	10.6	1.2	0.8	1.3	9.0	7.5
Ni	0.0	0.0	0.0	0.0	0.0	0.0
O	43.3	46.2	46.1	48.4	44.9	46.0
Sum	99.2	98.9	97.4	100.6	99.8	100.4
Fo	5.8	0.0	0.0	0.0	0.0	0.0
Fay	5.4	0.0	0.0	0.0	0.0	0.0
En	18.0	0.8	0.7	0.8	10.4	6.6
Fs	15.3	0.5	1.3	2.6	19.5	16.6
Wo	1.3	0.0	0.0	0.0	7.3	2.5
Or	3.8	34.1	46.0	47.9	23.6	31.9
Ab	10.9	12.8	15.4	8.5	4.5	7.8
An	33.4	36.4	19.7	9.2	14.5	13.7
Ilm	3.7	2.7	0.9	0.5	2.6	1.6
Chr	0.2	0.0	0.0	0.0	0.0	0.0
Qtz	0.0	10.3	15.6	30.1	17.6	19.2
Cor	0.0	2.4	0.3	0.3	0.0	0.0
Apa	2.1	0.0	0.0	0.0	0.0	0.0

Table IID-VI. Average compositions of Apollo 12 glasses and fines. The uncertainty represents one standard deviation of the mean.

	A	B	C	D	E
SiO_2	49.9 ± 1.8	48.4 ± 1.9	45.9 ± 1.6	45.7	45.2 ± 1.6
TiO_2	2.4 ± 0.6	2.3 ± 0.5	3.1 ± 0.9	2.8	0.30 ± 0.02
Al_2O_3	15.2 ± 2.7	15.4 ± 1.3	12.5 ± 1.5	13.0	25.3 ± 0.6
Cr_2O_3	0.23 ± 0.08	0.23 ± 0.07	0.41 ± 0.08	0.42	0.15 ± 0.04
FeO	11.6 ± 1.4	11.2 ± 1.3	16.7 ± 1.6	16.2	6.1 ± 0.6
MnO	0.18 ± 0.06	0.17 ± 0.04	0.24 ± 0.04	0.22	0.09 ± 0.07
MgO	8.3 ± 3.0	8.2 ± 0.9	9.9 ± 1.1	10.4	9.2 ± 0.8
CaO	10.1 ± 1.4	10.3 ± 0.5	10.1 ± 0.5	10.6	14.6 ± 0.7
Na_2O	0.48 ± 0.29	0.84 ± 0.26	0.34 ± 0.15	0.47	0.13 ± 0.08
K_2O	1.17 ± 0.59	0.80 ± 0.31	0.20 ± 0.08	0.25	0.02 ± 0.01
NiO	0.01 ± 0.01	0.01 ± 0.01	0.02 ± 0.02	0.0	0.03 ± 0.03
P_2O_5	0.98 ± 0.17	0.67 ± 0.27	0.21 ± 0.10	0.28	0.09 ± 0.03
SO_3	0.20 ± 0.10	0.17 ± 0.09	0.21 ± 0.13	0.17	0.02 ± 0.02
Sum	100.7	98.8	99.8	100.4	101.2

Key

A. Red-brown ropy glasses (41 analyses).

B. Greenish-yellow streaky glasses (21 analyses).

C. Cindery glasses (31 analyses).

D. Average of 12001 (Mason et al., 1971), 12042 (Rose et al., 1971), and 12070 (Willis et al., 1971).

E. Colorless glasses (5 analyses).

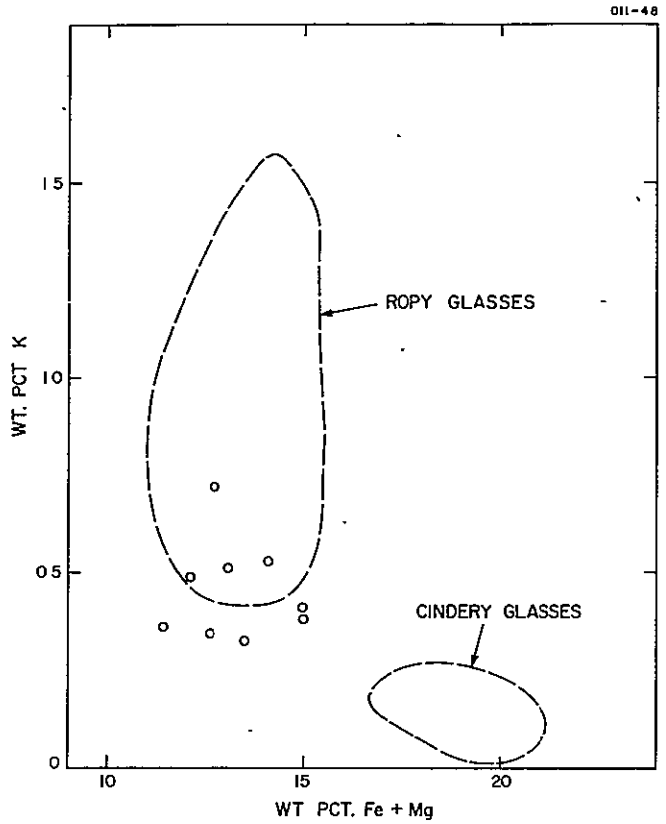

Figure IID-19. The particles displaying quench textures (e.g., Figure IID-18) have essentially the same compositions as the ropy glasses, as seen in this plot of K vs. Fe+Mg.

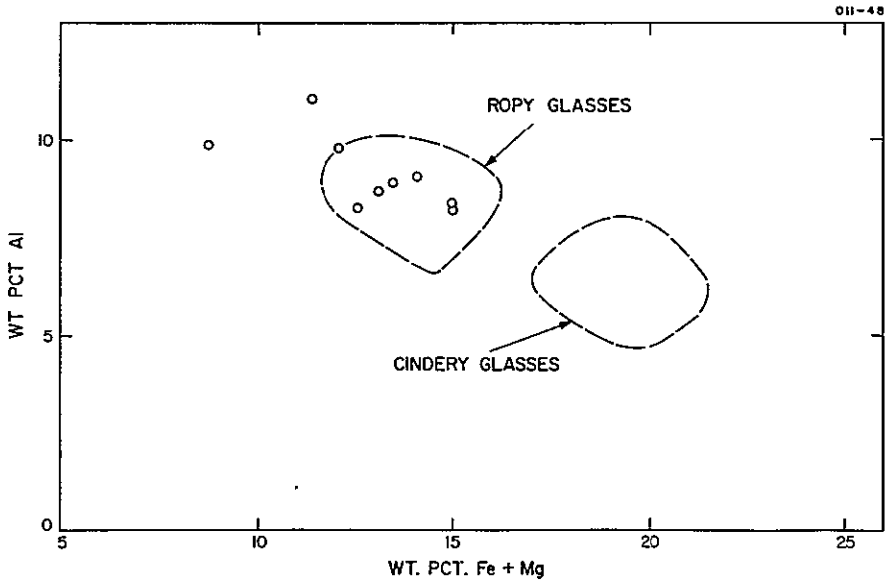

Figure IID-20. This plot of Al vs. Fe+Mg shows that the particles displaying quench textures have essentially the same compositions as the ropy glasses.

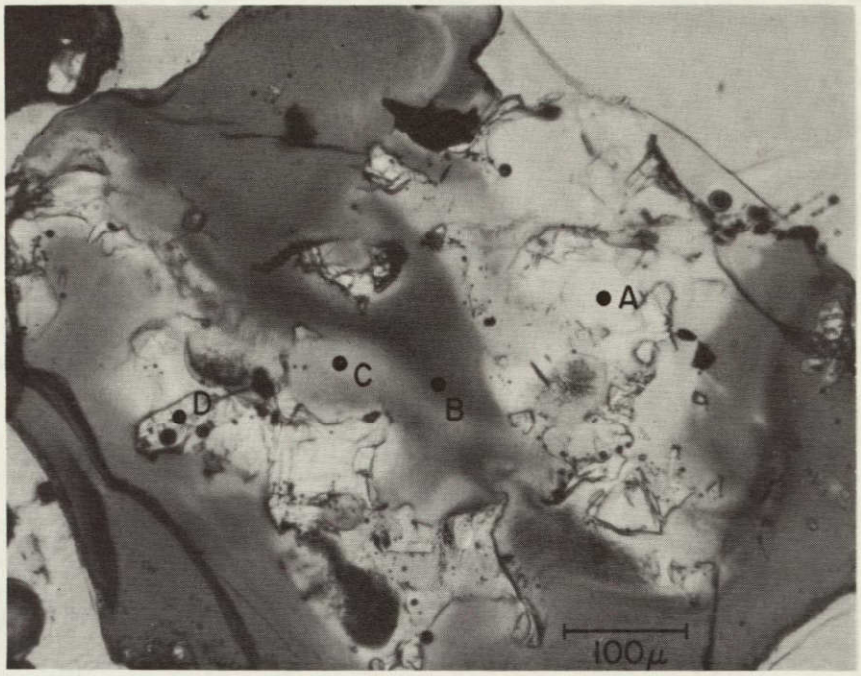

Figure IID-21. Inhomogeneous glass particle (110-10) in unpolarized transmitted light; a color photograph appears in Plate 1, E. The results of microprobe analyses made at the indicated points are shown in Table IID-IV.

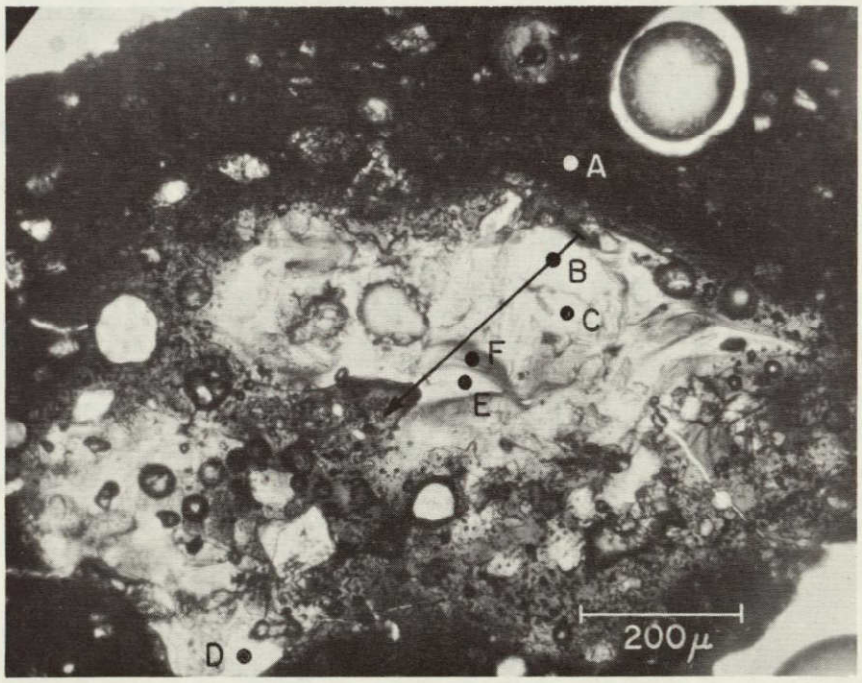

Figure IID-22. Inhomogeneous glass particle (124-11) in plain polarized light. Results of microprobe analyses at the indicated points appear in Table IID-V. The traverse appears in Figure IID-23.

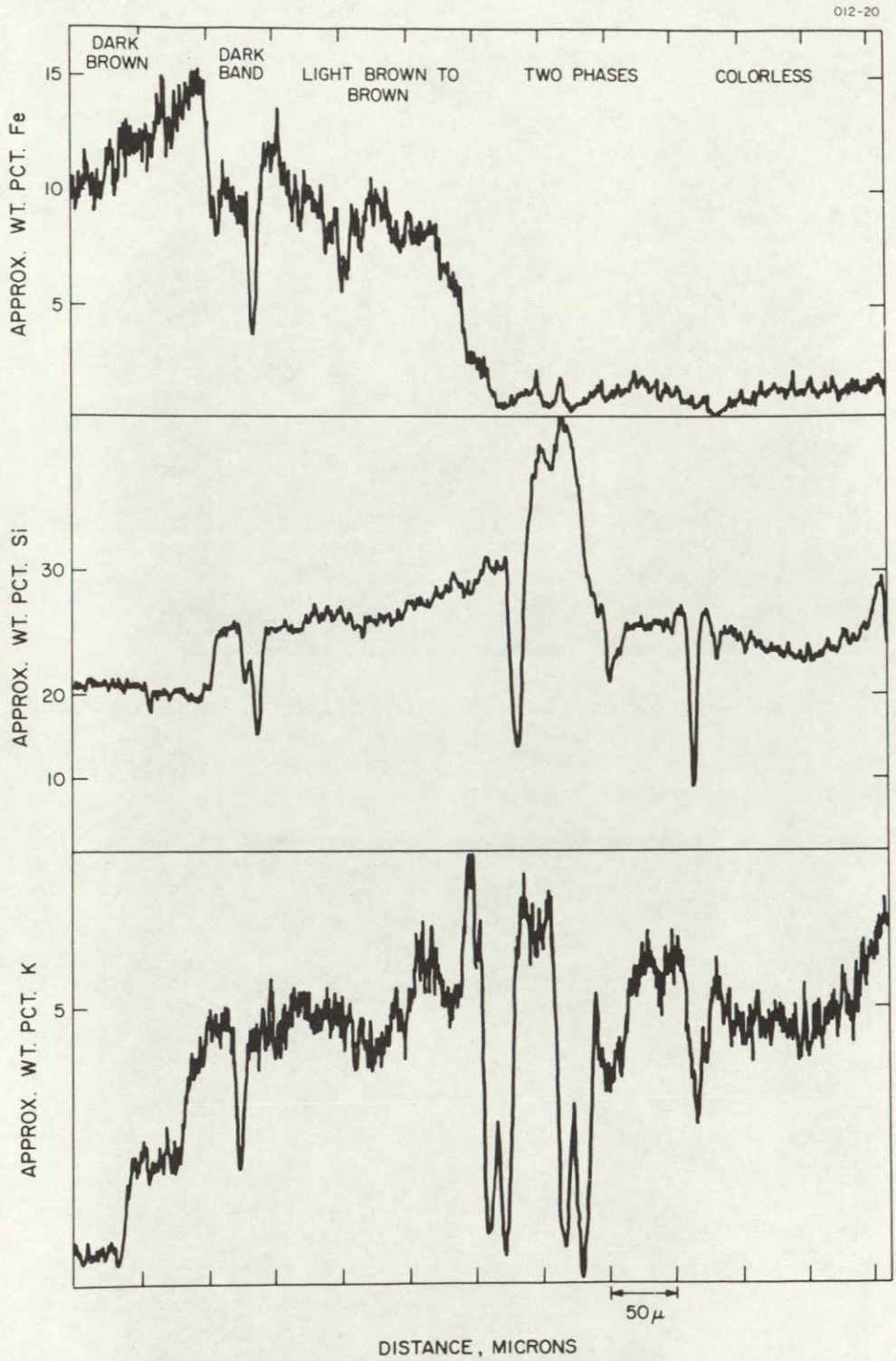

Figure IID-23. Variations in the concentrations of Fe, Si, and K along the traverse across the inhomogeneous glass particle shown in Figure IID-22. The concentrations given on the abcissa are only approximate. Precise analyses are given in Table IID-V. Motion in direction of arrow in Figure IID-22 is right to left in profiles above.

IIE. Microbreccias and Unconsolidated Soils

Microbreccias

Microbreccias are aggregates of fine-grained rock, mineral, and glass detritus that are a conspicuous rock type on the lunar surface. Their fragmental textures and admixture of diverse materials suggest that the microbreccias are samples of the lunar regolith upon which some degree of cohesion has been imposed (Figure IIE-1).

The universal identity of microbreccias with soils has, however, been challenged by Duke, Woo, Sellers, Bird, and Finklemen (1970), who suggest that some of the breccias from Tranquillity Base represent a distinct rock unit, probably shock-welded ejecta, derived from a specific impact event. An alternative suggestion was made by Mackay, Greenwood, and Morrison (1970), who described textural evidence that the Apollo 11 microbreccias were sintered during flight in base surge clouds.

After a detailed examination of our samples, we found three textural and chemical types of microbreccia and two types of soils. The mineralogy and composition of these materials will be compared in this section, and their possible source rocks and modes of origin will be discussed in Section IIIE.

Microbreccias occur in all size ranges from large hand specimens to fine particles weighing less than 1 mg. Among the hand specimens collected by the astronauts on the two Apollo missions, 50% (20 of 40 specimens) from Tranquillity Base and 4% (2 of 45 specimens) from Oceanus Procellarum are microbreccias. Most of the other specimens from both sites are basalts and gabbros.

This striking difference in proportions of microbreccia to igneous rocks was ascribed by the LSPET investigators (1970b) to a difference in thickness and maturity of the regolith. At Tranquillity Base, the regolith thickness is

estimated at about 3 to 6 m (Shoemaker et al., 1970). Few craters in that vicinity are believed to penetrate bedrock, and therefore much of the crater ejecta is lithified soil. At the Apollo 12 landing site, the regolith thickness is estimated at only 1 to 3 m (Swann et al., 1970). Most of the craters within 250 m of the landing site are partially excavated in bedrock, with the result that maria basalts are of greater abundance in the throwout than they were at Tranquillity Base.

The microbreccias in our soil samples differ markedly in the degree of compaction and remelting they display and in the character of their matrix materials. Some of them appear to be simply compact aggregates of coarse and fine angular debris showing no visible evidence of shock (other than breakage) and none of high temperatures. Many of these microbreccias are rather soft and easily friable. Others, however, consist mainly of glass with included rock and mineral fragments, some of which display micro-textures indicative of shock metamorphism. Unaltered and shock-melted breccias often occur together in the same small sample of lunar soil.

We have classified our breccias into the following categories according to the content of glass in the matrix:

Type 1. Compact aggregates with little or no visible glass in the matrix.

Type 2. Aggregates with thin wisps of glass in the matrix.

Type 3. Aggregates with matrices mainly of glass in a very fine leafy intergrowth with minute mineral fragments. The glass shows no flow-banding.

Particles in which glass plays an even more prominent role are treated in our section on glasses (see Section ID).

The proportions of microbreccias relative to other rock types in our soil samples are plotted in Section I, Figure I-16, where breccias are seen to be absent from the fraction 0.6 to 1 mm of Sample 12032,27, but are present in amounts of 20 to 40% in the same-size fraction of the

other four samples. Among the microbreccias, the relative abundances of the three types listed above are shown in Table IIE-I. Here, Type 3 makes up about 50% or more of the breccias in all size fractions; Type 1 is abundant only in Samples 12001,71 and 12037,20; Type 2 is present but minor in all samples.

At first glance, this result appears to contrast sharply with our findings in the Apollo 11 sample, where we reported that 53% of the particles, by volume, are soil breccias, only 10% of which are partially vitrified. We believe, however, that the difference is more apparent than real. The soil breccias from Tranquillity Base are dark in color and nearly opaque in ordinary thin sections owing to their high content of finely dispersed ilmenite, which tends to mask any glass in the matrices. Ultrathin sections of the Apollo 11 breccias, however, reveal the presence of glass similar in texture to that of our Type 3 microbreccias from Apollo 12. We estimate that glass and crystalline materials occur in approximately the same proportions in microbreccias from the two sites.

Type 1 microbreccias

Breccias of this type are aggregates of coarse and fine angular debris. Some are porous and very weakly cohesive and appear to be soil samples that have been subject to compaction or to some degree of sintering between particles. Others are firmly indurated and may have undergone shock welding along grain boundaries. Glass, as spherules or broken fragments, is common among the coarse inclusions but is not visible as an important component in the matrix.

Most of these microbreccias appear to be random aggregations of particles, as shown in Figures IIE-2 and IIE-3. A few give textural evidence of layering, either horizontal or concentric, on a very fine scale (Figure IIE-4).

Table IIE-I. Distributions of microbreccias by type in the coarser size fractions of five Apollo 12 lunar soil samples.

Sample Number	12032	12033		12001		12037		12070
Sample Split	27	66	23	88	71	42	20	35
Size Fraction (mm)	0.6-1	>1	0.6-1	>1	0.6-1	>1	0.6-1	0.6-1
(Wt. % of Total Sample)	6%	100%	9%	100%	7%	100%	12%	4%
Microbreccias (Frequency % of Size Fraction)								
Type 1	0	5	4	4	3	1	5	3
Type 2	0	1	4	21	17	7	9	6
Type 3	0	27	18	16	19	5	7	25
Total %	0	33	26	41	39	13	21	34

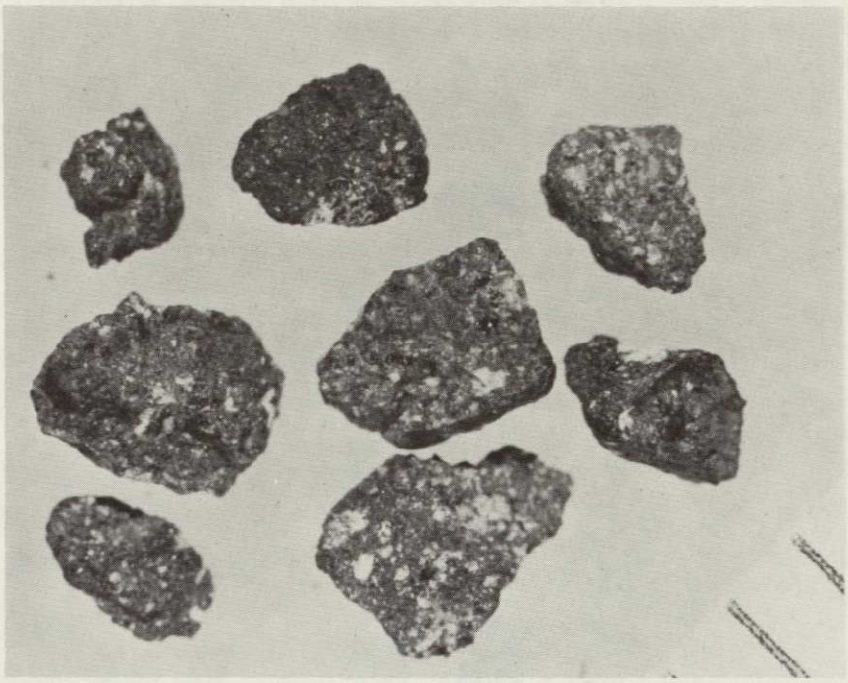

Figure IIE-1. Microbreccias from Sample 12037. Scale divisions 1 mm.

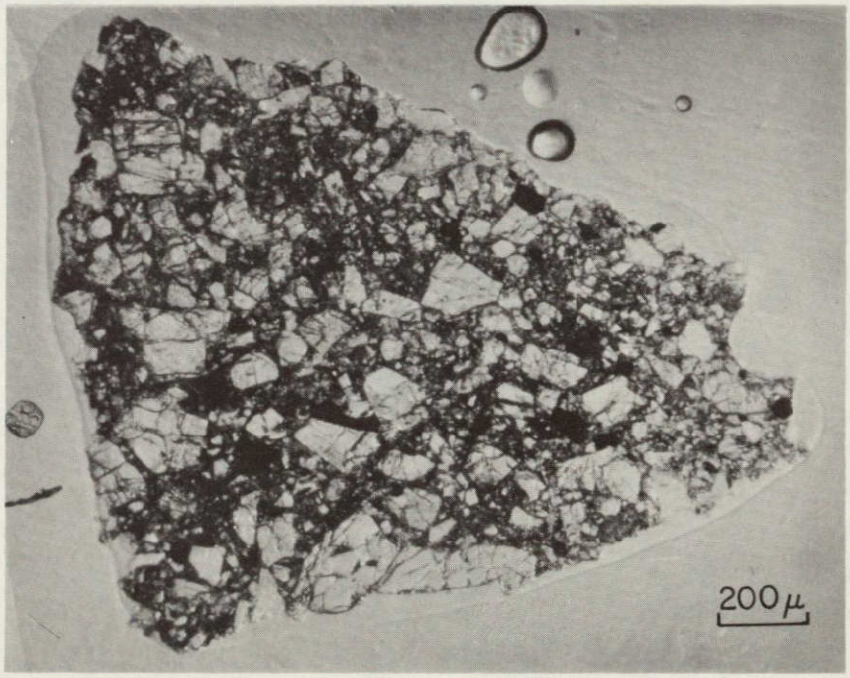

Figure IIE-2. Type 1 microbreccia (117-6). Angular mineral fragments in compact aggregate. Transmitted light.

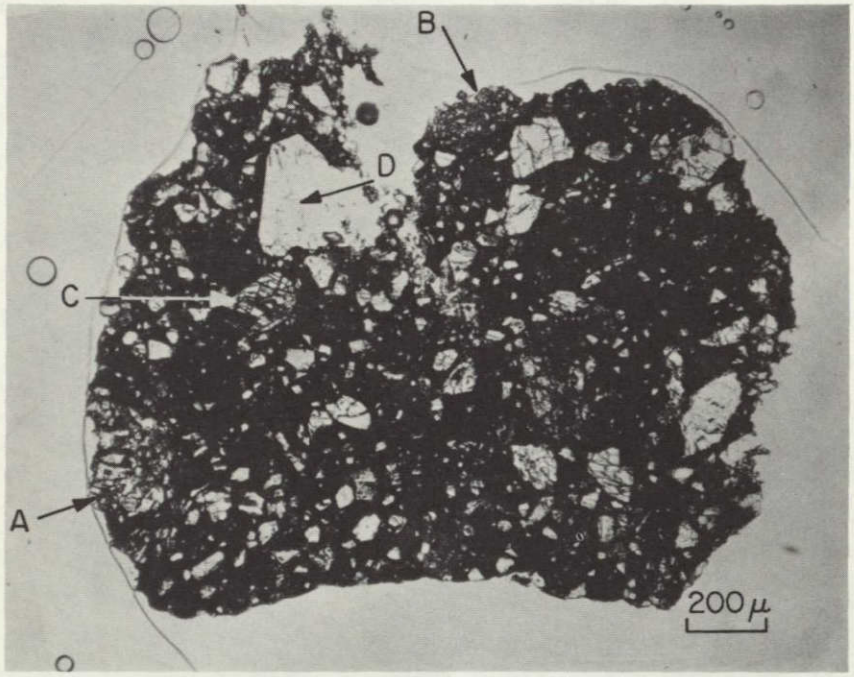

Figure IIE-3. Type 1 microbreccia (117-1) including shocked rock fragments; basalt at A, norite, B. Broken, but unshocked orthopyroxene (C) lies below large, white feldspar fragment (D). Matrix is compact, not visibly glassy. Transmitted light.

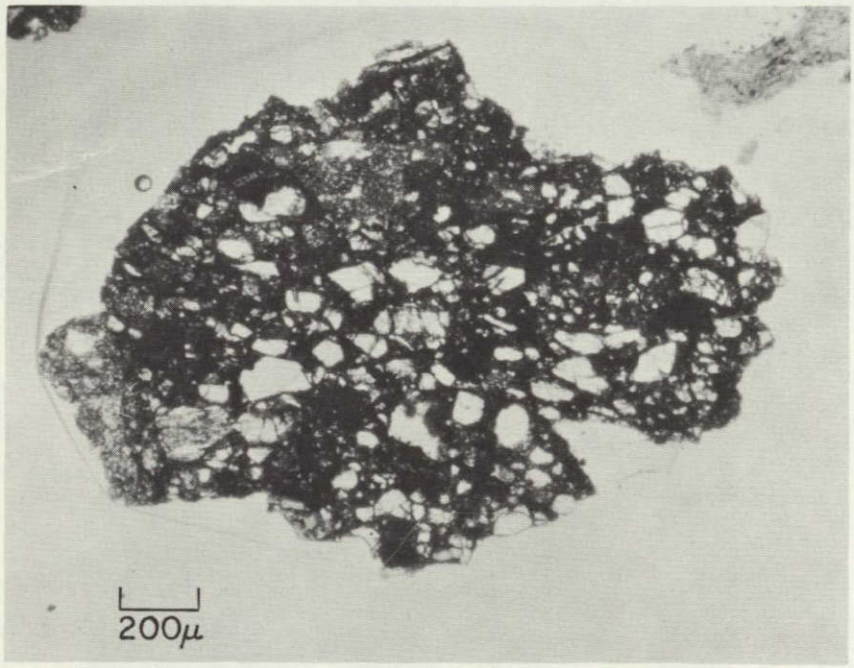

Figure IIE-4. Type 1 microbreccia (126-25). A wide variety of mineral and glass fragments in a weakly layered aggregate. Transmitted light.

The mineral and rock fragments in these breccias represent a wide range of source materials. Microprobe analyses of the matrix materials closely resemble bulk analyses of the fine-grained soils as shown below in Figure IIE-14.

Type 2 microbreccias

These microbreccias resemble Type 1 except for thin wisps of glass that reflect partial melting of the matrices during or after aggregation of the particles. Melting temperatures were, however, neither pervasive nor sustained. Figure IIE-5 illustrates a breccia of this type. Microprobe analyses of the dark, compact matrix and of the brown streak of glass (A in photograph) show that both lack normative olivine but that the glass is about 5% richer than the matrix in normative feldspar and 2% richer in normative quartz (Table IIE-IV).

The particle in Figure IIE-6 has a strongly developed concentric layering of detritus and streaks of glass around a large, broken olivine fragment at the center. Before thin sectioning, this particle resembled a very small, rough-surfaced volcanic bomblet. In thin section, the texture is an excellent example of the "accretionary lapilli" described by Mackay et al. (1970) in the Apollo 11 samples. These authors interpret the lapilli as formed by the accretion at high temperatures of solids and glass around a particle undergoing flight through a base surge cloud. Base surges are ring-shaped masses of dust and gas that travel outward, over the surface of the ground, from the site of a high-energy explosion of either volcanic or impact origin.

Type 3 microbreccias

Microbreccias of this type have no streaks of flow-banded glass binding them together, yet much of the matrix material is glass, as indicated by its isotropic character and its failure to produce distinct x-ray diffraction patterns. In thin sections, Type 3 matrices are seen as interlacing aggregates of glassy particles and very fine-grained mineral dust, which appear

to be welded together in situ. Matrix material of this kind tends to cohere during breakup of the microbreccias. As a result, tiny, leafy aggregates of glass and dust are the most abundant type of particle in our samples of the unconsolidated fines in size ranges below 74 μ. Figures IIE-7 and IIE-8 illustrate a Type 3 microbreccia along with a high-magnification photograph of the matrix. Figures IIE-9 to IIE-11 show examples of these breccias with varying proportions of mineral detritus and rock inclusions.

Constituents of microbreccias

Embedded rock fragments. If microbreccias are mechanical mixtures of lunar materials from widespread sources, we would expect to find embedded in them at least as many varieties of rocks, minerals, and glass as occur in the unconsolidated soils, and a wider range of lithologies than in the hand specimens collected by the astronauts. Our microbreccias contain basalt fragments of several textural varieties and also norites and anorthosites. Our microbreccia fragment (135-1), described below, clearly derives from a Ti-rich rock of strikingly different composition from any of the crystalline lithologies identified to date. This bears out our expectation of finding unique lunar materials among the microbreccias.

Mineral fragments. We have analyzed several hundred mineral fragments embedded in microbreccias in the search for a wider range of source materials than are represented by the rock fragments. With the sole exception of the niobian rutile described below, no minerals have been discovered that have not been identified in the basalts and norites.

The ranges of compositions we have found in mineral fragments from microbreccias are as follows:

Olivines: 39 to 77 mole % forsterite.

Pyroxenes: A wide variety of pyroxenes has been found, including pigeonites, augites, subcalcic augites, diopsidic augites, and pyroxferroite. The range of pyroxene compositions is broad, but no greater than in the basalts and very little greater than in the single pyroxene grain with the varying molecular components plotted in Figure IIA-24.

In Figure IIE-12, a comparison is drawn between the Fe and Cr contents of isolated pyroxene grains in Apollo 12 breccia fragments and pyroxenes in the Apollo 11 and Apollo 12 rock fragments. Clearly, the pyroxenes do not guide us to new, unique rock types.

Feldspars: 80 to 96 mole % anorthite.

We have found patches of K- and Si-rich glass, partially devitrified, but no definite crystals of potash feldspars in the breccias.

Silica minerals: Embedded fragments of essentially pure SiO_2 that are anisotropic and have a low index of refraction have been found in the breccias. The mineral is probably tridymite.

Ilmenite: Compositions range from the pure phase to varieties containing up to 4.5% MgO.

Chromite: Compositions range from the pure phase to Al-rich varieties containing up to 12.3% Al_2O_3 and to Ti-rich varieties (Cr-ulvöspinel) with 23.9% TiO_2.

Troilite: Small amounts occur, often in association with metallic iron.

Metals: Metallic iron grains and spherules ranging in Ni from 0.12 to 3.38% and in Co from 0.3 to 0.4% have been analyzed. In general, the microbreccias contain very few metal particles or spherules in comparison with the glasses and the noritic fragments. We interpret this to mean that the glasses are generated by the high temperatures near the sites of meteoroid impact. The breccias, on the other hand, are indurated by other processes or at distances sufficiently removed from impact events to avoid melting and significant contamination with meteoritic metals.

Niobian rutile: Fragment (106-318): A transparent, tawny yellow crystal of rutile, enriched in niobium and rare earths, was discovered in a thin section of a microbreccia fragment from Sample 12070,35. The rutile is enclosed within ilmenite but does not appear to be an exsolution product. The coexisting rutile and ilmenite, attached to a glassy Type 3 breccia matrix, are shown in Figures IIE-13a and b.

The rutile is uniaxial (+) and pleochroic with O = tawny yellow; E = olive green. Both indices of refraction are well above 2.10, the index of the highest available immersion oil. Rutile indices typically range from $\omega = 2.5$ to 2.6; $\epsilon = 2.8$ to 2.9. The color and pleochroism of the lunar material are similar to those of terrestrial niobian rutiles.

Electron-microprobe analyses of the rutile, ilmenite, and the breccia matrix are listed in Table IIE-II. The following formula for the rutile was calculated on the assumptions that all elements of less than 0.1 wt.% are nonessential and that Ce and V occur in the reduced state as Ce^{+++} and V^{+++}:

$$(Nb, Ta)_{0.04}(Cr, V, Ce, La)_{0.04}Ti_{0.92}O_2$$

This composition is unique among lunar and terrestrial rutiles. Our crystal is the first lunar mineral identified as concentrating niobium, and the first rutile from any source containing rare earths.

After microprobe analysis was complete, the rutile was chipped out of the thin section and a small flake of it, about 30 μ in diameter, was mounted for x-ray diffraction determinations on our two-axis rotating sample holder.

The x-ray diffraction pattern consists of 16 lines, including 6 that are faint but resolvable in the back-reflection region. All lines index on the tetragonal rutile lattice. The following unit-cell parameters were computed by means of the least-squares refinement program of Burnham (1962):

$a = 4.600 \pm 0.001$; $c = 2.962 \pm 0.002$ Å.

Cell volume: 62.683 ± 0.046 Å^3.

These parameters are slightly enlarged from those of standard rutile (TiO_2) (Straumanis, 1961): $a = 4.5937$; $c = 2.9581$ Å.

Rutiles of unexceptional compositions have been identified in the Apollo 11 and Apollo 12 samples by numerous investigators, including Wood et al. (1970) and Keil, Bunch, and Prinz (1970).

All previously described lunar rutiles occur as thin exsolution lamellae or as tiny grains, about 20 μ in diameter, within ilmenite. Some of these rutiles are essentially pure TiO_2, others contain several percent of FeO.

Iron is very common in terrestrial rutiles, where it ranges in value up to 10% or more; it occurs mainly as Fe^{+++}, but Fe^{++} is also reported. Chromium is less widespread but occurs, generally along with iron, in some rutiles. Vanadium is almost invariably present as a trace element in titanium minerals. Niobium and tantalum are rare constituents found in rutiles of two different geochemical environments. Members of the tetragonal solid-solution series rutile-tapiolite, $[TiO_2 - Fe(Ta, Nb)_2O_6]$, occur in some granite pegmatites. In these phases, Ta often exceeds Nb, and Fe^{++} is always present.

In alkalic rocks, especially carbonatites and carbonate veins, rutiles tend to be strongly enriched in Nb and poor in Ta (Heinrich, 1966). Iron is generally minor or absent. Rutile from a carbonate vein in Lemhi Co., Idaho, for example, has the following composition as calculated from a spectrographic analysis (Heinrich, Levinson, Axelrod, and Milton, 1958):

$TiO_2 = 76\%$, $Nb_2O_5 = 18\%$, $Ta_2O_5 = 0.1\%$.

Alkalic rocks also tend to show an enrichment in rare earths, but these elements have not been reported in rutiles.

Niobium and tantalum occur very sparingly in the lunar rocks and soils. Values ranging from about 5 to 50 ppm Nb and 0.01 to 3 ppm Ta were, for example, reported by Morrison et al. (1970, 1971) for bulk samples of

Apollo 11 and Apollo 12 rocks and fines. Rock 12013 contains about 170 ppm Nb; Ta was not determined (LSPET, 1970a).

Rare-earth elements are concentrated in some lunar glasses (Section IID) and in several lunar phosphate and zirconium-bearing minerals (see, for example, Albee and Chodos, 1970; Fuchs, 1970; Ramdohr and El Goresy, 1970). Such minerals also tend to contain rare earths when they occur in terrestrial rocks and in meteorites. Rare-earth-bearing rutiles, however, have not, to our knowledge, been reported in the literature. The presence of La and Ce in the lunar rutile was most unexpected in view of the very large ionic radii of these elements: La^{+++} 1.14, Ce^{+++} 1.07 Å. The radii of the other constituents are Ti^{+4} and Ta^{+5} 0.68, Nb^{+5} 0.69, Cr^{+3} 0.63, and V^{+3} 0.74 Å.

Although chromium occurs in both rutiles and ilmenites, it shows an extreme fractionation between these phases in the lunar fragment, with 0.4% Cr_2O_3 in the ilmenite and 3.2% Cr_2O_3 in the rutile. The resulting association of chromium with niobium is another unusual aspect of this rutile.

It is unfortunate that the rutile and ilmenite are attached to a microbreccia matrix rather than occurring in situ in a crystalline rock. The matrix, as shown in Table IIE-II, lacks normative olivine but contains about 40% normative pyroxene and 50% normative feldspar + quartz. In composition it resembles numerous other partially glassy breccia matrices analyzed in this laboratory (see Figure IIE-14) but does not match any specific lunar basalt or norite. The rutile and ilmenite thus appear to be embedded in a lithified soil that furnishes no clue to the nature of their parent rock.

Sporadic glass spherules

Glass spherules, if not wholly unexpected in the lunar samples by all investigators, were considered a most spectacular component by many who studied the Apollo 11 samples. It was our impression, on first examining the fine-fines of the Apollo 12 samples, that spherules, teardrops, dumbbells, and other free forms made up a much smaller proportion of these soils. To test this impression, we counted the spherules embedded in thin sections of microbreccias and cindery glasses from the two missions. In both cases, we avoided the unusual spherule-packed breccia types described at the end of this section. Our results are listed in Table IIE-III.

If any valid conclusion can be drawn from this survey, it is that the microbreccias of Apollo 12 Sample 12070 contain approximately the same number of spherules per square millimeter as those of Apollo 11 Sample 10085, possibly a few more. The microbreccias and cindery glasses

Table IIE-II. Electron-microprobe analyses of rutile, ilmenite, and microbreccia matrix, particle (106-318).

Weight percentages							
Rutile[a]		Ilmenite		Matrix[b]		Matrix Normative composition (wt. %)	
TiO_2	87.9	TiO_2	55.5	SiO_2	47.4	En	21.0
						Fs	19.3
Nb_2O_5	6.4	FeO	38.3	TiO_2	3.8	Wo	2.7
Ta_2O_5	0.2	MgO	5.3	Al_2O_3	16.5	Or	3.5
						Ab	6.9
Cr_2O_3	3.2	Cr_2O_3	0.4	Cr_2O_3	0.1	An	39.0
V_2O_3	0.4	MnO	0.4	FeO	13.9	Qtz	0.1
Ce_2O_3	0.8		99.9	MnO	0.2	Ilm	7.1
						Chr	0.2
La_2O_3	0.4			MgO	8.5	Mole %	
	99.3			CaO	9.3	En	55.3
						Fs	38.6
				Na_2O	0.8	Wo	6.1
				K_2O	0.6	Or	7.0
						Ab	14.8
				SO_3	0.3	An	78.2
					101.4		

[a]Elements also detected:

≤ 0.1% = Fe

≤ 0.06% = Mn, Mg, S, Si, Al, Y

≤ 0.01% = Sn, Cu, Zn, Zr.

Not detected:

Ni, P, Ba, Se, Te, Nd, Gd
Sm, Pr.

[b]Average of five defocused-beam microprobe analyses.

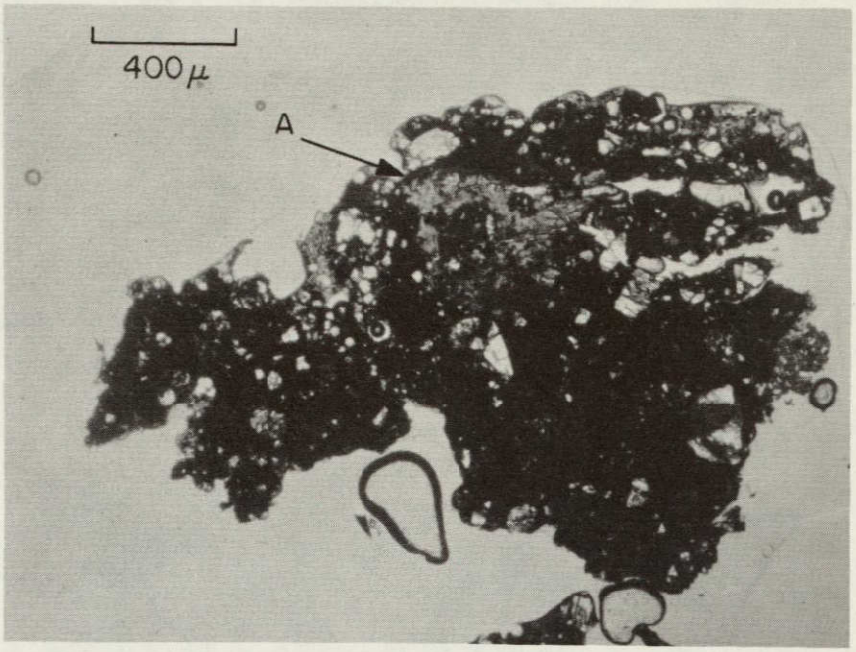

Figure IIE-5. Type 2 microbreccia (128-12) with thin streak of brown glass (A) in otherwise compact matrix. Analyses of the glass and matrix are compared in Table IIE-IV. Transmitted light.

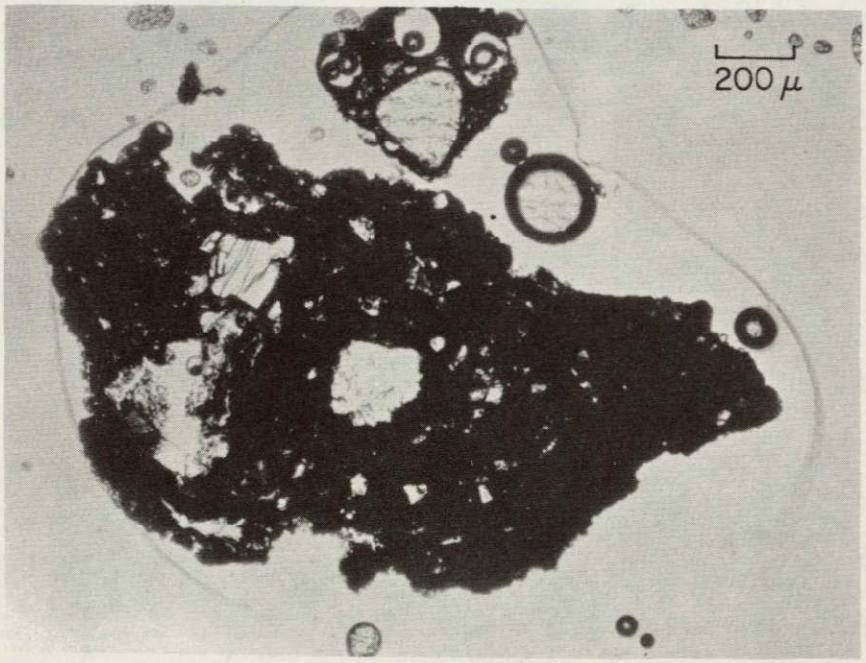

Figure IIE-6. Type 2 microbreccia (124-12), with fine-grained mineral fragments and streaks of glass in concentric layers enclosing broken grain of olivine. The texture is reminiscent of bomblets or lapilli from base-surge dust-gas clouds. Matrix analyses are given in Table IIE-IV. Transmitted light.

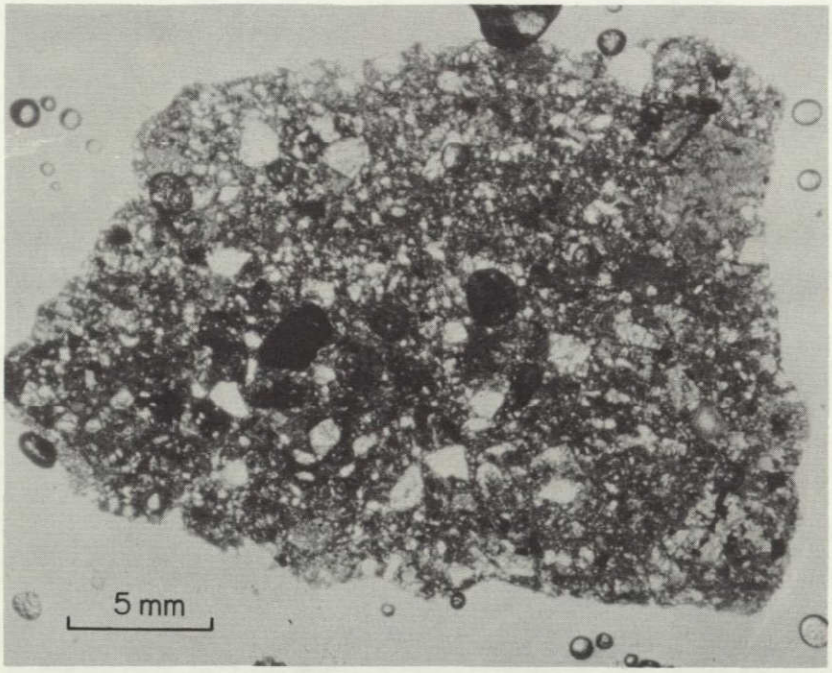

Figure IIE-7. Type 3 microbreccia (117-7) with an abundance of angular mineral fragments, many of which show shock effects. Transmitted light. Circular structures are bubbles in mounting medium.

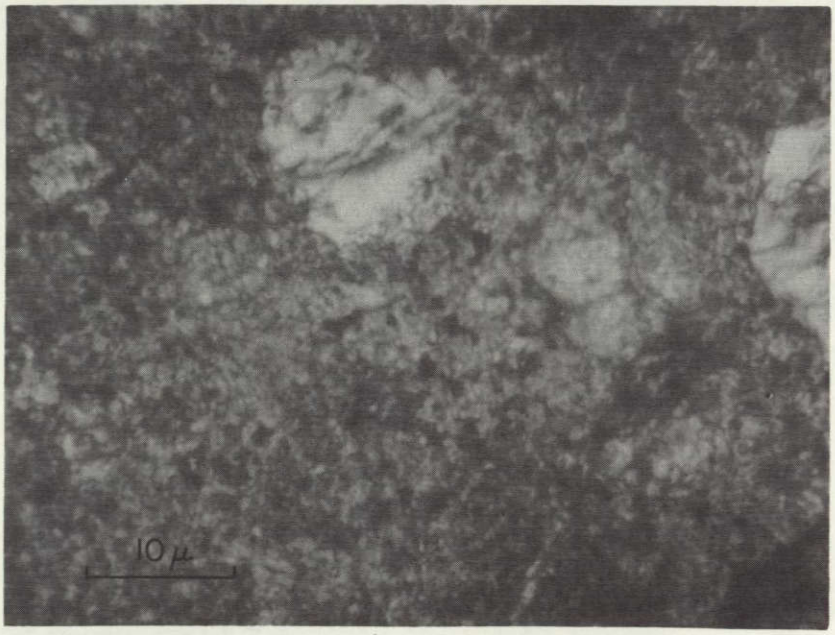

Figure IIE-8. Closeup of matrix of breccia in Figure IIE-7. The matrix material is mainly glass in a fine, lacy intergrowth with minute mineral grains. Transmitted light.

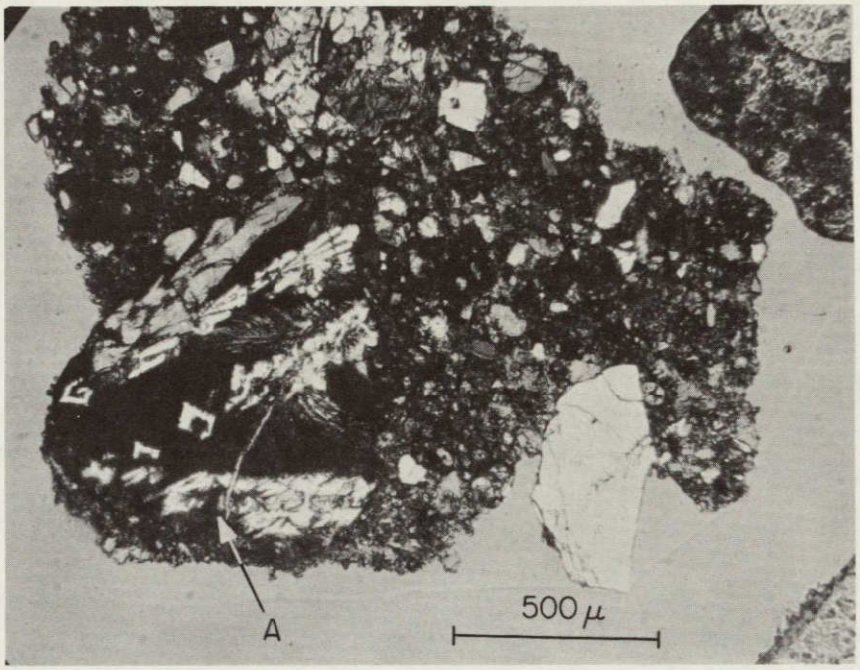

Figure IIE-9. Type 3 microbreccia (102-4), rich in coarse and fine mineral detritus and containing one large fragment of vitrophyric basalt showing quench texture at A. Partially polarized light.

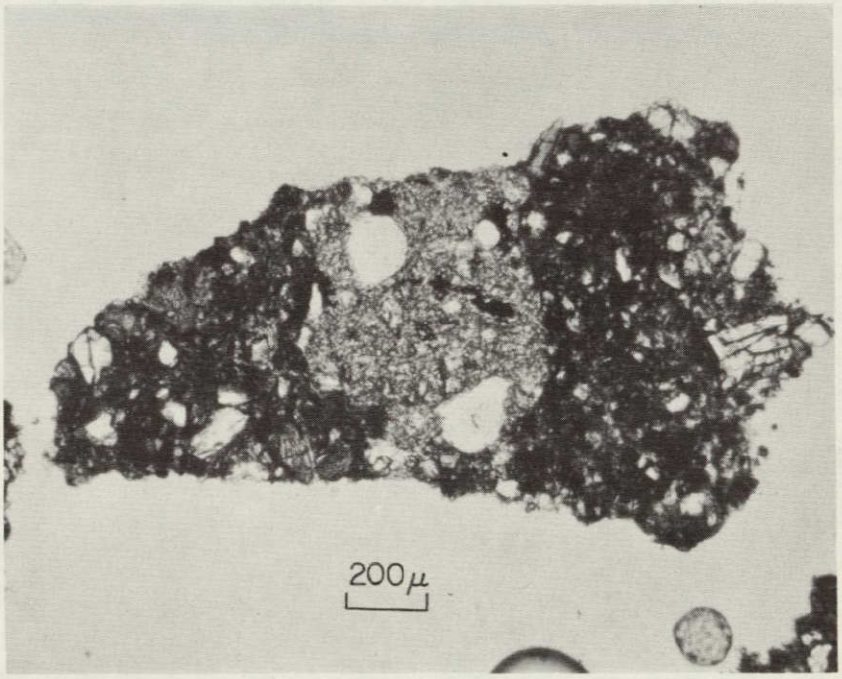

Figure IIE-10. Type 3 microbreccia (102-10), enclosing a large, light-colored fragment of norite. Transmitted light.

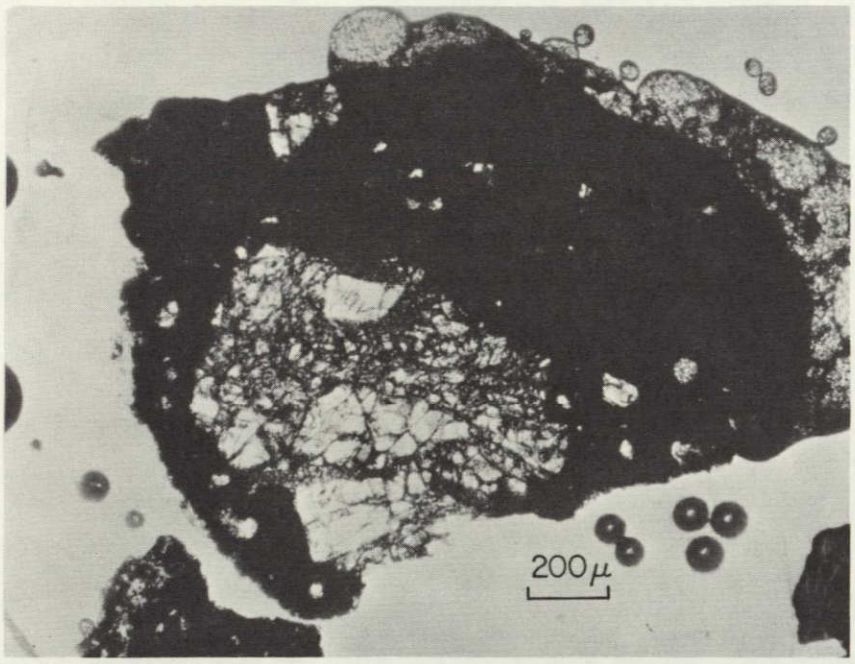

Figure IIE-11. Type 3 dense, dark-colored microbreccia (124-13) including a brecciated anorthositic particle. Such feldspathic fragments are more abundant in the red-brown glasses described in Section IID, but also occur in the darker microbreccias. Transmitted light.

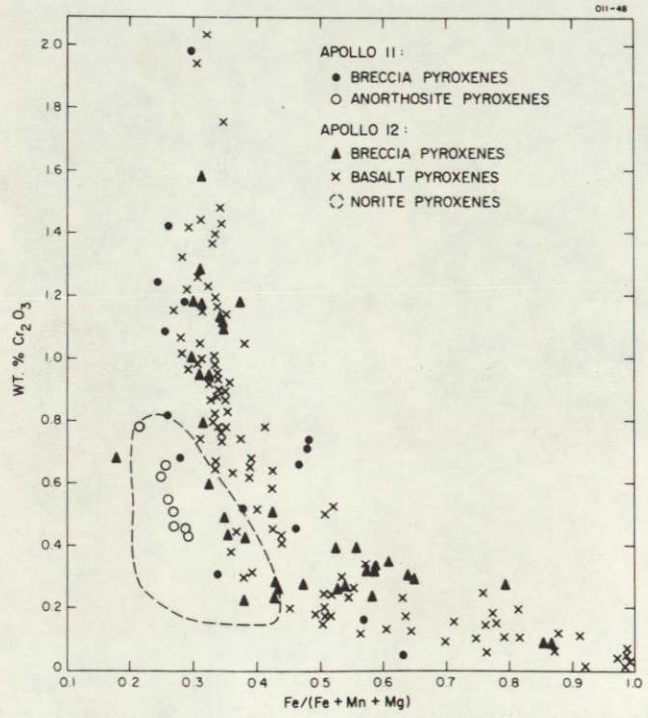

Figure IIE-12. Relationship of Cr content to Fe/(Fe + Mn + Mg) in Apollo 12 breccia pyroxenes (compared with pyroxenes in other lunar materials).

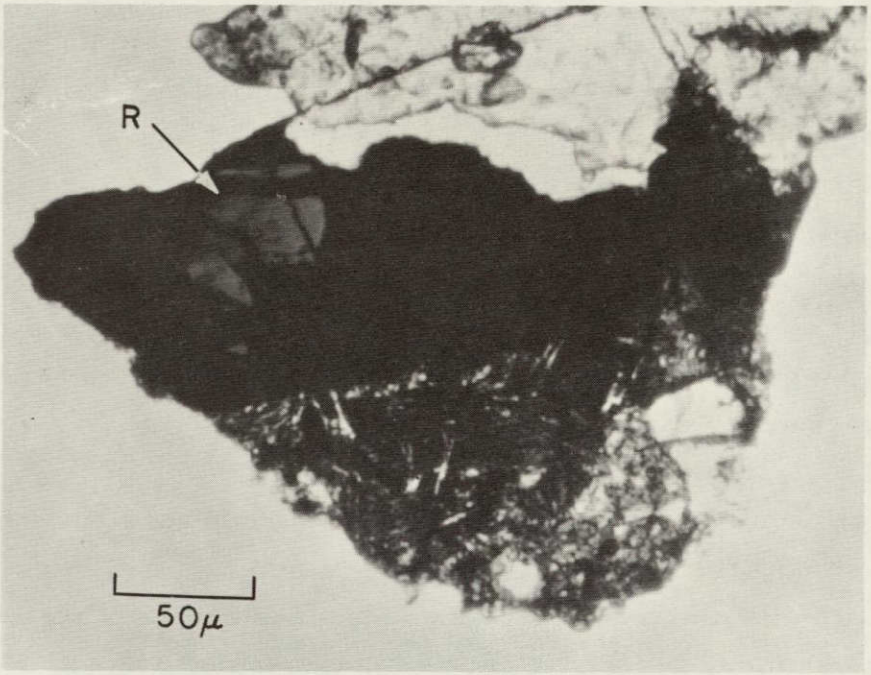

Figure IIE-13a. Niobian rutile (R) occurring as a transparent phase within ilmenite (black), in particle (106-318). Unpolarized transmitted light. The several angular areas of rutile share the same optical orientation and belong to one crystal.

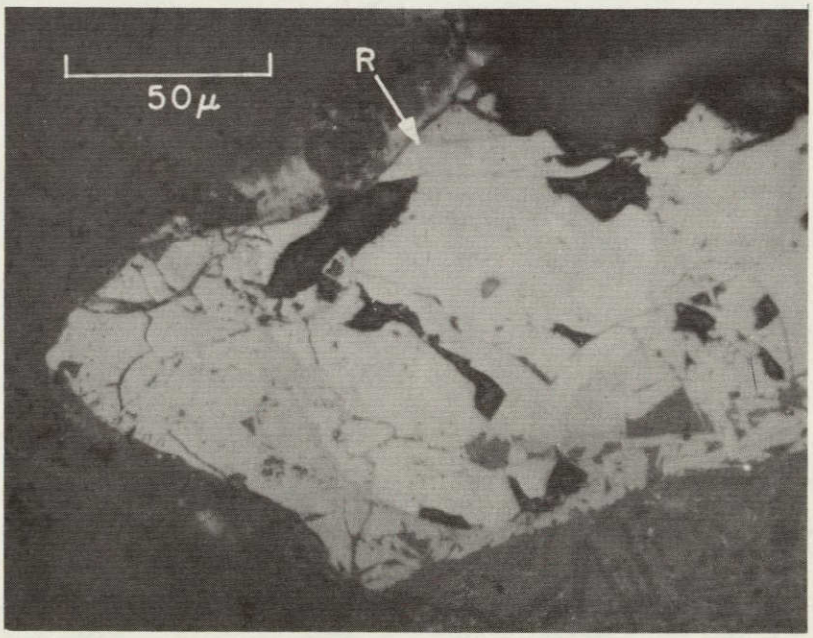

Figure IIE-13b. Rutile (R) within darker gray ilmenite. Reflected light shows a larger area occupied by rutile than can be seen in transmitted light.

examined in Samples 12032 and 12033, in contrast, contain no spherules at all. This would appear to indicate one more significant difference between our two types of lunar soils from the Apollo 12 site. A rapid nonquantitative survey of spherules in our unconsolidated fines seems to bear out the results of the microbreccia count.

Spherules do occur in Samples 12032 and 12033, and their numbers increase as the grain size decreases; yet in total numbers they are fewer than in Samples 12070 and 12001.

The significance of this broad conclusion is beclouded somewhat by the relatively high spherule count in the coarse (1 mm to 1 cm) microbreccias of Sample 12037. We have repeatedly emphasized the nonrepresentative nature of this sample, which was carried in the same sack with Rock 12036. The microbreccias, however, are probably fairly representative samples of the soils of the collecting site, and Sample 12037, with numerous spherules, was taken from the rim of Bench Crater close by the source of Sample 12032, with very few spherules.

Breccia matrix materials

The matrix materials of the three types of microbreccias were analyzed by means of a defocused beam with the electron microprobe. From these analyses (Table IIE-IV), the normative minerals have been calculated, and the results are given in Figure IIE-14 where feldspar + quartz (quarfeloids) are plotted against olivine + pyroxene (mafics). Oxides (ilmenite and chromite) run only 5 to 6% in these analyses and so have been ignored in the preparation of this diagram.

For purposes of comparison, we have also calculated the normative components of bulk samples of the lunar fines and of microbreccias from analyses published by LSPET (1970a), and of the Luna 16 sample, as published by the Tass Agency. These results (Table IIE-V) have also been plotted in Figure IIE-14, where they illustrate the following general relationships:

1. The Apollo 12 contingency sample, No. 12070, is about 11% richer in mafics and 7% poorer in quarfeloids than is Sample 12033, which was collected from the gray streak in the walls of the trench dug on the rim of Head Crater. The Luna 16 bulk soil sample from Mare Fecunditatis falls almost midway in composition between these two Apollo 12 soil samples.

2. The microbreccia matrices analyzed by us show a broad range in composition from 8% more mafic than bulk Sample 12070 to 8% more felsic than bulk Sample 12033. In general, however, the matrices fall in two clusters: one close to a basaltic composition, the other resembling that of the norites described in Section IIB.

3. Their higher content of oxides sets the Apollo 11 fines apart from the Apollo 12 fines and breccias (and apparently also from the one available sample of Mare Fecunditatis).

We conclude that in general the microbreccias of the Apollo 12 samples are chemically indistinguishable from the bulk soils from the same collection sites, and that both are admixed derivatives from two main types of source rocks: the Oceanus Procellarum basalts and the norites from a distant geological formation.

Unconsolidated Soils

Soil samples of particle size smaller than 1 mm are commonly referred to as "fine-fines." Five of our eight soil samples were of this category. The grain-size distributions in these samples are indicated in Section I, Table I-II.

All five samples show a generally poor degree of sorting, although particles finer than 74 μ predominate, making up 48 to 58% by weight excepting in Sample 12037,20, which inherited coarse materials from Rock 12036.

Table IIE-III. Glass spherule count per square millimeter of breccia area.

	mm^2 of breccia	Number of spherules	Spherules/mm^2
Apollo 11			
10085	88,900	26	2.92×10^{-4}
Apollo 12			
12070	34,700	13	3.75×10^{-4}
12001	7,200	1	1.4×10^{-4}
12032	8,600	0	
12033	12,900	0	
12037	35,400	17	4.90×10^{-4}

Table IIE-IV. Microprobe analyses of microbreccia matrix materials.

	Type 1		Type 2		Type 2		Type 3	
	1	2	3	4	5	6	7	8
				Weight percentages of oxides				
SiO_2	40.46	47.79	44.22	45.46	47.08	46.60	45.97	49.01
TiO_2	4.31	2.46	2.28	2.03	2.72	2.71	2.19	2.17
Al_2O_3	11.98	14.06	16.03	12.99	10.80	12.79	18.92	18.04
Cr_2O_3	0.41	0.32	0.14	0.18	0.35	0.47	0.14	0.23
FeO	18.37	15.19	14.44	15.76	17.47	13.81	13.31	10.17
MnO	0.21	0.14	0.12	0.27	0.23	0.28	0.11	0.08
MgO	13.48	9.08	7.43	11.17	8.34	9.42	9.15	10.44
CaO	8.54	9.59	11.12	9.41	10.97	10.46	9.60	10.34
Na_2O	0.29	0.38	0.64	0.68	0.55	0.22	0.75	0.96
K_2O	0.06	0.63	0.34	0.38	0.31	0.24	0.58	0.34
NiO	0.06	0.00	0.00	0.00	0.00	0.03	0 00	0.00
P_2O_5	0.00	0.00	0.00	0.00	0.00	0.00	0.00	0.00
SO_3	0.14	0.21	0.15	0.22	0.34	0 20	0.11	0.08
Total	98.31	99.86	96.91	98.55	99.16	97.23	100.83	101.86
				Norms (weight percentage)				
Fo	14.4	0.0	3.6	7.4	0.0	0.0	5.7	0.0
Fa	12.6	0.0	4.9	7.6	0.0	0.0	5.8	0 0
En	13.7	22.7	14.0	17.7	21.0	24.2	14.5	15.3
Fs	10.9	23.9	17.3	16.5	28.0	21.7	13.2	14.1
Wo	4.7	5.3	6.6	6.5	12.0	8.0	0.4	5.7
Or	0.4	3.7	2.1	2.3	1.9	1.5	3.4	3.6
Ab	2.5	3.2	5.6	5.8	4.7	1.9	6.3	11.0
An	31.8	34.9	41.2	31.8	26.4	34.3	46.3	44.8
Ilm	8.3	4.7	4.5	3.9	5.2	5.3	4.1	4.2
Chr	0.6	0.5	0.2	0.3	0.5	0.7	0 2	0.3
Qtz	0.0	0.9	0.0	0.0	0.2	2.4	0.0	0.9
S	0.1	0.1	0.1	0.1	0.2	0.1	0.1	0.0
				Mole percentages of end members				
Olivine								
Fo	62.3	0.0	58.6	51.6	0.0	0.0	58.9	0.0
Fa	37.7	0.0	41.4	48.4	0.0	0.0	41.1	0.0
Pyroxene								
En	52.2	49 9	49.4	42.6	39.9	50.8	58.0	49.5
Fs	31.8	39.9	34.9	40.0	40.5	34.7	40.4	34.7
Wo	15.7	10.2	15.7	17.4	19.6	14.6	1.5	15.8
Feldspar								
Or	1.0	8.9	5.7	4.2	5.6	3.9	6.0	6.0
Ab	7.6	8.1	15.4	12.1	15.0	5.4	11.9	19.5
An	91.4	83.0	78.9	83.7	79.4	90.7	82.1	74.5

Key

1,2 Matrix of (117-6) (Figure IIE-2).
3,4 Matrix of (124-12) (Figure IIE-6).
5 Matrix of (128-12) (Figure IIE-5).
6 Glass streak in (128-12) (Figure IIE-5).
7 Matrix (102-4) (Figure IIE-9).
8 Matrix (124-13) (Figure IIE-11).

Table IIE-V. Bulk compositions of lunar soil and microbreccia samples (LSPET, 1970a; Tass).

	1 12034 Microbreccia	2 12071 Microbreccia	3 12073 Microbreccia	4 12070 Contingency sample (soil)	5 12033 Soil (light layer) in trench)	6 Luna 16 (soil)
			Weight percentages of oxides			
SiO_2	47.00	42.00	41.00	42.00	41.00	41.70
TiO_2	2.50	3.10	3.10	3.10	2.60	3.39
Al_2O_3	15.10	15.00	15.00	14.00	16.00	15.32
Cr_2O_3	0.35	0.35	0.41	0.41	0.31	0.31
FeO	13.30	16.50	16.70	17.00	16.00	16.80
MnO	0.19	0.18	0.19	0.25	0.23	0.21
MgO	8.40	11.00	11.00	12.00	10.70	8.73
CaO	10.40	11.50	11.50	10.00	11.50	12.20
Na_2O	0.65	0.42	0.50	0.40	0.54	0.37
K_2O	0.42	0.22	0.25	0.18	0.39	0.10
NiO	0.02	0.02	0.04	0.02	0.02	0.00
P_2O_5	0.00	0.00	0.00	0.00	0.00	0.00
SO_3	0.00	0.00	0.00	0.00	0.00	0.00
Total	98.33	100.29	99.69	99.36	99.29	99.13
			Norms (weight percentages)			
Fo	0.0	13.5	15.8	13.3	16.6	8.9
Fa	0.0	13.7	16.3	12.8	17 4	11.5
En	21.3	8.0	5.0	11.2	3.1	9.2
Fs	20.7	7.4	4.6	9.8	3.0	10.7
Wo	6.2	7.8	8.0	5.8	7.1	8.7
Or	2.5	1.3	1.5	1.1	2.3	0.6
Ab	5.6	3.5	4.2	3.4	4.6	3.2
An	37.7	38.3	38.1	36.2	40.4	40.3
Ilm	4.8	5.9	5.9	5.9	5.0	6.5
Chr	0.5	0.5	0.6	0.6	0.5	0.5
Qtz	0.6	0.0	0.0	0.0	0.0	0.0
			Mole percentages of end members			
Olivine						
Fo	0.0	59.0	58.0	60.0	58.0	44.0
Fa	0.0	41.0	42.0	40.0	42.0	56.0
Pyroxene						
En	50.0	39.0	32.0	47.0	27.0	32.0
Fs	3.7	28.0	23.0	32.0	20.0	38.0
Wo	13.0	33.0	45.0	21.0	53.0	30.0
Feldspar						
Or	5.5	3.0	3.4	2.6	4.9	1.4
Ab	13.0	9.0	10.0	9.0	10.0	7.3
An	82.0	88.0	86.0	88.0	85.0	91.0

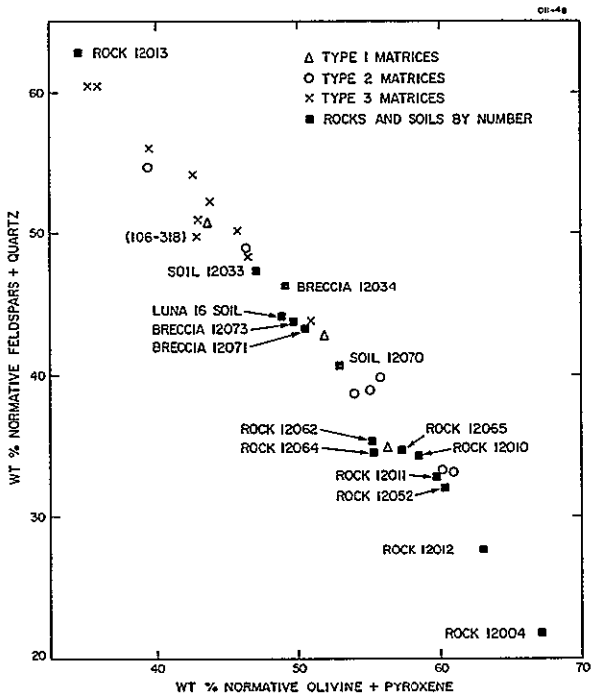

Figure IIE-14. Normative compositions of microbreccia matrices and bulk samples of rocks and soils from the Apollo 12 and Luna 16 missions. (106-318) is associated with Nb rutile.

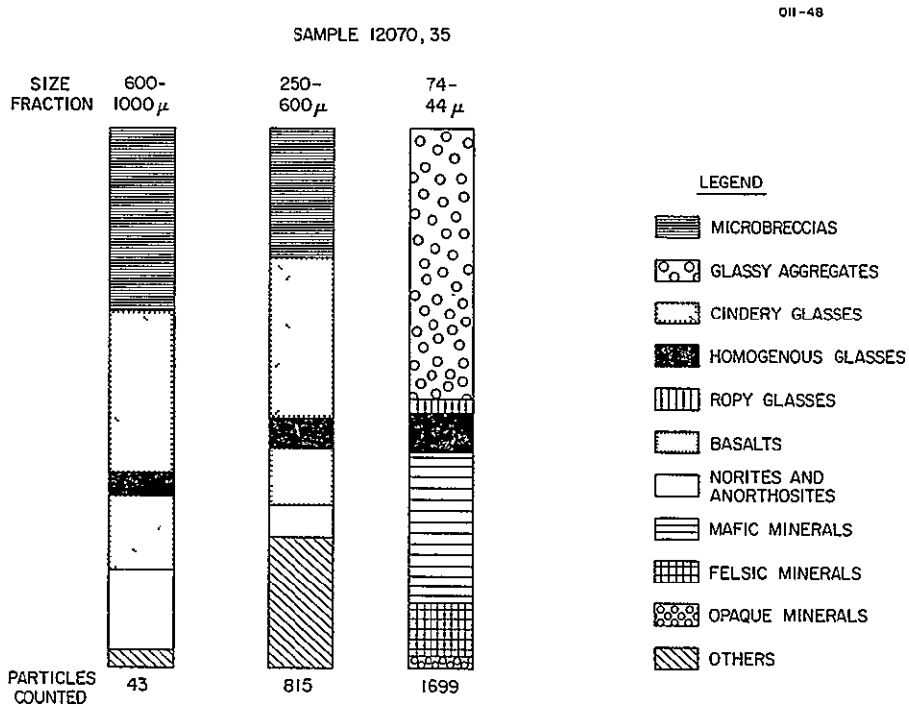

Figure IIE-15. Rock and mineral constituents of three size fractions of Soil Sample 12070.

In the soils, particle character varies, predictably, with size. Virtually 100% of the coarser grains are rock fragments or welded aggregates: basalts, norites, microbreccias, and cindery or ropy glasses. The few exceptions include large mineral grains, glass shards, one or two glass spherules (see the minisun, Figure IID-14), and a meteorite fragment (carbonaceous chondrite, Figure IIF-1). In the finer than 74-μ range, rock fragments are all but absent, being replaced by fine-grained glassy aggregates resembling the matrix materials of the Type 3 microbreccias. Mineral and glass fragments are also abundant; glassy spherules, common but minor.

This change in character with size is illustrated in Figure IIE-15, which shows particle types in three fractions of Sample 12070,35. Basalt fragments make up 14% of the 0.6- to 1-mm fraction and 10% of the 0.3- to 0.6-mm fraction. No recognizable basalts are present in the < 0.074-mm range, but 40% of this fraction consists of broken mineral grains in the following proportions: 29% pyroxene + olivine, 9% plagioclase, 2% opaques. Recalculated to 100%, these proportions equal about 72% pyroxene + olivine, 22% plagioclase, and 5% opaques, a fair equivalent to a mafic basalt.

The "aggregates," which make up 51% of this fraction, are small, shapeless clumps that are brownish to greenish to almost opaque, and essentially isotropic, with mean indices of refraction ranging from about 1.610 to 1.630. They appear to be largely glass with numerous tiny included mineral grains. X-ray films of these aggregates register either a weak pyroxene pattern or no pattern at all. We assume from their optical similarities that the aggregates are small pieces of the matrix materials of Type 3 microbreccias.

Figure IIE-16 shows the relative proportions of particle types as they occur in the 44- to 74-μ fractions of our five samples. The evidence recognized in the coarser fractions, that these samples represent two contrasting compositions of lunar soils (see Section I, Figure I-16), is present but less obvious in the fine fractions. Glassy aggregates make up 38 to 50% of the 44- to 74-μ fraction of Samples 12070,35 and 12001,71 but only 30 to 33%

of Samples 12032,27 and 12033,23. The latter two, however, contain 3 to 16% of the red-brown, ropy glass, described in Section IID, whereas the other two samples contain only about 2%.

Magnetic fractions

The intermediate-size fractions (74 to 600 μ) of each of our samples were separated by means of a hand magnet. The magnet we chose is too weak to attract ilmenite, yet a substantial proportion of each fraction clung to it.

The magnetic particles proved to be mainly those cindery glasses that contain tiny grains and spherules of nickel-iron, as described in Section IID. Metal grains also occur in basalts and norites, but generally in too small a proportion for these rock fragments to be picked up by our magnet.

Table IIE-VI shows the percentages, by weight, of magnetic materials in each of the three size fractions of our samples. In all three size ranges, Samples 12070 and 12001 are richer in magnetic particles than are the other three samples. This is one more piece of evidence pointing to the distinction between our two bulk samples of the maria regolith and the two samples that included light-colored materials of more specialized origin.

Zircon in the unconsolidated lunar soils

Zircon grains have been recovered from Samples 10084 (Apollo 11) and 12070 and 12037 (Apollo 12). In all cases, the zircon was found in non-magnetic fractions that had sunk in clerici solution of density 3.8 g/cc.

The zircons occur in three colors: brown, colorless, and pink. Their optical properties and unit-cell parameters are given in Table IIE-VII.

The brown zircon from Tranquillity Base is partially metamict, as shown by the low indices of refraction and the enlarged unit cell. After being x-rayed, our one grain of this material was split into two pieces, one

of which was mounted for analysis on the electron probe (Table IIE-VIII), while the other was sent to Dr. R. L. Fleischer for fission-track counting. He reported a track density too great to resolve ($>10^8$/cm) and a uranium content of 167 ± 19 ppm.

The colorless zircon from Apollo 12 Sample 12070 is nonmetamict. The uranium content (Fleischer, personal communication) is < 24 ppm (90% certainty).

Sample 12037 yielded three grains of lustrous pink zircon. The largest of these measured about 140 × 140 × 160 μ. The other two were irregular in shape and measured about 120 μ in largest diameter (Figure IIE-17). Unit cells measured on each grain show them to be slightly enlarged to different degrees. The color, as viewed in photographs, was pronounced by Dr. Leon T. Silver (personal communication) to be the typical "hyacinth" characteristic of zircons having low uranium contents and occurring in terrestrial Precambrian rocks. No uranium analyses or fission-track counts have been made on the lunar hyacinth zircons.

Zircon occurs in situ as an accessory mineral in the norites described in Section IIB (Figure IIB-20) and in the siliceous rocks represented by Specimen 12013 (Drake et al., 1970). In the norites, zircon is an interstitial phase that apparently crystallized late, at metamorphic temperatures. The crystals are irregular in shape, and they range in size from about 60 to 200 μ. These zircons are typically rich in tiny inclusions of other minerals.

The zircon grains found in the soils contain few, if any, inclusions. The large size and equant shape of at least one of the pink fragments suggest a rather coarse-grained source rock in which zircon lacks inclusions. Of the two lunar rocks known to contain zircon, however, the norites with their large, if irregular, crystals would appear the more likely parent material.

Apollo 12 fragment (135-1) is a microbreccia of highly specialized texture and composition. It was found in the coarse fines (>1 mm fraction) of Sample 12033, which was collected from the light-gray layer at a depth of 15 cm in the trench dug in the north rim of Head Crater.

A macroscopic photograph is shown in Figure IIE-18; the particle is a rather friable lump of fine-grained soil in which are embedded numerous black spherules. In thin section, by transmitted light, the particle is very dark and nearly opaque (Figure IIE-19). By use of a substage condenser, however, enough light comes through to show an abundance of spherules and broken shards of very deep red. By reflected light, the texture is clearly delineated (Figure IIE-20). The particle is a closely packed agglomerate of spherules, ranging in diameter from 20 to 110 μ, and angular detritus. Well over 90% of the material appears to be glass, though a few of the particles contain quenched crystallites of ilmenite (Figures IIE-21a and b). A few fragments of pyroxene and of olivine are also present.

Electron-microprobe analyses of three spherules and one glass shard gave the results listed in Table IIE-IX. The most striking chemical characteristic of this material is the consistently high content of titanium (16.6% TiO_2) and of normative ilmenite (31.5% ilm). These values are higher by a factor of 1.5 to 2 than those for the average basalts from Mare Tranquillitatis. Also of interest is the low content of normative feldspar (11 to 14%), which ranges in molecular proportions from Or_{1-18}, Ab_{0-10}, and An_{81-100}.

This microbreccia clearly corresponds to a rock type that has not yet been discovered among the crystalline lithologies in the lunar soils. The texture indicates melting and fragmentation at high temperatures, but the overall uniformity of composition suggests that little or no mixing of extraneous matter has occurred.

Particle (135-1) brought to mind a fragment of similar texture we observed in Apollo 11 Sample 10084 (Wood et al., 1970; Plate 1, F). This fragment (Figure IIE-22) is transluscent and brightly colored. Most of the spherules and many fragments in the groundmass are red orange, but the large spear-shaped particles in Figure IIE-23 and a few of the spherules are lighter yellow. These colors reflect markedly different chemical compositions, as shown in Table IIE-X.

Microprobe analyses show that chemically the yellow spherules and "spear-shaped" inclusion of fragment (50-1) are indistinguishable from some of the fine-grained Apollo 11 basalts. The more abundant bright orange spherules match the compositions of numerous Apollo 11 glasses of the same color, but do not match those of Mare Tranquillitatis basalts.

The normative compositions of glasses from fragments (135-1) and (50-1) are plotted on the triangular diagram of Figure IIE-24, where they are compared with some of the lunar basalts. On this diagram it is readily seen that fragment (135-1) has a unique composition and that fragment (50-1) has a composition that is unusual for its own environment. Texturally, both particles are spherule-packed in a manner reminiscent of chondritic meteorites, an observation we will discuss in Section IIIE.

Table IIE-VI. Percentage by weight of magnetic particles in three size fractions of Apollo 12 soil samples.

Grain size (μ)	12032,27	12033,23	12070,35	12001,71	12037,20
250-600	15%	6%	19%	19%	10%
149-250	10	22	29	33	9
74-149	17	6	29	20	9

Table IIE-VII. Optical properties and unit cell parameters of zircon from three Apollo soil samples.

	Optic	Refractive indices[a]	Color	Unit-cell dimensions (Å)	U Content[b]
Apollo 11 Soil 10084	Biaxial +, 2V ~ 5°	ϵ = 1.853 ω = 1.838	Brown	a = 6.663 ± 0.005 c = 6.080 ± 0.006	167 ± 19 ppm
Apollo 12 Soil 12070, 35	Uniaxial +	ϵ = 1.990 ω = 1.930	Colorless	a = 6.606 ± 0.001 c = 5.991 ± 0.002	< 24 ppm
Apollo 12 Soil 12037, 20					
Grain 1	Uniaxial +	ϵ = 1.980 ω = 1.925	Pink	a = 6.616 ± 0.001 c = 6.003 ± 0.005	
Grain 2			Pink	a = 6.626 ± 0.001 c = 6.006 ± 0.002	
Grain 3			Pink	a = 6.635 ± 0.001 c = 5.989 ± 0.005	
Standard Nonmetamict Zircon[c]	Uniaxial +	ϵ = 1.963 ω = 1.923	Colorless	a = 6.604 c = 5.979	

[a] ± 0.005.

[b] R. L. Fleischer (personal communication).

[c] See Swanson, Fuyat, and Ugrinic in NBS Circular 539, vol. 4, p. 69, 1955.

Table IIE-VIII. Electron-microprobe analysis of zircon from Apollo 11 Sample 10084.

Brown zircon[a] Sample 10084		Stoichiometric zircon
ZrO_2	66 ± 1%	67.2%
SiO_2	31 ± 2	32.8
HfO_2	1 ± 0.3	

[a]Also detected:

Al ≤ 0.2%, P ≤ 0.01%.

Not detected:

Fe, Ca, Ti, U, Th, REE.

Table IIE-IX. Microprobe analyses of representative spherules and shards in fragment (135-1).

	Spherule no. 2	Spherule no. 3	Spherule no. 4	Shard no. 5
	Weight percentages of oxides			
SiO_2	32.80	33.67	33.81	33.38
TiO_2	16.76	16.55	16.03	16.02
Al_2O_3	4.43	4.53	4.91	3.90
Cr_2O_3	0.80	0.84	0.97	0.76
FeO	23.97	24.43	23.92	23.76
MnO	0.24	0.31	0.26	0.36
MgO	13.48	13.87	12.51	13.42
CaO	6.41	5.14	6.30	6.25
Na_2O	0.05	0.01	0.00	0.13
K_2O	0.03	0.42	0.08	0.08
NiO	0.06	0.05	0.00	0.01
P_2O_5	0.00	0.00	0.00	0.00
SO_3	0.13	0.60	0.09	0.05
Total	99.16	100.42	98.88	98.12
	Norms (weight percentages)			
Fo	7.9	7.7	4.3	7.6
Fa	4.2	4.3	2.6	4.3
En	22.7	23.7	25.4	23.3
Fs	10.9	12.0	13.9	12.0
Wo	8.4	6.0	7.7	9.0
Or	0.2	2.5	0.5	0.5
Ab	0.4	0.0	0.0	1.1
An	11.9	11.2	13.3	10.0
Ilm	32.1	31.5	30.8	31.0
Chr	1.2	1.2	1.4	1.2
S	0.1	0.2	0.0	0.0
	Normative mineral formulas			
Olivine				
Fo	73.2	72.2	70.6	71.9
Fa	26.8	27.8	29.4	28.1
Pyroxene				
En	59.2	62.4	59.6	58.0
Fs	21.7	24.0	24.9	22.7
Wo	19.0	13.7	15.5	19.4
Feldspar				
Or	1.4	18.2	3.5	4.1
Ab	3.6	0.0	0.0	10.2
An	95.0	81.8	96.5	85.7

Table IIE-X. Microprobe analyses in Apollo 11 fragment (50-1).

	Orange spherule 2	Orange spherule 6	Orange spherule 7	Yellow spherules 11	Matrix
			Weight percentages of oxides		
SiO_2	37.93	38.31	38.25	42.26	37.52
TiO_2	10.28	10.16	10.59	8.54	9.35
Al_2O_3	5.34	5.47	5.28	11.41	7.41
Cr_2O_3	0.55	0.60	0.68	0.33	0.63
FeO	23.11	22.79	22.65	16.44	18.11
MnO	0.36	0.31	0.30	0.25	0.37
MgO	14.64	14.06	13.53	7.63	14.46
CaO	7.12	7.37	7.28	11.25	11.24
Na_2O	0.38	0.30	0.17	0.72	0.27
K_2O	0.06	0.03	0.05	0.10	0.10
NiO	0.00	0.00	0.00	0.03	0.02
P_2O_5	0.00	0.00	0.00	0.00	0.00
SO_3	0.05	0.09	0.12	0.00	0.39
Total	99.82	99.49	98.90	98.96	99.87
			Norms (weight percentages)		
Fo	13.0	10.4	7.4	0.0	17.6
Fa	10.1	8.2	5.8	0.0	9.7
En	18.0	20.4	23.5	19.2	11.1
Fs	12.7	14.6	16.8	16.5	5.5
Wo	9.5	9.7	9.6	11.9	15.5
Or	0.4	0.2	0.3	0.6	0.6
Ab	3.3	2.6	1.5	6.1	2.3
An	12.7	13.6	13.7	27.9	18.8
Ilm	19.5	19.4	20.3	16.4	17.8
Chr	0.8	0.9	1.0	0.5	0.9
Qtz	0.0	0.0	0.0	0.8	0.0
			Normative mineral formulas		
Olivine					
Fo	65.1	64.7	64.8	0.0	72.5
Fa	34.9	35.3	35.2	0.0	27.5
Pyroxene					
En	50.2	51.1	52.8	45.7	38.6
Fs	26.9	27.9	28.7	29.8	14.7
Wo	22.9	21.0	18.5	24.5	46.7
Feldspar					
Or	2.1	1.1	1.9	1.7	2.7
Ab	21.2	16.4	10.0	18.6	11.1
An	76.7	82.5	88.1	79.7	86.1

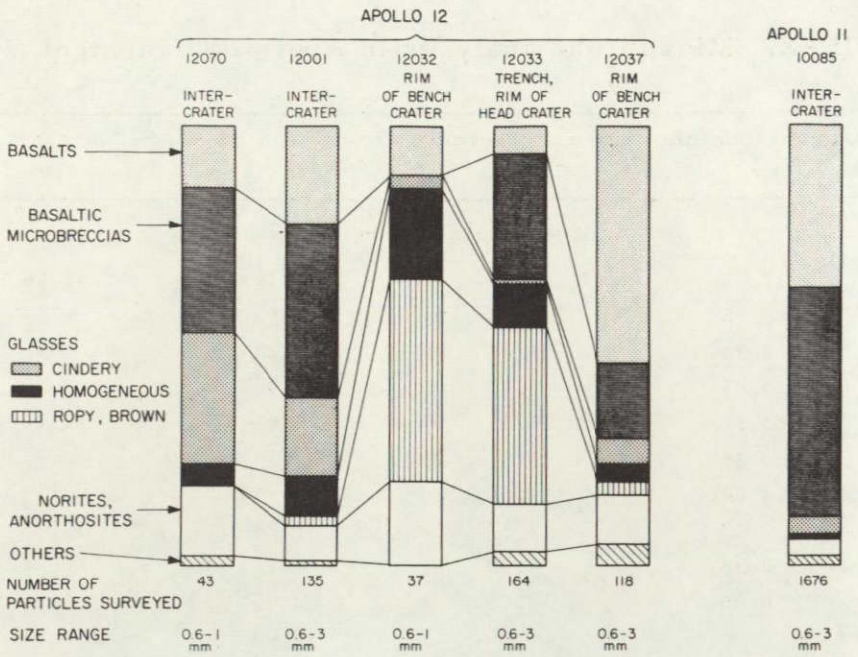

Figure IIE-16. Varying proportions of particle types in the 44- to 74-μ size fractions of five Apollo 12 soil samples.

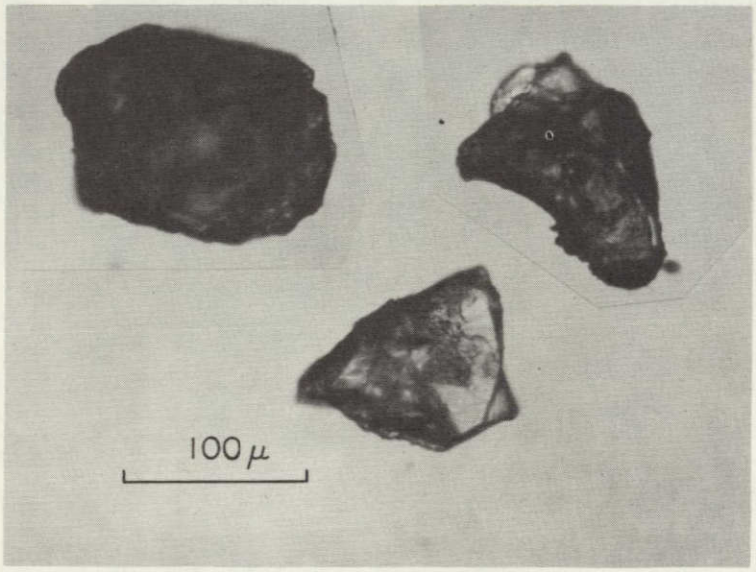

Figure IIE-17. Detrital grains of clear, pink zircon from Sample 12037. Photomicrographs of grains in immersion oil, index of refraction = 1.800, by transmitted light.

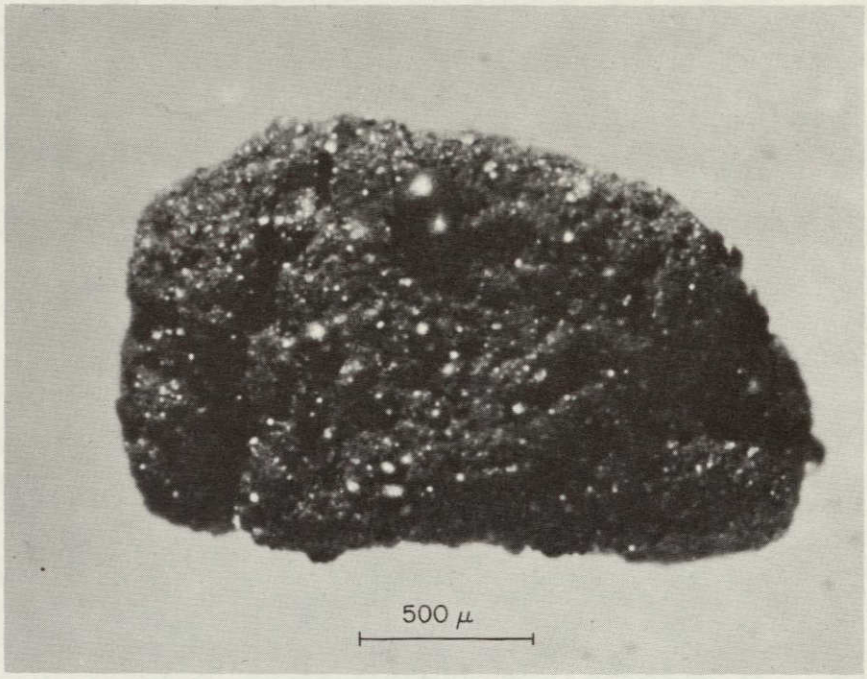

Figure IIE-18. Fragment (135-1). A unique microbreccia from Sample 12033, consisting of dark red glass spherules embedded in a groundmass of glass shards of the same color and composition.

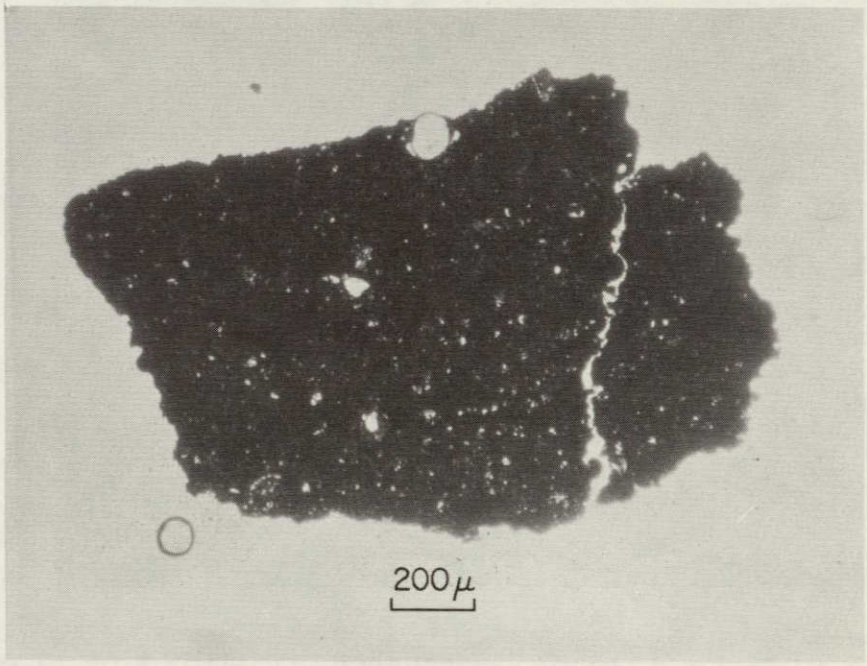

Figure IIE-19. Polished thin section of fragment (135-1) by transmitted light.

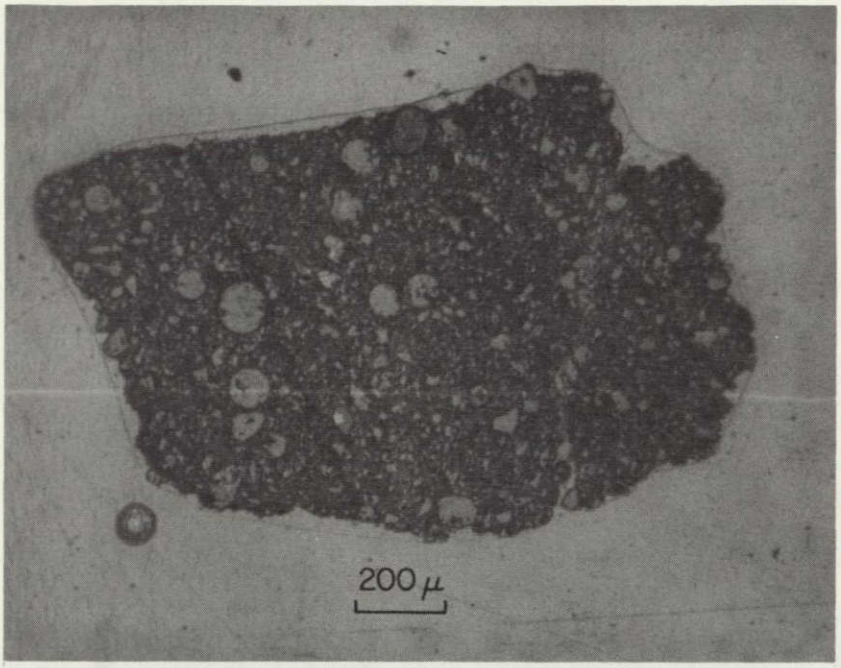

Figure IIE-20. Polished thin section of fragment (135-1) by reflected light. The dark, diagonal streaks, which suggest layering, are grinding scratches.

Figure IIE-21a. Fragment (135-1). Quenched crystallites of ilmenite in a glassy matrix. Reflected light.

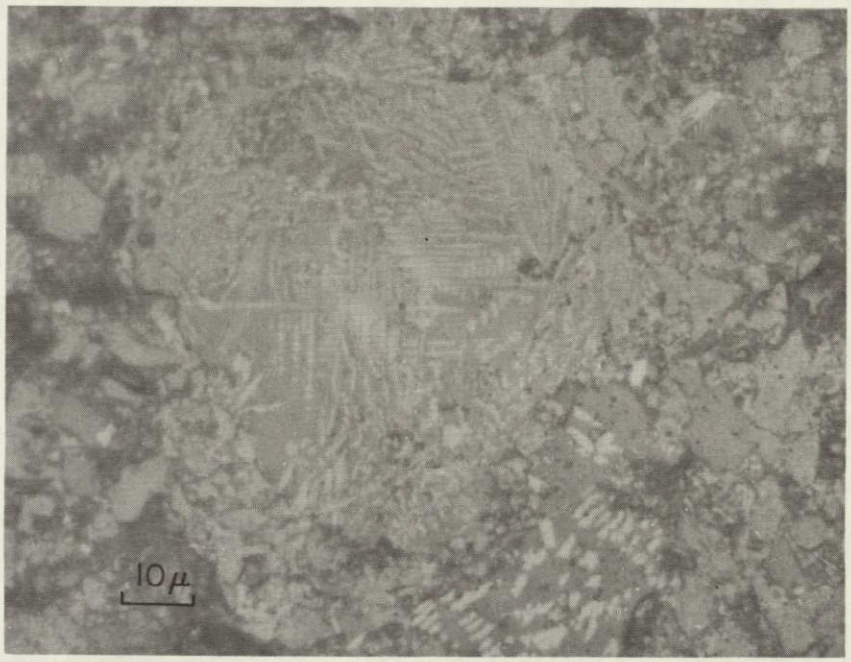

Figure IIE-21b. Fragment (135-1). Quenched crystallites of ilmenite in glass matrix. Reflected light.

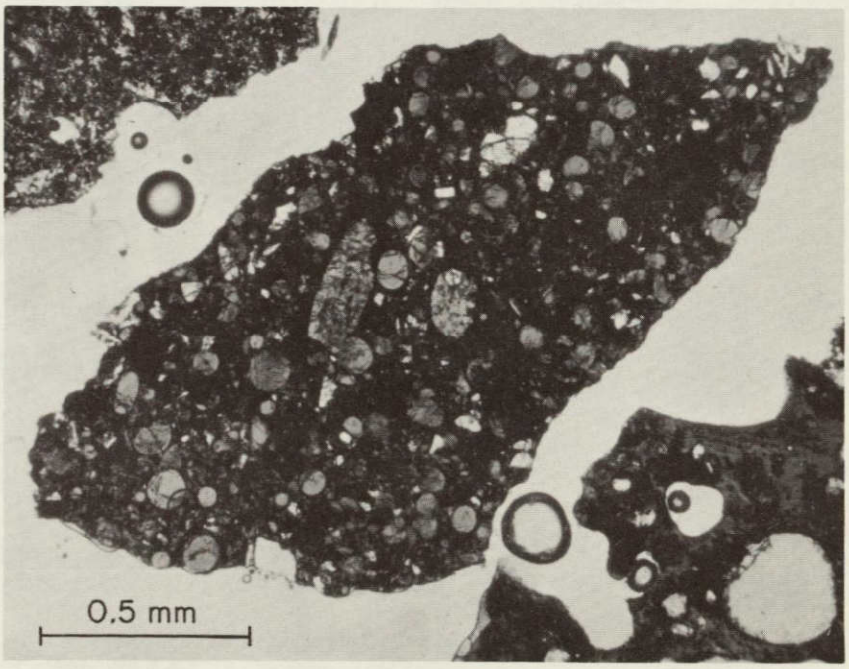

Figure IIE-22. Apollo 11 fragment (50-1). A compact aggregate of orange and yellow glass spherules embedded in orange glass shards and minute fragments of feldspar, ilmenite, and pyroxene. Transmitted light.

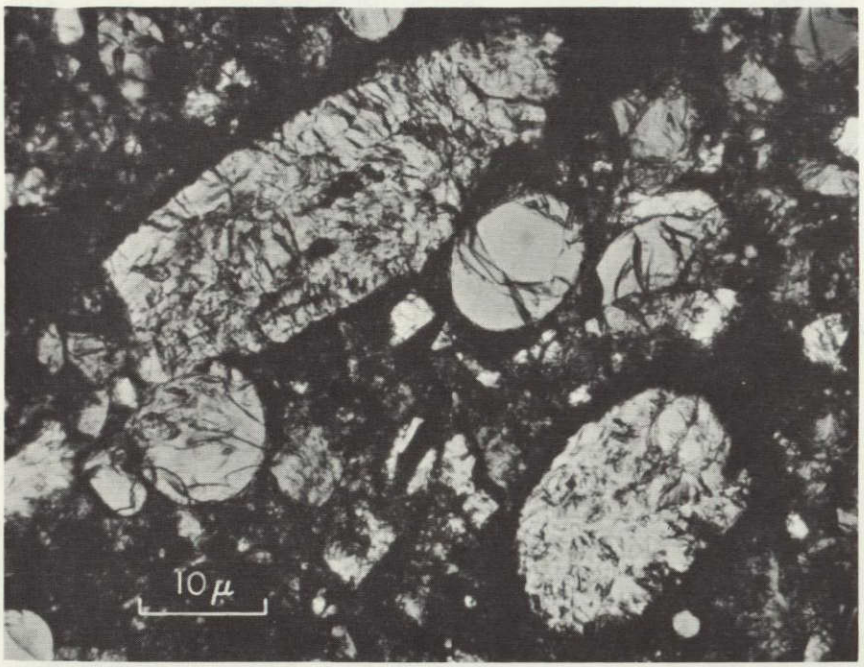

Figure IIE-23. High magnification view of spherules and matrix of fragment (50-1). Transmitted light.

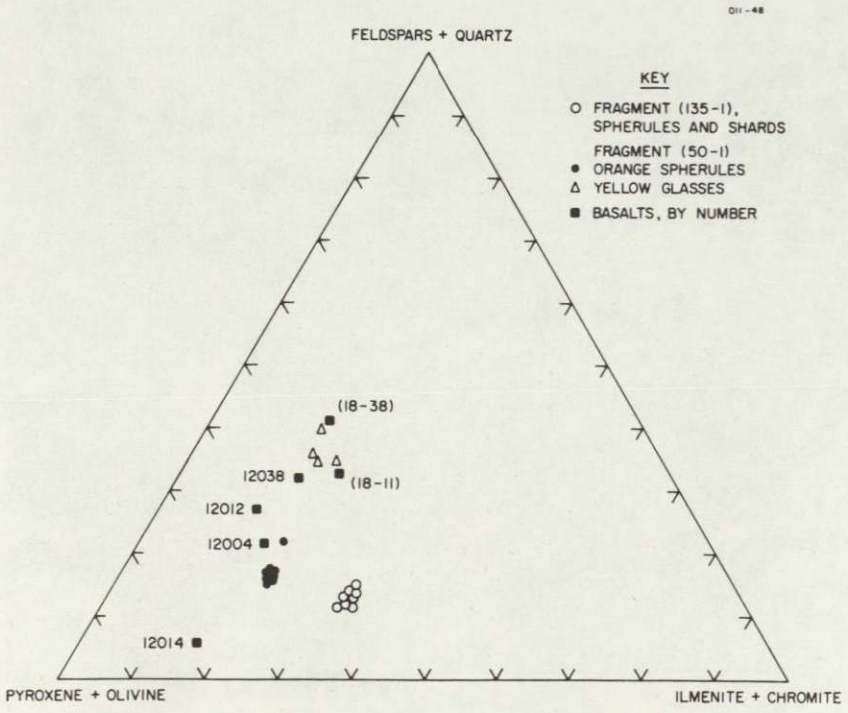

Figure IIE-24. Triangular diagram showing normative compositions of glasses in Apollo 12 fragment (135-1), Apollo 11 fragment (50-1), and six representative Apollo 11 and Apollo 12 basalts. The norms for Apollo 12 rocks were calculated from bulk analyses published in LSPET (1970a); (18-1) and (18-38) are basalt fragments from the Apollo 11 soil (analyses from Table IIB-IX, Wood et al., 1970).

IIF. Meteorites

Many investigators found metallic spherules and fragments in Apollo 11 glasses and breccias. Most of these metal particles contained more than a few percent Ni, which was taken as evidence of their meteoritic origin, since iron indigenous to the Apollo 11 basalts contained only 0.5% Ni. Subsequently, however, Reid, Meyer, Harmon, and Brett (1970) observed that metal in the Apollo 12 basalts contains substantial amounts of Ni (up to 38%), so it appears that Ni abundance alone does not prove a meteoritic origin. The Ni and Co levels taken together are a more reliable criterion, since metals indigenous to the lunar basalts contain more Co than meteoritic alloys (Reid et al., 1970). On this basis, Goldstein and Yakowitz (1971) concluded that most of the metal in the Apollo 12 soil samples originated on the Moon.

Although microscopic particles of lunar and/or meteoritic metals are relatively abundant in the lunar soil, coarser fragments of recognizable meteorite debris are very scarce. Fragments of iron meteorites have been reported by Goldstein, Henderson, and Yakowitz (1970) and by Quaide and Bunch (1970). Wood et al. (1970) found a millimeter-sized fragment of a mesosiderite. The paucity of recognizable meteorite fragments is not surprising in the light of hypervelocity impact studies (Gault, Shoemaker, and Moore, 1963), which have shown that in a single event the mass of excavated material is between 10^3 and 10^4 times the mass of the projectile. Moreover, a large proportion of the projectile is so heavily shocked (if not melted or vaporized) that it can no longer be recognized. This is particularly true of the silicate fraction of chondritic meteorites, because most material surviving the impact would be melted or pulverized and, once incorporated into the regolith, would be difficult to distinguish from fragments of lunar rocks.

Carbonaceous Chondrite Fragment (112-6)

In spite of these difficulties, we found a fragment of a carbonaceous chondrite in our sample of coarse fines from 12037 (Figure IIF-1). The particle was quite dark in color, but displayed brassy-colored outcroppings of a sulfide mineral. It was attracted to a hand magnet and measured about 3 mm long and 1.5 mm wide. As viewed in thin section, the particle is largely opaque but contains yellow-orange transparent patches. The composition of these patches corresponds to that of pyroxene (see microprobe analysis in Table IIF-I). The Fe content is higher than that in pyroxene in the Type II carbonaceous chondrites investigated by Wood (1967a), who found that virtually all the low-Ca pyroxene contained less than 10 mole % $FeSiO_3$. By polarized light, these transparent regions display a mosaic texture very much like that described by Carter, Raleigh, and DeCarli (1968) in artificially shocked olivine and pyroxene (Figure IIF-2). It appears that these yellow regions are pyroxene chondrules that have been shocked, presumably during the impact of this meteorite upon the Moon. Type II carbonaceous chondrites are characterized by the presence of chondrules, though most of these are rich in olivine, as contrasted with the pyroxene chondrules found in the lunar specimen. The chondrules in the lunar carbonaceous chondrite are shocked to a much greater degree than those in terrestrial collections; this is undoubtedly because our lunar carbonaceous chondrite struck the Moon's surface with its full cosmic velocity (~15 km/sec), whereas terrestrial chondrites were gradually decelerated by the atmosphere before landing on the Earth's surface.

By reflected light (Figure IIF-3), two principal opaque minerals are visible: magnetite, occurring as spherules or clusters of spherules; and iron sulfide, present as squarish grains. The Fe, Ni, and Mg were measured by microprobe analysis in a number of different magnetite spherules; results are shown in Table IIF-II. (Sums range from 100% to 103.7%. This may be due to analytical error, but it may also reflect a slight departure from the Fe^{+3}/Fe^{+2} ratio of 1 that was assumed in the calculation of the amount of oxygen present.) The low Mg and low Ni (except, for the latter, in two cases) are characteristic of the magnetite in carbonaceous chondrites.

The Ni content of the sulfide was measured in 20 randomly selected grains; the distribution is shown in Figure IIF-4. The grains with more than 5% Ni are probably pentlandite, $(Fe, Ni)_9S_8$; microscopically, these grains display slightly higher reflectivity than does troilite, and they appear to be isotropic. However, they are also much smaller than the Ni-poor sulfide grains, so positive identification is difficult. The Ni-poor grains are troilite; most (11 of the 20 points measured) contain less than 1.0%. The wide range of Ni contents in the iron sulfide phases of this chondrite is characteristic of Type II carbonaceous chondrites (Wood, 1967b), although the predominance of low Ni troilite is unusual.

The Ni content of the opaque matrix was measured by microprobe at 10 points. (Corrections were applied by assuming an olivine composition, Fo_{90}, for the matrix.) Ni levels in the range 0.8 to 3.2% were found; 7 of the 10 points had Ni contents in the range 1 to 2%. This is in the range found by Wood (1967b) for Type II carbonaceous chondrites. We also attempted to measure the abundance of carbon in the matrix, but the specimen had been carbon coated and it was not certain that all the carbon could be removed from the uneven surface of the matrix by polishing.

Discussion

Our meteorite fragment is similar to Type II carbonaceous chondrites in that it contains:

1. High-temperature mineral (pyroxene) in "chondrules."
2. Magnetite low in Ni.
3. Some iron sulfide rich in Ni.
4. An opaque, fine-grained, Ni-rich groundmass.

It is dissimilar in certain details:

1. Pyroxene richer in Fe than other Type II carbonaceous chondrites.
2. Absence of olivine chondrules.
3. Exceptional abundance of troilite.
4. Very low Ni content (< 1.0%) of most of the troilite.

We conclude that the meteorite is a Type II carbonaceous chondrite, but that it is different from those examined heretofore in terrestrial collections.

It is interesting that of over 2000 fragments of coarse fines examined in this laboratory (Apollo 11 and 12), only 2 have been recognizable as stony meteorites. Of these two, one is a relatively friable carbonaceous chondrite, and the other, which had been impact melted, seems more likely to have been at the outset a carbonaceous chondrite than anything else (Wood et al., 1970). Although the statistics for meteoritic debris on the Moon are poor, it is beginning to appear that carbonaceous chondrites may be much more abundant in the solar system than is indicated by the proportion of meteorite types among terrestrial falls.

Table IIF-I. Pyroxene compositions in carbonaceous chondrite fragment (112-6)

	Compositions of five selected pyroxenes				
MgO	31.1	26.6	32.8	31.5	30.9
Al_2O_3	4.3	5.4	4.0	4.0	4.6
SiO_2	52.4	50.7	52.3	51.3	51.1
CaO	0.3	0.3	0.2	0.3	0.3
Cr_2O_3	0.8	2.9	0.7	1.0	0.8
FeO	10.0	12.1	9.7	9.8	10.0
NiO	0.0	0.0	0.0	0.0	0.0
Sum	98.9	98.1	99.6	97.9	97.7
En[a]	84.3	79.1	85.4	84.6	84.2
Fs	15.2	20.3	14.2	14.8	15.3
Wo	0.5	0.6	0.4	0.6	0.5

[a]Mole percentages of the pyroxene end members enstatite (En), ferrosilite (Fs), and wollastonite (Wo), recalculated to 100%.

Table IIF-II. Composition of magnetite in carbonaceous chondrite fragment.

	O[a]	Fe	Mg	Ni	Sum
1	27.6	72.5	0.0	0.0	100.2
2	28.4	74.4	0.1	0.0	103.0
3	28.2	73.9	0.1	0.0	102.3
4	28.5	74.4	0.0	0.3	103.4
5	28.7	74.8	0.2	0.0	103.7
6	28.3	73.6	0.4	0.0	102.4
7	28.1	73.4	0.2	0.0	101.7
8	28.4	74.0	0.2	0.3	103.0
9	28.2	73.4	0.4	0.0	102.0
b	27.5	72.5			100.0

[a]Oxygen was calculated by stoichiometry by assuming that Mg and Ni were bivalent and that Fe was partitioned equally between bivalent and trivalent sites.

[b]Stoichiometric magnetite.

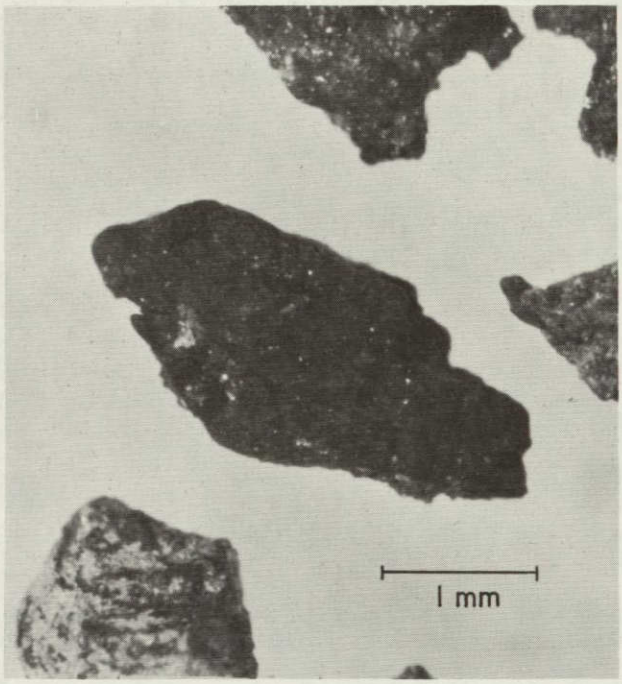

Figure IIF-1. Macroscopic photograph of the carbonaceous chondrite fragment found in Sample 12037, (112-6). The bright specks are grains of iron sulfide.

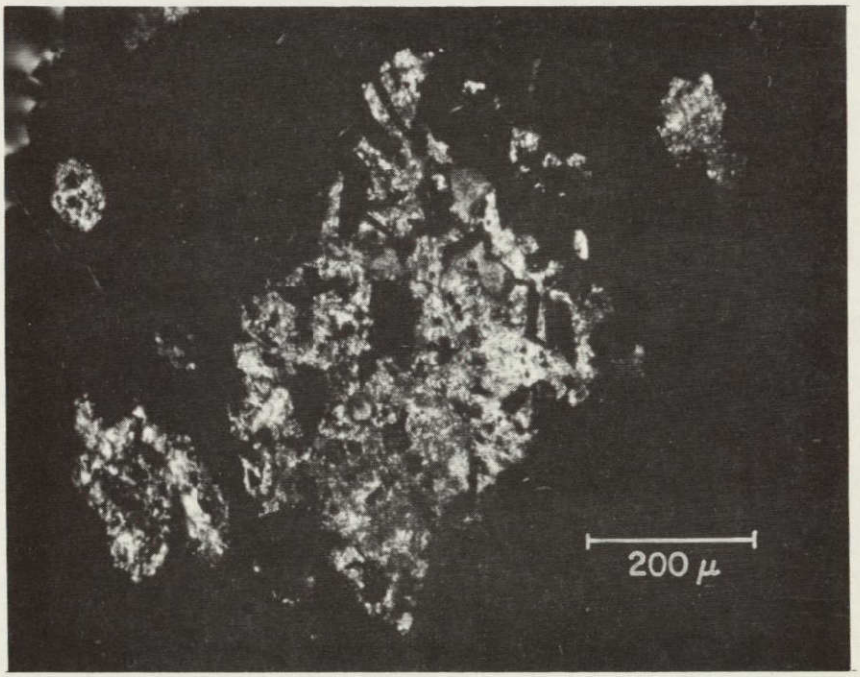

Figure IIF-2. Photomicrograph in transmitted light with crossed polars of pyroxene in the carbonaceous chondrite fragment. The patchy extinction is strikingly similar to the mosaic texture observed by Carter et al. (1968) in artificially shocked pyroxene. The black areas consist of either the opaque groundmass or opaque minerals.

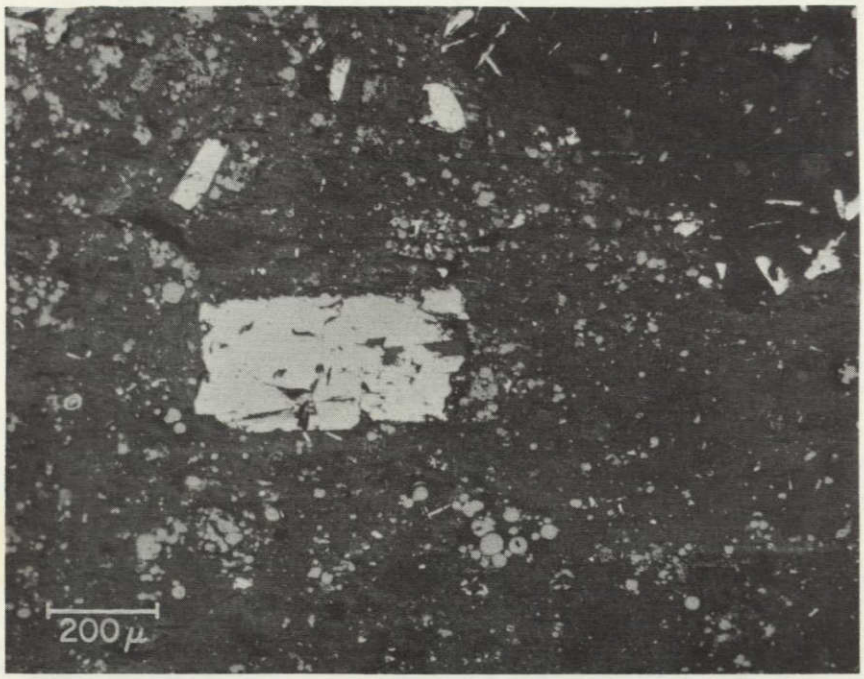

Figure IIF-3. View in reflected light of the carbonaceous chondrite fragment. The light-gray, squarish grains are iron sulfide; the gray, rounded grains are magnetite (Fe_3O_4). The black interstitial material is the fine-grained, opaque, Ni-rich matrix.

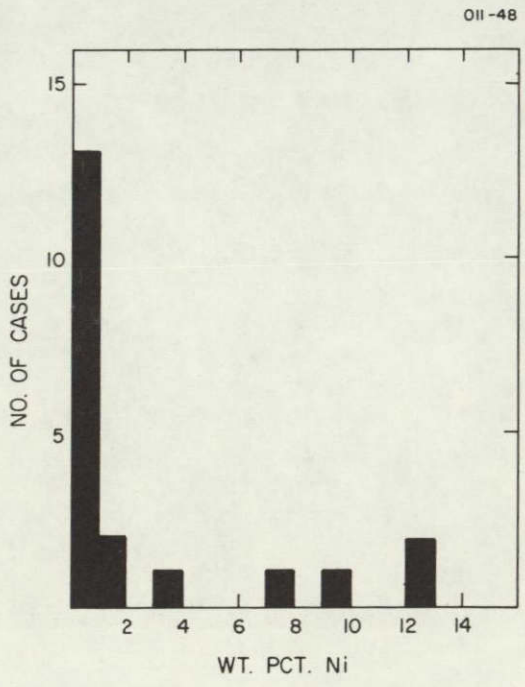

Figure IIF-4. Histogram of the Ni contents in iron sulfide grains. The wide range is typical of Type II carbonaceous chondrites, but the predominance of low Ni contents is unusual.

IIG. Luminoscopy

In this section, we report on the cathodoluminescence effects exhibited by our Apollo 12 samples. The samples were examined with a Nuclide Corp. Luminoscope (see Section IV for experimental details), with the main emphasis on finding unusual mineral phases and elucidating the textures of the crystalline rocks.

Principals of Luminescence

Luminescence arises when a substance reemits as light a portion of the energy it has absorbed from an incident beam of radiation. In the present work, the radiation was provided by an electron beam, so the process is properly called cathodoluminescence. The emission of light is not the normal method by which the atoms in a substance transfer the excess energy acquired as a result of charged-particle bombardment. Usually, the atoms transfer energy via nonelastic collisions with neighboring atoms. However, impurities in a crystal can act as centers for luminescence. The precise nature of the luminescence depends on the type and concentration of the activator elements, their sites in the host crystal, and the latter's composition and structure.

Norite–Anorthosite Rocks (Type A)

Feldspar occurs in two forms in Type A noritic–anorthositic fragments: as small (10 to 20 μ), fairly uniformly sized grains in fabrics that appear to be thoroughly recrystallized; and as larger (50 to 200 μ) clasts that are sometimes embedded in the fine-grained fabrics just noted. Where the two forms occur together, luminescence properties help to demonstrate that recrystallization has affected small feldspar grains in the matrix, but not the larger clasts: the large feldspar crystals luminesce pale pinkish or yellowish, while the small grains luminesce bright blue. The large clasts are lacking in some particles, and it is less obvious texturally that these were once breccias; but

the fact that their feldspar luminesces bright blue indicates that these too are recrystallized, not primary igneous, fabrics. Sippel (1968) has found similar differences between the luminescence properties of detrital quartz grains and the recrystallized quartz that cements them together. He suggests that the difference in luminescence is due to different physical-chemical environments of formation of the two types of quartz. This also seems to be the case for the lunar anorthosites. It appears that relatively large feldspar grains formed from a melt and accumulated into anorthositic rocks; subsequently, these were brecciated and the more finely crushed feldspar fragments were recrystallized by solid-state processes at substantially different temperatures than those at which they initially formed.

The anorthositic rocks also contain some interesting accessory minerals (see Section IIB). Most display no notable luminescence properties; either they luminesce like feldspars, or not at all. One large crystal of whitlockite (Figure IIB-17), however, did luminesce a distinctive dark red. With extended exposure to the electron beam, this mineral ceased luminescing.

Basaltic Rocks

The main luminescent mineral in the basaltic rocks is, again, plagioclase. In general, the plagioclase displays a pale-yellow color much less intense than the yellow luminescence of plagioclase in the noritic rocks. This difference in luminescence properties suggests that different activator elements or concentrations of activator elements are present in the feldspars of the two different rock types and provides one line of evidence that the basaltic and noritic rock series are not closely related.

The basalts also contain glassy interstitial material rich in SiO_2. These areas are easily located by their bright-blue luminescence. The bluish color is distinctively different from the pale-yellow luminescence color of the plagioclase.

Breccia and Glassy Particles

The mineral and lithic fragments in many breccias are mainly mafic, whereas in other breccias they are chiefly feldspathic. The abundances of the two components can easily be distinguished in the luminoscope because the feldspars are the only major phase to luminesce. Moreover, the fine-grained matrix material in breccias is also variable in its feldspar content, as seen from its variable luminescence. In general, the more feldspathic the fragments in a breccia particle are, the more feldspathic the matrix is.

The feldspar fragments in the breccias exhibit a variety of luminescence colors, from the typical pale yellow seen in lunar basalts to the bright blue of recrystallized norite–anorthosites. In addition, some feldspars luminesce a yellow that is much brighter than that of either the basalts or norites. Sippel and Spencer (1970) have suggested that this effect is due to shock. Certainly, some of the fragments in breccias have been shocked, so this seems to be a reasonable explanation. The feldspars that luminesce a bright yellow do not show petrographic evidence of severe shock (e.g., planar features), but they often display nonuniform extinction, perhaps indicative of low- to medium-shock pressures.

No unusual minerals were discovered by the luminescence technique. It was found, however, that two grains of a silica phase luminesced a bright purple.

Ultraviolet Luminescence

The sections were examined at low magnification with ultraviolet light, at both short (~2500 Å) and long (~3650 Å) wavelengths. No mineral luminesced to an observable degree.

III. DISCUSSION AND INTERPRETATION

IIIA. Petrology of Mare Basalts

Based on their textures and mineral compositional relationships, the basaltic particles in our Apollo 12 soil samples appear to have been derived from thin flows that underwent some differentiation by crystal settling during crystallization. Properties of the rocks are not consistent with crystallization in deep lava lakes that might have been created by catastrophic mare-forming collisions.

Evidence from the Rocks' Textures

As seen in Figure IIIA-1, the basalt particles exhibit considerable textural variety. All but 4 of the 202 particles we have examined can be matched quite closely to one or another of these 10 textural types. Whether or not they are genetically related, these textural examples show a smooth decrease from upper left to lower right in the inferred cooling rate. Pyroxene vitrophyres (nos. 1 and 2) with ultra-fine groundmasses and skeletal phenocrysts suggestive of very rapid cooling grade smoothly through rocks with comparable phenocryst size, but coarser matrices (nos. 3 through 8), to still coarser gabbroic rocks (again with comparable phenocryst size; nos. 9 and 10), many of which show cumulate texture. From this textural sequence alone, it is reasonable to suppose that the quickly chilled vitrophyres represent the surface layers of a flow, that the somewhat coarser variolitic and subophitic basalts are derived from layers on the order of a few meters below the surface, and that the coarse cumulate gabbros may have been parts of the lower levels of the flow, where early crystallizing olivines, pyroxenes, and spinels were concentrated by crystal settling. Put another way, if the 10 textural photomicrographs in Figure IIIA-1 were arranged vertically with no. 1 at the top, they would approximate the rock types encountered in drilling a core through a typical Apollo 12 basalt flow of roughly 10 m thickness.

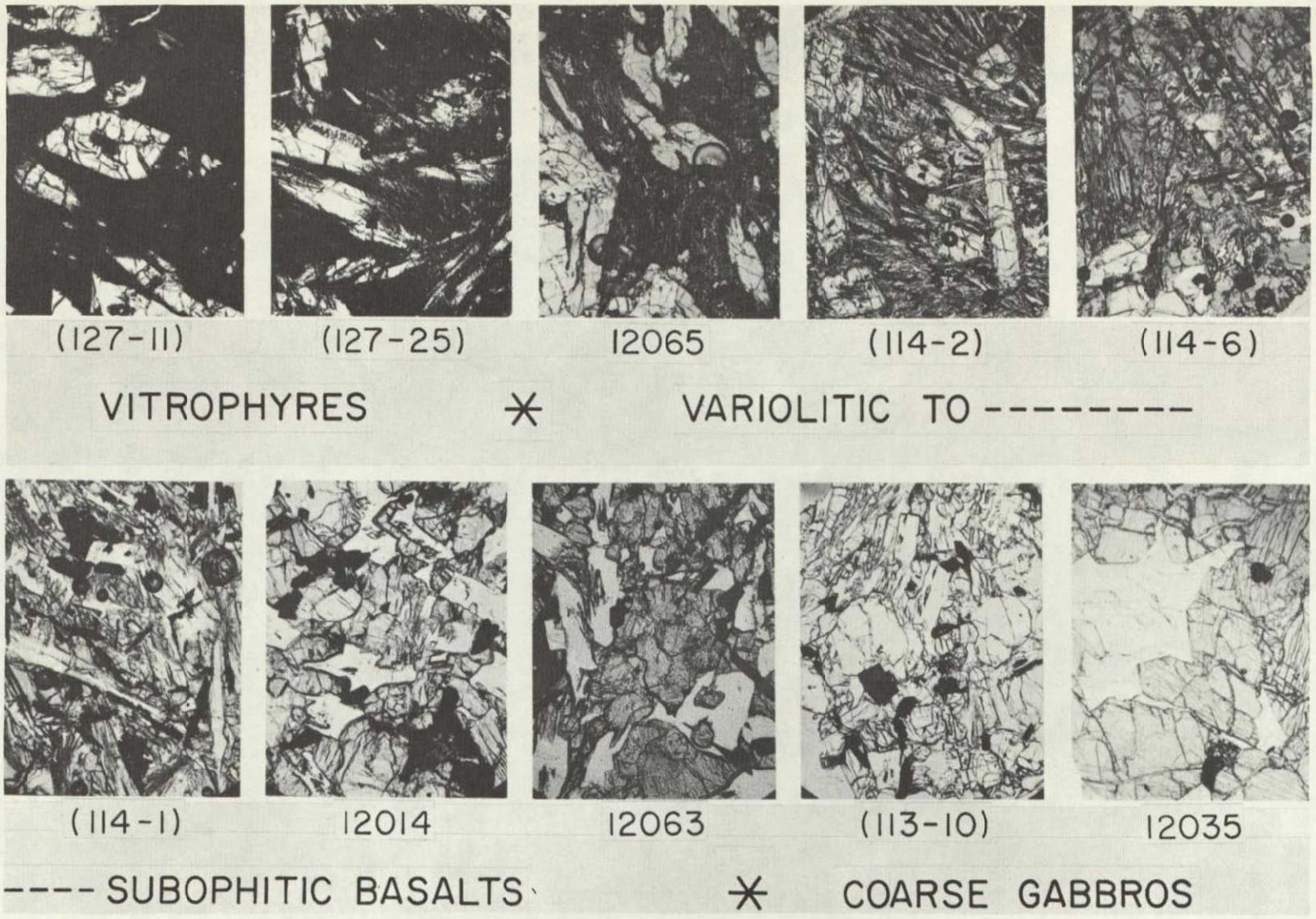

Figure IIIA-1. Ten examples of rock textures observed in basaltic particles from Apollo 12 soil samples; summary of Figures IIA-2 through IIA-11. All are viewed by unpolarized transmitted light, to the same scale. Textures are arranged (from top left to lower right) in order of decreasing rate of cooling and crystallization.

Evidence from Mineral Compositional Relationships

As seen in Figures IIA-18 through IIA-21, the textural appearance and compositional zoning of spinel grains vary as a function of position in the proposed stratigraphic column shown in Figure IIIA-1. In the surface rocks (quickly chilled vitrophyres), spinels have euhedral and uniformly chrome-rich cores, which are coated by thin films of Ti-rich spinel (Figure IIA-18). In the subsurface variolitic and subophitic basalts (Figures IIA-19 and IIA-20), the size of the Ti-rich rims relative to the Cr-rich cores increases, and the sharpness of the color and compositional boundary between cores and rims becomes less well defined. In the coarse cumulate gabbros (Figure IIA-21), no color differences are apparent, though large smoothly continuous compositional variations within single spinel grains persist. We feel that the Cr-rich cores of spinel grains in all rock types were present as homogeneous chromites in the melt at the time of extrusion onto the lunar surface and that the addition of Ti-rich spinels commenced when pigeonite began to crystallize and quickly depleted the melt in Cr. In the quickly cooled surface vitrophyres, the Ti-rich rims are very thin (Figure IIA-18). In the subsurface variolitic basalts (Figure IIA-19), the Ti-rich rims grew wider because crystallization was more leisurely but are still sharply discontinuous with their cores in composition. In the somewhat coarser subophitic basalts (Figure IIA-20), slower cooling has allowed a partial reequilibration between core and rim to occur, resulting in a diffused contact. Still slower cooling in the basal portions of the flow (the coarse cumulate gabbros) has allowed further, yet incomplete reequilibration between core and rim (Figure IIA-21). If the Apollo 12 basalts were derived from a thick lava lake on the order of kilometers in depth, cumulate rocks would not be expected to have retained any compositional zoning, nor would phenocryst grain size be so nearly the same as that in the quickly chilled surface vitrophyres (Figure IIIA-1).

As in terrestrial basalts, early crystallizing phases in the lunar basalts are enriched in Mg relative to Fe and in Cr relative to Ti. The zoning with respect to these elements is strong in the mafic silicates, and particularly so in the spinels. When their variations in Mg/Fe and Cr/Ti are considered

simultaneously (Figure IIA-31), spinels plot on different trends depending on the position of their host rock in the proposed stratigraphic column in Figure IIIA-1. Spinels in surface and near-surface basalts (solid and half-solid symbols in Figure IIA-31) fall on nearly identical trends, while those in the deeper-seated coarse basalts (open symbols) differ in general from one another and from those in the fine-grained basalts. For spinels in fine-grained basalts 12014, 12052, 12063, 12065, and (127-19) (Figure IIA-31a, b, c), compositional trends consist of two straight line segments of very different slope. Early spinels in each of these rocks are chrome-rich and show considereable variation in Mg/Fe. They are found in close association with early crystallizing Mg-rich olivines, whose formation depletes the liquid in Mg relative to Fe; we feel that this event is reflected in Mg/Fe variability of early spinels. Following the onset of crystallization of pigeonite, which accommodates large quantities of Cr_2O_3 (see Figure IIA-25), spinels quickly become Ti-rich.

The trends for spinels from coarser basalts (occurring at low levels in the proposed stratigraphic column in Figure IIIA-1) are straight, near-vertical lines occurring at various positions along the Fe/(Fe + Mn + Mg) abscissa. The spinel trends richest in Mg are found in gabbroic rocks 12035 and (108-2) (Figure IIA-31a, c), which consist largely (about 70%) of pyroxene and olivine phenocrysts whose mutual contacts along euhedral faces are indicative of cumulate origin. These spinel trends intersect the trend for the fine-grained basalts at compositions rich in Mg and Cr. If spinel trends like those of the fine-grained basalts trace the crystallization history of the liquid, the divergence of spinel trends for the coarse cumulate gabbros 12035 and (108-2) from the parent trend at compositions rich in Mg and Cr can be interpreted to mean that the minerals in 12035 and (108-2) crystallized and separated from such a melt at an early stage in the solidification of the flow.

Other coarse gabbro fragments are rich in plagioclase and poor in olivine and pyroxene (e. g., (110-3) and (113-1) in Figure IIA-31c). Their spinels are exclusively Ti- and Fe-rich, consistent with crystallization late

in the solidification of the flow. We feel that these plagioclase-rich fragments are derived from intermediate depths in the flow, where cooling was slowest and solidification occurred last.

Corroboration of our model has been found in an experimental study of several Apollo 12 basalts by Green (1971). He measured the compositions of the olivine phenocrysts in the rocks and compared them with the compositions of olivines crystallizing from experimental melts having the same bulk compositions as the rocks. In the case of the vitrophyre 12009, lunar and experimental olivine compositions were very nearly identical. This is an indication that 12009 solidified as a closed system, as its quickly quenched vitrophyric texture suggests. Other rocks contain olivines that do not have the same compositions as those crystallizing from melts of the rocks' bulk composition. In the case of 12040, an olivine-rich gabbro similar to the cumulate rock 12035 of the present study, the olivines in the rock itself are less Mg-rich than those crystallizing from an experimental melt of the 12040 composition. This is consistent with the idea that 12040 contains an accumulation of olivine that crystallized from a less magnesian system than 12040 itself. In the case of 12063, a medium-grained, relatively plagioclase-rich, olivine-poor subophitic basalt also examined in the present study, the olivines in the rock itself are more Mg-rich than those crystallizing from a melt of the 12063 composition under closed-system conditions. The indication here is that 12063 retains only a small part of the olivine that crystallized from its initial liquid and that the remainder has settled out. In the textural continuum seen in our particles, 12040 would fall in the tenth position (Figure IIA-11), 12009 in the first position (Figure IIA-2), and 12063 in the eighth position (Figure IIA-9).

Since the quick-chilled vitrophyres preserve a record of melt compositions at the time of eruption, evidence for differentiation that might have taken place in magma chambers beneath the lunar surface should be manifested as compositional differences among the vitrophyres. Such differences have been sought in the vitrophyre fragments in our soil samples; if present, they are not obvious in terms of textural or mineral compositional relationships.

On the other hand, the vitrophyres among the large lunar rocks collected (e. g., 12009) differ from those in our soil samples in that they are considerably more olivine-rich. Sample 12009 consists of olivine and some pyroxene phenocrysts imbedded in a matrix of glass and skeletal stringers of olivine; while in the vitrophyres of our soil samples, pyroxene is the dominant mineral, and groundmasses consist of ultra-fine variolitic clinopyroxene, ilmenite, and plagioclase. These two vitrophyre types probably represent the surface layers of flows whose normative olivine contents fall into two groups.

Compston et al. (1971) have reported trace-element data from a number of the large lunar rock specimens from which they conclude that no fewer than five magmas are involved in Apollo 12 basalts. A variety of initial Sr^{87}/Sr^{86} ratios has been found for a group of Apollo 12 basalts by the Albee et al. (1971), an additional indication of a multiplicity of source magmas for these rocks. The basalt fragments in our soil samples are too coarse-grained to allow accurate determination of whole-rock major element compositions by defocused-beam electron-probe analysis, so we are not able to specify which fragments may belong to a particular flow unit. Even though a number of magma generations may be represented in the basaltic fragments from our soil samples, we believe that the textural and mineral compositional arguments outlined above are valid. The point we wish to make is that each of these magma generations appears to have erupted onto the lunar surface in a flow on the order of tens of meters thick, and during solidification it underwent some differentiation by crystal settling. The idea that the mare basalts were generated in a catastrophic impact event and crystallized in lava lakes on the order of kilometers in thickness is not supported by our findings.

IIIB. Petrology of Norites and Anorthosites

Type A Recrystallized Breccias

As noted in Section IIB, a large proportion of the light-colored lithic fragments from both Apollo 11 and Apollo 12 soil samples are texturally the same kind of rock: an assemblage of broken mineral fragments (breccia) that has been healed into massive rock, presumably by thermal recrystallization. (At a later time, of course, this rock was refragmented into the soil particles we have described; but relict textures of the earlier fragmental stage may still be observed within each of the present soil particles.) Apollo 11 Type A particles are on average much more feldspathic (anorthositic) than Apollo 12 Type A particles, but properties of the two sets of particles tend to grade into one another (Figure IIB-36): we believe Type A rocks from both sites are genetically related, i.e., a common magma system gave rise to a range of primary igneous rock types that were subsequently brecciated to form the various Type A particle compositions we observe.

Differentiation in an early lunar surface magma system

In common with other writers, we (Wood et al., 1970) have argued that crystal fractionation must have produced the lunar anorthosites. (When a magma cools, crystals that form in it do not in general have the same specific gravity as the residual liquid surrounding them; they tend to float or sink in the liquid, depending on the nature of the density contrast, and accumulate at the top or bottom of the magma system. Lunar plagioclase is less dense than the melts of known lunar mafic rocks (see Table IIIF-I), so crystallizing plagioclase probably tended to float upward in early lunar magma systems. Apparently, anorthosite forms much of the lunar surface (in highland terrains); accumulation of plagioclase at the surface implies a

parent magma system that was itself awash on the surface of the Moon, not deeply buried as were the known extensive terrestrial magma systems of past ages when they crystallized.)

Norites of the type described in this report can be related to the Apollo 11 anorthosites in one of two ways:

1. Norite may be representative of the original composition of an early lunar surface magma system, from which anorthosites (and also sunken cumulates of mafic minerals) were to form by crystal fractionation.

2. Norite may be representative of the composition of a residual magma that was left between layers of floating anorthosite and sunken ultramafics, after extensive crystal fractionation had occurred in an early lunar surface magma system.

We favor the second possibility, for several reasons. Its high content of trace and minor elements (K, Y, rare earths, Zr, U, Th) that are not easily accommodated in plagioclase, pyroxene, or olivine suggests that lunar norite was a late residual liquid, from which a large volume of "clean" crystals had been removed. The more magnesian (Figure IIB-10) and silica-poor (undersaturated) character of mafic minerals in lunar anorthosites than in norites is also important. If norite represented the starting composition of the lunar surface magma system, the deviant composition of anorthosite mafic minerals would have to be attributed to rafting upward of early-crystallized mafics along with floating plagioclase, to lack of large-scale uniformity in the composition of the Moon and its early surface magma system, or to mixing of appropriately different meteoritic silicate minerals into lunar surface rocks at various times and places on the Moon. None of these are very satisfying explanations. If anorthosite is an early differentiate and norite a later residuum, on the other hand, the differences in character of mafic minerals are those that silicate phase diagrams predict. (Laboratory experimentation has established that in systems of appropriate bulk composition, as crystallization proceeds more siliceous minerals appear (olivine gives way to pyroxene), and the equilibrium Fe/Mg ratio in these minerals increases.)

If this interpretation is correct, the bulk composition of the early lunar surface magma system can best be learned from the Apollo 11 anorthositic fragments. We can assume that virtually all mafic and oxide minerals in the Type A recrystallized breccias, and an approximately equal amount of plagioclase, derive from intercumulus liquid in the original igneous anorthosite (i. e., from remnants of early-type magma that filled the spaces between adjacent plagioclase crystals, once these had packed together in a floating "raft" at the surface of the Moon).

It is difficult to understand the place the curious olivine-plagioclase particle (130-9) (Figure IIB-33) would occupy in such a system. Perhaps this is plagioclase that crystallized at an early stage from the lunar surface magma system, and in so doing enveloped crystals of early-formed (and therefore Mg-rich) olivine. If so, the particle is a rare sample of primary igneous rock from the hypothetical magma system, unaltered since its formation except for a reheating episode that caused eutectic melting along plagioclase-olivine interfaces.

As noted in Section IIB, "Luny Rock I" is a Type A norite, and the Sr-Rb model age of this rock fragment is 4.4×10^9 yr, consistent with formation of norites from a very early lunar magma system (Albee et al., 1970a). However, it should be borne in mind that all lunar materials so far studied display similarly old model ages, though the isochron ages of some (the basalts) are considerably younger.

Brecciation of the Type A materials

Type A norites and anorthosites do not have the coarse igneous textures (Figure IIIB-1) that should develop in rocks crystallizing in magma systems as extensive as the hypothetical lunar surface magma system (the scale of which will be discussed in Section IIIF); indeed, most Type A particles do not have igneous textures at all. They are recrystallized breccias, and their textures (distribution of clast sizes, absence of juxtaposed fragments that fit together) are suggestive of origin by repeated fragmentation and

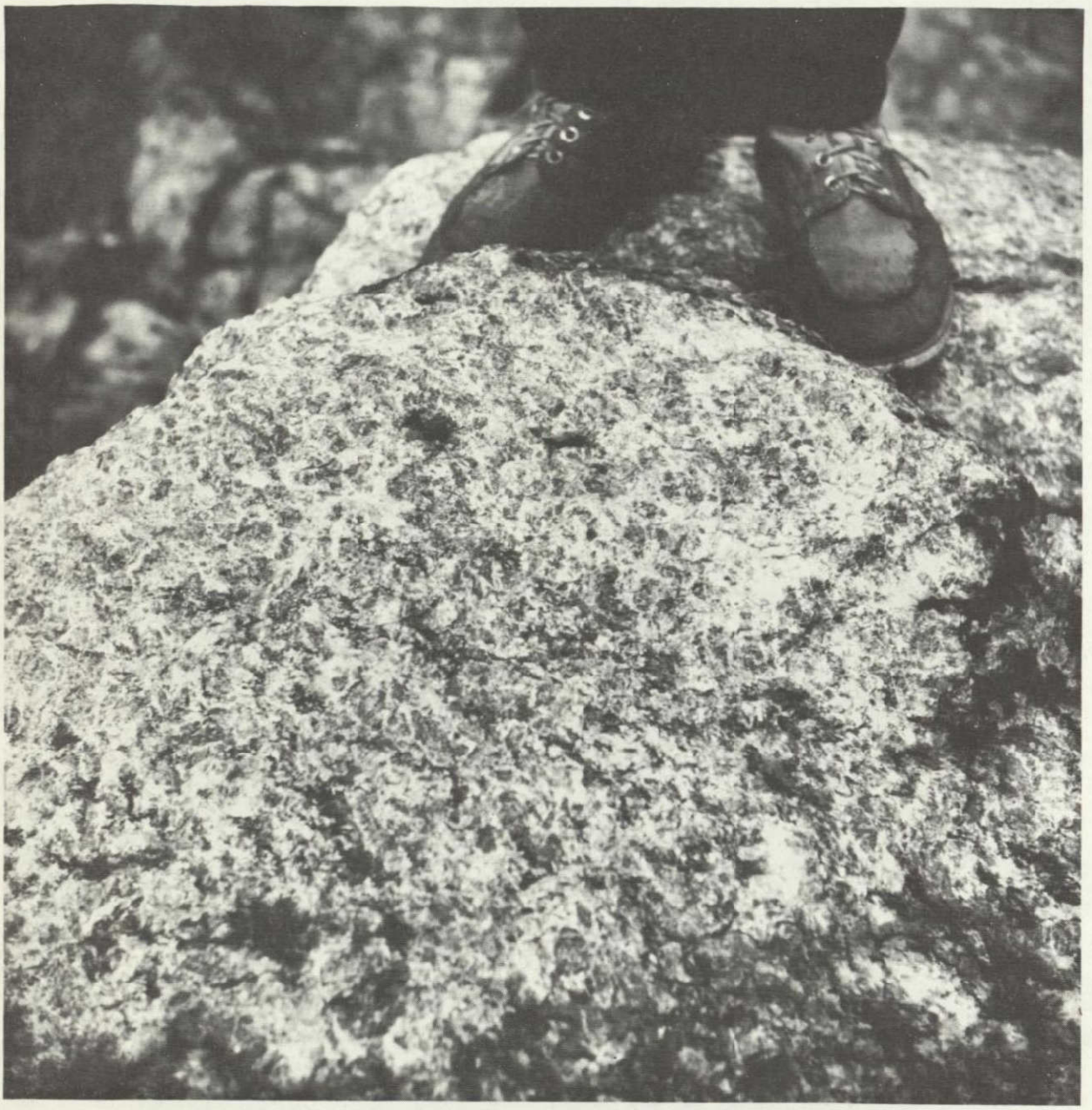

Figure IIIB-1. Outcrop of anorthositic rock in the Adirondack Mountains, New York, showing coarse crystallinity of terrestrial massif anorthosites. Plagioclase crystals (dark) are typically 1 to 2 cm in dimension.

mixing as in a regolith, not by one-impact in situ shock brecciation of igneous-rock types. Except for the effects of thermal recrystallization, they are texturally similar to the known lunar soil breccias. Chao, Boreman, and Minkin (1971) have observed glass spherules (characteristic of soil breccias) in Apollo 12 noritic breccias.

An early-formed anorthositic layer at the surface of the Moon would have been exposed to meteoroid bombardment through all of geologic time, and an anorthositic regolith would inevitably be created; thus it is not surprising that much of the anorthositic material available at the lunar surface has the character of a soil breccia. The existence of noritic soil breccia is less easy to account for, since the noritic residual magma was presumably overlain by thick slabs of floating anorthosite and shielded by it from the meteoroid bombardment. It appears that locally on the Moon norite rather than anorthosite was exposed at the surface, and a noritic regolith was created. This circumstance will be further discussed in Section IIIF.

Recrystallization of the Type A breccias

The great majority of Type A particles are fragments of breccias that have been healed into massive rock. Pore space (such as can be seen in lunar basaltic soil breccias) has been completely eliminated. Wholesale remelting of the breccias cannot be responsible for this healing, or the angularity of clasts would have been lost. If these rocks were terrestrial, the healing effect of aqueous solutions might be appealed to, but on the all-but-water-free Moon this is not possible. The massive nature of Type A breccias can best be understood as an effect of thermal recrystallization. Polycrystalline substances, when held at high temperature for protracted times, tend to reorder their crystal fabrics via solid-state diffusion of individual atoms through crystal lattices and along crystal grain boundaries. Changes wrought are elimination of the smallest crystals (their substance is added to larger crystals in the system), decrease in the amount of surface area (both crystal-crystal and crystal-pore interfaces) in the system, elimination of phases unstable at the recrystallization temperature, and homogenization of chemical composition of each discrete phase or mineral in the

system. The process is utilized by industry to manufacture sintered ceramic and metal products.

However, in the case of the lunar Type A breccias, the existence in at least some particles or zones of glassy residual material of composite composition (Figure IIB-16; norms of analyses A and B, Table IIB-IV) indicates that recrystallization occurred at somewhat above the eutectic temperatures of these rocks and that incipient melting occurred. The presence of even a small amount of silicate melt in the pore space of the original breccias would have greatly facilitated and speeded their recrystallization into massive rocks.

Breccia recrystallization was not thoroughgoing enough to eliminate all unstable phases, as is shown by the coexistance of three pyroxenes (orthopyroxene, pigeonite, and augite) in many if not all the Type A norite particles, whereas only two pyroxenes can stably coexist (see, e. g., Deer, Howie, and Zussman, 1963, p. 129). Nor were mineral compositions homogenized within the volumes represented by the particles studied (Figures IIB-9 and IIB-15). Plagioclase and pyroxene compositions were nonuniform in the original breccias, probably because the clasts of these minerals were derived from nonuniform (zoned) crystals in igneous rocks that preceded the breccias, and also because mixing of minerals from widely separated sources occurred in the regoliths that gave rise to the breccias; these heterogeneities (at least in part) survived the recrystallization.

Whitlockite and zircon are normally early-formed minerals in igneous rocks and preserve euhedral outlines; but in the Type A norites, it is clear from their complex anhedral forms (Figures IIB-18 and IIB-20) that they were emplaced late in the crystallization sequence. Presumably they took up these forms during the thermal recrystallization of the breccias.

Sustained high temperatures in early noritic and anorthositic regoliths appear to be required to produce the Type A breccias. Means of satisfying this requirement will be discussed in Section IIIF.

Type A igneous rocks

A minority of Type A particles are unquestionably igneous (Figure IIB-3), but like the breccias they are too fine grained to be samples of primary igneous rock from the early lunar surface magma system. We think it more likely that these are counterparts of the Type A breccias that were completely melted by the high-temperature event that recrystallized and partly melted the breccias.

Type B Unrecrystallized Breccias

The light-colored particles from both the Apollo 11 and the Apollo 12 sites also have in common a second textural type: coarse breccias of angular clasts, the latter sometimes not far separated from other fragments with matching surfaces, from which they were obviously sundered. Between the clasts is glass of noritic composition (at least in the Apollo 12 Type B particles), not a K-rich residuum. These are obviously shock breccias, containing shock-melted glass, and are not recrystallized soil breccias, as the Type A particles appear to be. Clasts in the Type B breccias are almost invariably monocrystalline; the parent rocks that were brecciated to form this type were relatively coarse grained. An upper limit cannot be put on the grain size of the parent rock, but a lower limit of 200 μ can be set (from Type B clast sizes), much coarser than the prevalent grain size in Type A recrystallized breccias. Type A breccias can be excluded as a parent material on textural grounds alone.

Type B and Type A breccias also differ in the proportions and compositions of their major minerals. Apollo 12 Type B particles, unlike their Type A counterparts, are often genuine anorthosites, though there are also noritic or gabbroic Type B particles in the Apollo 12 samples (Figure IIB-5). The plagioclase is more sodic (Figure IIB-8) and the iron content of pyroxene is higher (Figure IIB-10) in Type B than Type A particles, which points to derivation of the Type B breccias from parent rocks that formed during a later stage of magmatic evolution than the Type A norites. (Remember that

the norites in turn seem to represent a later stage of magmatic evolution than the Apollo 11 anorthosites.) It appears that early in the history of Oceanus Procellarum (a) noritic magma erupted and crystallized at the surface (where it was subsequently bombarded by meteorites, and ground into a regolith), and (b) later (at a later stage of magmatic evolution, at any rate; probably also later in time), at a position not exposed to the meteorite bombardment, additional rock crystallized, under circumstances that permitted growth and gravity differentiation of relatively coarse crystals. It is hard to escape the conclusion that stage (b) occurred under the noritic surface layer of stage (a).

An early formed surface layer of undifferentiated noritic composition would insulate underlying magma, allow coarse crystals to grow, and give them time to separate into floating anorthositic and sunken mafic layers. The anorthosite would consist of accumulated plagioclase crystals interspersed with residual noritic rock. We envisage the formation of such a subsurface anorthosite. Although it was too deeply sited to be affected by the day-to-day regolith-forming meteorite bombardment, occasional very large cratering events (perhaps the Imbrium impact itself) penetrated to this layer, crushing the plagioclase crystals and fusing the lower-melting constituents of the rock (in general, the noritic intercumulus material). Masses of mixed plagioclase clasts and noritic melt (later glass) were ejected from the crater and eventually found their way into the Apollo 12 soil samples.

Where anorthosite occurs at the lunar surface (source of the Apollo 11 Type A anorthosites), Type B breccia probably represents samples of the same cumulate layer taken from depths that were not affected by the regolith-forming bombardment.

IIIC. Petrology of Potash Rhyolite

The eutectic composition for many rock systems is enriched in K, Si, and Fe; that is, the last liquid to crystallize from a cooling melt, or the first to appear as a rock is heated, contains these elements in larger proportions than the melt or rock as a whole. The lunar basalts contain patches of K-rich glass (Roedder and Weiblen, 1970) that are obviously solidified volumes of eutectic liquid residual after crystallization of the major rock-forming minerals. Lunar rhyolite or granite (such as our particle (102-5)) is compositionally very similar to the K-rich glasses in basalts (see Table IIC-I) and must have formed in the same manner, except that the eutectic liquid segregated into larger volumes than have been observed in lunar basalts and crystallized instead of quenching to glass. An extreme degree of igneous fractionation (via crystallization at super-eutectic temperatures) was required to produce a residual liquid with such a high Fe/Mg ratio as (102-5): 9.6 vs. an average of 4.7 for the basaltic K-rich residua of Roedder and Weiblen. An even more highly differentiated granitic particle, containing nearly pure fayalite (Fe_2SiO_4) as the mafic mineral, has been observed by Mason et al. (1971) in the Apollo 12 soil.

Rock 12013, one of the most intensively studied of all lunar samples, is a complex noritic breccia containing veins and ovoid inclusions of granitic material (Drake et al., 1970). The latter is chemically very similar to our particle (102-5) in almost all respects; compare columns A and B in Table IIC-I. However, Fe/Mg is not particularly high (1.3) in the 12013 granitic material; this value comes close to Fe/Mg for pyroxenes in the noritic portions of 12013, but it falls far short of Fe/Mg in (102-5). Particle (102-5) and the granitic zones of 12013 also differ texturally, the former consisting of a micrographic intergrowth of silica and K-feldspar minerals (Figure IIC-I) while the latter contain randomly oriented stumpy phenocrysts of feldspar and plates of silica.

The lunar rock unit from which particle (102-5) was broken must have been derived by magmatic fractionation from some more mafic parent magma, but was this of the noritic or the mare basalt kindred? We cannot say for certain. In favor of a noritic heritage is the observed association of granitic material similar to (102-5) with norite in 12013; against it is the fact that residual K-rich glasses in the norites we studied are not compositionally very similar to (102-5): Residual K-rich glasses in the mare basalts provide a much closer match (Table IIC-I). Conceivably, granitic magma was segregated during both the early epoch of igneous activity that produced lunar norites (Section IIIF) and the later episode of basaltic vulcanism that filled the maria.

Nor is it possible to say whether segregation of granitic liquids in the Moon produced major bodies of granitic or rhyolitic rock, or if this lithology occurs only as small-scale veins and inclusions in other rock types, as is the case with 12013. The evidence seems to be against major amounts of granite on the Moon: Granitic rock samples were not returned by the Apollo 11, 12, or 14 missions, and lithic fragments of granitic composition are very rare in the soils of the first two missions. The micrographic texture of (102-5) is characteristic of the crystallization of eutectic liquids, suggesting the coexistence of the (102-5) liquid in small amounts with large proportions of crystalline material, which would have hindered mobility of the liquid and made its segregation into large masses unlikely. We have not attempted to identify (102-5) with any of the mappable geologic units on the Moon (Section IIIE), or included granite among the components of our structural model of the Moon (Section IIIF).

IIID. Formation of the Lunar Regolith

Lunar bedrock is covered by a layer of weakly coherent, coarse and fine fragmental debris called the regolith, a term borrowed from terrestrial soil mechanics. As all samples returned by the astronauts are collected from the regolith, it is of paramount importance to try to understand its character and mode of formation. The regolith contains essentially undamaged fragments of lunar bedrock, together with materials (glass, breccias) that have been much altered or degraded by processes operative on the lunar surface. The main processes involved appear to be a) the fragmentation of bedrock to bodies ranging in size from a few microns to several meters; b) the mixing of particles from widely separated sources; c) glass formation at high temperatures followed by quenching; d) shock transformation of rock textures; and e) the consolidation of some particle admixtures to microbreccias. These processes require high energies and high temperatures, which could derive from either volcanism or meteoroid impact. Of these two, we conclude that meteoroid impact has been predominant for the reasons outlined below.

Volcanism vs. Meteoroid Impact in Regolith Formation

Volcanism

Vast tonnages of fragmental materials are produced by terrestrial volcanoes. Has lunar volcanism been an important process contributing to the lunar regolith?

The Apollo missions settled an ancient controversy by demonstrating that the lunar maria are basaltic lava flows. Volcanism was therefore active during the first billion years of lunar history. The surface rocks of Mare Tranquillitatis were extruded about 3.6×10^9 yr ago; those of Oceanus Procellarum, about 3.4×10^9 yr ago (Albee et al., 1970a; Papanastassiou and Wasserburg, 1970). The extent and type of more recent lunar volcanism remains highly speculative.

Among terrestrial volcanics the broad generality holds that the more siliceous the magma, the higher is its viscosity, and the more explosive the eruption. With some notable exceptions, basalts ($SiO_2 \sim 50\%$) tend to be extruded quietly over large areas as thin flows of molten rock whereas rhyolites ($SiO_2 \sim 70\%$) produce explosive clouds of gas and debris including vesicular particles, dust, ash, volcanic bombs, and angular rock fragments. Explosions of exceptionally high energies create nuée ardentes, highly mobile gas-dust clouds that move along the surface of the ground as incandescent "landslides." Within such clouds glassy particles sometimes acquire free forms — spherules, teardrops, rods — and angular particles act as accretionary nucleii, picking up shells of dust and glass as they tumble in flight or roll along the ground. Such particles are termed accretionary lapilli.

As the gases disperse, the detritus falls to the ground either as unconsolidated accumulations of loose particles, or if very hot, as glass-welded layers (welded tuffs). In physical characteristics some of the unconsolidated deposits would be virtually indistinguishable from the lunar soils, and some welded tuffs would resemble the lunar microbreccias. The probability of a volcanic component in the regolith must therefore be weighed not on textural but on chemical and geological grounds.

Basaltic lavas have covered about one-third of the Earth-facing surface of the Moon. Has explosive volcanism, operating within the last 3.5×10^9 yr, created the regolith? On the Earth, explosive volcanism always involves violent degassing of a magma system that is rich in water and volatiles under compression. The maria basalts are, however, water-free, which suggests that the degassing of the Moon took place very early in lunar history. Large-scale, post-mare production of ash volcanoes or nuée ardentes would therefore seem highly unlikely. We cannot show that explosive volcanism has not occurred at all since emplacement of the mare basalts, but on these grounds as well as from the arguments based on our glassy particles discussed below, we conclude that it has not contributed in any important degree to the formation of the lunar regolith at the Apollo 11 and 12 sites.

Meteoroid impact

On the airless Moon, the impact of every particle, large or small, traveling at velocities of >2.4 km/sec, contributes to the disruption of the surface. The effects on bedrock range from pitting, spalling, and crushing by small particles to the excavation of vast basins ringed with structural valleys and cordilleras produced by the radiation of shock waves through the crust of the Moon.

Experimental and theoretical studies of hypervelocity impact effects by D. E. Gault and coworkers at the NASA Ames Research Center suggest that a typical meteoroid impact would affect the lunar regolith as sketched in Figure IIID-1. The figure shows high-temperature events — glass formation and vaporization — occurring at the point of impact and affecting a mass of material equal to 2 to 3 times the mass of the projectile. Shock lithification of soils to cohesive breccias is effective throughout a hemispherical mass equaling 10 to 100 times the mass of the projectile. Beyond that, a much larger mass of material is excavated and projected outward to form a crater. The bulk of this material falls back on the crater rim and flanks; a small percentage jets outward in thin streaks or rays.

Impacts of large projectiles are expected to produce base surges, ring-shaped clouds of dust and gas that have been observed to move rapidly outward along the ground from terrestrial explosion sites. The base surges that accompany nuclear explosions bear a strong physical resemblance to the volcanic nuée ardentes dust-gas clouds. They carry fragments, some of which melt and acquire free forms, while others develop as accretionary lapilli. Clearly some of the rocks pulverized in a large impact event are likely to mimic volcanic particles. Since we have discarded lunar volcanism as a likely source of the lunar soils, we conclude that the regolith consists of an admixture of fragmental materials from impact cratering events, large and small. A special problem in interpreting the origin and sources of some lunar soils involves the lunar rays.

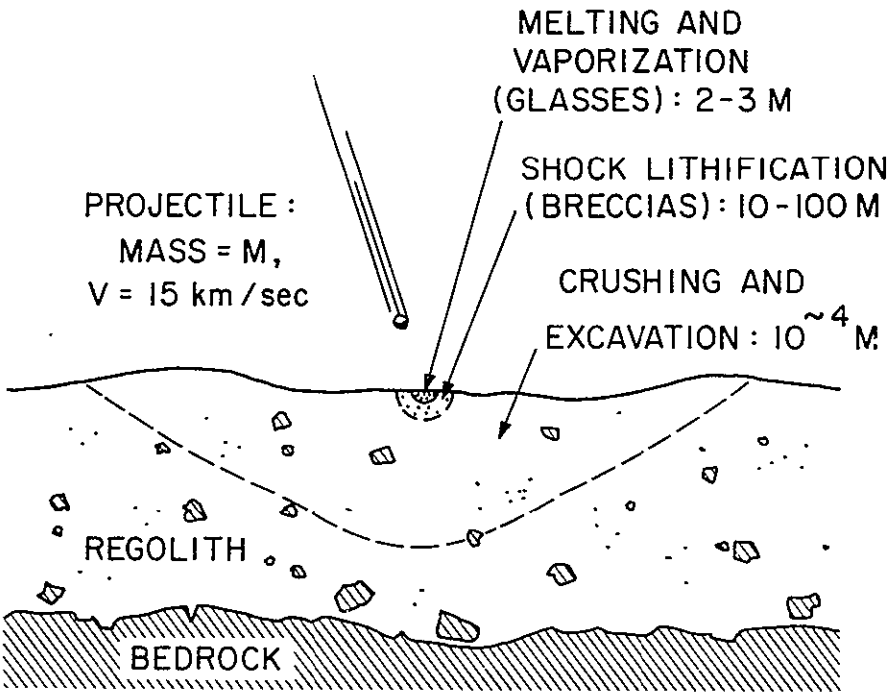

Figure IIID-1. Diagram showing predicted effects of an impacting projectile on unconsolidated target materials. Damage estimates by D. E. Gault (personal communication).

The lunar rays

The rays are brightly reflecting streaks, loops, or plume-shaped features that can be seen only at full Moon. They converge toward certain lunar craters to which they are either radial or tangent. The rays are superimposed over other lunar features including maria, craters, domes, and mountains.

Relatively few lunar craters have rays. Those having them are judged to be young, partly because the rays preserve their continuity as they cross "older" formations and partly because their scarcity suggests that rays are ephemeral and are destroyed in the course of time. Copernicus, with looped rays, and Tycho with straight, tangent rays, have the most extensive systems. Some of the rays of Tycho extend for at least 1000 km. All rayed craters are classed as "Copernican" in age (see Section I) not because Copernicus is necessarily the youngest, largest, or most important of the rayed craters, but because it lies within the first quadrangle to be mapped geologically by scientists of the U.S. Geological Survey (Shoemaker and Hackman, 1962).

The physical nature of lunar rays is problematical. They have been interpreted as cracks in the lunar crust resulting from high-energy impact events, and, conversely, as long linear mounds of crater ejecta. The lunar rays cast no shadows, however (with one or two possible exceptions), so it seems that they are not features having any marked topographic relief. The possibility remains that they are streaks of crater ejecta differing in color, texture, or crystallinity from the underlying regolith. A color contrast alone is insufficient to explain the rays, however. Light-colored streaks should show at any sun angle and should stand out in greater contrast to the dark maria than to the light highlands. Rays are in fact as visible over the terrae as they are over the plains.

Detailed photometric surveys show that rays are subdivided into linear or feathery segments ranging in length from 15 to 50 km. Each segment has a fine texture of discrete, telescopically unresolved bright patches that

decrease in number and in density of distribution along the ray and toward its margins (van Diggelen, 1969). The bright patches are probably secondary craterlets, each of which has excavated and roughened the soils of its vicinity.

Lunar Orbiter photographs (see Figure I-5) show part of the ray system from Copernicus crossing the Apollo 12 landing site. The astronauts reported light streaks on the surface that they traversed and also in the walls of the trench they dug in the rim of Head Crater. Two gray layers occur in the core tube sample, one at a depth of 18 to 22 cm, another that begins at 39 cm and continues for 2 cm to the bottom of the sample. The 39-cm layer in the core can be correlated with the one occurring at 15-cm depth in the trench (W. Quaide, personal communication). A crucial issue in interpreting the soils from this mission involves the relative proportions of material derived from Copernicus and from small, local craters.

From studies of the spectral reflectivity of the lunar surface and the Apollo 11 and Apollo 12 soil samples, Adams and McCord (1971) have concluded that ray materials include higher percentages of crystalline materials as opposed to dark-colored glass than does the background regolith. The crystallinity contributes to the high albedo of fresh crater ejecta and ray materials on both the dark-colored maria and the light-colored terrae. These authors suggest that the rays and ejecta blankets fade with time not so much from "gardening" by micrometeoroid impact as from vitrification on a fine scale due to meteoroid impact. The crystalline basalts turn to dark glass; the light-colored anorthositic rocks of the highlands become glassy and, because of contamination by dark mare material, darker. Adams and McCord report evidence that in addition to the light streaks sampled by the astronauts, the entire surface at the Apollo 12 site is enriched in ray material. Our samples of the light-colored soils are, however, highly enriched in glassy particles at the expense of crystalline materials, the reverse of the situation pictured by Adams and McCord. We cannot, therefore, concur with the conclusion that ray material is predominantly crystalline.

Formation of the Lunar Glasses and Microbreccias

Glasses

On the Earth, natural glasses are produced either by volcanism or meteorite impact. By analogy, we might expect to find glasses on the Moon formed by the same two processes. The most abundant types of glassy particles in the Apollo 12 soil samples are the highly vesicular cindery aggregates and the convoluted, red-brown to yellow-brown ropy glasses. Cindery glass is the easiest to interpret. Its composition is the same as the bulk composition of the lunar soil and significantly different from that of the mare basalts (see Figures IID-7 through IID-11, and Table IID-VI). This glass was produced by a process that directly melted the lunar soil; the only plausible mechanism is impact melting.

The ropy glasses present a more difficult problem. They are clearly related to norites, but, as we showed in Section IID, they are actually a mixture of norite and basalt: Their composition is intermediate between those of norites and basalts, and they contain inclusions of basaltic minerals. If volcanic, as suggested by LSPET (1970b), the magma that produced the ropy glass must have been contaminated with basaltic material. We think it more likely that the ropy glasses are shock-melted debris from a regolith that consisted chiefly of noritic bedrock with a small admixture of mare basalt. The presence of severely shocked mineral fragments in ropy glass particles (shock-isotropized feldspar, strongly fractured pyroxene, droplets of ilmenite and metal, etc.) supports the impact-melting hypothesis. S. V. Margolis (personal communication) has argued that the surface textures and morphology of these particles are consistent with an impact origin and not with a volcanic one.

Although both the cindery and the ropy glasses were formed by meteorite impact, they have very different textures. We reproduced the highly vesicular texture of the cindery glass by melting small samples of Apollo 11 and Apollo 12 soil in tungsten boats in an evacuated bell jar. During these experiments it was apparent that the glass had reached the boiling point and was not merely releasing trapped gases. The cindery glasses, therefore,

were formed by meteorite impacts that were sufficiently energetic to melt and boil the lunar soil. There is no orderly flow texture in the cindery glasses; they seem to have been melted and forced through the soil, picking up rock and mineral fragments as they moved, and finally coming to rest as a mass of glass and debris.

The ropy glasses, however, have a distinct flow texture and no vesicles. Apparently they were not heated to the boiling point and were able to flow before solidifying. One possible explanation is that the ropy glasses were formed during a very large impact. Large impacts produce a relatively high-density cloud of gas ejecta similar to a terrestrial nuée ardente. Perhaps the gas pressure was temporarily high enough to prevent the newly formed ropy glasses from boiling. McKay, Morrison, Clanton, Ladle, and Lindsay (1971) have invoked this mechanism to explain the size-sorted nature of the mineral fragments that are welded to the outer surfaces of the ropy glass particles. Furthermore, a large impact would have deposited material in a layer on the lunar surface, the thickness of which would depend on the distance from the crater. This would explain why the ropy glass is concentrated in a discrete layer at the Apollo 12 landing site.

According to McKay et al. (1971) the abundance of cindery glass in a soil sample is proportional to the time the sample spent at the lunar surface. Since Samples 12032 and 12033 contain very little cindery glass it appears that they did not reside at the surface for very long (relative to other samples) before being buried by debris from another impact. Because these samples were exposed at the surface for a shorter time than other samples, they should contain less solar-wind-implanted rare gases. Inert gas measurements by Funkhhouser, Bogard, and Schaeffer (1971) show that, as expected, the rare-gas contents of Samples 12032 and 12033 are far below those of other Apollo 12 soil samples.

The lunar glasses exhibit a spectrum of colors. Of particular significance is the difference in color between the red-brown ropy glasses and the greenish-yellow streaky glasses, since these have essentially the same

composition. The color of a glass depends mainly on three factors: the concentration of the transition metals (e.g., Fe, Ti, Cr), the ionic environment of these metals in the glass, and oxidation states. The ionic coordination of the transition metals in a glass depends mainly on the composition (Morey, 1954). As the streaky and ropy glasses have very similar compositions, it appears that the red-brown and greenish-yellow colors must be due to a difference in oxidation state of their transition metals. The results of the melting experiments described in Section IID suggest that the red-brown glasses are more oxidized than the greenish-yellow ones. The difference between the yellow-orange color of Apollo 11 cindery-type glasses (Plate 1D) and the yellow-green of Apollo 12 (Plate 1, A and B), however, is clearly due to the difference in the Ti content of the glasses (Ti is about twice as abundant in the Apollo 11 glass as Apollo 12, while the Fe levels are about the same; see Table IID-I).

Inhomogeneous glass particles

The inhomogeneous glass particles described in Section IID are a mixture of two lunar substances: ropy glass, with an affinity to the norite—anorthosite clan, and material characterized by very high K contents and high Fe/Mg ratios, similar to the potash rhyolite fragment described in Section IIC. The intimate association of these two materials in glass particles suggests that they are related and are not separate rock units on the lunar surface. It also supports the interpretation that lunar potash rhyolite is a residual material occurring within the norite series, rather than in the mare basalts, a possibility raised in Section IIIC.

Microbreccias

The mode of formation of the majority of lunar soil breccias involves nothing mysterious. Particles are reduced to small sizes and mixed together by meteoroid impact. The lithification of soils occurs near the sites of impact and varies in effectiveness from glass-welding to simple compaction. Extraordinary breccias, more difficult to account for, include the spherule-packed types described in Section IIE and discussed below.

Ti-rich microbreccia

The titanium-rich microbreccia (135-1), described in Section IIE, was found in Sample 12033, taken from the light layer in the trench in Head Crater. It consists mainly of dark blackish-red glass that differs in bulk composition from all previously described lunar rock specimens and lithic fragments. The glass contains about 31% normative ilmenite, 12% normative olivine, 45% normative pyroxene, and 12% normative feldspar (see Table IIE-IX). Admixed with the spherules and shards of glass are tiny fragments of pyroxene (subcalcic augite) and olivine (Fa_{30}). Unlike the majority of lunar microbreccias, which are admixtures of diverse source materials, fragment (135-1) appears to represent a discrete rock type that has been melted, fragmented, and reagglomerated.

When the composition of the red glass is compared with that of the more Ti-rich basalts from Mare Tranquillitatis, the differences are more striking than the similarities. The glass is richer, by 50%, than the basalt in normative ilmenite; poorer, by the same factor, in normative feldspar, and is olivine- rather than quartz-normative.

The origin of this microbreccia by the impact distillation of a basalt seems highly unlikely. The Ti-rich basalts of Mare Tranquillitatis, for example, contain about 19% of normative anorthite whereas the red glass contains about 11% normative An. Anorthite is not a volatile substance that would be expected to distill off to half its original abundance. The sodium content of the glass is lower than that of the basalts, which might be explained by volatilization, but the potassium content is equal to or higher than that of basalts. The alkali metals have not behaved consistently during volatilization. Furthermore, if impact distillation could produce fragment (135-1) from basalts, such materials should be common in the lunar regolith. We believe the composition of the red glasses in (135-1) must reflect fairly accurately the composition of a source rock type somewhere on the Moon.

A titanium-rich rock to serve as the source material for the red glass might originate as a basaltic differentiate or as an ilmenite cumulate in a

norite—anorthosite series. The calcic clinopyroxene (subcalcic augite), which occurs as a normative constituent of the glass and also as small fragments in the matrix, argues in favor of a basaltic affinity. Furthermore, the included fragments of olivine contain about 0.3% of Cr_2O_3, a value that lies in the range for basaltic olivines but is much too high for those of noritic olivines (see Figure IIA-22a). The combination of high ilmenite and normative olivine suggests that the source rock for our red glass was an early differentiate, perhaps formed by crystal settling from a Ti-rich basaltic magma.

It is easier to visualize the formation of a source rock for fragment (135-1), despite its unusual chemical composition, than it is to reconstruct the process by which that source rock was melted, dispersed, cooled, shattered, and reaggregated in situ before being projected to the regolith of the Apollo 12 landing site. Impact melting, base surges, and nuée ardentes are all capable of creating spherules; but they also disperse and mix them with other materials. Only one other microbreccia fragment in our experience has shown a similar concentration of spherules. This is Apollo 11 fragment (050-01), described in Section IIE. It consists of abundant spherules of orange glass, with 19% normative ilmenite and 23% normative olivine, together with spherules of yellow glass having 16% normative ilmenite and 1% normative quartz. In composition the yellow glass corresponds rather closely to some Apollo 11 mare basalts; the orange glass resembles some of the Apollo 12 basalts. The Apollo 11 microbreccia appears to be a mixture of spherules from two types of basalts, only one of which is common at the site of collection.

The aggregation as well as the production of glass spherules apparently results from some high-energy process that affects only a miniscule proportion of the material of the lunar surface. The resulting textures bear some resemblance to those of chondritic meteorites. Chondrules, however, are an abundant component in the most common class of stony meteorites, whereas spherule-packed microbreccias are a very minor constituent of the lunar regolith. If impact or volcanic processes can mimic chondrites, they do not do so frequently on the Moon.

IIIE. Sources of the Rock Fragments in the Apollo 12 Soil Samples

Recognizing in full the tentative nature of our project, in this section we attempt to trace the particles of our lunar soil samples back to their sources in the geological formations described in Section I. For this purpose we assume that the regolith is generated by meteoroid impact according to the principles outlined by Shoemaker et al. (1970). These authors constructed the "3-hop curve" shown in Figure IIIE-1, which indicates the probable distribution across the lunar surface of particles that originated at a point source and were dispersed by repeated impact cratering events. The curve is equally useful for predicting the abundances of particles derived from various surrounding sources in a soil sample collected at a given point on the lunar surface.

We applied this principle to the regolith of the Apollo 12 landing site by drawing five range circles, at radii read from the 3-hop curve, on the geological map of Figure IIIE-2. Here the innermost circle, 3.1 km in diameter, encloses the probable source area for 50% of the particles in Apollo 12 soils. The territory between the first and second circles contributes another 25% of the soil particles, and the areas between the next three pairs of circles contribute 20%, 2%, and 2%, respectively. The fifth circle, which passes through Copernicus and includes the entire Fra Mauro region of the Moon, has a radius of 470 km and should, therefore, enclose 99% of the source area of the Apollo 12 soils. The remaining 1% comes from even greater distances. (Similar range circles for the Apollo 11 landing site are shown in Figure IIIE-3).

The proportion of each ring occupied by the various types of source material was determined by copying the map and range circles on tracing paper and then cutting out and weighing the aggregate of scraps representing each geological formation. The weighted proportions computed for the total area, within the radius of 470 km, are listed in Table IIIE-I.

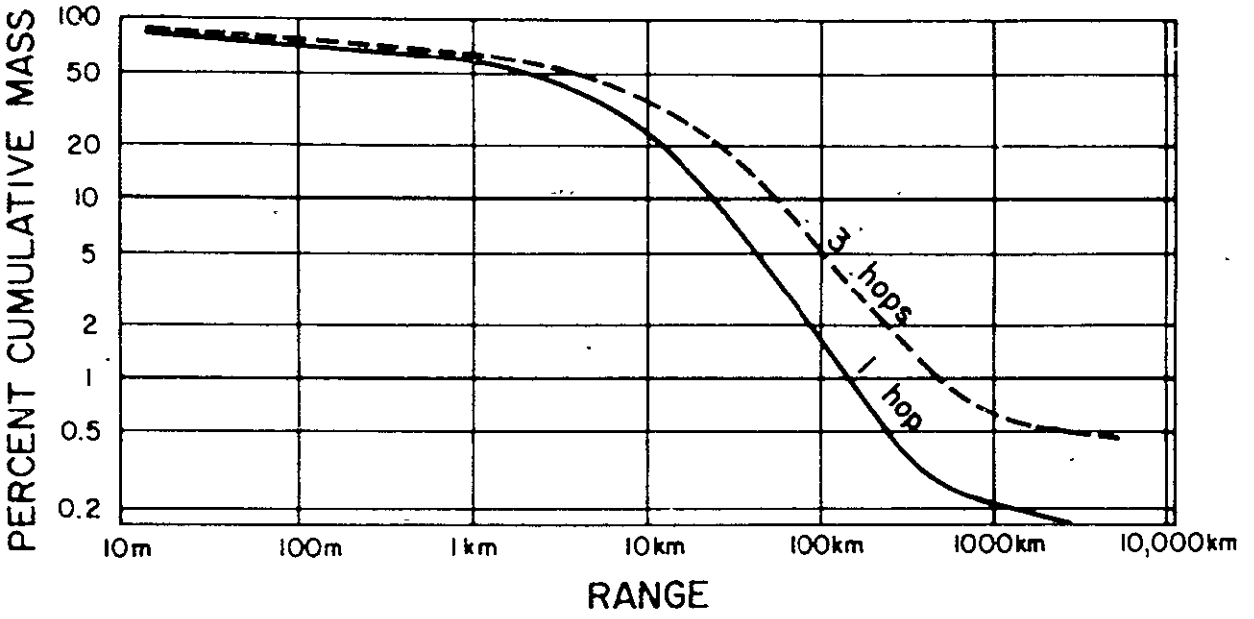

Figure IIIE-1. Cumulative curves demonstrating the percentages of debris fragments projected to various distances by a single hypervelocity impact on hard target material (1 hop), based on experimental and theoretical studies of cratering dynamics. The 3-hop curve assumes each particle was affected by three such impacts, which is probably a more realistic approximation of the transport histories of soil particles in the lunar regolith. The curves demonstrate not only the distribution of landing sites of fragments derived from a single point on the Moon, but they can also be used in the reverse sense, to tell us of the distribution of distances to the sources of a collection of soil particles taken from a single point on the Moon. Figure from Shoemaker et al. (1970).

LEGEND

U.S.G.S AGE UNIT

CId
DARK MANTLING MATERIAL

Cc
CRATER MATERIAL

COPERNICAN SYSTEM

Em
MARE MATERIAL
(includes dome material, End)

Ec
CRATER MATERIAL

ERATOSTHENIAN SYSTEM

Im
MARE MATERIAL
(includes dome material, Id)

Ic
CRATER MATERIAL

Ip
PLAINS MATERIAL
(includes Ihf on south border)

Ial
ALPES FORMATION

If
FRA MAURO FORMATION

IMBRIAN SYSTEM

IpIt, It
TERRA MATERIAL

pIr
RUGGED MATERIAL
(includes lineated material, pIl on east border)

pIc

PRE-IMBRIAN

RADII OF CIRCLES	PERCENTAGE OF SOURCE AREA ENCLOSED
3.1 km	50 %
18.8 "	75 %
100 0 "	95 %
235.0 "	97 %
470.0 "	99 %

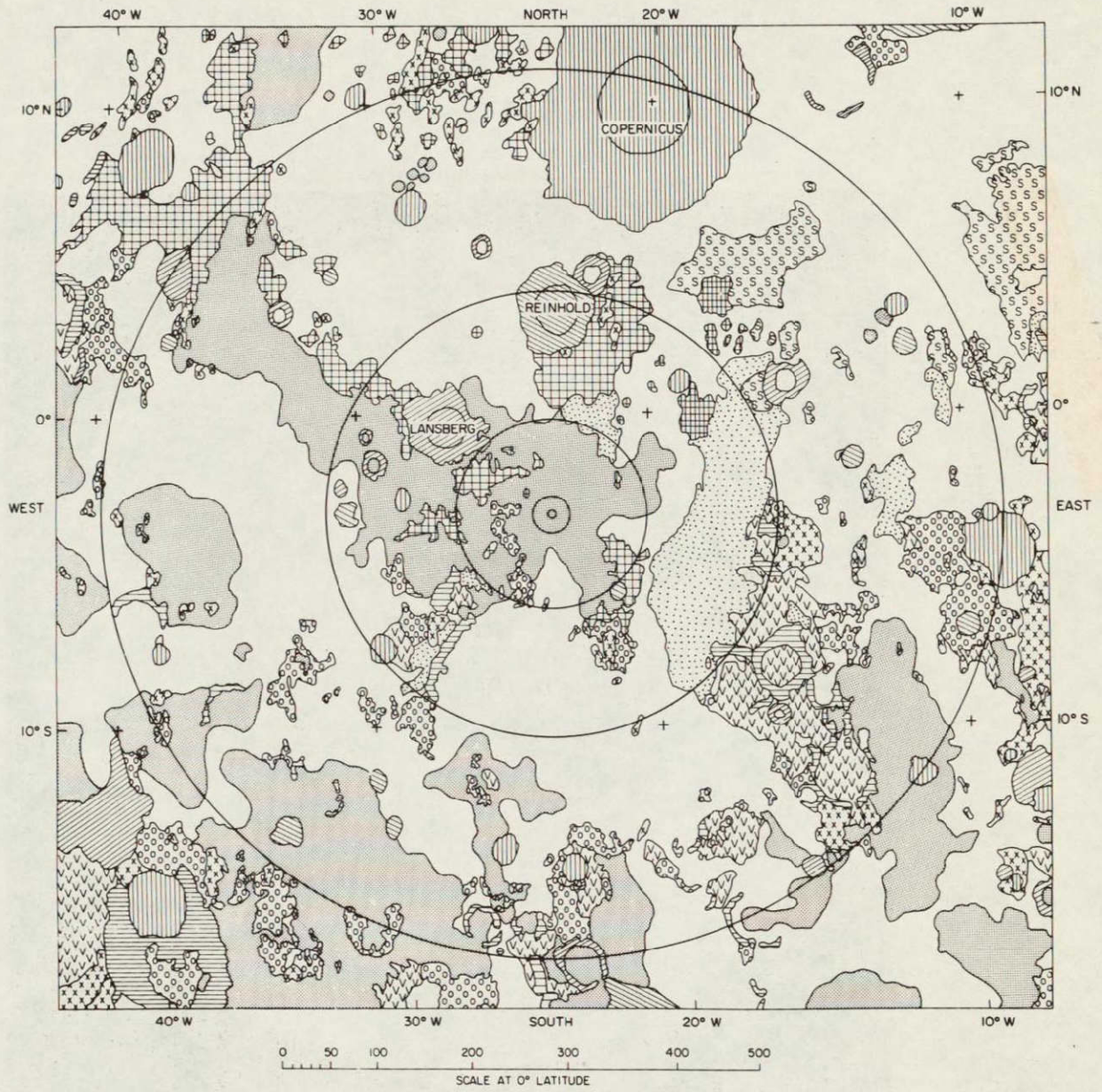

Figure IIIE-2. Regional geology of the Apollo 12 landing site. Range circles at radii taken from Figure IIIE-1 enclose predicted source areas for 99% of the regolith particles. (Geology taken from Wilhelms and McCauley (1971)).

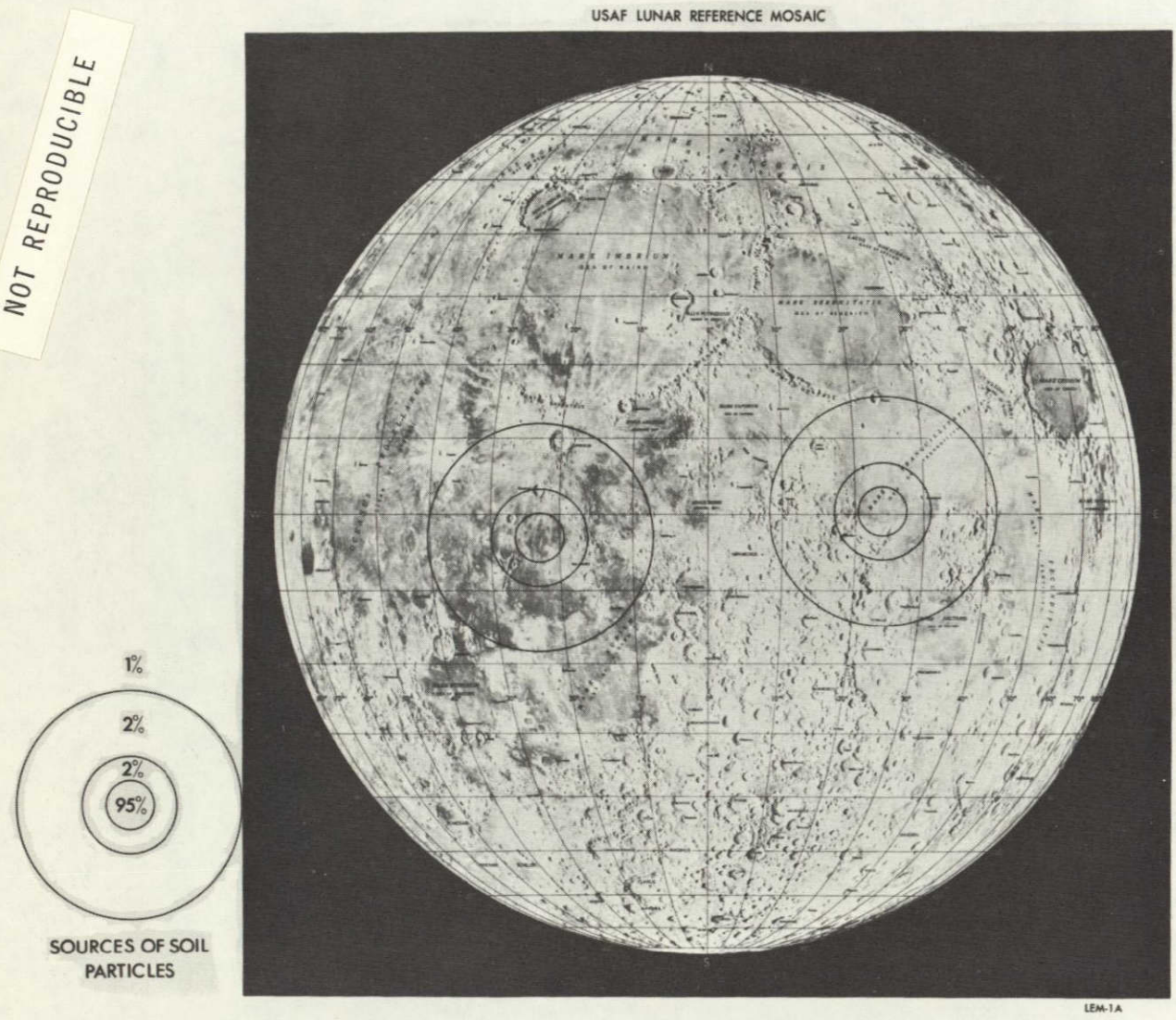

Figure IIIE-3. Range circles similar to those of Figure IIIE-2, showing predicted source areas for regolith materials at Apollo 11 and Apollo 12 landing sites.

Table IIIE-I. Predicted sources of Apollo 12 regolith particles, calculated from range-frequency distribution of geological formations.

			Percent
Dark Mare Materials			
Em	Eratosthenian basalt	89.5	93.9
Im	Imbrian basalt	4.4	
Ancient Light Terra Material			
IpIt	Undivided terra	1.0	1.4
pIr	Pre-basin rock	0.3	
pIc	Terra crater material	0.1	
Material with Uncertain Affinities			
Ial	Alpes Formation		2.5
Imbrium Ejecta			
If	Fra Mauro Formation		0.8
Early Light Plains Material			
Ip	Cayley Formation and other units		0.1
Post – pI Crater and Mantling Materials			
Cc, CId, Ec, Ic			0.4
			99.1

The range-frequency calculations are applicable only to randomly mixed regolith materials. From the sampling descriptions furnished by the astronauts, and from the diversity of particle types they contain, we conclude that our two most representative samples are 12070 and 12001. How do the contents of these samples, as shown in Section I, Table I-I, compare with those predicted by the range-frequency distribution of sources in Table IIIE-I?

Correlation of Rock Types with Source Areas

Basalts

According to Table IIIE-I, about 94% of the particles in the regolith at the Apollo 12 site should be mare materials. Of these, 90% should be Eratosthenian basalt and 4% should be Imbrian basalt. Table I-I shows that our Samples 12070 and 12001 contain 14% and 22%, respectively, of basalt rock chips together with an additional 63% and 58%, respectively, of degraded basaltic materials — soil microbreccias and cindery glasses Some of the homogeneous glasses in these samples may also be basaltic. However, both samples contain about 15% fewer basaltic particles than predicted.

The basalts of our Apollo 12 samples differ in several significant respects from the Ti-rich Apollo 11 suite. We have no way of judging whether or not the Ti-rich Apollo 11 basalts are typical of all the vast expanses of mare materials mapped as Imbrian by the U. S. Geological Survey. We found no fragments of the Apollo 11 type to correlate with the 4% of Imbrian basalts predicted in Table IIIE-I.

Norites, anorthosites

Our range-frequency data predict that the Apollo 12 regolith should contain about 6% of light-colored particles derived from several relatively high-albedo sources including areas mapped as terra material, and as Alpes, Fra Mauro, and Cayley Formations. Our coarse splits of Samples 12070 and 12001 actually contain about 18% and 10%, respectively, of light-colored

particles. Of these, the majority are the noritic rocks described in Section IIB and glasses of similar composition. Sample 12070 also contains the one grain we are calling a potash rhyolite.

Clues to the possible source rocks of the light-colored particles are furnished by their textures. The fine-grained, recrystallized fabric of the Type A norites indicates a complicated history of crystallization followed by brecciation and thermal recrystallization. We believe these particles were once part of an ancient regolith that overlay an expanse of noritic bedrock; the soil in this regolith was recrystallized at high temperatures. Subsequently, particles of it became admixed in the present mare regolith by impact projection from considerable horizontal distances and/or by excavation from beneath the local mare basalts. We believe both sources contributed. The broad field relations, where small "islands" of pre-mare terra materials protrude above the mare surface within 20 km of the landing site, suggest that the basaltic flows are shallow in this region of Oceanus Procellarum. We suggest that they cover a noritic regolith that has been partially excavated by local post-mare cratering events. A derivation from beneath the basalts as well as from the visible terra "islands" would help to explain the unexpectedly high percentage of light particles in the mare soils.

Unlike the noritic particles of Type A, those of Type B show no sign of post-shock recrystallization. They appear to have been violently excavated from a coarse-grained anorthositic bedrock. We suggest that these particles, which are relatively rare in Samples 12070 and 12001, derive from the Fra Mauro or Alpes Formations or both and therefore came, ultimately, from depth in the Imbrium basin.

Potash rhyolite

Our fragment of potash rhyolite is, we believe, too siliceous a material to represent any widespread geological formation. We suggest that its source rock is a minor, Si- and K-rich differentiate from one of the norite–anorthosite formations.

Red-brown ropy glass

This material predominates in Samples 12032 and 12033, which were taken from light streaks or layers of soil. These layers demonstrate that the assumption of random mixing does not hold for all regolith samples. The glass must therefore derive from a special source. Several investigators, including Hubbard et al. (1970) and Meyer, Aiken, Brett, McKay, and Morrison (1971), have proposed that the glass is part of the Copernican ray material seen on photographs of the landing site. We concur that it probably comes from Copernicus, not only because ray material ought to be present in the Apollo 12 soils, but also because the fragments of noritic rock and basaltic pyroxenes included in the ropy glass particles suggest a mixing of the rock types that occur in the vicinity of that crater. We do not think any substantial percentage of the Type A norite particles in the soil is derived from Copernicus, in spite of their compositional similarity to the ropy glass, since the abundance of norite particles in ropy glass-bearing soils is not greater than it is in those soils that are essentially devoid of ropy glass (12070 and 12001; see Figure I-16).

On the map, Copernicus appears to have been excavated in mare basalt. The original crater, however, is estimated to have been 10 to 20 km deep, so it undoubtedly penetrated to underlying materials: pre-Imbrian terra, Fra Mauro Formation, or both. This is consistent with chemical and mineralogical evidence that the red-brown glassy material is an admixture of norite and basalt (Section IIID), possibly representing an old pre-crater regolith, that was fused and projected to the Apollo 12 site in the Copernican event.

The greenish-yellow ropy glasses are absent from our samples of supposed ray materials and therefore cannot be ascribed to the Copernican event. We suggest that they are melted noritic rock produced by high-energy cratering events elsewhere.

Ti-rich microbreccia

The source rock of this breccia is probably a dense, ilmenite-rich cumulate formed by the settling of the earliest crystals from a basaltic magma, as discussed in Section IIID. If so, the microbreccia could have been derived from cratering events (satisfying the peculiar conditions needed to melt and reaggregate particles of the source rock) anywhere in the Imbrian or Eratosthenian basalts surrounding the landing site. The extreme rarity of breccias of this composition constitutes the main argument against undifferentiated mare basalt as the source rock.

As an alternative, the microbreccia may derive from a deposit of the dark mantling material, of Imbrian to Copernican age, mapped by the U.S. Geological Survey and interpreted as volcanic in origin. Exposures of this material (CId on Figure IIIE-2) occur between 250 and 350 km to the northeast of the Apollo 12 sampling sites.

IIIF. Structure and Evolution of the Moon

Major Types of Lunar Rock

Studies of lithic fragments from soils collected at two points on the lunar surface (and preliminary observations on material from a third site) have revealed to us the compositions of several different types of near-surface lunar rock. Since we have examined a large number of fragments (several thousand), a few percent of which are not locally derived but came from sources scattered over the near face of the Moon, it is possible that by now we have seen examples of most or all of the major rock types that comprise the outermost layer or "crust" of the Moon. These are the following:

Mare basalts,
Anorthosite,
Norite.

The lunar soils also contain rare rhyolitic fragments, but we doubt that this rock type is abundant on the Moon.

These materials are certainly underlain by some altogether different type or types of mantle rock. A lunar model in which mare basalts, anorthosite, and/or norite extend to the center of the Moon would fail to reproduce the mean mass density of the Moon, or would be completely molten at the present time (because of the high levels of radioactivity in norite and mare basalt), or both. The three rock types named are "light" igneous differentiates, and elsewhere in the Moon complementary "heavy" differentiates must exist, rocks composed of minerals that sank or were left behind when the "light" differentiates rose to the lunar surface. By analogy with terrestrial igneous systems, it seems likely that these "heavy" differentiates are composed largely of pyroxenes or olivine or both. This would be consistent with the composition of the primordial solar nebula out of which the Moon and planets

condensed; Mg, Si, and Fe were presumably the most abundant lithophile elements in the nebula, as they are in the present solar photosphere.

A Model Relating Lunar Anorthosites and Norites

We have observed (Section IIB) that two of the lunar crustal rock types, anorthosite and norite, are probably genetically related; but it seems clear from differences in chemical and mineralogical compositions and radiometric ages that the mare basalts are unrelated (or only distantly related) to the light-colored rocks. Since the latter appear to comprise the lunar terrae that surround, underlie, and predate the maria, their petrological history can be considered apart from that of the (later) mare basalts.

In Section IIIB we noted that the pyroxenes of Type A anorthosites contain less iron (lower Fe/Mg) than those of Type A norite, which in turn contain less iron than Type B anorthosite pyroxenes. The situation is summarized on the left of Figure IIIF-1, where fields representing these three classes of pyroxenes are labeled I, II, and III, respectively, in a pyroxene quadrilateral. If we are right in believing these three lunar rock types are genetically related, then the Type A anorthositic pyroxenes (I) crystallized first from the parent magma system; the norites with their pyroxenes (II) crystallized later, after crystal fractionation had increased Fe/Mg in the residual magma; and Type B anorthosites (pyroxenes III) crystallized last of all. Plagioclase compositions (Figure IIB-8) are also consistent with the crystallization of norites at an earlier stage than Type B anorthosites, though they prove nothing about the relative positions of Type A anorthosite and norite in the crystallization sequence, since the mean plagioclase compositions in these two rock types are essentially identical.

We argued in Section IIIB that the lunar anorthosites must have been formed by crystal fractionation (flotation); that the norites probably derive from magma residual after the crystallization and flotation that formed a surface anorthositic layer; and that Type A anorthositic and noritic rock (but not Type B anorthosite) was exposed on the lunar surface and crushed by the

meteorite bombardment into a fragmental layer or regolith. A model incorporating these conditions and the crystallization sequence discussed above is sketched at the right in Figure IIIF-1.

A cooling lunar surface magma system is pictured, in which continued crystallization of plagioclase and mafic minerals causes Fe/Mg and Na/Ca in the residual liquid (and in minerals separating from it at any given time) to increase with time. A floating layer of plagioclase crystals (anorthosite) forms, with low-Fe/Mg liquid in its interstices; crystallization of this liquid produces pyroxene (I). Major cratering impacts strip the anorthositic layer away locally, and noritic magma wells up. At its surface, the liquid crystallizes abruptly, much like the chill zone in a magma intrusion, to form noritic rock with pyroxene (II) whose composition reflects a more evolved state of the magma. Under the noritic "chill zone," crystallization proceeds more slowly and fractional crystallization resumes its effect, so that floating plagioclase crystals again accumulate into anorthosite, this time beneath the norite surface layer. Pyroxenes (III) in this latest anorthosite layer would have a higher Fe/Mg ratio than those in the previously formed units. Meteorite bombardment would form regoliths on the oldest anorthosite and norite exposures (the source of Type A materials) but would not often affect the deeper-seated, youngest anorthosite; this could be reached and excavated (producing Type B particles) only by especially deep cratering events.

Obviously this is a greatly simplified model, and the chaotic state of affairs on the lunar surface during the early intense bombardment of meteorites and/or planetesimals would have included remelting and mixing in various proportions of the three rock types named, at many points on the lunar surface. However, we feel the model has value as a tentative framework in which the chemical and age differences between early lunar rocks might be interpreted.

A Lunar Crustal Model Based on Gravity and Topography

We can deduce something about the placement and extent of various types of rock on the Moon from considerations of gravity and topography. Since

inhomogeneities of lunar gravity do not correspond to topographic irregularities (i.e., topographic highs do not give rise to positive gravity anomalies), the lunar surface must be underlain by bodies of rock of diverse mass density. If we can assume that masses of mare basalt, anorthosite, and norite are the principal building blocks that comprise the lunar crust, we can use the mass densities of these three rock types to conclude where each lies in the lunar crust, and what thickness of it must be present to reconcile lunar gravity with lunar topography.

Consider the hypothetical profile across the Moon shown in Figure IIIF-2, extending from Mare Imbrium to Mare Nectaris. This profile, straightened out, appears at the bottom of Figures IIIF-3, IIIF-4, and IIIF-5. Available topographic data are summarized in Figure IIIF-3; these are all the lunar elevations within 150 km of the line of profile that were measured by the U.S. Air Force A.C.I.C. (Meyer and Puffin, 1965). The topograhic form of the profile is summarized in Figure IIIF-4 and compared with variations in gravitational acceleration along the same line (Muller and Sjogren, 1969). The lack of correspondence of gravity to topography is obvious. If the lunar surface were underlain by a homogeneous material of uniform density, the two curves should have the same shape. We can say qualitatively that the lunar highlands are underlain by a less dense material than Oceanus Procellarum and Mare Nubium, since the value of gravity is essentially uniform in all these regions in spite of the presence of excess topography in the highlands. Further, Oceanus Procellarum and Mare Nubium are underlain by less dense materials than Mare Imbrium and Mare Nectaris, since the latter are topographically lower and yet exert more gravitational effect than Procellarum/Nubium. Thus,

$$\rho_{\substack{\text{highlands}\\\text{rock}}} < \rho_{\substack{\text{Procellarum and}\\\text{Nubium rock}}} < \rho_{\substack{\text{Imbrium and}\\\text{Nectaris rock}}}$$

Mass densities have not been measured for most types of lunar rock; computed values for model lunar rocks are shown in Table IIIF-I. (Note that lunar plagioclase at 1400°C is less dense than norite liquid, though not

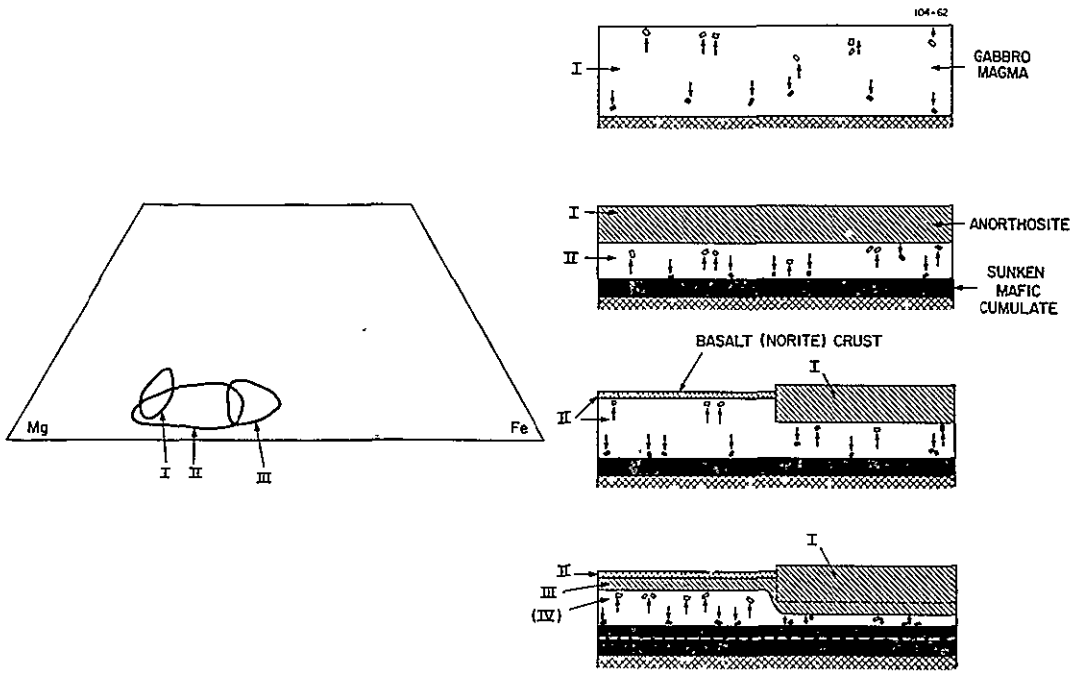

Figure IIIF-1. Left: Summary of compositional differences between pyroxenes in Type A anorthosites (I), Type A norites (II), and Type B anorthosites (III); from Figure IIB-10. Right: four-step petrological model that would account for compositional and textural differences between lunar light-colored rock types; discussed in text.

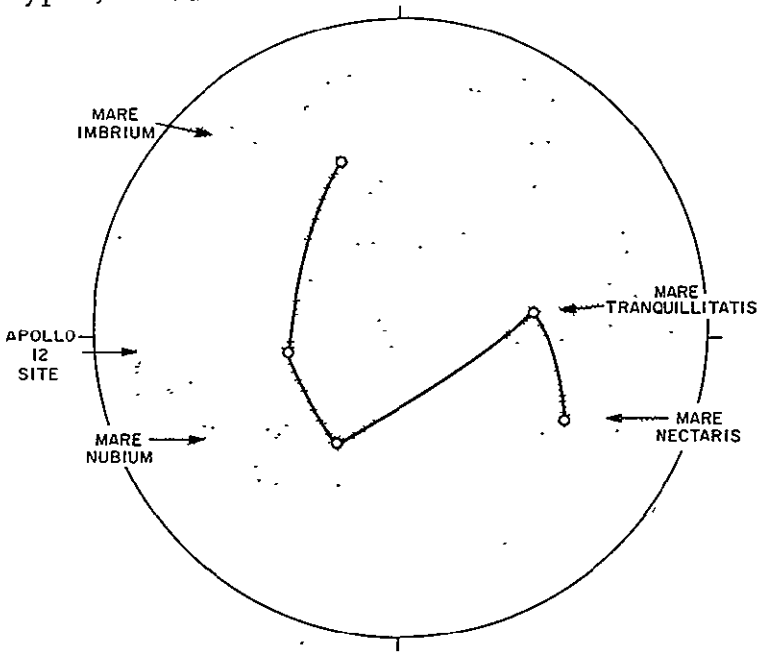

Figure IIIF-2. Lunar surface traverse leading from Mare Imbrium to Mare Nectaris. Topographic, gravitational, and subsurface structural variations along this traverse are discussed in the text and pictured in the next three figures.

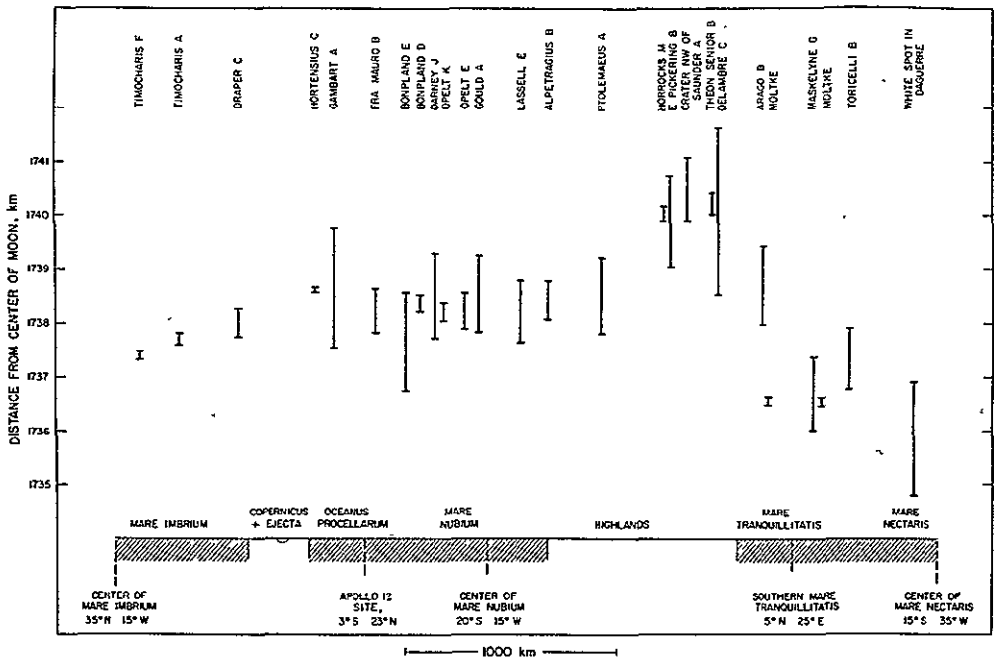

Figure IIIF-3. Lunar elevations along the traverse of Figure IIIF-2, derived from ground-based telescopic observations of the Moon at extreme librations. Data from Meyer and Puffin (1965).

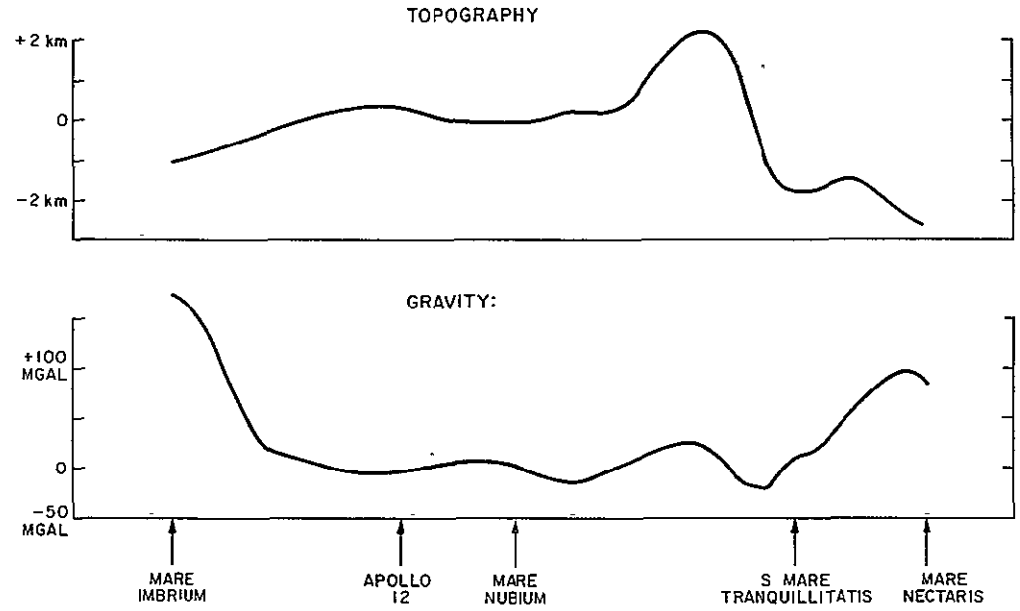

Figure IIIF-4. Comparison of topography (above: summarized from Figure IIIF-3) and variations in the acceleration due to gravity (below: Muller and Sjogren, 1969) along the traverse shown in Figure IIIF-2. Lack of similarity of the two curves means that materials having different mass densities underlie the traverse.

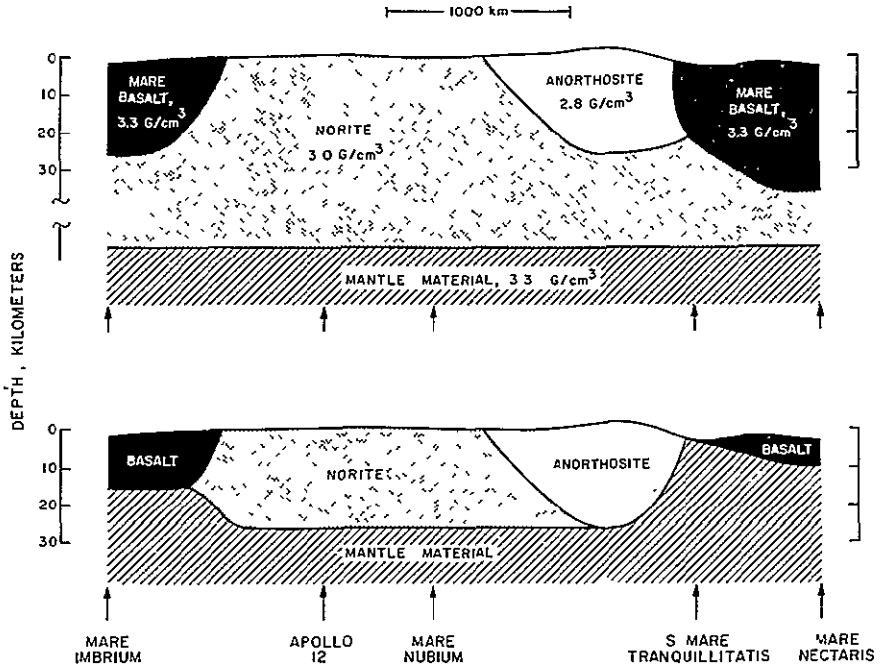

Figure IIIF-5. Two models of lunar subsurface structure that would reconcile the differences in topography and gravity shown in Figure IIIF-4. Model 1 (above) assumes no relief on the crust/mantle interface; model 2 (below) minimizes the amount of norite in the system. Basalt/mantle interfaces in model 2 are drawn arbitrarily and can be readjusted to suit the reader.

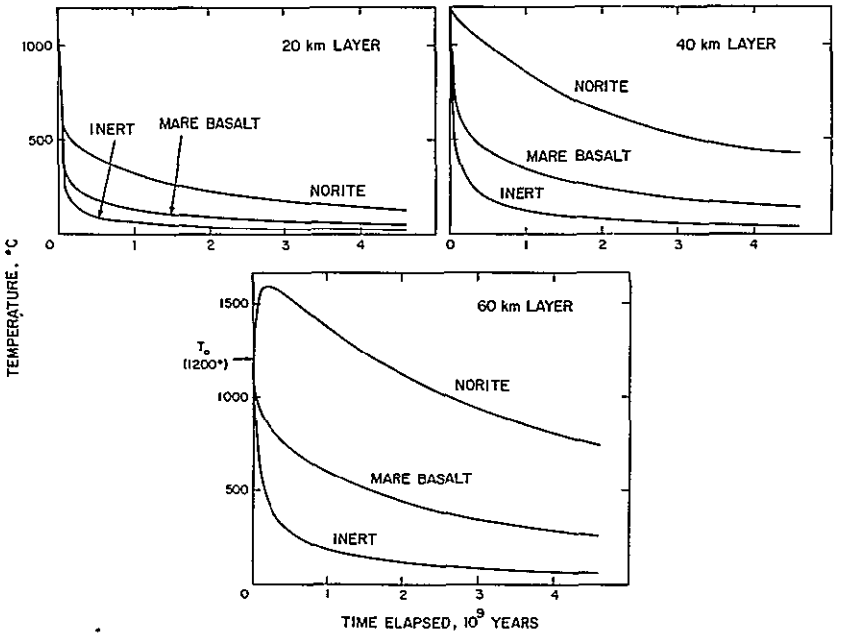

Figure IIIF-6. Thermal histories at the lunar crust/mantle interface, assuming crustal thicknesses of 20, 40, and 60 km; crustal compositions of norite, mare basalt, and inert material; a mantle (lunar interior) composed of inert material; and an initial temperature throughout the Moon of 1200°C.

Table IIIF-I. Specific gravities of representative lunar minerals and rocks, in solid and liquid states.[a]

	Mineral	Composition (mole %)	ρ, g/cm^3 25°C	ρ, g/cm^3 1400°C (solid)
A	Plagioclase	$Ab_8\ An_{92}$	2.75	2.70
B	Low-Ca pyroxene	$En_{70}\ Fs_{30}$	3.40[b]	3.26
C	Augite	$En_{40}\ Fs_{20}\ Wo_{40}$	3.48	3.33
D	Olivine	$Fo_{70}\ Fa_{30}$	3.58	3.39
E	Ilmenite		4.79	4.55

Model Rock	Composition (wt. %)	ρ, g/cm^3 (computed) 25°C	1400°C (solid)	1400°C (liquid)[c]
Tranquillitatis basalt	$A_{37}\ C_{44}\ E_{19}$	3.32	3.22	3.17
Procellarum basalt	$A_{32}\ C_{59}\ E_9$	3.28	3.17	3.04
Anorthosite	$A_{87}\ B_8\ D_5$	2.81	2.76	--
Norite	$A_{63}\ B_{34}\ E_3$	2.98	2.90	2.89

[a]Data from Clark (1966), unless otherwise indicated.

[b]Average of densities for orthopyroxene and pigeonite containing 30 mole % ferrosilite; Deer, Howie, and Zussman (1963).

[c]Computed from bulk chemical composition of model rock, by the method of Bottinga and Weill (1970).

by a wide margin; this is consistent with the idea that a plagioclase cumulate would float to the surface, not sink, as is usually the case in terrestrial basic stratiform bodies.) Anorthosite is seen to be the lightest rock type, followed by norite, and then mare basalt (the density difference between Tranquillitatis and Procellarum basalts appears to be insignificant). We propose that these three rock types, respectively, fill the roles of three progressively less dense lunar materials required by lunar gravity and topography (inequalities above).

This assignment of roles is consistent with the nature of Apollo samples returned to date. The basaltic character of lunar maria is now established, so it is not unreasonable to postulate thicknesses of it in Mare Imbrium and Nectaris sufficient to account for positive gravitational anomalies (mascons). On the other hand, we must suppose that the basaltic layer in Oceanus Procellarum is thin, affecting the local value of gravitational acceleration much less than does a thick layer of norite that underlies it. The presence of abundant norite in the Apollo 12 soils supports the idea that this rock type is near at hand; in addition, the Copernican impact appears to have penetrated the basalt layer in Oceanus Procellarum and excavated norite, which was melted and ejected along the Copernican rays. Finally, with rare exceptions anorthosite has been found only in soils collected near ancient highland terrains (Apollo 11, Luna 16 (Vinogradov, 1971)).

The Apollo 14 soil appears to consist largely of norite, not anorthosite; this would mean that the Imbrium impact (which ejected debris to the Fra Mauro region) occurred in terrain that was akin to (perhaps an extension of) the Oceanus Procellarum basin, not in a highlands area.

Using the formula for gravitational attraction over an infinite slab

$$g_z(\text{mgal}) = 41.9\ \rho L$$

(where L is the slab thickness in km) and mass densities of the three key rock types, it is possible to compute approximately the thicknesses of rock

units needed to account for the disparity in lunar gravity and topography, though no unique model can be derived. Two possible models of lunar structure that reconcile gravity with topography are shown in Figure IIIF-5.

The upper model makes the simplifying assumption that there is no relief on the lunar "moho," i.e., that the interface between crustal rocks and the lunar mantle (taken to have a mass density of 3.3 g/cm^3, the mean density of the Moon) is a spherical surface. It also involves unspecified but substantial thicknesses of norite.

This model is probably unrealistic because it involves great thicknesses of rocks that are relatively rich in radioactivity (basalt, ~ 1500 ppm K, ~0.5 ppm U, ~2 ppm Th; norite, ~5800 ppm K, ~2 ppm U (Hubbard, Gast, and Meyer, 1971), ~7 ppm Th (if Th/U is assumed to be the same as in basalt)). As G. J. Wasserburg (personal communication) has stressed repeatedly, radioactive decay in such a system would drive subcrustal temperatures to very high values. Thermal histories at the base of a crustal layer of norite, or mare basalt, or inert material, for layer thicknesses of 20, 40, and 60 km, are displayed in Figure IIIF-6. These assume a Moon that is otherwise devoid of radioactivity, but which began at a uniform initial temperature of 1200°C. Thus we are able to see how much difference basaltic or noritic radioactivity makes in the cooling history of a lunar crust that overlies an initially hot Moon. Beneath 30 km of mare basalt, the approximate amount required by model 1 of Figure IIIF-5, the temperature would stand at ~250°C after one billion years, or more if the basalt were underlain by norite as shown in model 1. At the base of a 30-km norite layer, the temperature after a billion years would be ~600°.

These temperatures are important because they affect the strength of the Moon. The maria that contain mascons are out of isostatic equilibrium and have been prevented from sinking to an equilibrium level only by the physical strength of the rock underlying them. The higher the temperatures are under the mascon maria (and therefore the higher the temperatures are in the mantle beneath), the weaker the system is and the less likely it is that the mascons

would have been supported through most of geologic time (a point reiterated on numerous occasions by H. C. Urey). Our model of lunar crustal structure gains in plausibility by minimizing the thickness of K, U, Th-rich rock in or under the mascon maria; a more credible model is shown in the lower half of Figure IIIF-5.

Here we assume that plastic flow in the lunar mantle has forced plugs of mantle material up into the mascon mare basins as suggested by Wise and Yates (1970). Levels of radioactivity in the mantle would presumably be low, so this is the best possible material with which to try to support the mascons. The depth to the mare basalt/mantle interface cannot be deduced from gravitational considerations, since the mass densities of the two substances are essentially identical. The basalt thicknesses shown in model 2 were chosen arbitrarily. If mantle plugs rose to levels of isostatic equilibrium in the mare basins before basalt filling began, only ~1 km of (superisostatic) basalt would have to be deposited to create the observed gravitational anomalies (mascons). The heating effect of radioactivity in such a thin layer of basalt would be negligible.

Model 2 still involves a substantial thickness of norite beneath Oceanus Procellarum (and, presumably, the other non-mascon maria). The high temperatures this would entail do us no harm, however, since these areas do not have to have strength to support loads that are out of isostatic equilibrium. Indeed, warmth and weakness would make it easier to understand the remarkably constant elevation of the Oceanus Procellarum – Mare Nubium plain (Figure IIIF-3).

An Evolutionary Model

A sequence of events is suggested in Figure IIIF-7 that would lead to the crustal structure discussed above. The process ends (Stage 6) with a structural cross section that is simply a more stylized version of model 2, Figure IIIF-5.

Stage 1. The fact that rocks (anorthosite, norite, granite), which are older than the mare basalts (from radiometric dating and apparent geologic relationships), are igneous differentiates requires that the Moon was at least partially melted in very early times (within 1 to 2×10^8 yr of the origin of the solar system). The minimum fraction of the Moon required to be melted and differentiated to produce structure on the scale of Figure IIIF-5 can be estimated from mass balance considerations, for any assumed overall lunar composition. Early heating may have been due to kinetic energy deposited during very rapid accretion, dissipation of tidal energy during close interaction with the Earth, electrical interactions with an early intense solar wind (T Tauri phase of the solar system), or absorption of radiant energy during a high-luminosity phase of the Sun's evolution. Most of these hypothetical processes would have concentrated their effect near the surface of the Moon. Tidal heating would be more intense at depth in the Moon (Kaula, 1963), unless surface melting had been initiated by one of the other mechanisms; in this case, tidal energy dissipation would probably be concentrated in the surface magma "oceans," possibly causing additional melting. Stage 1 in Figure IIIF-7 assumes that partial melting of the outermost layers of the Moon has generated a layer of gabbroic, possibly noritic, magma.

Stage 2. The magma system has cooled and largely crystallized; flotation of plagioclase crystals has produced an anorthosite layer at the surface, and mafic minerals have sunk to form ultramafic cumulates. Between these, a residual layer of noritic liquid remains.

Stage 3. Major planetesimal impacts have stripped away the anorthositic layer locally (as in the present Oceanus Procellarum and non-mascon maria), and underlying noritic liquid has welled up to fill them to levels of isostatic equilibrium. Obviously this involves some lateral movement of noritic liquid, from under areas of intact anorthosite to the holes in the crust.

Stage 4. The system has cooled and solidified completely; additional major impacts create mare basins (the present mascon mare basins) that are not filled by liquid.

Stage 5. Dense mantle material, possibly still relatively warm and weak from the early high-temperature stage of the Moon's outer layers or from energy deposited by the recent basin-forming collisions or both, has forced its way up into the late mare basins, in an effort to attain isostatic equilibrium. This phase of lunar history was first suggested by Wise and Yates (1970). The drawing for Stage 5 assumes that mantle plugs rose to positions of isostatic equilibrium, and in fact that the entire lunar landscape is isostatically equilibrated at this time. Note that there are highlands and lowlands in spite of the state of isostasy; the former are underlain by low-density rock, the latter by high-density material.

Stage 6. At a much later time the outer layers of the Moon have cooled and become stronger, while the interior of the Moon has been heated by K, U, and Th decay. Lava generated at depth in the Moon has erupted on the surface. It does not cover the lunar surface uniformly but fills the low places preferentially. Since the lunar surface was isostatically equilibrated before this latest lava eruption, the addition of lava at only a few localities on the surface must give rise to positive gravity anomalies (mascons) in those areas (the late mare basins). We postulate that the sub-basin mantle material had cooled sufficiently to be able to support these mascons once formed, and that lava flowed into the basins in such a way (through one-dimensional conduits) as not to warm and weaken the basin floors significantly.

This sequence of events, based on our geophysical model of crustal structure, agrees with and embraces the model of petrological evolution discussed earlier in this section and pictured in Figure IIIF-1. Regolith formation (brecciation) would have occurred on anorthositic surfaces from Stage 2 onward, and on noritic surfaces during Stages 4 and 5. We postulate that whatever energy source melted the lunar surface magma system in the first place did not halt abruptly but tapered off in intensity, so that for some time after a solid surface layer had crystallized, it and its regolith were maintained at high temperatures. At this time, much regolith material was recrystallized to form the massive Type A anorthositic and noritic breccias. It is not difficult to picture accretional activity at the lunar surface, and heat generated by it, tapering off in this fashion.

One apparent discrepancy between the two evolutionary models sketched in this section is that massive norite underlies Oceanus Procellarum in Figure IIIF-7, while in Figure IIIF-1, this material has further differentiated. However, the differentiation involves only a vertical rearrangement of densities, so would produce no significant change in the value of gravity over Oceanus Procellarum. Thus, the differentiated structure shown under Oceanus Procellarum in Figure IIIF-1 could have been specified in Figures IIIF-5 and IIIF-7 instead of uniform norite, and on petrological grounds probably should have been.

Again it is essential to recognize the high degree of simplification in this model and to be prepared for many situations where the Moon has been affected in contrary and more complicated ways. For example, the (presumably anorthositic) highlands contain many major craters filled with light-colored plains-forming material (the Cayley Formation). We would interpret this as noritic lava that flowed into the craters from beneath the anorthositic layer during Stages 2 and 3 of Figure IIIF-7. Because of the very substantial percentage of highland surface that consists of Cayley Crater fill, we predict that gamma-ray measurements of K, U, and Th levels over the lunar highlands will reveal neither the low concentrations appropriate to lunar anorthosite nor the high concentrations that would denote norite, but something in between.

Generation of the Mare Basalts

The evolutionary model in Figure IIIF-7 suggests that two great episodes of igneous activity occurred at the lunar surface: First, extensive melting and differentiation occurred at the time when the Moon was formed or soon after; and substantially later, an epoch of volcanic activity filled the mare basins with basaltic lava. Radiometric dating on the admittedly very limited suite of lunar samples collected to date tends to support this picture. Model ages for the lunar soils and for Luny Rock I and the time of the first magmatic event involved in the history of Rock 12013 (Albee, Burnett, Chodos, Haines, Huneke, Papanastassiou, Podosek, Russ, and Wasserburg, 1970b) fall in the range 4.4 to 4.6×10^9 yr; isochron ages of the basaltic rocks from the

Apollo 11 and Apollo 12 samples are generally 3.4 to 3.6×10^9 yr. The "episodes" postulated were not thermal spikes but spanned substantial periods of time; however, there is as yet no evidence of extensive lunar igneous activity in the period between them (3.6 to 4.4×10^9 yr), or later than 3.4×10^9 yr ago.

Some insight into the thermal history of the Moon can be gained by carrying out model heat-flow calculations. Results of a series of such computations are shown in Figures IIIF-8 through IIIF-10 (Wood, 1971). These figures do not show the detailed evolution of lunar temperature profiles, but only the times and places in the Moon where temperatures would have been above the melting point of basalt and where the lavas that filled the mare basins might have been generated. Parameters used in the calculations are shown in Table IIIF-II.

Model A (Figure IIIF-8) shows the appearance of a melting zone at depth (>500 km) in the simplest possible model, one that starts off uniformly cold (0°C) and contains chondritic levels of radioactivity. Model B assumes higher initial temperatures, but is otherwise identical to A. (All energy of accretion of the Moon is assumed to be conserved as heat in B, and this accretional temperature is superimposed on the 0°C of initial temperature assumed for A. This results in highest temperatures in the outermost layers of the Moon, since the more massive the Moon grew, the more strongly it attracted accreting objects and the more energetically they would have impacted. As seen in model B, 100% efficient retention of accretional energy would have heated the outermost 500 km of the Moon to above the melting temperature of basalt.)

Model B shows that the effects of an early epoch of surface melting, and later melting at depth due to radioactive decay, would have blended smoothly together. The net effect would have been a zone of melting that migrated downward in the Moon. The depth to the top of the melting zone increases monotonically with time, and one supposes that lava would erupt to the surface less and less frequently. A resurgence of volcanic activity one billion years after the Moon was formed is not predicted.

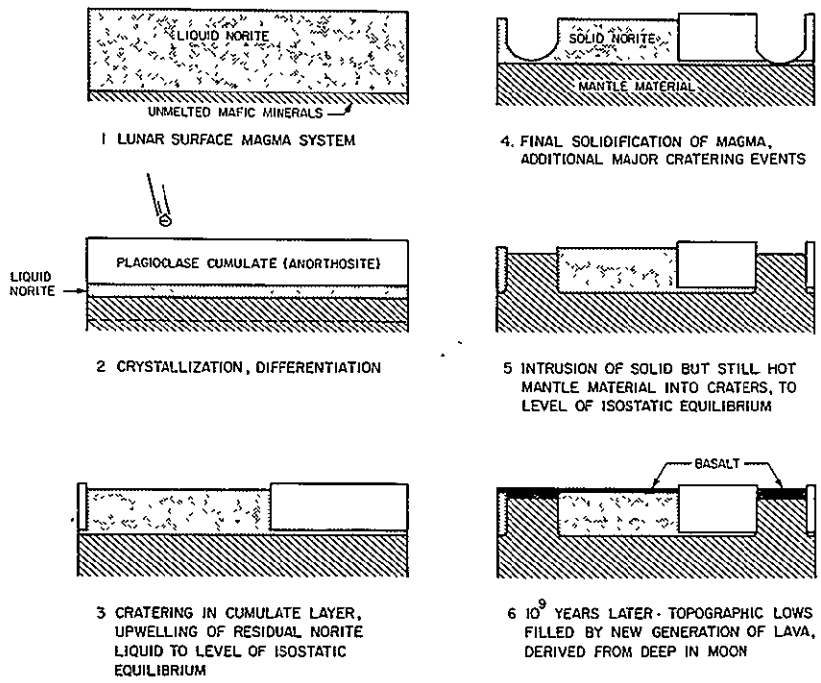

Figure IIIF-7. Sequence of events on the Moon that would give rise to near-surface structure similar to model 2 of Figure IIIF-5.

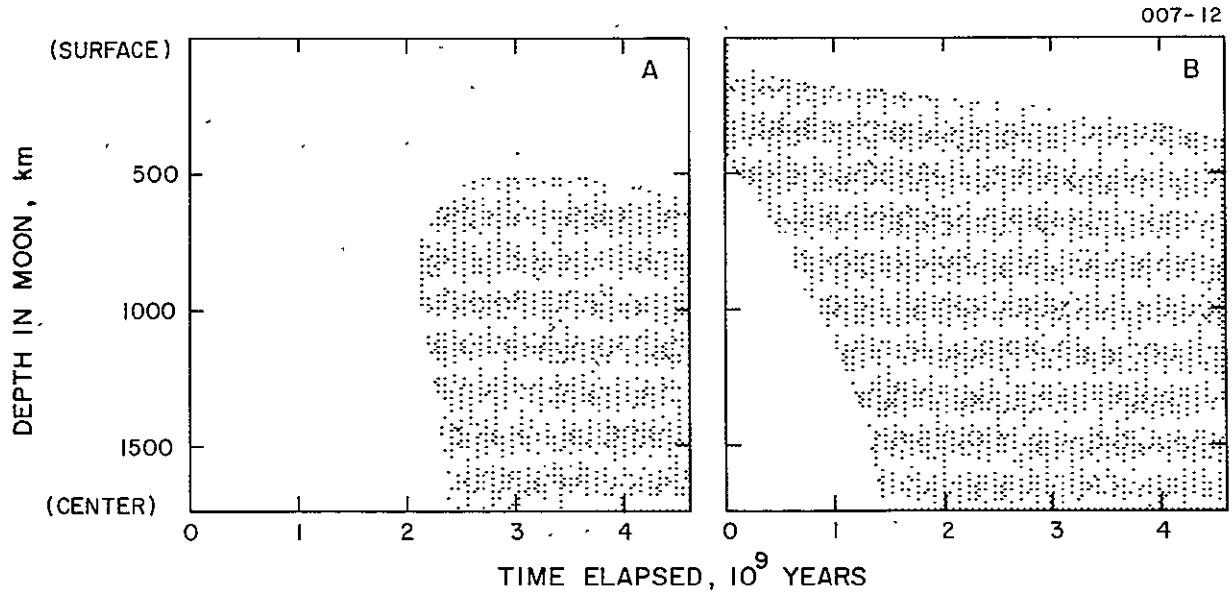

Figure IIIF-8. Melting diagrams for lunar models in which magma migration does not redistribute radioactivity. Shaded regions are above the melting temperature of basalt. A, initially cold Moon (uniform starting temperature of 0°C); B, Moon in which 100% of accretional energy is retained as heat.

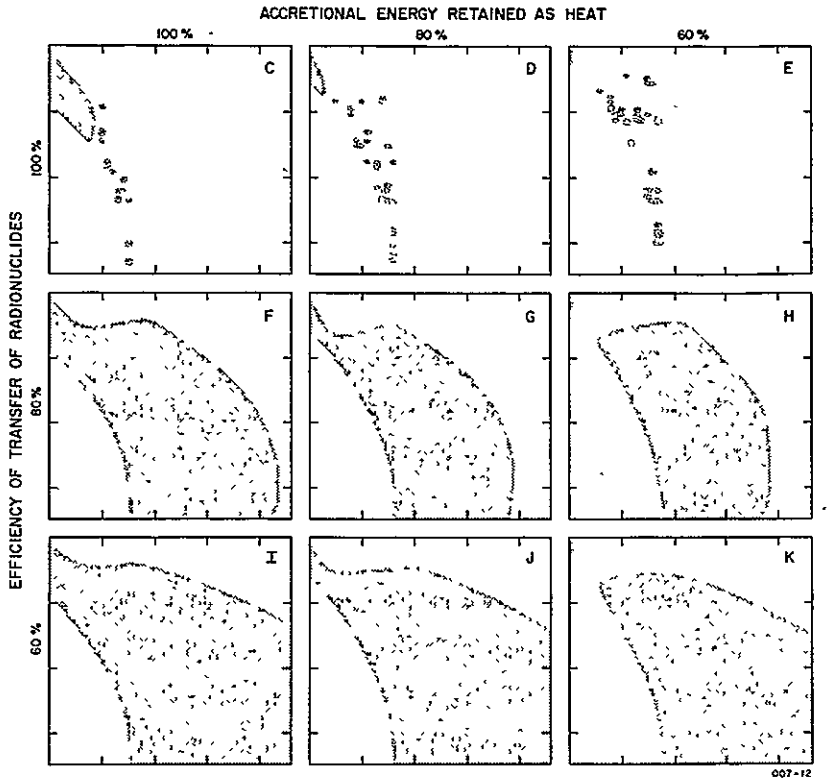

Figure IIIF-9. Melting diagrams for lunar models in which magma migration redistributes radioactivity. Several different transfer efficiencies are tried, and several values for completeness of retention of accretional energy. These models display "humps" 1.5 to 2×10^9 yr after the lunar origin, when the zone of melting rises in the Moon.

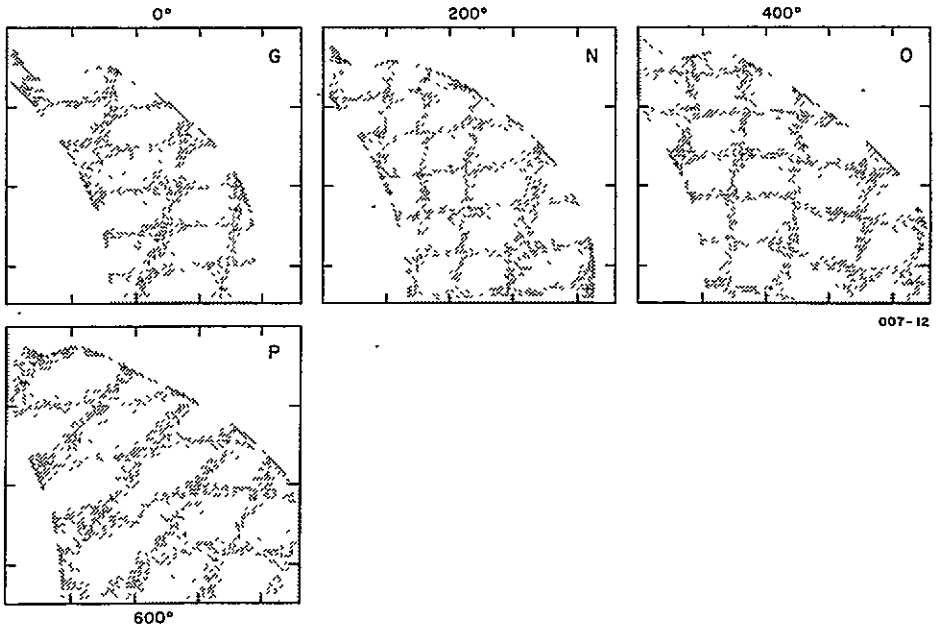

Figure IIIF-10. Comparison of model G (Figure IIIF-9) with models that start at higher base initial temperatures but are otherwise similar to G. Higher base initial temperatures cause the "hump" to occur earlier.

Table IIIF-II. Parameters employed in computer heat-flow calculations reported in Figures IIIF-8 through IIIF-10.

Radial interval between computation points: 20 km
Time interval between successive computations: 10^6 yr
Surface temperature of the Moon: 0°C
Thermal properties of lunar material:
heat capacity, 1.2 joules/g °C
lattice conductivity, 10^{-2} cal/cm sec °C
mass density, 3.35 g/cm^3
opacity, 10 cm^{-1}
refractive index, 1.7
Temperature at which basalt begins to melt:
1150°C (surface of Moon)
1627°C (center of Moon)
Present-day abundances of radioactive elements in the Moon (chondritic levels):
K, 1000 ppm
U, 0.01 ppm
Th, 0.04 ppm

The above models omit one important aspect of the high-temperature behavior of planets. It is an accident of geochemistry that the heat-generating elements K, U, and Th tend to concentrate in the first eutectic liquid that appears when a rock begins to melt. If the melt is less dense than the residual solids, as is generally the case, and tends to be driven toward the surface of the planet by density differences, it carries part of the heat-generating potential of the planet with it. This can affect the thermal history of the planet profoundly (Reynolds, Fricker, and Summers, 1966).

This effect can be at least crudely imitated in heat-flow calculations. One specifies in the program that, once a point in the Moon rises above the melting temperature of basalt, the radioactivity (or some appropriate fraction of it) at that point is translated outward along the lunar radius until it reaches a point that is below the basalt melting temperature; there it is deposited. The heat-flow models in Figure IIIF-9 include this effect. A matrix of models is shown, for several assumed values of efficiency of transfer of radioactivity and several percentages of accretional energy retained as heat. Interestingly, in most cases the melting diagram displays a "hump": The zone of melting rises closer to the surface about two billion years after the Moon was formed. This effect was first noted by McConnell, McClaine, Lee, Aronson, and Allen (1967) and is due to the accumulation of very high concentrations of radioactivity (released by melting at depth in the Moon) at the top of the melting zone. It seems plausible that this temporary rise in the boundary of the melting zone would be accompanied by increased volcanic activity at the lunar surface.

By assuming higher initial temperatures (Figure IIIF-10) or higher levels of radioactivity in the Moon, interior melting can be made to occur sooner, bringing radioactivity to the top of the melting zone at an earlier date. In this way the hump in the melting zone can be shifted to a position only one billion years after the formation of the Moon, in correspondence with the episode of volcanic activity that filled the lunar maria.

The use of chondritic proportions of radioactive elements in computing the above heat-flow models is probably very unrealistic (G. J. Wasserburg,

personal communication), but experimental runs using other elemental proportions have shown that this is relatively unimportant. The absolute amount of heat-generating potential in the system is what counts, and a level of K + U + Th (in the true lunar proportions) can be found that produces melting diagrams closely approximating those of Figures IIIF-8 through IIIF-10.

These melting diagrams seem to indicate that the lunar interior is molten at present. The actual meaning of the diagrams is that temperatures are above the melting point of basalt, but this would promote only partial melting of the lunar material; and it is not unreasonable to assume that most or all of the liquid migrated surfaceward, leaving hot but solid refractory minerals in the lunar interior. Even so, the final internal temperatures of the Moon are at odds with those deduced for the lunar interior from interactions of the Moon with the interplanetary magnetic field (Sonnett et al., 1971), unless solid-state convection has operated to cool the lunar interior more efficiently than the conductive and radiative heat transfer that were assumed for the heat-flow calculations reported above (Turcotte and Oxburgh, 1969).

It is worth noting that lava erupted at the lunar surface in connection with the appearance of a "hump" in the melting diagram would not have had a simple history. It would not have been partially melted from virgin lunar material and translated straightway to the lunar surface. Magma generated in the lunar interior would have solidified at the top of the melting zone to be subsequently remobilized when the radioactivity concentration and temperature grew high enough. The evolutionary history of mare basalts was at least this complicated, a fact that needs to be kept in mind when constructing models of trace-element fractionation.

IV. ANALYTICAL PROCEDURES

For the most part, analytical procedures employed were those we described in Section V of Wood et al. (1970). The only new technique employed was luminoscopy; this is described briefly below. We have also discussed in some detail the uncertainties involved in performing bulk chemical analyses of rocks by the defocused-beam microprobe technique, since this type of analysis has come to play an important role in lunar sample analysis.

IVA. Luminescence Techniques

We used a Nuclide Corp. luminoscope (Model ELM 2) in our luminescence studies. The instrument consists of a specimen chamber and cold cathode discharge tube, both of which are evacuated by a mechanical vacuum pump, and a high-voltage power supply. The electron beam is produced in the discharge tube and accelerated toward an anode by a potential of up to 15 kv. A slit in the anode allows a portion of the beam to pass through and onto the sample surface. A sample area of about 1 cm^2 is irradiated. The sample chamber, which rests on a microscope stage, has windows on the top and bottom, so the sample (an uncovered thin section) can be illuminated by transmitted light. A switch on the luminoscope allows the observer to alternate between transmitted light and luminescence effects while viewing the sample through the microscope. The luminescence produced is relatively feeble, so the study must be performed in a darkened room.

IVB. Defocused-Beam Analyses (DBA)

Some of the most interesting lunar rock types (anorthosite, norite, rhyolite) have so far been encountered in the lunar samples only in the form of small fragments, typically 1 or 2 mm in dimension, in the soil samples. It is important to obtain at least approximate bulk chemical compositions for

these rock types, but it is not practical to batch them for analysis by wet chemical or x-ray fluorescence techniques because similar-appearing particles can vary widely in their chemistry (e. g., the K_2O content of light-colored particles varies by two orders of magnitude). We need to analyze them individually, preferably after they have been classified petrographically. The only available means of chemically analyzing a soil fragment after it has been incorporated in a thin section is by the defocused-beam microprobe technique. This involves making a finite number of microprobe analyses, at points randomly chosen on the section surface, and averaging them. No effort is made to place the beam on discrete mineral grains; instead the beam is defocused to the maximum practical extent, so as to generate x-rays in as large a sample of section surface and as many mineral grains as possible. In our laboratory the beam is defocused to 50-μ diameter (greater spot sizes violate the focusing condition of the spectrometers seriously), and we usually perform 10 analyses on each soil fragment. More analyses would be desirable, but would severely limit the number of fragments we could analyze. As it is, we can perform full analyses (13-14 oxides) of two lithic fragments per day.

The limitations of such a technique are obvious. These stem from violation of the assumptions implicit in microprobe data reduction and from (usually) inadequate sampling of the rock.

The corrections routinely performed in reducing microprobe data assume that the sample is homogeneous, meaning that the composition of the target material that all the x-rays passed through (and were absorbed by) before emergence at the surface is taken to be identical to the composition reflected by the spectrum of x-rays emitted. In the DBA mode, however, this is not actually true. If the defocused spot covers a variety of mineral types, characteristic x-radiation of a great many elements (e. g., Si, Al, Ca, Fe, and Mg) will be excited, yet some of it will have passed through minerals (feldspars) that contain Si, Al, and Ca but no Fe or Mg, before emergence, while other x-rays will have passed through pyroxenes (for example) containing Fe, Mg, and Si but no Al and little Ca. The standard

data-reduction procedure (which we have continued to apply, in spite of this deficiency) assumes that all x-radiation was absorbed and otherwise modified by all these elements.

The sampling problem can be expressed straightforwardly in terms of the statistical uncertainty in the concentration of any oxide, as a function of its distribution in the section and the sampling geometry. This (and the breakdown of microprobe data reduction) will be discussed for several rock grain-size regimes.

Rocks with Grain Size Less than 1 μ (i.e., smaller than the depth of penetration of electrons during microprobe analysis)

In this case, x-rays traverse several mineral grains, usually of diverse composition, on their way out of the sample; a very large number of mineral grains is sampled; the preferred condition of a homogeneous target material is approximated, and errors in oxide levels reported should be small (a few percent of the amounts reported).

Grain Sizes Ranging from 1 μ up to ~100 μ (the latter dimension such that each 50-μ spot is likely to fall largely or wholly on one mineral grain)

The grain size of the great majority of lithic fragments from the lunar soil falls in this range. Here the statistical uncertainty (one sigma) in the concentration obtained for a given element or oxide, in the simplest case where it occurs in only one mineral species, can be estimated from the formula

$$\sigma = \frac{\sqrt{N}}{N} \times 100 = \frac{d}{\sqrt{Am}} \times 100 \quad ,$$

where

σ = uncertainty (percent of the concentration reported),

N = number of grains of the mineral bearing that element, falling in the area swept by the probe,

d = mean linear dimension of the above mineral,

A = total area sampled by defocused probe spots, and

m = modal proportion of the above mineral in the rock.

Sampling uncertainties calculated for our analytical conditions, assuming several different grain dimensions and modal proportions for the mineral containing the element reported, are shown in Table IVB-I.

The problem of unrealistic probe data-reduction procedures is at its worst in this size range. However, the corrections applied amount to at most about 15% of the concentration reported (absorption correction for Al in the presence of Mg); only a portion of this correction is likely to be erroneous; and there is a tendency for errors in corrections to average out, though not completely, among 10 spots analyzed. The amount of error introduced during data reduction is small compared with sampling uncertainty under most circumstances (Table IVB-I), except possibly for Al.

Grain Sizes Ranging from ~100 μ to ~300 μ (the limit beyond which so few mineral grains are contained in a rock fragment from the lunar soil that it is impossible to obtain a decently representative analysis by DBA or any other means)

Sometimes it seems worthwhile to obtain approximate analyses of relatively coarse-grained rocks. In this range the microprobe data-reduction problem diminishes, because most analyses are performed in homogeneous monomineralic target material, even if the beam is defocused. The expression for sampling uncertainty changes: The total area analyzed no longer matters; if the grain size is so coarse that the analytical spot is bound to fall in a single mineral grain, it is immaterial whether the spot diameter is 50 or 1 μ in diameter. What counts is the number of spots averaged, and the interval between them. If the interval between spots is larger than the grain dimension, so that multiple analyses are unlikely to be performed in a single grain (this condition is satisfied in the 100- to 300-μ grain size range; our analytical points are determined by a grid pattern, expanded to fill the lithic fragment as uniformly as possible), the sampling uncertainty becomes

Table IVB-I. Sampling error (1σ) in DBA analysis of an element occurring in a single mineral species, assuming 10 spots of 50-μ diameter are analyzed and averaged.

Grain diameter (d)	Modal proportion of mineral in rock (m)		
	1%	10%	30%
1 μ	7%	2.2%	1.3%
10 μ	70	22	13
$\geq$100 μ	316	100	58

$$\sigma = \frac{\sqrt{N}}{N} \times 100 = \frac{1}{\sqrt{mn}} \times 100 \quad ,$$

where n is the number of spot or point analyses averaged. Sampling uncertainties for ≥100-μ grain size reported in Table IVB-I are computed from this formula, for 10 analysis spots.

As a check of the DBA technique, we have analyzed two terrestrial basalts of different grain size, whose compositions are known from wet-chemical analyses. Results of defocused-beam analyses of the USGS standard diabase W-1 (average grain size about 1000 μ), and of a finer grained Hawaiian tholeiite (K-3) from the 1955 Keekee flow east of Kilauea (average grain size, 20 μ), are shown in Table IVB-II. Compositions based on the average of groups of 10 points and 20 points are compared with accepted wet-chemical values in each case.

The grain size of K-3 is comparable to lunar lithic fragments; W-1 is very much coarser. The latter would appear to be too coarse to attempt to analyze, according to the criteria discussed above, but since our sample of W-1 was a full-sized thin section instead of a millimeter-sized lithic fragment, we were able to expand the grid of analysis points to intervals greater than the grain size. In this case, the sampling uncertainty (per 10 points) is that given in line three of Table IVB-I.

The reproducibility of two 10-spot analyses should be better for K-3 than for W-1, and it is. Deviations between DBA analyses of K-3 are consistent with the sampling errors predicted by Table IVB-I. On the other hand, taking all elements into account, the DBA of W-1 should be more accurate than that of K-3 if errors in microprobe data reduction are important, since these should be less serious in the very coarse-grained W-1 than in K-3. In fact, the match between DBA and wet-chemical analysis is better for K-3. The nature of analytical discrepancies for W-1 shows that a disproportionately large number of plagioclase grains were sampled during both 10-spot DBAs, relative to the samples of W-1 analyzed by wet chemistry. It seems likely that our whole thin section is more feldspathic than W-1 in general is.

Table IVB-II. A comparison of defocused-beam analyses with wet-chemical analyses for two terrestrial basalts.

	USGS Standard Diabase W-1				Hawaiian Tholeiite K-3			
	DBA				DBA			
	Spots 1-10	Spots 11-20	Spots 1-20	Wet-chemical analysis[a]	Spots 1-10	Spots 11-20	Spots 1-20	Wet-chemical analysis[b]
SiO_2	55.15	52.10	53.63	52.64	51.29	51.22	51.26	50.55
TiO_2	0.63	0.28	0.46	1.07	2.97	2.64	2.81	3.65
Al_2O_3	20.38	18.79	19.58	14.85	15.51	16.36	15.92	13.84
Cr_2O_3	0.00	0.03	0.02	0.01	0.01	0.01	0.01	0.02
FeO	5.72	6.64	6.18	9.98	10.46	11.59	11.00	12.12
MnO	0.14	0.12	0.13	0.17	0.17	0.18	0.18	0.18
MgO	4.17	5.14	4.66	6.62	5.46	5.40	5.43	6.19
CaO	9.02	10.77	9.90	10.96	10.35	9.78	10.08	10.10
Na_2O	3.36	2.60	2.98	2.15	2.65	2.81	2.72	2.61
K_2O	0.32	0.59	0.46	0.64	0.59	0.57	0.58	0.67
NiO	0.00	0.02	0.01	0.008	0.02	0.02	0.02	0.02
P_2O_5	nd	nd	nd	0.14	nd	nd	nd	—
SO_3	0.05	0.05	0.05	—	0 04	0.07	0.05	0.00
Total	98.94	97.14	98.04	100 05	99.54	100.64	100.07	100.15

[a]Fleischer (1969).

[b]MacDonald and Eaton (1964).

The discrepancy in Al_2O_3 for W-1 can be attributed to this feldspar excess, but in the case of K-3 it is probably due to the breakdown of microprobe correction procedures. The latter assume that Al characteristic radiation has to pass through and be absorbed by Mg-bearing target material, and they increase the amount of Al reported to compensate for this; much of the correction is unwarranted, however, because most Al radiation is in fact generated in plagioclase and escapes from that mineral without having been absorbed by Mg (which resides in pyroxene grains). Consequently, Al_2O_3 levels gotten by DBA tend to be too high.

DBA analyses of both rocks are deficient in TiO_2. We are at a loss to understand this discrepancy. For other elements, a satisfactory agreement exists between DBA and wet-chemical analysis. In the present report, the principal use of DBA was to obtain the analyses of light-colored particles reported in Table IIB-I. From Tables IVB-I and IVB-II, we estimate the following overall uncertainties for the Table IIB-I analyses: SiO_2, ~2% of the amount reported; Al_2O_3, FeO, MnO, MgO, CaO, and Na_2O, ~15%; Cr_2O_3 and K_2O, ~30%; TiO_2 and P_2O_5, ~70%.

V. ACKNOWLEDGMENTS

NASA grant NGL 09-015-150 supported our research in part and paid the salary of two of us (JSD and JBR). We are grateful to Thomas C. Marvin for assistance in evaluating the geologic sources of our lithic fragments, and to J. Jedwab (Free University of Brussels) and A. N. Simonenko (Committee on Meteorites of the U. S. S. R. Academy of Sciences) for translating our abstract into French and Russian.

VI. REFERENCES

ADAMS, J. B., and McCORD, T. B.

1971. Alteration of lunar optical properties: age and composition effects. Science, vol. 171, pp. 567-571.

AGRELL, S. O., BOYD, F. R., BUNCH, T. E., CAMERON, E. N., DENCE, M. R., DOUGLAS, J. A. V., HAGGERTY, S. E., JAMES, O. B., KEIL, K., PECKETT, A., PRINZ, M., PLANT, A. G., and TRAILL, R. J.

1970. Titanian chromite, aluminian chromite and chromian ulvöspinel from Apollo 11 rocks. Proc. Apollo 11 Lunar Sci. Conf., Geochim. Cosmochim. Acta, vol. 34, Suppl. 1, pp. 801-837.

ALBEE, A. L., BURNETT, D. S., CHODOS, A. A., EUGSTER, O. J., HUNEKE, J. C., PAPANASTASSIOU, D. A., PODOSEK, F. A., RUSS, G. P., SANZ, H. G., TERA, F., and WASSERBURG, G. J.

1970. and 1970a. Ages, irradiation history, and chemical composition of lunar rocks from the Sea of Tranquillity. Science, vol. 167, pp. 463-466.

ALBEE, A. L., BURNETT, D. S., CHODOS, A. A., HAINES, E. L., HUNEKE, J. C., PAPANASTASSIOU, D. A., PODOSEK, F. A., PRICE, G., TERA, F., and WASSERBURG, G. J.

1971. Rb-Sr ages, chemical abundance patterns and history of lunar rocks. Paper presented at Apollo 12 Lunar Science Conference, Houston, January (unpublished proceedings).

ALBEE, A. L., BURNETT, D. S., CHODOS, A. A., HAINES, E L., HUNEKE, J C, PAPANASTASSIOU, D. A., PODOSEK, F. A., RUSS, G. P., and WASSERBURG, G. J.

1970b. Mineralogic and isotopic investigations on lunar rock 12013. Earth Planet. Sci. Lett., vol. 9, pp. 137-163.

ALBEE, A. L., and CHODOS, A. A.

1970. Microprobe investigations on Apollo 11 samples. Proc. Apollo 11 Lunar Sci. Conf., Geochim. Cosmochim. Acta, vol. 34, Suppl. 1, pp. 135-157.

BOTTINGA, Y., and WEILL, D. F.

1970. Densities of liquid silicate systems calculated from partial molar volumes of oxide components. Amer. Journ. Sci., vol. 269, pp. 169-182.

BURNHAM, C W.

1962. Crystallography lattice constant refinement. Carnegie Inst. Wash. Year Book 6, vol. 132, pp. 132-135.

CARTER, N. L., RALEIGH, C. B., and DeCARLI, P. S.

1968. Deformation of olivine in stony meteorites. Journ. Geophys. Res., vol. 73, pp. 5439-5461.

CHAO, E. C. T., BOREMAN, J. A., and MINKIN, J. A.

1971. Unshocked and shocked Apollo 11 and 12 microbreccias: characteristics and some geologic implications. Paper presented at Apollo 12 Lunar Science Conference, Houston, January (unpublished proceedings).

CLARK, S. P., Jr.

1966. Handbook of Physical Constants. Geol. Soc. Amer. Mem., vol. 97, 587 pp.

COMPSTON, W., CHAPPELL, B. W., VERNON, M. J., BERRY, H., and KAYE, M.

1971. Chemistry and Rb-Sr ages for Apollo 12 lunar material. Paper presented at Apollo 12 Lunar Science Conference, Houston, January (unpublished proceedings).

DEER, W. A., HOWIE, R. A., and ZUSSMAN, J.

1963. Chain Silicates. Vol. 2 of Rock-Forming Minerals, Longmans, Green & Co. Ltd., London, 379 pp.

DRAKE, M. J., McCALLUM, I. S., McKAY, G. A., and WEILL, D. F.

1970. Mineralogy and petrology of Apollo 12 sample no. 12013: a progress report. Earth Planet. Sci. Lett., vol. 9, pp. 103-123.

DUKE, M. B., WOO, C. C., SELLERS, G. A., BIRD, M. L., and FINKLEMAN, R. B.

1970. Genesis of lunar soil at Tranquillity Base. Proc. Apollo 11 Lunar Sci. Conf., Geochim. Cosmochim. Acta, vol. 34, Suppl. 1, pp. 347-361.

FLEISCHER, M.

1969. U.S. geological standards – I. Additional data on rocks G-1 and W-1, 1965-1967. Geochim. Cosmochim. Acta, vol. 33, pp. 65-80.

FUCHS, L. H.

1970. Fluorapatite and other accessory minerals in Apollo 11 rocks. Proc. Apollo 11 Lunar Sci. Conf., Geochim. Cosmochim. Acta, vol. 34, Suppl. 1, pp. 475-479.

1970. Orthopyroxene – plagioclase fragments in the lunar soil from Apollo 12. Science, vol. 169, pp. 866-868.

FUNKHOUSER, J. G., BOGARD, D. D., and SCHAEFFER, O. A.

1971. Rare gas analysis of Apollo 11 and 12 core tubes. Paper presented at Apollo 12 Lunar Science Conference, Houston, January (unpublished proceedings).

GAULT, D. E., SHOEMAKER, E. M., and MOORE, H. J.

1963. Spray ejected from the lunar surface by meteoroid impact. NASA Tech. Note D-1767, 39 pp.

GIBB, F. G. F., STUMPFL, E. F., and ZUSSMAN, J.

1970. Opaque minerals in an Apollo 12 rock. Earth Planet. Sci. Lett., vol. 9, pp. 217-224.

GOLDSTEIN, J. I., HENDERSON, E. P., and YAKOWITZ, H.

1970. Investigation of lunar metal particles. Proc. Apollo 11 Lunar Sci. Conf., Geochim. Cosmochim. Acta, vol. 34, Suppl. 1, pp. 499-512.

GOLDSTEIN, J. I., and YAKOWITZ, H.

1971. Metal particles and inclusions in the Apollo 12 lunar soil. Paper presented at Apollo 12 Lunar Science Conference, Houston, January (unpublished proceedings).

GREEN, D. H.

1971. Experimental petrology and petrogenesis of Apollo 12 basalts. Trans. Amer. Geophys. Union, vol. 52, p. 272.

HEINRICH, E. W.

1966. The Geology of Carbonatites. Rand McNally, Chicago, 555 pp.

HEINRICH, E. W., LEVINSON, A. A., AXELROD, J. M., and MILTON, C.

1958. Niobium-tantalum rare earth minerals of Ravalli County, Montana, and Lehmi County, Idaho (abstract). Bull. Geol. Soc. Amer., vol. 69, pp. 1580-1581.

HUBBARD, N. J., GAST, P. W., and MEYER, C.

1971. The origin of the lunar soil based on REE, K, Rb, Ba, Sr, P and $Sr^{87/86}$ data. Paper presented at Apollo 12 Lunar Science Conference, Houston, January (unpublished proceedings).

HUBBARD, N. J., MEYER, C., Jr., GAST, P. W., and WEISMANN, H.

1971. The composition and derivation of Apollo 12 soils. Earth Planet. Sci. Lett., vol. 10, pp. 341-350.

KAULA, W. M.

1963. Tidal dissipation in the moon. Journ. Geophys. Res., vol. 68, pp. 4959-4965.

KEIL, K., BUNCH, T. E., and PRINZ, M.

1970. Mineralogy and composition of Apollo 11 lunar samples. Proc. Apollo 11 Lunar Sci. Conf., Geochim. Cosmochim. Acta, vol. 34, Suppl. 1, pp. 561-598.

LSPET

1970a. Lunar sample information catalog — Apollo 12. LRL, NASA Manned Spacecraft Center, Houston.

1970b. Preliminary examination of lunar samples from Apollo 12. Science, vol. 167, pp. 1325-1339.

MacDONALD, G. A., and EATON, J. P.

1964. Hawaiian volcanoes during 1955. U.S. Geol. Surv. Bull. 1171.

MASON, B., MELSON, W. G., HENDERSON, E. P., JAROSEWICH, E., and NELEN, J.

1971. Mineralogy and petrography of some Apollo 12 samples. Paper presented at Apollo 12 Lunar Science Conference, Houston, January (unpublished proceedings).

McCONNELL, R. K., McCLAINE, L. A., LEE, D. W., ARONSON, J. R., and ALLEN, R. V.

1967. A model for planetary igneous differentiation. Rev. Geophys., vol. 5, pp. 121-172.

McKAY, D. S., GREENWOOD, W. R., and MORRISON, D. A.

1970. Origin of small lunar particles and breccia from the Apollo 11 site. Proc. Apollo 11 Lunar Sci. Conf., Geochim. Cosmochim. Acta, vol. 34, Suppl. 1, pp. 673-694.

McKAY, D., MORRISON, D., LINDSAY, J., and LADLE, G

1971. Apollo 12 soil and breccia. Paper presented at Apollo 12 Lunar Science Conference, Houston, January (unpublished proceedings).

MEYER, C., Jr., AIKEN, F. K., BRETT, R., McKAY, D. S., and MORRISON, D. A.

1971. Rock fragments and glasses rich in K, REE, P in Apollo 12 soils: Their mineralogy and origin. Paper presented at Apollo 12 Lunar Science Conference, Houston, January (unpublished proceedings).

MEYER, D. L., and PUFFIN, B. W.

1965. Coordinates of lunar features: Group I and II solutions. Aeronautical Chart and Information Center Tech. Paper No. 15, 95 pp.

MOORE, C. B., LEWIS, C. F., and NAVA, D.

1969. Superior analyses of iron meteorites. In Meteorite Research, ed. by P. M. Millman, Springer-Verlag, New York, pp. 738-748.

MOREY, G. W.

1954. The Properties of Glass. Reinhold Publ. Co., New York.

MORRISON, G. H., GERARD, J. T., KASHUBA, A. T., GANGADHARAM, E. V., ROTHENBERG, A. M., POTTER, N. M., and MILLER, G. B.

1970. Elemental abundances of lunar soil and rocks. Proc. Apollo 11 Lunar Sci. Conf., Geochim. Cosmochim. Acta, vol. 34, Suppl. 1, pp. 1383-1392.

MORRISON, G. H., GERARD, J. T., POTTER, N. M., GANGADHARAM, E. V., ROTHENBERG, A. M., and BURDO, R. A.

1971. Elemental abundances of lunar soil and rocks from Apollo 12. Paper presented at Apollo 12 Lunar Science Conference, Houston January (unpublished proceedings).

MULLER, P. M., and SJOGREN, W. L.

1969. Lunar gravity map. Distributed at Goddard Institute for Space Studies, Conference on Recent Developments in Lunar Studies, New York, June 6-7.

PAPANASTASSIOU, D. A., and WASSERBURG, G. J.

1970. Rb-Sr ages from the Ocean of Storms. Earth Planet. Sci. Lett., vol. 8, pp. 269-278.

PATTERSON, J. H., TURKEVICH, A. L., FRANZGROTE, E. J., ECONOMOU, T. E., and SOWINSKI, K. P.

1970. Chemical composition of the lunar surface in a terra region near the crater Tycho. Science, vol. 163, pp. 825-828.

QUAIDE, W., and BUNCH, T. E.

1970. Impact metamorphism of lunar surface materials. Proc. Apollo 11 Lunar Sci. Conf., Geochim. Cosmochim. Acta, vol. 34, Suppl. 1, pp. 711-729.

RAMDOHR, P., and EL GORESY, A.

1970. Opaque minerals of the lunar rocks and dust from Mare Tranquillitatis. Science, vol. 167, pp. 615-619.

REID, A. M., MEYER, C., Jr., HARMON, R. S., and BRETT, R.

1970. Metal grains in Apollo 12 igneous rocks. Earth Planet. Sci. Lett., vol. 9, pp. 1-5.

REYNOLDS, R. T., FRICKER, P. E., and SUMMERS, A. L.

1966. Effects of melting upon thermal models of the earth. Journ. Geophys. Res., vol. 71, pp. 573-582.

RINGWOOD, A. E., and ESSENE, E.

1970. Petrogenesis of Apollo 11 basalts, internal constitution, and origin of the moon. Proc. Apollo 11 Lunar Sci. Conf., Geochim. Cosmochim. Acta., vol. 34, Suppl. 1, pp. 769-799.

ROEDDER, E., and WEIBLEN, P. W.

1970. Lunar petrology of silicate melt inclusions, Apollo 11 rocks. Proc. Apollo 11 Lunar Sci. Conf., Geochim. Cosmochim. Acta, vol. 34, Suppl. 1, pp. 801-837.

ROSE, H. J., Jr., CUTTITTA, F., ANNELL, C. S., CARRON, M. K., CHRISTIAN, R. P., DWORNIK, E. J., HELZ, A. W., and LIGON, D. T., Jr.

1971. Semi-micro analysis of Apollo 12 samples. Paper presented at Apollo 12 Lunar Science Conference, Houston, January (unpublished proceedings).

SHOEMAKER, E. M., and HACKMAN, R. J.

1962. Stratigraphic basis for a lunar time scale. In The Moon, ed. by Z. Kopal and Z. K. Mikhailov, Academic Press, London, pp. 289-300.

SHOEMAKER, E. M., HAIT, M. H., SWANN, G. A., SCHLEICHER, D. L., SCHABER, G. G., SUTTON, R. L., DAHLEM, D. H., GODDARD, E. N., and WATERS, A. C.

1970. Origin of the lunar regolith at Tranquillity Base. Proc. Apollo 11 Lunar Sci. Conf., Geochim. Cosmochim. Acta, vol. 34, Suppl. 1, pp. 2399-2412.

SIPPEL, R. F.

1968. Sandstone petrology, evidence from luminescence petrography. Journ. Sed. Pet., vol. 38, pp. 530-554.

SIPPEL, R. F., and SPENCER, A. B.

1970. Luminescence petrography and properties of lunar crystalline rocks and breccias. Proc. Apollo 11 Lunar Sci. Conf., Geochim. Cosmochim. Acta, vol. 34, Suppl. 1, pp. 2413-2426.

SMITH, J. V., ANDERSON, A. T., NEWTON, R. C., OLSEN, E. J., and WYLLIE, P. J.

1970. Petrologic history of the moon inferred from petrography, mineralogy, and petrogenesis of Apollo 11 rocks. Proc. Apollo 11 Lunar Sci. Conf., Geochim. Cosmochim. Acta, vol. 34, Suppl. 1, pp. 897-925.

SONNETT, C. P., SMITH, B. F., COLBURN, D. S., SCHUBERT, G., SCHWARTZ, K., DYAL, P., and PARKIN, C. W.

1971. The lunar electrical conductivity profile: mantle-core stratification, near surface thermal gradient, heat flux and composition. Paper presented at Apollo 12 Lunar Science Conference, Houstor January (unpublished proceedings).

STRAUMANIS, M. E., EJIMA, T., and JAMES, W. J.

1961. The TiO_2 phase explored by the lattice constant and density method. Acta Crystall., vol. 14, pp. 493-497.

SWANN, G. A., SCHABER, G. G., and SUTTON, R. L.

1970. Geology of the Apollo 11 and Apollo 12 landing sites (abstract). Annual meeting, Geol. Soc. Amer., vol. 2, no. 7, pp. 697-698.

SWANSON, H. E., FUYAL, R. K., and UGRINIC, G. M.

1955. National Bureau of Standards Circular 539, vol. 4, p. 69.

TURCOTTE, D. L., and OXBURGH, E. R.

1969. Implications of convection within the moon. Nature, vol. 223, pp. 250-251.

VAN DIGGELEN, J.

1969. A photometric investigation of the lunar crater rays. The Moon, vol. 1, pp. 67-84.

VINOGRADOV, A. P.

1971. Preliminary data on lunar ground brought to earth by automatic probe "Luna-16." Paper presented at Apollo 12 Lunar Science Conference, Houston, January (unpublished proceedings).

WARNER, J. L.

1970. Apollo 12 crystalline rocks — a preliminary classification. NASA Manned Spacecraft Center preprint.

WEILL, D. F., McCALLUM, I. S., BOTTINGA, Y., DRAKE, M. J., and McKAY, G. A.

1970. Mineralogy and petrology of some Apollo 11 igneous rocks. Proc. Apollo 11 Lunar Sci. Conf., Geochim. Cosmochim. Acta, vol. 34, Suppl. 1, pp. 937-955.

WILHELMS, D. E., and McCAULEY, J. F.

1971. Geologic map of the near side of the moon. U. S. Geodetic Survey Miscellaneous Investigation, MAP I 703, in press.

WILLIS, J. P., AHRENS, L. H., DANCHIN, R. V., ERLANK, A. J., GURNEY, J. J., HOFMEYR, R. K., McCARTHY, T. S., and ORREN, M. J.

1971. Some inter-element relationships between lunar rocks and fines, and stony meteorites. Paper presented at Apollo 12 Lunar Science Conference, Houston, January (unpublished proceedings).

WISE, D. U., and YATES, M. T.

1970. Mascons as structural relief on a lunar 'Moho.' Journ. Geophys. Res., vol. 75, pp. 261-268.

WOOD, J. A.

1967a. Olivine and pyroxene compositions in Type II carbonaceous chondrites. Geochim. Cosmochim. Acta, vol. 31, pp. 2095-2108.

WOOD, J. A.

1967b. Chondrites: their metallic minerals, thermal histories, and parent planets. Icarus, vol. 6, pp. 1-49.

1970. Petrology of the lunar soil and geophysical implications. Journ. Geophys. Res., vol. 75, pp. 6497-6513.

1971. Thermal history and early magmatism in the moon. In The Geophysical Interpretation of the Moon, ed. by G. Simmons, in preparation.

WOOD, J. A., MARVIN, U. B., POWELL, B. N., and DICKEY, J. S., Jr.

1970. Mineralogy and petrology of the Apollo 11 lunar sample. Smithsonian Astrophys. Obs. Spec. Rep. No. 307, 99 pp.

GLOSSARY OF TERMS

We have not tried to define every scientific term used; some familiarity with mineral and rock names is assumed of the reader.

Albedo. A measure of the proportion of light incident on a surface that is reflected by that surface. A "high albedo" feature on the Moon is one that is relatively bright (light-colored).

Anhedral. See euhedral.

Armalcolite. $Mg_{0.5}Fe_{0.5}Ti_2O_5$, a new mineral found in the Apollo 11 samples and named in honor of the three Apollo 11 astronauts, Armstrong, Aldrin, and Collins.

Chromian Pleonaste. See spinel.

Chromite – Chromian Ulvöspinel. See spinel.

Detritus. Debris produced by the mechanical disintegration of a parent rock material; examples are the detrital sediment carried by a stream, the debris at the base of a cliff, and ejecta from an impact crater.

Euhedral. Adjective; referring to a mineral grain all of whose edges are well-defined crystal faces. The opposite of euhedral is anhedral, where the mineral grain has an irregular shape unrelated to its crystal structure. A grain exhibiting intermediate character (some crystal faces) is said to be subhedral.

Geikielite. See ilmenite.

Ilmenite. $FeTiO_3$, a black opaque mineral common in the lunar basalts. Substitution of Mg for Fe gives rise to compositions grading into geikielite, $MgTiO_3$.

Isostasy. A state of buoyant equilibrium that can exist between arbitrarily defined blocks of a planet's crust, as if the blocks were floating in a liquid bath. Under these circumstances, if block A is thicker than block B, or made of a lower density material than B, the upper surface of A will stand at a higher elevation than that of B.

Mafic. Adjective; rich in Mg and Fe.

Maskelynite. A glass equivalent in composition to plagioclase, from which it formed by shock. The glass often retains the lath-like outline of the original plagioclase crystal.

Mesostasis. See porphyritic.

Metamict. Adjective; referring to a mineral whose crystalline structure has been damaged by radiation, usually from decay of uranium and thorium impurities within the mineral itself.

Micrographic. Adjective; referring to rock textures in which quartz and alkali feldspar are intergrown, on a microscopic scale, in such a regular pattern as to resemble cuniform writing.

Microlites. Extremely tiny (microns) crystals.

Modal Composition. A statement of the relative proportions of the minerals actually composing a rock, as determined by a systematic survey of a section of the rock under a microscope (see, for comparison, normative composition).

Myrmekitic. A texture occurring in some terrestrial igneous rocks, in which minute worm-like bodies of one mineral are enclosed by a second phase. The term myrmekite applies specifically to the case where worm-like fingers of quartz are enclosed by plagioclase.

Norm. A type of recalculation of rock analyses done to facilitate their petrologic interpretation. Major element analyses are recalculated into a set of simple mineral molecules by a standard set of manipulations, with the expectation that the derived set of normative minerals corresponds approximately to those actually present. A rough idea of the mafic vs. sialic nature of a rock is seen in its quantity of normative olivine, or in its absence, of normative quartz. It is often convenient to lump certain groups of normative minerals together, giving rise to terms such as normative mafics (normative olivine plus pyroxene), normative feldspars and feldspathoids (orthoclase, albite plus anorthite; nepheline plus leucite) and normative oxides (ilmenite, rutile, chromite, wustite, periclase, quartz, and corundum). The table below lists the normative minerals used in our work along with their molecular formulas.

forsterite	Mg_2SiO_4	normative olivine	normative mafics
fayalite	Fe_2SiO_4		
enstatite	$MgSiO_3$	normative pyroxene	
ferrosilite	$FeSiO_3$		
wollastonite	$CaSiO_3$		
orthoclase	$KAlSi_3O_8$	normative feldspar	
albite	$NaAlSi_3O_8$		
anorthite	$CaAl_2Si_2O_8$		
nepheline	$NaAlSiO_4$	normative feldspathoid	
leucite	$KAlSi_2O_6$		

ilmenite	$FeTiO_3$	normative oxide
rutile	TiO_2	
chromite	$FeCr_2O_4$	
wustite	FeO	
periclase	MgO	
quartz	SiO_2	
corundum	Al_2O_3	

Normative "quarfeloids" is the sum of normative quartz, feldspar, and feldspathoids.

Normative Composition. See norm.

Normative Feldspathoids. See norm.

Normative Quartz. See norm.

Ophitic. Adjective; of an igneous texture in which euhedral plagioclase laths are intergrown with coarse subhedral pyroxene, and in thin section appear to be largely or entirely enclosed by the pyroxene. When the feldspars are longer than the average pyroxene grain dimension, the pyroxene only partially encloses the average plagioclase grain, and the texture is said to be subophitic.

Perthite. An intergrowth of a sodic and potassic feldspar, resulting from exsolution. At high temperatures the solid solution between Na-rich and K-rich feldspars is complete, but an initially homogeneous feldspar of intermediate composition will, upon cooling, become unstable and a finely laminated two-feldspar perthite becomes the stable form.

Phenocryst. See porphyritic.

Pleonaste. See spinel.

Poikilitic. Adjective; describing an igneous rock texture in which early crystallizing phases are enclosed by large continuous crystals of a later crystallizing phase. In some of the coarser basalts from Apollo 12, late-crystallizing plagioclase encloses earlier olivines, pyroxenes, and spinels, resulting in a poikilitic texture.

Porphyritic. Adjective; of an igneous rock texture in which large crystals (phenocrysts) are imbedded in a fine-grained or glassy matrix, sometimes called the mesostasis. The texture suggests a two-stage cooling history: an early period of slow cooling during which the large phenocrysts formed, followed by a rapid solidification of the remaining liquid to a fine-grained matrix or mesostasis. The abrupt increase in the cooling rate usually occurs when the liquid and its early phenocrysts are erupted onto a planetary surface.

Pyroxferroite. An iron-rich pyroxenoid with a composition intermediate to ferrosilite ($FeSiO_3$) and hedenbergite ($CaFeSi_2O_6$); first noted in the Apollo 11 lunar materials.

Quarfeloids. The sum of light-colored, sialic minerals (quartz, feldspar, plus feldspathoids) present in a rock.

Rhyolite. A volcanic rock, equivalent in composition to granite. The dominant phases are orthoclase, quartz, and sodic plagioclase.

Spinel. A family of oxide minerals of the form AB_2O_4. Varieties include chromite ($FeCr_2O_4$), true spinel ($MgAl_2O_4$), hercynite ($FeAl_2O_4$), and ulvöspinel (Fe_2TiO_4). In the Apollo 12 basalts, a complete gradation exists between aluminous chromite ($(Mg, Fe)(Cr, Al)_2O_4$) and chromian ulvöspinel (see Figures IIA-30 and IIA-32). The term pleonaste describes spinels along the join ($MgAl_2O_4$-$FeAl_2O_4$) for which the Mg/Fe ratio ranges from 3 to 1. Chromian pleonaste also involves a certain amount of substitution of Cr for Al.

Subhedral. See euhedral.

Subophitic. See ophitic.

Ulvöspinel. See spinel.

Variolitic. Adjective; of an igneous texture in which sheaves of several minerals, each in extremely elongate crystals, occur in radiating patterns, often interstitial to larger earlier formed phenocrysts (see Figure IIA-4, IIA-5, and IIA-16). The texture results from rapid crystallization.

Xenocryst. A large crystal genetically unrelated to the fine-grained matrix in which it was incorporated. It might have been detached from the wall of a fissure the magma passed through, for example. A phenocryst, by contrast, is genetically related to its fine-grained matrix.

BIOGRAPHICAL NOTES

JOHN A. WOOD received the B.S. degree from Virginia Polytechnic Institute in 1954 and the Ph.D. degree from the Massachusetts Institute of Technology in 1958.

Dr. Wood was a research associate at the Enrico Fermi Institute for Nuclear Studies at the University of Chicago from 1963 to 1965. Since 1965, he has been a geologist at SAO and a research associate at Harvard University.

Dr. Wood's general fields of investigation are chemical analyses and mineralogical studies of meteoritic and lunar material; the study of primitive planetary material, specifically meteorites; and the problem of the origin of the planets and the solar system in general.

URSULA B. MARVIN received the B.A. degree from Tufts University, and the A.M. and Ph.D. degrees from Harvard University in geology.

Her career includes three years of teaching mineralogy and petrology at Tufts University, and six years of laboratory and field investigations of mineral deposits in the United States, Brazil, and West Africa.

Dr. Marvin joined the staff of the Smithsonian Astrophysical Observatory as a geologist in 1961 and became an associate of Harvard in 1965.

Her primary fields of investigation are mineralogical studies of lunar samples, meteorites, and the identification of cosmic dust. She is also interested in impact structures and the geological implications of satellite geodesy.

JOHN B. REID, Jr., was graduated from Williams College with a major in physics in 1962. He taught high school physics for three years before entering the Massachusetts Institute of Technology, where he received the Ph. D. degree in geochemistry in September 1970. He has been on the SAO staff since then.

Dr. Reid's interests are in the nature of planetary interiors and the processes by which volcanic rocks are generated from them.

G. JEFFREY TAYLOR graduated from Colgate University in 1966, with an A. B. in physics. He received the Ph. D. in geology from Rice University in 1970 and has been doing scientific research at the SAO since September 1970.

Dr. Taylor is interested in the chemistry and mineralogy of meteorites and lunar samples.

JANICE F. BOWER received her B. A. at Coe College in 1946.

She has been an electron microprobe analyst at SAO since 1967.

BENJAMIN N. POWELL was graduated from Amherst College in 1963, with a major in geology. He received the Ph. D. in geology from Columbia University in January 1969. Dr. Powell was a member of the SAO staff from January 1969 until August 1970. His present address is Rice University, Department of Geology, Houston, Texas.

Dr. Powell is an igneous petrologist, currently specializing in the study of extraterrestrial materials, including meteorites and lunar samples.

JOHN S. DICKEY, Jr., received his Ph. D. in geology from Princeton University in 1969. Dr. Dickey was a member of the SAO staff from January 1969 until August 1970. His present address is the Geophysical Laboratory, Carnegie Institution of Washington, Washington, D. C.

Dr. Dickey is a petrologist, specializing in the chemistry of igneous rocks.

NOTICE

This series of Special Reports was instituted under the supervision of Dr. F. L. Whipple, Director of the Astrophysical Observatory of the Smithsonian Institution, shortly after the launching of the first artificial earth satellite on October 4, 1957. Contributions come from the Staff of the Observatory.

First issued to ensure the immediate dissemination of data for satellite tracking, the reports have continued to provide a rapid distribution of catalogs of satellite observations, orbital information, and preliminary results of data analyses prior to formal publication in the appropriate journals. The Reports are also used extensively for the rapid publication of preliminary or special results in other fields of astrophysics.

The Reports are regularly distributed to all institutions participating in the U. S. space research program and to individual scientists who request them from the Publications Division, Distribution Section, Smithsonian Astrophysical Observatory, Cambridge, Massachusetts 02138.